Quantum Many-Body Dynamics of a Disordered Electronic Spin Ensemble in Diamond

Citation	Choi, Joonhee. 2019. Quantum Many-Body Dynamics of a Disordered Electronic Spin Ensemble in Diamond. Doctoral dissertation, Harvard University, Graduate School of Arts & Sciences.
Citable link	http://nrs.harvard.edu/urn-3:HUL.InstRepos:42029771
Terms of Use	This article was downloaded from Harvard University's DASH repository, and is made available under the terms and conditions applicable to Other Posted Material, as set forth at http://nrs.harvard.edu/urn-3:HUL.InstRepos:dash.current.terms-of-use#LAA

Quantum Many-body Dynamics of a Disordered Electronic Spin Ensemble in Diamond

A dissertation presented
by

Joonhee Choi

to
The School of Engineering and Applied Sciences
in partial fulfillment of the requirements
for the degree of
Doctor of Philosophy
in the subject of

Applied Physics

Harvard University
Cambridge, Massachusetts
April 2019

Dissertation Advisor: Author

Professor Mikhail D. Lukin **Joonhee Choi**

Quantum Many-body Dynamics of a Disordered Electronic Spin Ensemble in Diamond

Abstract

A strongly interacting driven spin system can display a variety of interesting many-body quantum phenomena due to the interplay of interaction, disorder and coherent driving. Using a dense electronic spin ensemble of atom-like impurities in diamond, we study non-equilibrium quantum many-body dynamics involving $\sim 10^6$ spins. Specifically, we describe: (1) investigation of thermalization dynamics of a closed quantum system in the presence of long-range interactions and on-site disorder, (2) realization of new non-equilibrium phases of matter, such as discrete time crystals, and (3) probing emergent phase transitions in a driven many-body system. In addition, the high-density spin ensembles in the solid state also show great promise for practical sensing applications. As a practical application of these studies, we demonstrate high sensitivity magnetic-field sensing with fault-tolerant pulsed control. These studies demonstrate that dense electronic spin ensembles in the solid state can be a powerful tool to simulate quantum many-body dynamics, explore new coherent non-equilibrium phenomena and to detect external signals with superior sensitivity and high spectral and spatial resolution.

Contents

Citations to Previously Published Work

Most of the chapters in this thesis have previously appeared in print elsewhere. These are:

Chapter 2 and Appendix A:

> **Joonhee Choi***, Soonwon Choi*, Georg Kucsko*, Peter C. Maurer, Brendan J. Shields, Hitoshi Sumiya, Shinobu Onoda, Junichi Isoya, Eugene Demler, Fedor Jelezko, Norman Y. Yao, Mikhail D. Lukin, *Depolarization dynamics in a strongly interacting solid-state spin ensemble*, Phys. Rev. Lett. **118**, 093601 (2016)

Chapter 3 and Appendix B:

> Georg Kucsko*, Soonwon Choi*, **Joonhee Choi***, Peter C. Maurer, Hengyun Zhou, Renate Landig, Hitoshi Sumiya, Shinobu Onoda, Junich Isoya, Fedor Jelezko, Eugene Demler, Norman Y. Yao, Mikhail D. Lukin, *Critical thermalization of a disordered dipolar spin system in diamond*, Phys. Rev. Lett. **121**, 023601 (2018)

Chapter 4 and Appendix C:

> Soonwon Choi*, **Joonhee Choi***, Renate Landig*, Georg Kucsko, Hengyun Zhou, Junichi Isoya, Fedor Jelezko, Shinobu Onoda, Hitoshi Sumiya, Vedika Khemani, Curt von Keyserlingk, Norman Y. Yao, Eugene Demler, Mikhail D. Lukin, *Observation of discrete time-crystalline order in a disordered dipolar many-body system*, Nature **543**, 221-225 (2017)

Chapter 5 and Appendix D:

> **Joonhee Choi***, Hengyun Zhou*, Soonwon Choi, Renate Landig, Wen Wei Ho, Junichi Isoya, Fedor Jelezko, Shinobu Onoda, Hitoshi Sumiya, Dmitry A. Abanin, and Mikhail D. Lukin, *Probing quantum thermalization of a disordered dipolar spin ensemble with discrete time-crystalline order*, Phys. Rev. Lett. **122**, 043603 (2019)

* These authors contributed equally to this work.

Acknowledgments

First and foremost, I would like to express my sincere gratitude to my advisor Mikhail Lukin. Initially, when I started the Ph.D. program, I hoped to work on something new and exciting that is quite different from what I had studied before. After spending a year as a rotation student, I was lucky to join Misha's group. When starting in his group, I was very much impressed by not only the exciting research themes of the group but also a unique family-like lab culture. Looking back at my time here, I can absolutely say that conducting research in Misha's group was my turning point, illuminating an exciting path forward. I deeply appreciate Misha's persistent guidance and support as well as his great scientific insight and intuition. I also sincerely thank Federico Capasso, Philip Kim, Hongkun Park and Jene Golovchenko for being my thesis and qualifying exam committee members and giving me warm advice and support. I am also grateful to Dmitry Abanin, Eugene Demler, Fedor Jelezko, Junichi Isoya, Ronald Walsworth, Aravinthan Samuel, Paola Cappellaro, Daniel Needleman and Susan Mango for their helpful and inspirational discussions on the works presented in this thesis.

Over my Ph.D. years, I have been privileged to be part of an amazing research group and work with great people. Without collaboration and teamwork, many projects in this thesis would have not been possible. In particular, I would like to thank Georg Kucsko, Soonwon Choi, Hengyun (Harry) Zhou and Renate Landig who have been closely working with me and serving as the core members of the "Black Diamond" team. Especially, I really miss the early days when I worked with Georg and Soonwon. Georg and Soonwon are my best friends and colleagues who I have interacted with during my Ph.D. times, and are both amazingly brilliant, intelligent and creative. Georg, as a senior graduate student at the time, introduced me to experimental quantum physics at the beginning. Georg and I

have shared numerous exciting moments in the lab where we found out many interesting (or sometimes bad) results. Soonwon, as a theorist in our team, has significantly contributed to the theoretical understanding of a crazy sample, and more importantly, has been my "coffee/soju buddy". I really enjoyed working with them and directly experienced the strong power of having a collaboration between the theorist and the experimentalist. We are indeed the pioneers of black diamond research, discovering beautiful physics from scratch by slowly solving mysterious puzzles from a piece of scary dark-looking stone. Later on, Harry and Renate joined the team as a junior student and a postdoc, respectively. I truly appreciate Harry's critical viewpoints and innovative ideas. Harry has always been very impressive, extremely good at almost everything, even including basketball. I have been enjoying a lot working with Harry for the second half of my Ph.D. and there has been a lot of remarkable progress and many breakthroughs by working together with Harry. I also would like to thank Renate working with me for two years. It has been a great synergy to have her in the team. She impressively showed how to perform meticulous German-standard experiments and generously shared a secret recipe for making homemade rhubarb cake.

Moreover, I was fortunate to have close interactions with Norman Yao. I still vividly remember our endless nights in Jefferson 330, writing papers together while eating chicken wings at 3 am in the morning. It is needless to say that I have learned countless things from Norm. I do respect his enormous passion for physics (and Starcraft). I also would like to thank Peter Maurer who has been very helpful and supportive for our research. Although this thesis does not cover another exciting biology project which I have been working on, I appreciate many fruitful discussions that I have had with him.

In addition, it has been a great pleasure to work with Helena Knowles who recently joined the team and I also thank Wen Wei Ho and Vedika Khemani for their contributions to theoretical analyses for the time crystal projects. I also very much appreciate Nathalie de Leon, Ruffin Evans, Bart Machielse, Kristiaan de Greve and Andrey Sushko for their tremendous support in assisting sample fabrication and nanobeam transfer. I would also like to thank Brendan Shields, Alp Sipahigil, Christian Nguyen, David Levonian and Michael Goldman for lending their setups to help me measure important data sets.

Most of the experiments in this thesis would not have been possible without technical support by Alexander Zibrov, Stan Contreau and Jim MacArthur and administrative assistance by Samantha Dakoulas and Clare Ploucha. I deeply appreciate all their kind and constant help throughout my Ph.D. years.

My thanks extend to all Lukin group people for many fun and successful years shared in the lab. In particular, I would like to give special thanks to our sensing lab B24 members, Tamara Sumarac, Elana Urbach, Igor Lovchinsky, Alec Douglas, Philipp Vetter, Ryan Cimmino and Xiaofei Yu, for sharing fun and productive times with me. In addition, my six years at Harvard are full of happy memories, laughter and fun moments due to the presence of many friends outside the Lukin lab as well - Young-Ik Sohn, Hyungmok Son, Minjae Cho, Jong Yeon Lee, Seung Hwan Lee, Sooshin Kim, Junghyun Lee, Junhyun Lee, Jaehoon Lee, Donggyu Kim, Nanxi Li, Nabila Tanjeem, Hemant Gandhi and Li Yu.

Finally, I would like to thank my parents and wife, Sawool Kim, for their endless love, support and encouragement.

To my parents, and my wife Sawool Kim.

Chapter 1

Introduction

1.1 Motivation

In recent years the ability to isolate, control and measure quantum systems such as atoms and photons has reached an unprecedented level, opening the door to new powerful technologies that harness quantum mechanical effects. In particular, there has been remarkable progress in the realization and manipulation of coherent many-body systems, which can provide insights into strongly correlated quantum dynamics, illuminate the role of quantum entanglement in information processing, and enable discoveries and studies of new states of matter.

In particular, electronic spins in the solid state are interesting many-body systems since they exhibit coherent quantum dynamics with favorable properties. One example is the nitrogen-vacancy (NV) center in diamond, which provides a number of remarkable features for quantum applications ranging from quantum information processing to quantum sensing. For instance, the NV center has an isolated spin degree of freedom which can be manipulated and read out by optical and microwave fields with high precision. The spin lifetime and quantum coherence of the NV center is surprisingly long compared to other solid-state spin systems, allowing them to reliably operate at room temperature under ambient conditions. More crucially, each NV center can coherently interact with multiple NV centers at a distance via long-range magnetic dipolar interactions, which gives rise to quantum correlations and entanglement of a large number of spins. In diamond, there are also other types of impurities, such as P_1 centers and ^{13}C nuclear spins, serving as the environment of NV ensembles. The coupling between such impurities and NV centers generates on-site disorder potentials, leading to inhomogeneous broadening of spin-resonance frequencies. Such disorder potentials usually give rise to a decay of quantum coherence; however, one can effectively isolate the NV centers from the environment by employing dynamical decoupling schemes.

Due to such remarkable properties, recently there has been an increasing interest in fabricating high-density NV-based electronic spin ensembles. The interacting NV spin ensemble with strong disorder is a promising platform to investigate quantum many-body dynamics for fundamental physics as well as for potential applications. For example, a disordered quantum system may evade heating even in the presence of periodic driving if the drive frequency is sufficiently fast. This is quite surprising since the external drive is typically expected to cause the system to heat up to infinite temperature. Periodic driving in the regime of high frequency can thus be used to explore exotic quantum behavior, such as the emergence of a new phase of matter−the discrete time crystals. On the practical side, spin ensembles periodically driven at a particular frequency can also detect external signals, such as AC magnetic fields, with superior sensitivity due to the large number of sensor spins inside a small detection volume. The versatility and flexibility of the NV-ensemble spin system will keep providing unique opportunities for understanding complex many-body dynamics and for gaining insight into its future use in quantum technologies.

1.2 Overview

In this thesis, we present multiple studies exploring quantum many-body dynamics in a disordered electronic spin system in diamond. In particular, we demonstrate that the interplay of long-range interactions, on-site disorder, and coherent driving in many-body systems can lead to a variety of interesting quantum phenomena, such as slow sub-diffusive thermalization and new phases of matter in non-equilibrium conditions. In addition, we also show that the dense electronic spin ensemble can serve as an ultra-sensitive quantum sensor with superior sensitivity and high spectral and spatial resolution, opening up new avenues of applications in quantum metrology.

1.2.1 Anomalous depolarization of interacting spin ensembles

In Chapter 2, we study the depolarization dynamics of a dense ensemble of dipolar interacting spins, associated with nitrogen-vacancy centers in diamond. We observe anomalously fast, density-dependent, and non-exponential spin relaxation. To explain these observations, we propose a microscopic model where an interplay of long-range interactions, disorder, and dissipation leads to predictions that are in quantitative agreement with both current and prior experimental results.

1.2.2 Critical quantum thermalization of a disordered spin system

In Chapter 3, we report the observation of critical thermalization in a three dimensional ensemble of $\sim 10^6$ electronic spins coupled via dipolar interactions. Statistical mechanics underlies our understanding of macroscopic quantum systems. It is based on the assumption that out-of-equilibrium systems rapidly approach their equilibrium states, forgetting any information about their microscopic initial conditions. This fundamental paradigm is challenged by disordered systems, in which a slowdown or even absence of thermalization is expected. By controlling the spin states of nitrogen vacancy color centers in diamond, we observe slow, subexponential relaxation dynamics and identify a regime of power-law decay with disorder-dependent exponents; this behavior is modified at late times owing to many-body interactions. These observations are quantitatively explained by a resonance counting theory that incorporates the effects of both disorder and interactions.

1.2.3 Discrete time-crystalline order in a driven quantum system

In Chapter 4, we report the experimental observation of a new phase of matter in non-equilibrium conditions. Understanding quantum dynamics away from equilibrium is an outstanding challenge in the modern physical sciences. It is well known that out-of-equilibrium systems can display a rich array of phenomena, ranging from self-organized synchronization to dynamical phase transitions [1, 2]. More recently, advances in the controlled manipulation of isolated many-body systems have enabled detailed studies of non-equilibrium phases in strongly interacting quantum matter [3, 4, 5, 6]. As a particularly striking example, the interplay of periodic driving, disorder, and strong interactions has recently been predicted to result in exotic "time-crystalline" phases [7, 8], which spontaneously break the discrete time-translation symmetry of the underlying drive [9, 10, 11, 12]. Here, we report the experimental observation of such discrete time-crystalline order in a driven, disordered ensemble of $\sim 10^6$ dipolar spin impurities in diamond at room-temperature [13, 14, 15]. We observe long-lived temporal correlations at integer multiples of the fundamental driving period, experimentally identify the phase boundary and find that the temporal order is protected by strong interactions; this order is remarkably stable against perturbations, even in the presence of slow thermalization [16, 17]. Our work opens the door to exploring dynamical phases of matter and controlling interacting, disordered many-body systems [18, 19, 20].

1.2.4 Stability of discrete time crystal as a probe of thermalization

In Chapter 5, we investigate thermalization dynamics of a driven dipolar many-body quantum system through the stability of discrete time crystalline order. Using periodic driving of electronic spin impurities in diamond, we realize different types of interactions between spins and demonstrate experimentally that the interplay of disorder, driving, and interactions leads to several qualitatively distinct regimes of thermalization. For short driving periods, the observed dynamics are well described by an effective Hamiltonian which sensitively depends on interaction details. For long driving periods, the system becomes susceptible to energy exchange with the driving field and eventually enters a universal thermalizing regime, where the dynamics can be described by interaction-induced dephasing of individual spins. Our analysis reveals important differences between thermalization of long-range Ising and other dipolar spin models.

1.2.5 Quantum sensing with fault-tolerant control

In Chapter 6, we report the application of a dense spin ensemble for high-sensitivity metrology with fault-tolerant control. Quantum sensing allows the detection of weak signals with high sensitivity and precision, enabling a myriad of applications ranging from nanoscale nuclear magnetic resonance spectroscopy of biomolecules to local probing of exotic condensed matter phenomena. In principle, the sensitivity can be improved by increasing the density of sensors in a given volume; however, beyond a critical density, this improvement is severely hindered by undesirable interactions between the sensors themselves as well as increased inhomogeneity. Here, using a dense ensemble of dipolar interacting electronic spins in diamond, we demonstrate a novel approach to detecting oscillating magnetic fields that overcomes such limitations. By designing a robust pulse sequence that decouples interactions and disorder, and is simultaneously fault-tolerant to the leading-order control imperfections of the system, our method enables a five-fold enhancement in coherence time compared to the conventional XY-8 sequence. Combined with optimal initialization and readout protocols, we demonstrate a 30% enhancement in sensitivity relative to the XY-8 sequence, breaking the sensitivity limit imposed by interactions. This opens a promising avenue for the development of nanoscale ensemble magnetometers with unprecedented sensitivity.

Chapter 2

Depolarization Dynamics in a Strongly Interacting Solid-State Spin Ensemble

2.1 Introduction

Electronic spins associated with solid-state point defects are promising candidates for the realization of quantum bits and their novel applications [21, 22, 23, 24, 25]. In particular, the precise quantum control of *individual* nitrogen-vacancy (NV) centers in diamond has led to advances in both fundamental physics [26, 27, 28] and the development of applications ranging from nanoscale sensing to quantum information science [24, 29, 30, 31, 32, 33, 34]. This high degree of control naturally suggests the use of strongly interacting, *dense* NV ensembles to explore quantum many-body dynamics. Indeed, recent experiments demonstrate that such a system is a promising testbed to study controlled many-body spin dynamics and novel quantum phases of matter [17, 35].

However, a key challenge in this context is the apparent reduction of the electronic spin lifetime at high defect densities [36, 37]. Such effects were first observed in phosphorus doped silicon over five decades ago [38], where it was suggested that anomalously fast spin relaxation could arise from electronic hopping between nearby impurities. In addition to reduced spin lifetimes, recent experiments in dense NV ensembles have also observed that this relaxation is relatively insensitive to temperature over a wide range [36, 37], implying that the underlying mechanism is qualitatively different from the phonon-induced depolarization of single, isolated NV centers [39].

In this study, we characterize the depolarization dynamics of high-density NV ensembles at room temperature. In particular, we perform spin lifetime measurements under different conditions, varying initial state populations, resonant spin densities, and microwave driving strength. To explain the observed features in the spin dynamics, we introduce a spin-fluctuator model, in which a network of short-lived spins (fluctuators) causes depolarization of nearby NV centers via dipolar interactions. Moreover, additional measurements reveal the presence of charge dynamics, providing a potential microscopic origin for such fluctuators.

2.2 Experimental results

Our sample is fabricated from a type-Ib HPHT single crystal diamond with an initial nitrogen concentration of $\sim$100 ppm. The sample is irradiated with high energy electrons at $\sim$2 MeV to create vacancies. A high concentration of NV centers was achieved via high fluence and *in situ* annealing. The resulting sample contains ~ 45 ppm of NV centers, corresponding to a typical dipolar interaction strength, $J \sim (2\pi)$ 420 kHz. The high spin density and strong NV-NV interactions are confirmed by independent measurements [17].

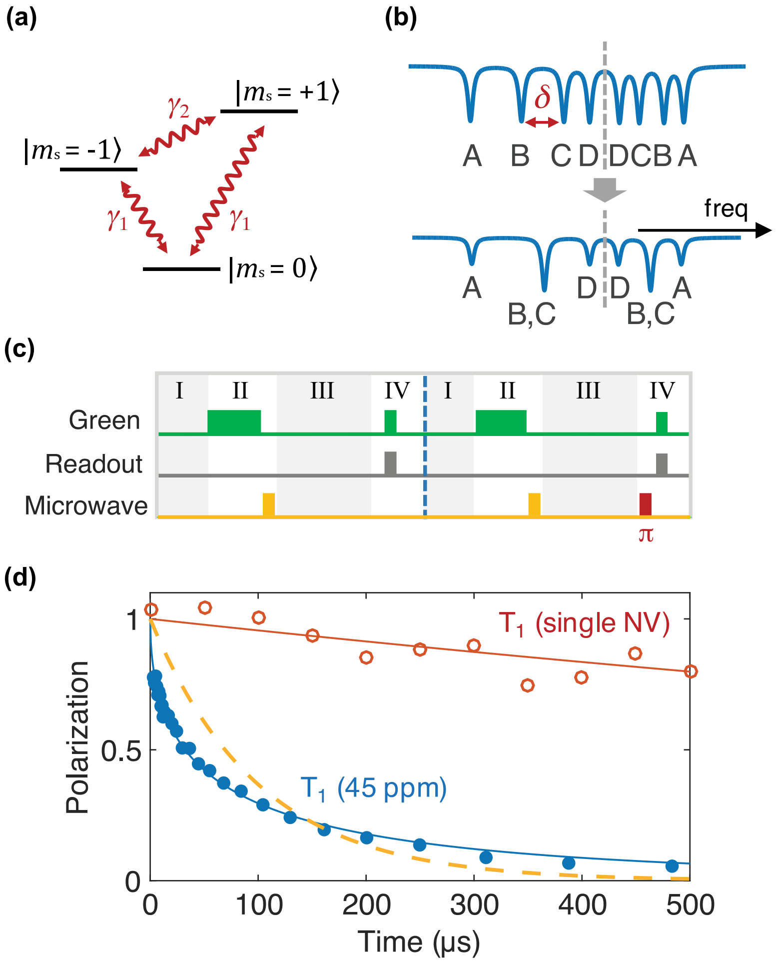

Figure 2.1: **Experimental System.** **(a)** Level diagram for NV centers. The degeneracy of the $|m_s = \pm 1\rangle$ spin states can be lifted by an external magnetic field. Red arrows indicate possible spin decay channels, γ_1 and γ_2. **(b)** Schematic electron spin resonance (ESR) spectrum of four groups of NV centers A,B,C,D with spectral separation δ between B and C (upper curve). The effective density of resonant spins can be tuned by changing the orientation of the external magnetic field (lower curve). **(c)** Experimental sequence used to measure NV dynamics. I: charge equilibration (~ 100 μs duration); II: spin polarization (10 μW laser power, ~ 200 μs duration) and subsequent microwave manipulation to modify the initial state; III: time evolution; IV: spin state readout. Red π-pulse is used to measure the population in an orthogonal state. **(d)** Comparison of depolarization timescales between a single NV (red data, exponential fit) and a dense ensemble of NVs (~ 45 ppm, blue data, stretched-exponential fit with $T_1 \sim 67$ μs). The dashed line is a simple exponential curve with a time constant of 100 μs for comparison.

To achieve a high degree of spatial control over the optical excitation region, a diamond nanobeam (300 nm × 300 nm × 20 μm) is created via angle-etching and used for all experiments in this work unless otherwise noted.

Each NV center constitutes an effective spin-1 system, which can be optically initialized, manipulated, and read out at ambient conditions [40]. In the absence of an external magnetic field, the spin states $|m_s = \pm 1\rangle$ are separated from the $|m_s = 0\rangle$ state by a crystal field splitting $\Delta_0 = (2\pi)\, 2.87$ GHz. Applying a magnetic field further splits the $|m_s = \pm 1\rangle$ states via a Zeeman shift, which is proportional to the projection of the field onto the NV quantization axis (Fig. 2.1a). Since NVs can be oriented along any of the four crystallographic axes of the diamond lattice, we can spectrally separate four groups of NV centers $\{A, B, C, D\}$ and independently control them via coherent microwave driving (Fig. 2.1b). By tuning the direction of the magnetic field, we can additionally tune the number of spectrally overlapping groups and hence the effective density of spins.

To probe the depolarization dynamics of strongly interacting NV ensembles, we utilize the pulse sequence illustrated in Fig. 2.1c. This sequence allows one to prepare and measure the population in an arbitrary spin state. By repeating a specific sequence with an additional π-pulse (right panel, Fig. 2.1c), one measures the population of an orthogonal spin state and can use the difference between the two measurements, $P(t)$, to extract the depolarization dynamics [36].

To begin, we measure the depolarization time for a subensemble of NV centers with a particular orientation (Fig. 2.1d). The observed decay time $T_1 \lesssim 100\ \mu s$ is significantly reduced when compared to isolated NVs, where typical lifetimes reach several milliseconds at room temperature [41, 42, 43]. Moreover, the decay profile deviates from a simple exponential. Phenomenologically we find that it is characterized by a stretched exponential with exponent 1/2

$$P(t) = e^{-\sqrt{t/T_1}}, \tag{2.1}$$

consistent with several previous observations [36, 37, 43]. At different spatial locations, the extracted T_1 exhibits small variations possibly due to an inhomogeneous NV concentration.

The depolarization dynamics associated with differing spin states is shown in Fig. 2.2a,b.

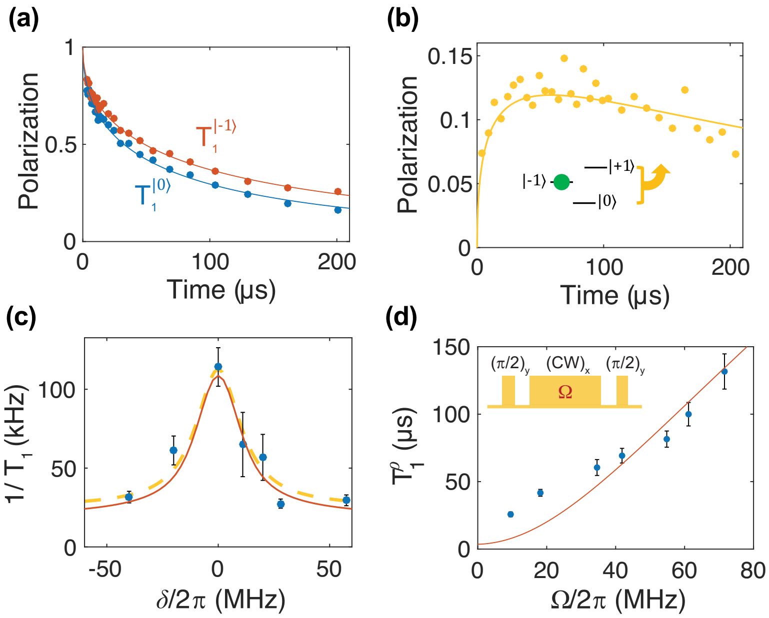

Figure 2.2: **Depolarization Dynamics.** **(a)** NV depolarization timescale probed for different initial states. Solid lines represent stretched-exponential fits with corresponding T_1 of 56 ± 2 μs ($|m_s = 0\rangle$, blue data) and 80 ± 2 μs ($|m_s = -1\rangle$, red data). **(b)** Population difference between $|m_s = 0\rangle$ and $|m_s = 1\rangle$ as a function of time for initialization into $|m_s = -1\rangle$. Solid line corresponds to a rate equation model of magnetic noise induced spin depolarization (see Appendix A). **(c)** Measured depolarization rates, $1/T_1$, as a function of the spectral distance, δ, between two subensembles B and C. A Lorentzian fit (dashed orange line) is used to extract the full width at half maximum (FWHM) of (2π) 25 ± 6 MHz. **(d)** Spin-lock lifetime T_1^ρ as a function of driving strength Ω. In (c) and (d), red lines indicate the predictions from the spin-fluctuator model at an optimized value of $n_f = 16$ ppm and $\gamma_f = (2\pi)$ 3.3 MHz.

For an initial state $|m_s = 0\rangle$, we find a decay time of $T_1 \sim 56$ μs. For an initial state $|m_s = -1\rangle$, however, we observe an extended lifetime, $T_1 \sim 80$ μs, suggesting that the depolarization mechanism is spin-state dependent (Fig. 2.2a). This is further confirmed by monitoring the population difference between $|m_s = 0\rangle$ and $|m_s = 1\rangle$ after initialization into $|m_s = -1\rangle$ (Fig. 2.2b). We find that the $|m_s = -1\rangle$ state preferentially decays into the $|m_s = 0\rangle$ state, before reaching a maximally mixed state. Such preferential decay at room temperature is a strong signature that depolarization is induced by an effective magnetic noise [44].

Our next set of measurements probes the density dependence of the NV ensemble's relaxation rate. By tuning the external magnetic field, we can bring two groups of NVs with different orientations of the NV axis into resonance (Fig. 2.1b). We monitor the depolarization rate of group B, initialized in $|m_s = 0\rangle$, as a function of detuning δ between group B and C. As depicted in Fig. 2.2c, the depolarization rate increases by a factor of ~ 4 as the two subensembles become degenerate, suggesting that interactions among NV centers play an important role in the depolarization mechanism. Interestingly, the measured width $\Gamma = (2\pi)$ 25 ± 6 MHz of this resonant feature significantly exceeds the inhomogeneous linewidth of our sample, $W = (2\pi)$ 9.3 ± 0.4 MHz (extracted from an electron spin resonance measurement) as well as the typical dipolar interaction strength [17]. These results imply that the effective magnetic noise originates from interactions among NV centers with a correlation time $\sim 1/\Gamma$.

We further investigate the role of interactions in the depolarization dynamics by performing a spin-locking measurement [45]. The spins are initialized into a superposition state $|+\rangle = (|m_s = 0\rangle + |m_s = -1\rangle)/\sqrt{2}$ and strong microwave driving is then applied along the axis coinciding with this spin state. The driving defines a new dressed-state basis with eigenstates $|+\rangle$ and $|-\rangle = (|m_s = 0\rangle - |m_s = -1\rangle)/\sqrt{2}$, separated in energy by the Rabi frequency of the microwave field, Ω (see Appendix A). Following time evolution, the population difference between the $|\pm\rangle$ states is measured.

In the context of NMR, spin-locking is known to decouple nuclear spins from their environment and to suppress dipolar exchange interactions by a factor of two [46, 47]. However, in our case, the combination of spin-locking and the $S = 1$ nature of the NV can cause a *full* suppression of the flip-flop interactions between the $|\pm\rangle$ states at large Ω [17]. We measure the spin-locking relaxation time, T_1^ρ, as a function of Ω as shown in Fig. 2.2d. At large Ω, we find that T_1^ρ is extended well beyond the bare lifetime T_1.

2.3 Spin-fluctuator model

One possible mechanism for the fast, density-dependent depolarization observed above is collectively enhanced spontaneous emission (superradiance) [48]. Indeed, in our system, the average NV separation is well below the wavelength of resonant phonons, potentially enabling multiple spins to couple with a single phonon mode. However, the lack of temperature dependence observed in high density samples is inconsistent with a phonon-limited spin lifetime [36]. Another possible explanation is related to spin diffusion induced by dipolar interactions [49]. However, dipolar spin diffusion predominantly affects the boundary of the probed region, and a quantitative estimate suggests a decay which is significantly slower than the observed timescale (see Appendix A).

To explain our observations, we now introduce a simple phenomenological model, in which we assume that a certain fraction of NV centers undergo rapid incoherent depo-

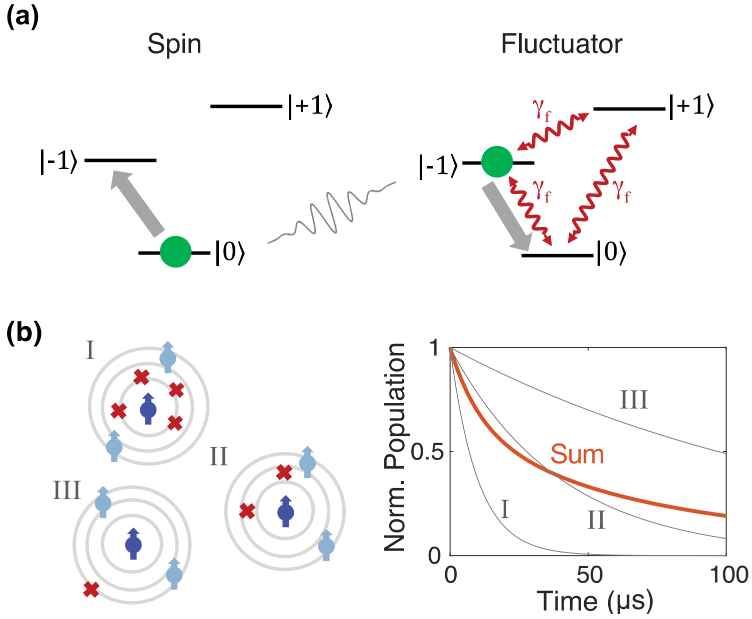

Figure 2.3: **Spin-Fluctuator Model.** **(a)** Level diagram of a single spin and fluctuator in two different spin states (green disk). Red arrows indicate fast depolarization channels of a fluctuator. Solid gray arrows depict spin exchange via dipolar interactions between spin and fluctuator. **(b)** Schematic representation of several spins I, II, and III (dark blue) in the ensemble with different depolarization rates owing to random positions of surrounding fluctuators (red crosses). Ensemble averaging of such depolarization rates gives rise to a stretched exponential (red solid line).

larization, providing a mechanism for local energy relaxation [50, 51]. These short-lived spins (termed fluctuators) can then lead to depolarization of the entire ensemble via dipolar interactions (Fig. 2.3a).

We now focus on the quantitative analysis of ensemble depolarization arising from the interplay of dipolar interactions, disorder, and dissipative fluctuator dynamics. Let us assume that fluctuators are randomly positioned in the lattice at density n_f and depolarize at rate γ_f (Fig. 2.3a). When γ_f dominates the dipolar interaction strength, each fluctuator can be treated as a localized magnetic noise source with spectral width $2\gamma_f$ (half width at half maximum). From Fermi's Golden rule, the depolarization rate of an NV spin induced by a nearby fluctuator is

$$\gamma_s(\vec{r}) \sim \left(\frac{J_0}{r^3}\right)^2 \frac{2\gamma_f}{(\delta\omega)^2 + (2\gamma_f)^2} \tag{2.2}$$

where $\vec{r}$ is distance between the fluctuator and the spin, $J_0 = (2\pi)\,52\,\text{MHz}\cdot\text{nm}^3$ is the dipolar interaction strength, and $\delta\omega$ is the difference in transition frequencies from the inhomogeneous broadening W (see Appendix A). For each spin, the effective depolarization rate is obtained by summing over all fluctuator-induced decay rates: $\gamma_s^{\text{eff}} = \sum_{i\in\text{fluctuators}} \gamma_s(\vec{r}_i)$ (Fig. 2.3b). Owing to the random position of fluctuators, γ_s^{eff} follows a probability distribution, $\rho(\gamma) = e^{-1/4\gamma T}/\sqrt{4\pi\gamma^3 T}$ with the characteristic timescale

$$\frac{1}{T} = \left(\frac{4\pi n_f J_0 \bar{\eta}}{3}\right)^2 \frac{\pi}{\gamma_f}, \tag{2.3}$$

where $\bar{\eta}$ characterizes both the spin exchange matrix element (averaged over all orientations) and the inhomogeneous broadening (see Appendix A).

This model quantitatively captures all of the observations in our experiments. First, resonant dipolar interactions only allow for the exchange of a single unit of spin angular momentum, naturally explaining the spin-state dependence of the depolarization rate. Second, the stretched exponential profile of $P(t)$ arises from integrating over the distribution $\rho(\gamma_s^{\text{eff}})$; in particular, while each individual spin undergoes a simple exponential decay, the macroscopic ensemble depolarizes with an averaged profile $P(t) = \int_0^\infty \rho(\gamma) e^{-\gamma t} d\gamma = e^{-\sqrt{t/T}}$, precisely matching Eq. (1) (Fig. 2.3b). We emphasize that the functional form of $\rho(\gamma)$ results from a combination of dimensionality and the long-range power-law [52]; more generally, when the spin-spin interaction scales as $\sim 1/r^\alpha$ in a d-dimensional system, one expects a decay profile, $P(t) = \exp[-(t/T)^{d/2\alpha}]$ (see Appendix A). Third, when the two

NV groups are tuned into resonance, $\delta = 0$, the effective density of fluctuators n_f doubles, thereby enhancing the depolarization rate by a factor of ~ 4, consistent with our previous observations. By computing the effective NV decay rates $(1/T_1)$ as a function of δ and comparing with the experimental data (Fig. 2.2c), we can extract the density $n_f \sim 16$ ppm and the average decay rate of fluctuators $\gamma_f \sim (2\pi)$ 3.3 MHz (see Appendix A). Finally, the extension of the spin lifetime via spin-locking is captured by the suppression of flip-flop interactions [17]. In the ideal case, where the depolarization mechanism results only from resonant exchange, this should lead to a factor of 12 improvement in T_1^ρ as compared to T_1 (see Appendix A). However, since T_1^ρ is also affected by interactions with NV spins in non-resonant groups, we expect a more modest enhancement in the experiment. Incorporating both effects, we compare the theory-predicted lifetimes with the experimental data in Fig. 2.2d, finding reasonable agreement without any additional free parameters.

2.4 Charge dynamics

The extracted fluctuator density, $n_f \sim 16$ ppm, is a sizable fraction of the 45 ppm of NV spins present in our sample. In practice, such fluctuators may arise as a consequence of charge dynamics. More specifically, electrons may tunnel among a network of closely spaced NV centers, and as the charge state of an NV center changes, its spin state is not necessarily conserved. We note that such dynamics inevitably occur in high density spin ensembles when impurity wavefunctions overlap and foreshadow the formation of an impurity band [38].

To probe the existence of such charge hopping, we optically induce a non-equilibrium charge distribution in our bulk diamond sample and monitor the subsequent relaxation back

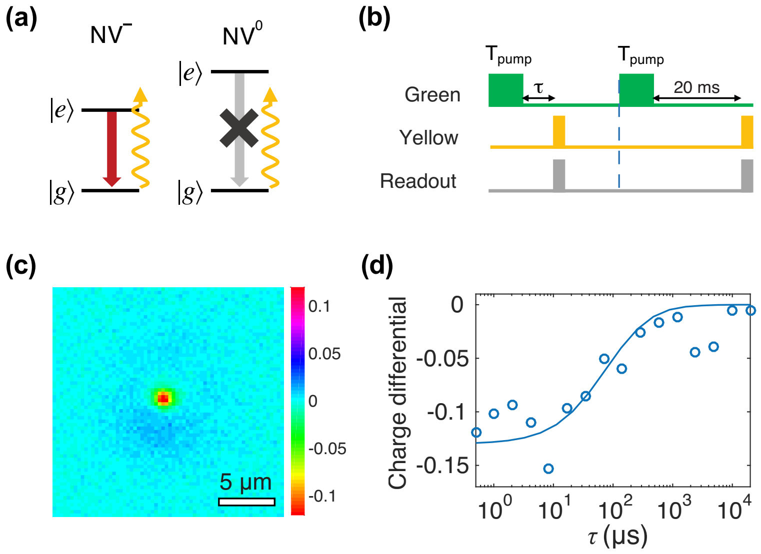

Figure 2.4: **Charge-State Dynamics** **(a)** Level diagram, showing optical ground state, $|g\rangle$, and excited state, $|e\rangle$, for NV^0 and NV$^-$ under illumination. Yellow laser (λ = 594 nm) can off-resonantly excites NV$^-$, leading to a strong fluorescence signal. NV^0, however, remains in its ground state due to a higher transition frequency, allowing optical detection of NV charge states.**(b)** Pulse sequence used to measure charge distribution. A green laser is used to create an out-of equilibrium initial state. The resulting charge distribution can be measured via short yellow laser pulses. **(c)** Relative charge distribution measured via a yellow scanning laser (27 μW) after a strong green laser illumination at the center (100 μW). **(d)** Relaxation of charge distribution at the center over time (open circles) and theoretical fit based on a classical diffusion model (solid line).

to equilibrium. In the presence of optical illumination at 532 nm, a small fraction of NV centers located at the intensity maximum are excited to the conduction band via a two photon process. Electrons in the conduction band are delocalized and can recombine with neutral nitrogen-vacancy defects (NV^0) located within a mean free path. This charge redistribution can be experimentally measured by scanning a yellow (λ = 594 nm) probe laser beam, which selectively excites NV$^-$, relative to the position of the strong ionization beam at λ = 532 nm (Fig. 2.4a,b) [26, 53]. Fig. 2.4c depicts the creation of a non-uniform charge distribution, with electron depletion at the position of the ionization beam and a surplus in the surrounding regions. By monitoring the NV charge state at the origin, after a variable dark interval, we extract a charge recovery timescale of ~ 100 μs as illustrated in Fig. 2.4d. Interestingly, this recovery occurs in the absence of both optical and thermal excitation, supporting the picture of tunneling-mediated charge diffusion. Such fluorescence dynamics have previously been observed in dilute samples on much slower timescales [54]. Using a classical diffusion equation, we find a timescale for charge hopping T_{hop} $\sim$10 ns, which is comparable to the independently extracted fluctuator decay time $1/\gamma_f$ (see Appendix A). This analysis strongly supports the hypothesis that spin fluctuators are associated with charge hopping between proximal NV centers.

2.5 Conclusion and outlook

We have investigated the depolarization dynamics in a dense ensemble of interacting NV centers and have proposed a spin-fluctuator model that quantitatively captures all of the observed dynamics. Moreover, we suggest a possible microscopic understanding for these fluctuators based on tunneling-mediated charge dynamics. We demonstrate that fluctuator-induced depolarization can be mitigated by advanced dynamical decoupling techniques. In particular, the use of spin-locking allows one to explore many-body quantum dynamics at long time scales well beyond bare T_1 [17, 35]. Furthermore, we expect that the depolarization can be controlled by altering the Fermi level via doping [55]. In such highly doped, disordered systems, experiments of the kind reported here could provide new insights into coupled spin and charge dynamics, complementary to conventional transport measurements. We also note that the experimental techniques as well as the theoretical model in the present work can be readily adapted to other types of strongly interacting, solid state spin defects. Thus, our results could provide important guidelines for understanding the nature of many-body dynamics in strongly interacting spin ensembles [56, 57].

Chapter 3

Critical Thermalization of a Disordered Dipolar Spin System in Diamond

3.1 Introduction

Nearly six decades ago, Anderson predicted that the interplay between transport and disorder in long-range-interacting quantum systems can lead to a novel regime of slow, subdiffusive thermalization [16]. This is in stark contrast to the case of short-range interactions, where he showed that disorder can arrest dynamics, resulting in the breakdown of ergodicity. Termed localization, this effect has been observed in systems ranging from acoustic waves to cold atomic gases [58, 59, 60, 61, 62]; more recently, it has been shown that localization can persist even in strongly-interacting, isolated quantum systems, a phenomenon dubbed many-body localization [3, 63, 64, 65, 66]. In addition to raising fundamental questions, such systems have also become a basis for the exploration of novel non-equilibrium phases of matter, including Floquet symmetry protected topological phases [67] and discrete time crystals [35, 68]. The addition of long-range coupling tends to facilitate delocalization, leading to a regime where both localization and ergodicity compete [56, 69]. This so-called critical regime is precisely realized by dipolar spins in 3D, where a combination of power-law transport, dimensionality, and disorder govern the microscopic dynamics. Such systems have long been explored in the context of nuclear magnetic resonance spectroscopy, where a wide variety of techniques have been developed to effectively engineer and control spin dynamics [70, 71, 72, 73, 74]. Despite this, the direct observation of slow, critical dynamics in the presence of strong, controllable disorder remains an outstanding challenge, owing in particular to difficulties in preparing a low-entropy nuclear spin state.

3.2 Experimental results

Our approach to the realization and study of critical dynamics makes use of disordered, strongly interacting electronic spin impurities associated with Nitrogen Vacancy (NV) centers in diamond. In particular, we study the thermalization dynamics of an initially polarized spin ensemble coupled to a bath of unpolarized spins (Fig. 3.1A). We directly probe the spin decay dynamics as a function of disorder and identify a regime of critically slow relaxation. Our experimental system consists of a dense ensemble of NV centers under ambient conditions (Fig. 3.1B). Each NV center constitutes a $S = 1$ electronic spin with three internal states $|m_s = \pm 1\rangle$ and $|m_s = 0\rangle$, which can be initialized, manipulated and optically read out (Fig. 3.1C). The NV concentration in our sample is approximately 45 ppm (see Appendix B), yielding an average NV-to-NV separation of 5 nm and a corresponding typical dipolar interaction strength $J \sim (2\pi)\ 420\,\text{kHz}$; crucially, this is significantly faster than the typical spin coherence times [75]. Owing to lattice strain and an abundance of other

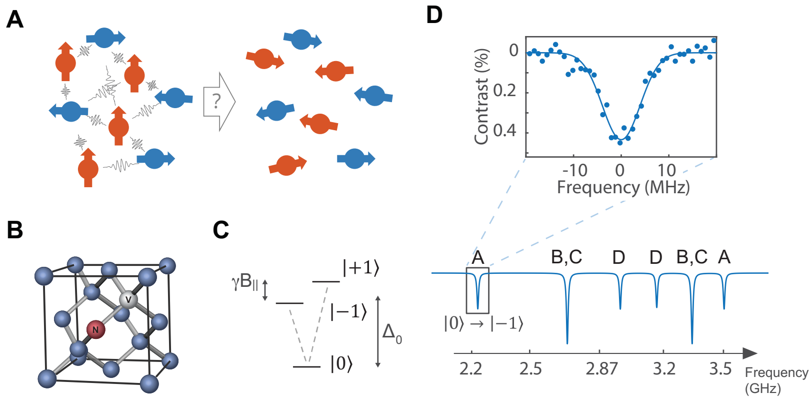

Figure 3.1: **Experimental System.** **(A)** Schematic depicting two groups of spin ensembles interacting via long-range dipolar interactions. An initially polarized system (red arrows) strongly coupled to a bath of unpolarized spins (blue arrows) will eventually thermalize to an unpolarized spin state. **(B)** The crystallographic structure of diamond contains four possible NV quantization axes, defined by the position of the nitrogen atom and the adjacent vacant lattice site. **(C)** Simplified NV level scheme showing the spin degrees of freedom in the optical ground state. A large zero-field splitting $\Delta_0 = (2\pi)$ 2.87 GHz in combination with a magnetic field induced Zeeman shift $\gamma B_{||}$ leads to individual addressability of the spin sub-levels. **(D)** The lower image shows a simulated ESR scan, revealing the spin transitions of all four NV groups $\{$A, B, C, D$\}$. For example, the orientation of the external magnetic field can be chosen in such a way that NV groups B and C experience the same magnetic field projection, leading to spectral degeneracy. The upper figure shows an ESR scan of a single transition of NV spins (blue points). Blue solid line represents a Gaussian fit with standard deviation W, corresponding to the average disorder in the sample.

paramagnetic impurities (consisting mainly of P1 centers and ^{13}C nuclear spins), our system is also characterized by strong disorder; for each NV, this disorder arises from effective random fields generated by its local environment. The magnitude of the disorder W can be directly extracted from an electron spin resonance (ESR) measurement (Fig. 3.1D), yielding a Gaussian distribution with a standard deviation $W \approx (2\pi)\ 4.0$ MHz (see Appendix B). Such an environment can also undergo its own dynamics (e.g. due to spin diffusion among the impurities), resulting in possible variation of the effective random fields over time.

Each NV center in the ensemble can be oriented along any of the four crystallographic

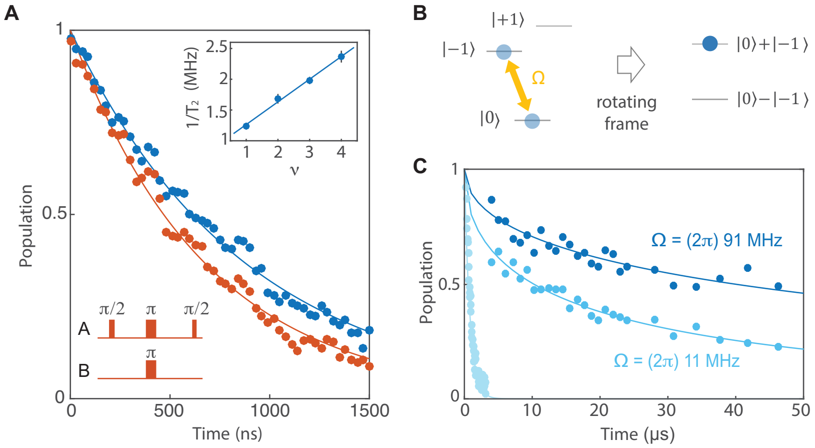

Figure 3.2: **Interacting Spin Ensemble.** **(A)** Spin echo on NV group A (blue points) and DEER scan on groups A and B (red points). The bottom left inset illustrates the DEER pulse sequence. Solid lines indicate exponential fits to the data. The inset shows the spin echo coherence time as a function of resonant NV groups (blue points). The blue solid line represents a linear fit to the data. **(B)** Schematic diagram depicting the NV level scheme during a spin-lock sequence with a driving strength Ω. In the rotating frame, the spin-locking creates a dressed spin basis with the two eigenstates $(|m_s = 0\rangle + |m_s = -1\rangle)/\sqrt{2}$ and $(|m_s = 0\rangle - |m_s = -1\rangle)/\sqrt{2}$. **(C)** Spin-lock coherence decay for low (light blue points) and high (dark blue points) CW driving power, showing significant extension beyond the spin echo decoherence (gray-blue points). The decay curves are fitted to a stretched exponential function $\exp[-\sqrt{t/T}]$ [76].

axes of the diamond lattice. Different projections of an external magnetic field naturally lead to distinct energy splittings and define four unique NV groups, {A, B, C, D}, which can be individually addressed and controlled in a finite B-field via resonant microwave radiation. By tuning the direction of the magnetic field, one can modify the number of spectrally overlapping groups (e.g. groups B, C in Fig. 3.1D) and hence the effective density of spins. To directly probe the interaction strength within our system, we perform a double electron-electron resonance (DEER) measurement between two spectrally separated NV groups, A and B (Fig. 3.2A, bottom inset). In this measurement the spin echo protocol decouples group A from slowly varying magnetic noise. However, the additional π-pulse on group B after half of the total evolution ensures that the dephasing induced by interactions between the two groups is not decoupled. As depicted in Fig. 3.2A, by comparing the decay of group A with and without the π-pulse, this measurement allows us to extract the interaction strength $\sim (2\pi)\ 420$ kHz (see Appendix B). By tuning additional NV groups into spectral resonance, we can confirm that the spin dynamics are dominated by interactions. As a function of the number of resonant groups, ν, we find a total dephasing rate, $\gamma_T = \gamma_b + \nu\gamma_0$, with $\gamma_b \approx 0.9$ MHz and $\gamma_0 \approx 0.4$ MHz, consistent with 45 ppm NV center density (Fig. 3.2A inset) (see Appendix B). The linear dependence of γ_T on ν suggests that the dephasing is dominated by coherent interactions, whose strength is proportional to the density of resonant NV groups.

Central to our thermalization experiments is the ability to tune both the disorder strength and interactions. This is achieved by using spin-locking and Hartman-Hahn (HH) resonances, both of which rely upon continuous microwave driving resonant with the $|m_s = 0\rangle \rightarrow |m_s = -1\rangle$ transitions of the respective NV groups [45, 77]. For excitation with Rabi frequency Ω, this defines a "dressed-state" basis, $|\pm\rangle \approx (|m_s = 0\rangle \pm |m_s = -1\rangle)/\sqrt{2}$ (Fig. 3.2B). In the rotating frame, the energies of these two states are split by the effective on-site potential $\sqrt{\Omega^2 + \delta_i^2}$, where δ_i is the local disorder potential for spin i (of order W). In the limit of strong driving $\Omega \gg \delta_i$, we obtain an effective disorder potential $\tilde{\delta}_i$ with the reduced width $W_{\text{eff}} \sim W^2/\Omega$, allowing us to tune the disorder by simply adjusting the Rabi frequency. For spin-locking, we initialize NVs along the $\hat{x}$-axis via a $\pi/2$-pulse around the $\hat{y}$-axis, thereby polarizing spins in the dressed-state basis. Following coherent driving around the $\hat{x}$-axis for time τ, an additional $\pi/2$-pulse allows the measurement of the polarization in this basis. Figure 3.2C shows a spin-lock experiment performed at two

Rabi frequencies. In comparison to the spin coherence time obtained from a spin-echo measurement, we observe a dramatic enhancement of the lifetime. We find that the lifetime is limited by interactions with short-lived spins in our system, which is suppressed by increasing Ω [76]. Thus, spin-locking enables us to prepare a single group of polarized NVs with tunable disorder and long lifetime.

To control interactions, we utilize a HH resonance permitting cross-polarization transfer between the two spin ensembles [45, 77]. To identify the HH resonance condition, two groups of NVs are initialized along $+\hat{x}_A$ (group A) and $-\hat{x}_B$ (group B), and spin-locked along $+\hat{x}_A$ and $+\hat{x}_B$ with Rabi frequencies Ω_A and Ω_B, respectively (Fig. 3.3A). This prepares two oppositely polarized spin ensembles in the dressed-state basis with energy splittings Ω_A and Ω_B. The interaction between the groups results in spin exchange and leads to a resonant cross-relaxation when $\Omega_A = \Omega_B$ (HH condition). Figure 3.3B depicts the results of a spin-lock measurement on group A as a function of Ω_B, revealing a sharp resonance with a linewidth significantly narrower than the on-site disorder strength W. The linewidth of this resonance can be monitored as a function of the common Rabi frequency $\Omega = \Omega_A = \Omega_B$, showing a strong decrease for higher Ω caused by a reduction of the effective disorder W_{eff} (Fig. 3.3B inset).

This method allows us to probe the controlled thermalization dynamics with tunable disorder. To this end, we investigate the dynamics of an initially polarized spin sub-ensemble (group A) in HH resonance with another, unpolarized sub-ensemble (group B). Physically, this situation corresponds to the thermalization of a polarized spin ensemble in contact with a spin bath held at infinite effective temperature. To extract the coherent thermalization dynamics, we normalize the polarization decay with a sufficiently detuned

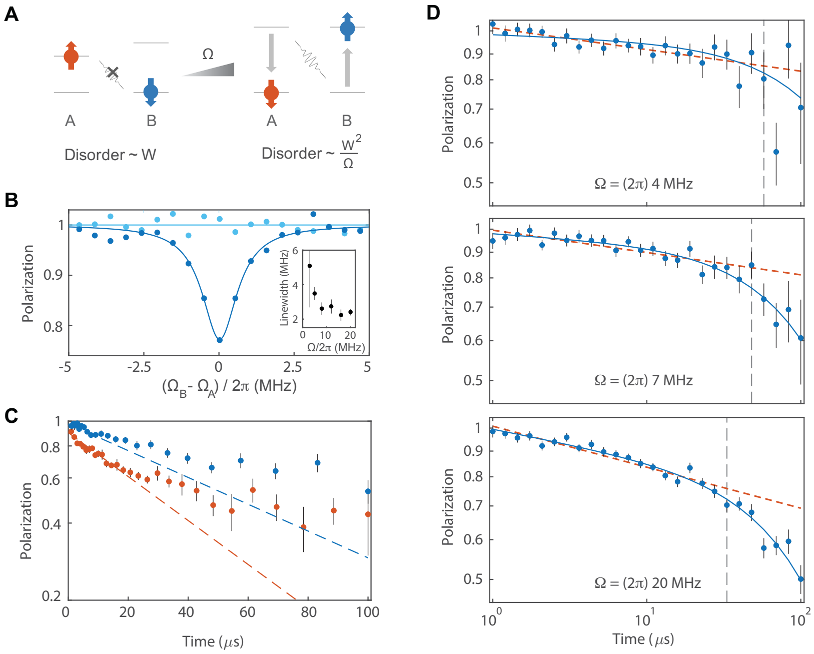

Figure 3.3: **Spin Cross-Relaxation. (A)** Schematic diagram depicting two oppositely polarized groups of spins (A and B) in the dressed state spin basis. Microwave fields with a common driving strength Ω are independently applied to the respective group parallel to their spin polarization directions. Under spin-locking, the effective disorder reduces from the natural disorder W with increasing Ω, thereby enhancing the rate of resonant spin exchange. **(B)** Population of group A as a function of driving power of group B, showing the HH resonance (dark blue points). Light blue data shows spin-lock coherence without driving of other groups. The corresponding solid curves represent a Lorentzian and constant fit to the data. Inset shows the HH resonance linewidth as a function of applied Rabi frequency. **(C)** Polarization dynamics of group A interacting with an oppositely polarized (red) and unpolarized (blue) spin bath, group B, at the HH condition with $\Omega = (2\pi)$ 9 MHz as a function of evolution time (on a semi-log scale). The polarized spin bath leads to faster polarization decay (see Appendix B). Dashed lines represent an exponential decay, illustrating significant deviation at long times. **(D)** Double-logarithmic plot of polarization decay of group A under HH conditions with unpolarized group B for different driving strengths. Dashed red lines are power-law fits to the data in the time window up to the vertical line. Curved solid lines are the fits to our theory model including time-dependent disorder. All errorbars correspond to 1 σ.

HH measurement (see Appendix B), wherein we observe a decay profile that fits neither a diffusive power law ($\sim t^{3/2}$) nor a simple exponential (Fig. 3.3C). By varying the driving strength Ω, we find that the polarization decays faster for larger Ω, consistent with a smaller effective disorder (Fig. 3.3D). Interestingly, the functional profile of the decays is consistent with power laws for over a decade, followed by accelerated relaxation at late times.

3.3 Resonance counting analysis

To understand these observations, we turn to a theoretical description of our system. Spin dynamics are governed by the interplay between disorder and long-range dipolar interactions. Working in the dressed state basis with the quantization axis along $\hat{x}$, we find that the form of this interaction depends on whether spins reside in the same or in distinct groups. For spins in different groups (A and B), dipolar interactions naturally lead to spin exchange, $H_{AB} = \sum_{i \in A, j \in B} J_{ij}/r_{ij}^3 \; (\sigma_i^+ \sigma_j^- + \sigma_i^- \sigma_j^+)$, where r_{ij} is the distance between spins, J_{ij} is the orientation dependent coefficient of the dipolar interaction with typical strength $J_0 = (2\pi)$ 52 MHz·nm^3, and $\vec{\sigma}$ are spin-1/2 operators with $\sigma_i^\pm = \sigma_i^y \pm i\sigma_i^z$ (see Appendix B). However, for spins in the same group, the $S = 1$ nature of the NV centers and energy conservation in the rotating frame lead to an absence of spin exchange (see Appendix B); rather, the coupling between spins takes the form of an Ising interaction, $H_{A(B)} = \sum_{i,j \in A(B)} J_{ij}/r_{ij}^3 \; \sigma_i^x \sigma_j^x$. Thus, when initially polarized, a spin may depolarize only through exchange with spins of the other group. Specifically, in the limit of strong disorder, one expects the dynamics to be dominated by rare resonant exchange processes between the two groups. To describe such dynamics, we consider a simplified model, where a single group A excitation is located at the center of an ensemble of group B spins

(Fig. 3.4A). The dynamics of this excitation are captured by an effective Hamiltonian,

$$H_{\text{eff}} = \sum_i \tilde{\delta}_i \sigma_i^x - \sum_{ij} \frac{J_{ij}}{r_{ij}^3} (\sigma_i^+ \sigma_j^- + h.c.). \tag{3.1}$$

where $\tilde{\delta}_i = \sqrt{\Omega^2 + \delta_i^2} - \Omega$ is the effective quenched disorder potential. While this single-particle model neglects the many-body nature of our experiments such as intra-group Ising interactions and complex dynamics of group B excitations, it captures the key features of slow relaxation in critical systems; however these additional features will be necessary to accurately describe the long time thermalization behavior.

To characterize the spin decay dynamics governed by H_{eff}, we calculate the survival probability, $P(t)$, of the excitation via a simple resonance counting analysis. For a given disorder realization, this resonance counting proceeds as follows. Two spins at sites i and j are on resonance at time t if: (1) their energy mismatch is smaller than their dipolar interaction strength, $|\tilde{\delta}_i - \tilde{\delta}_j| < \beta J_0 / r_{ij}^3$ (β is a dimensionless constant of order unity), and (2) the interaction occurs within the time-scale t, $J_{ij}/r_{ij}^3 > 1/t$. $P(t)$ is approximately given by the probability of having found no resonances up to time t or equivalently up to distance $R(t) \equiv (J_0 t)^{1/3}$ (see Appendix B). This probability can be computed as the product of probabilities of having no resonant spins at any r,

$$P(t) = \prod_r^{R(t)} \left(1 - 4\pi n r^2 dr \frac{\beta J_0 / r^3}{W_{\text{eff}}}\right) \propto t^{\frac{-4\pi n \beta J_0}{3 W_{\text{eff}}}}. \tag{3.2}$$

$P(t)$ exhibits power-law decay with a disorder dependent exponent $\eta = 4\pi n \beta J_0 / (3 W_{\text{eff}})$, where n is the density of spins that are oppositely polarized to the central excitation. This sub-exponential relaxation is the essence of the slow critical dynamics predicted by Anderson [16]. Such single-particle power-law relaxation is also consistent with results obtained from random-banded matrix theory [78, 79] and is numerically verified for up to $N = 10^4$

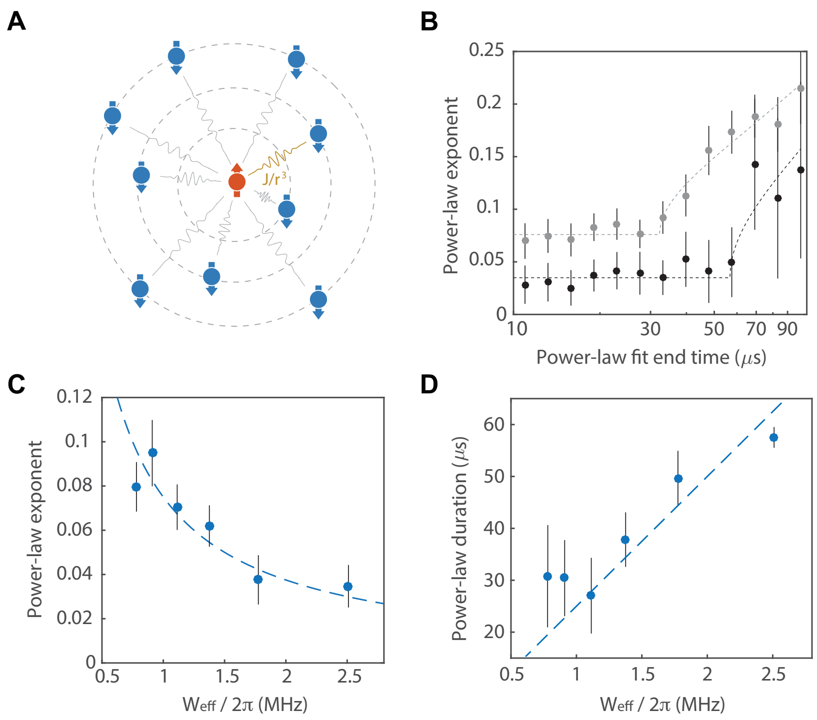

Figure 3.4: **Understanding Thermalization Dynamics.** **(A)** Schematic diagram of single particle resonance counting argument predicting a power-law decay profile. **(B)** Variation of power-law exponents extracted from a subset of data, consisting of seven subsequent points, swept from the beginning to the end of thermalization time traces. Black and gray data corresponds to the case of $\Omega = (2\pi)$ 4 and 9 MHz, respectively. Dotted lines corresponds to phenomenological fits, identifying the duration over which the power-law exponents remain constant. **(C)** Exponent of the power-law decay of group A polarization as a function of effective disorder W_{eff}. Dashed line corresponds to a theoretical prediction based on the single particle resonance counting. **(D)** Duration of power-law dynamics extracted for various strengths of effective disorder W_{eff}. Dashed line corresponds to a theoretical prediction based on a refined resonance counting including time-dependent disorder. All errorbars correspond to 1 σ.

spins (see Appendix B).

A detailed comparison of our experimental observations with these theoretical predictions is summarized in Fig. 3.4. In order to quantify the slow dynamics, we take subsets of our depolarization time trace over half-decade windows, fit the data to power laws, and extract the resulting exponents. Varying the starting time of the windows, we find that the extracted exponents remain constant up to a long time $T^* \gg 1/J$, beyond which they increase, indicating the deviation of the thermalization dynamics from a simple single particle prediction (Fig. 3.4B). Interestingly, the exponents scale linearly with the inverse effective disorder, as predicted by the counting argument (Fig. 3.4C). Furthermore, we find that their values are in excellent agreement with our theory based on numerical simulations of a single-particle Hamiltonian (see Appendix B).

At late times ($t > T^*$), the observed decay accelerates and deviates significantly from the power law. This is natural since the effects of multi-particle interactions cannot be neglected when a significant fraction of spins have already undergone depolarization. In particular, intra-group Ising interactions among randomly positioned spins $\delta_i^I \equiv \sum_j J_{ij}/r_{ij}^3 \langle \sigma_j^x \rangle$ may behave as an additional disorder that change in time with characteristic strength $J/4 \sim (2\pi)\,105\,\text{kHz}$. Additionally, weak coupling to the bath may also give rise to corrections to our single particle model.

3.4 Time-dependent on-site disorder

To understand this behavior, we modify our theoretical model by considering the time dependence of the on-site disorder potential. More specifically, we assume that the disorder potential consists of both static and dynamic parts with standard deviations W_s and W_d. The dynamic disorder is assumed to vary at a slow rate $1/\tau_d$. The survival probability $\tilde{P}(t)$ can then be computed using a modified resonance condition where two spins are considered resonant at time t, if at any prior time t', their energy mismatch is smaller than their dipolar interaction strength, $|\tilde{\delta}_i(t') - \tilde{\delta}_j(t')| < \beta J_0/r_{ij}^3$ (see Appendix B). Repeating our previous analysis, we find an analytical expression of $\tilde{P}(t)$ which, in the limit of strong quenched disorder ($1/\tau_d < W_d \ll W_s$), can be approximated by $\tilde{P}(t) \propto e^{-t/T^*} t^{-\eta}$ with $T^* \equiv 3W_s\tau_d/(4\pi n\beta J_0)$, predicting the deviation from the power law at time scale T^*. Intuitively, $1/T^*$ characterizes the rate at which a pair of initially off-resonant spins comes into resonance as the local potentials vary in time. Figure 3.3D shows that $\tilde{P}(t)$ provides an excellent fit to our observation over all time scales. Both extracted parameters $W_d \sim (2\pi)\,0.5\,$MHz and $\tau_d \sim 40\,\mu$s are comparable to the strength of Ising interactions and independently measured NV depolarization time, respectively [76]. This suggests that the dynamical disorder is dominated by intrinsic contributions from Ising interactions, which is related to the predicted thermalization enhancement due to multi-particle resonances and higher order processes [56, 69]. Moreover, the extracted power-law duration agrees well with the predicted linear dependence of T^* on effective disorder strengths (Fig. 3.4D). The quantitative agreement of the functional form $\tilde{P}(t)$, the disorder dependence of power-law exponents and durations, and the extracted values of W_d and τ_d corroborates our theoretical model describing the microscopic mechanism of thermalization dynamics in a critical system.

3.5 Conclusion and outlook

We have demonstrated that dense ensembles of NV centers constitute a powerful platform for exploring quantum dynamics of strongly correlated many-body systems. Complementary to recent studies of localization in cold atomic systems [3, 5], these spin systems exhibit slow, disorder-dependent relaxation associated with critical thermalization dynamics. The quantitative agreement between the observed spin relaxation and resonance counting demonstrates that the dynamics are dominated by rare resonances. Moreover, the observed deviations from simple theory reveal the subtle role that many-body effects and coupling to the environment can play in such systems. These studies can be extended along several directions. A higher degree of spatial quantum control can be obtained via spin-based sub-wavelength imaging techniques [80]. Advanced dynamical decoupling can enable the engineering of a broader class of interaction Hamiltonians and the direct measurement of quantum entanglement dynamics [81, 82]. The use of strong magnetic field gradients or the fabrication of diamond nanostructures can allow for the exploration of spin dynamics in lower dimensional systems [83], where the existence of many-body localization is still in debate [52, 69]. In combination, these directions may enable the study of dynamical phase transitions from localization to thermalization [3, 4, 84] as well as exotic non-equilibrium phases of matter [35, 67, 68], and open up new opportunities for controlling such complex interacting systems [85, 86].

Chapter 4

Discrete Time-Crystalline Order in a Disordered Dipolar Many-body System

4.1 Introduction

Conventional wisdom holds that the periodic driving of isolated, interacting systems inevitably leads to heating and the loss of quantum coherence. In certain cases, however, fine-tuned driving can actually decouple quantum degrees of freedom from both their local environment [87] and each other [88]. Recently, it has been shown that strong disorder, which leads to many-body localization [63, 89], allows a system to retain memory of its initial state for long times, enabling the observation of novel, out-of-equilibrium quantum phases [3, 5, 90]. One example is the discrete time crystal [9, 10, 11, 12] - a phase that is nominally forbidden in equilibrium [91, 92]. The essence of the discrete time-crystalline (DTC) phase is an emergent, collective, subharmonic temporal response. Although this phenomenon resembles the coherent revivals associated with dynamical decoupling [14], its nature is fundamentally different because it is induced and protected by interactions rather than by fine-tuned control fields. It is especially intriguing to investigate the possibility of DTC order in systems that are not obviously localized [93]. This is the case for dipolar spins in three dimensions, where the interplay between interactions and disorder can lead to critical subdiffusive dynamics [17, 76].

4.2 Experimental results

We experimentally investigate the formation of discrete time-crystalline order in an ensemble of nitrogen-vacancy spin impurities in diamond. Each nitrogen-vacancy center has an electronic $S = 1$ spin, from which we isolate an effective two-level system by applying an external magnetic field. These isolated spin states can be optically initialized, detected and manipulated via microwave radiation [14, 15] (see Fig. 4.1a and Appendix C). Our sample has a high concentration (45 p.p.m.) of nitrogen-vacancy centers, giving rise to strong long-range magnetic dipolar interactions [17]. The spins are also subject to multiple sources of disorder, owing to lattice strain, paramagnetic impurities and the random positioning of nitrogen-vacancy centers. A strong, resonant microwave field is used to control spin orientations, resulting in an effective Hamiltonian (in the rotating frame) [17],

$$\begin{aligned} H(t) = &\sum_i \Omega_x(t) S_i^x + \Omega_y(t) S_i^y + \Delta_i S_i^z \\ &+ \sum_{ij} (J_{ij}/r_{ij}^3)(S_i^x S_j^x + S_i^y S_j^y - S_i^z S_j^z). \end{aligned} \tag{4.1}$$

Here, S_i^μ ($\mu \in \{x, y, z\}$) are Pauli spin-$1/2$ operators acting on the effective two-level system spanned by the spin states $|m_s = 0\rangle$ and $|m_s = -1\rangle$, $\Omega_{x(y)}$ is the Rabi frequency of the microwave driving, Δ_i is a disordered on-site field with approximate standard deviation

$W = 2\pi \times 4.0$ MHz, r_{ij} is the distance between spins i and j (average nearest-neighbor separation $r_0 \approx 8$ nm), and J_{ij} are the orientation-dependent coefficients of the dipolar interaction. The average interaction, $J_{ij}/r_0^3 \approx 2\pi \times 105$ kHz [17], is much faster than typical spin coherence times [15].

To probe the existence of time-crystalline order, we monitor the spin dynamics of an initial state that is polarized along the $+\hat{x}$ direction. We begin by applying continuous microwave driving (spin locking) along $\hat{x}$ with Rabi frequency $\Omega_x = 2\pi \times 54.6$ MHz for a duration τ_1 (Fig. 4.1a). Next, we rotate the spin ensemble by an angle θ around the $\hat{y}$ axis using a strong microwave pulse with $\Omega_y = 2\pi \times 41.7$ MHz for duration $\tau_2 = \theta/\Omega_y \ll \tau_1$. This two-step sequence defines a Floquet unitary with a total period $T = \tau_1 + \tau_2$ and is repeated n times, before the polarization $P(nT)$ along the $\hat{x}$ axis is measured. The resulting polarization dynamics are analyzed in both the time and frequency domain (ν). Repeating these measurements with various values of τ_1 and θ allows us to independently explore the effect of interactions and global rotations.

Figure 4.1b-d depicts representative time traces and the corresponding Fourier spectra, $S(\nu) \equiv \sum_n P(nT)e^{i2\pi n\nu}$, for various values of τ_1 and θ. For relatively short interaction times ($\tau_1 = 92$ ns) and nearly perfect π pulses ($\theta \approx \pi$), we observe that the spin polarization $P(nT)$ alternates between positive and negative values, resulting in a sub-harmonic peak at $\nu = 1/2$ (Fig. 4.1b). In our experiment, the microwave pulses have an intrinsic uncertainty 0.9% stemming from a combination of spatial inhomogeneity in the microwave fields, on-site potential disorder, and the effect of dipolar interactions (see Appendix C). These effects eventually cause the oscillations to decay, after approximately 50 periods. Although such temporal oscillations nominally break discrete time-translation symmetry, their physical

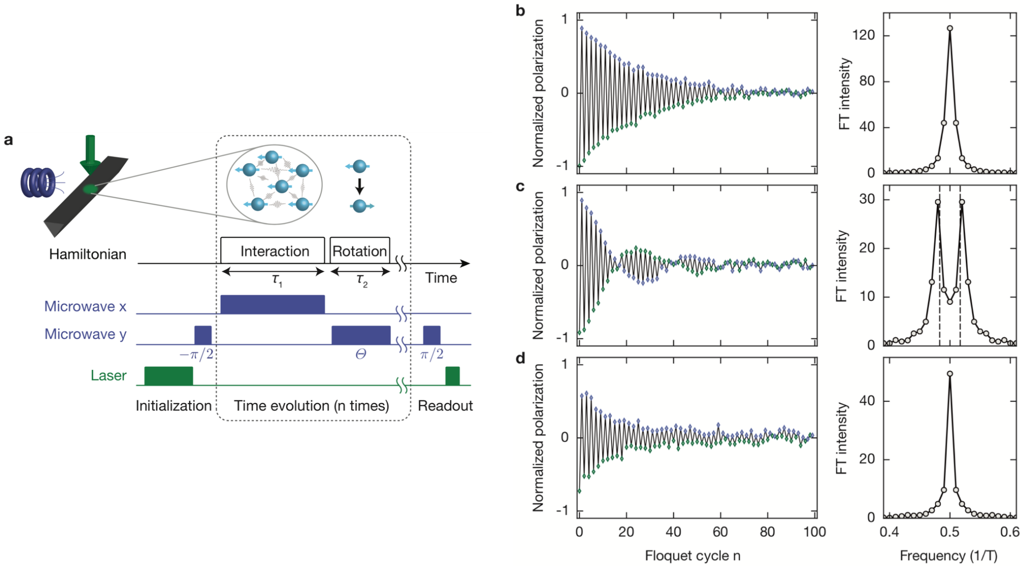

Figure 4.1: **Experimental setup and observation of time-crystalline order. a**, Nitrogen-vacancy centers (blue spheres) in a nanobeam fabricated from black diamond are illuminated by a focused green laser beam and irradiated by a microwave source. Spins are prepared in the $(|m_s = 0\rangle + |m_s = -1\rangle)/\sqrt{2}$ state using a microwave $(-\pi/2)$ pulse along the $\hat{y}$ axis. Subsequently, within one Floquet cycle, the spins evolve under a dipolar interaction and microwave field Ω_x aligned along the $\hat{x}$ axis for duration τ_1, immediately followed by a global microwave θ pulse along the $\hat{y}$ axis. After n repetitions of the Floquet cycle, the spin polarization the $\hat{x}$ axis is read out. We choose τ_1 to be an integer multiple of $2\pi/\Omega_x$ to minimize accidental dynamical decoupling [87]. **b-d**, Representative time traces of the normalized spin polarization $P(nT)$ measured at even (green) and odd (blue) integer multiples of T and respective Fourier spectra, $|S(\nu)|^2$, for different values of the interaction time τ_1 and θ: (**b**) $\tau_1 = 92$ ns, $\theta = \pi$, (**c**) $\tau_1 = 92$ ns, $\theta = 1.034\pi$, and (**d**) $\tau_1 = 989$ ns, $\theta = 1.034\pi$. Dashed lines in **c** indicate $\nu = 1/2 \pm (\theta - \pi)/2\pi$. Data are averaged over more than $2 \cdot 10^4$ measurements.

origin is trivial. To see this, we note that for sufficiently strong microwave driving, $\Omega_x \gg W, J_{ij}/r_0^3$, the dynamics during τ_1 are governed by an effective polarization-conserving Hamiltonian [17], $H_{\text{eff}} \approx \sum_i \Omega_x S_i^x + \sum_{ij}(J_{ij}/r_{ij}^3)S_i^x S_j^x$. During τ_2, the evolution can be approximated as a global spin rotation $R_y^\theta \approx e^{-i\theta\sum_i S_i^y}$. When $\theta = \pi$, this pulse simply flips the sign of the $\hat{x}$ polarization during each Floquet cycle, resulting in the $\nu = 1/2$

peak. However, this $2T$-periodic response originates from the fine tuning of θ and should not be robust against perturbations. Indeed, a systematic change in the average rotation angle to $\theta = 1.034\pi$ causes the $2T$-periodicity to completely disappear, resulting in a modulated, decaying signal with two incommensurate Fourier peaks at $\nu = 1/2 \pm (\theta - \pi)/2\pi$(Fig. 4.1c). Remarkably, we find that a rigid $2T$-periodic response is restored when interactions are enhanced by increasing τ_1 to 989 ns, suggesting that the $\nu = 1/2$ peak is stabilized by interactions. In this case, we observe a sharp peak in the spectrum at $\nu = 1/2$ and the oscillations in $P(nT)$ continue beyond $n \approx 100$ (Fig. 4.1d), indicating a persistent subharmonic temporal response.

The robustness of this apparent periodic order is further explored in Fig. 4.2. With an interaction time $\tau_1 = 790$ ns and $\theta = 1.034\pi$, the polarization exhibits an initial decay followed by persistent oscillations over the entire time window of our experimental observations (Fig. 4.2a). We perform a Fourier transform on subsections of the time trace with a sweeping window of size $m = 20$ (Fig. 4.2a) and extract the intensity of the $\nu = 1/2$ peak as a function of the sweep position, n_{sweep} (Fig. 4.2b). The intensity of the $\nu = 1/2$ peak clearly exhibits two distinct decay timescales. At short times, we observe a rapid initial decay that corresponds to non-universal dephasing dynamics, whereas at late times we observe a slow decay. Only near the phase boundary ($\theta = 1.086\pi$) is the lifetime substantially decreased. We fit the slow decay to an exponential to extract a lifetime for the periodic order. As shown in Fig. 4.2c, for $\theta = 1.034\pi$, this lifetime increases with the interaction time (τ_1) and eventually approaches the independently measured spin depolarization time $T_1^{\rho} \approx 60\ \mu$s. This demonstrates that, for sufficiently long interaction times, the observed periodic order is limited by only coupling to the environment [76]. We associate this with

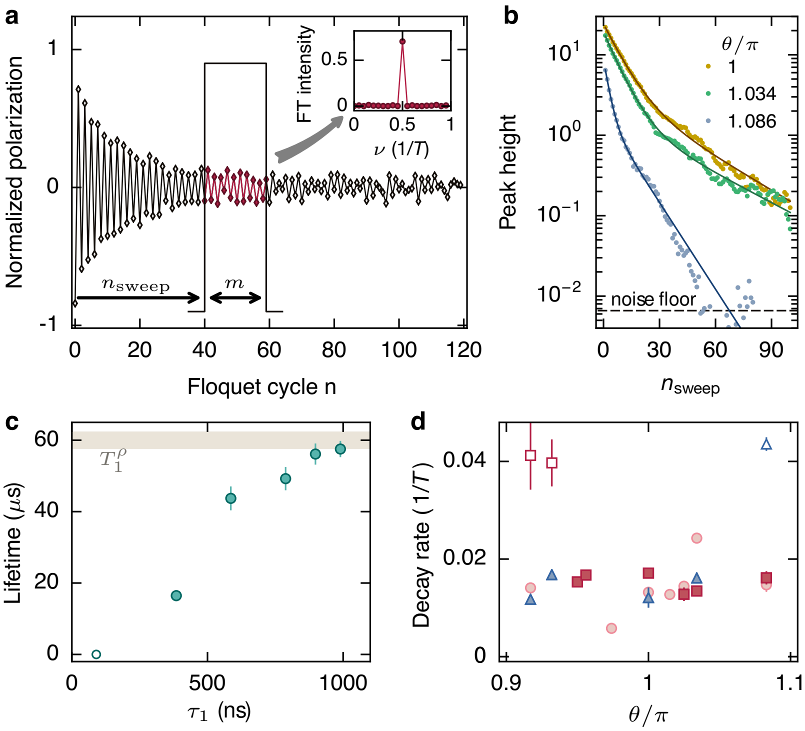

Figure 4.2: **Long-time behavior of discrete time-crystalline order.** **a** Representative time trace of the normalized spin polarization $P(nT)$ in the crystalline phase ($\tau_1 = 790\,\text{ns}$ and $\theta = 1.034\pi$). The time-dependent intensity of the $\nu = 1/2$ peak (inset) is extracted from a short-time Fourier transformation with a time window of length $m = 20$ shifted from the origin by n_{sweep}. **b** Peak height at $\nu = 1/2$ as a function of n_{sweep} for different pulse imperfections at $\tau_1 = 790\,\text{ns}$. Lines indicate fits to the data using a phenomenological double exponential function. The noise floor corresponds to 0.017, extracted from the mean value plus the standard deviation of $\sum_\nu |S(\nu)|^2$ excluding the ν = 1/2 peak. **c** Extracted lifetime of the time-crystalline order as a function of the interaction time τ_1, for $\theta = 1.034\pi$. Shaded region indicates the spin life-time $T_1^\rho = 60 \pm 2\ \mu s$ (extracted from a stretched exponential [76]) due to coupling with the external environment. **d** Extracted decay rate of the time-crystalline order as a function of θ for different interaction times, τ_1= 385 ns (circle), 586 ns (square) and 788 ns (triangle). Only very weak dependence on $\theta - \pi$ is observed within the DTC phase, contrary to a dephasing model (see Appendix C). In **c** and **d**, the vertical error bars display the statistical error (s.d.) from the fit and empty symbols mark data near the time-crystalline phase boundary.

DTC order [9, 10, 11, 12]. Remarkably, within the DTC phase, the lifetime is essentially independent of θ, indicating exceptional robustness (Fig. 4.2d).

We examined whether the observed periodic order could arise from an accidental XY sequence [87] or from inhomogeneous dephasing resulting from the effective single-particle disorder in the dressed state basis. To avoid the former, τ_1 is always choosen as an integer multiple of $2\pi/\Omega_x$. For the latter, although it has been shown that disorder alone is insufficient for stabilizing a DTC phase in the absence of interactions [9, 10, 11, 12], we verified this experimentally; implementing a rotary echo sequence that reduces such dephasing, we find no change in the lifetime of the DTC order and an enhancement in the subharmonic response at late times (see Appendix C). In principle, fast Markovian dephasing could also lead to apparent periodic order at extremely small values of $\theta - \pi$ by eliminating coherences along both $\hat{y}$ and $\hat{z}$, leaving only $\hat{x}$ polarization dynamics. In such a case, the decay rate of periodic order should increase quadratically with $\theta - \pi$. However, this explanation is inconsistent with the observed robustness of the lifetime of the DTC order for a range of $\theta - \pi$ (Fig. 4.2d) and the independently measured dephasing rate (see Appendix C).

To experimentally determine the DTC phase boundary, we focus on the long-time behavior of the polarization time traces ($50 < n \leq 100$) and compute the "crystalline fraction", which is defined as the ratio of the $\nu = 1/2$ peak intensity to the total spectral power, $f = |S(\nu = \frac{1}{2})|^2 / \sum_\nu |S(\nu)|^2$ (see Appendix C). Figure 4.3a shows f as a function of θ for two different interaction times. For weak interactions ($\tau_1 = 92$ ns), f has a maximum at $\theta = \pi$ and rapidly decreases as θ deviates by approximately 0.02π. However, for stronger interactions ($\tau_1 = 275$ ns), we observe a robust DTC phase which manifests as a large crystalline fraction over a wide range $0.86\pi < \theta < 1.13\pi$. We associate a phenomenological phase boundary with $f = 10\%$ and observe that the boundary enlarges with τ_1, eventually saturating at $\tau_1 \approx 400\,\text{ns}$ (Fig. 4.3b). The phase boundary can also be visualized as the

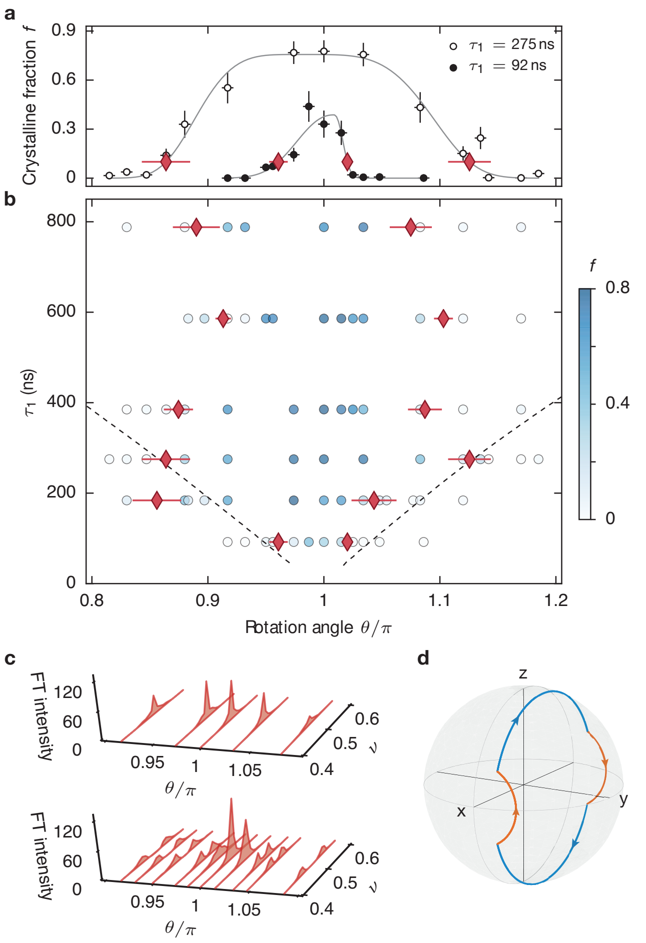

Figure 4.3: **Phase diagram and transition.** **a** Crystalline fraction f(**a**) and its associated phase diagram (**b**) as a function of θ and τ_1 obtained from a Fourier transform at late times ($50 < n \leq 100$). The red diamonds mark the phenomenological phase boundary, identified as a 10% crystalline fraction; horizontal error bars denote the statistical error (s.d.) from a super-Gaussian fit. In **a**, vertical error bars of data points (circles) are limited by the noise floor (see Appendix C) and horizontal error bars indicate the pulse uncertainty of 1%. Grey lines denote the fit to extract the phase boundary (see Appendix C). In **b**, the colors of the data points (circles) represent the extracted crystalline fraction at the associated parameter set. The dashed line corresponds to a disorder-averaged theoretical prediction for the phase boundary. Asymmetry in the boundary arises from an asymmetric distribution of rotation angles (see Appendix C). **c** Evolution of the Fourier spectra as a function of θ for two different interaction times, $\tau_1 = 385$ ns (top) and $\tau_1 = 92$ ns (bottom). **d** Bloch sphere indicating a single spin trajectory of the $2T$-periodic evolution under the long-range dipolar Hamiltonian (red) and global rotation (blue).

vanishing of the $\nu = 1/2$ peak and the simultaneous emergence of two incommensurate peaks (Fig. 4.3c).

The rigidity of the $\nu = 1/2$ peak can be qualitatively understood by constructing effective eigenstates of $2T$ Floquet cycles, including spin-spin interaction. We approximate the unitary time evolution over a single period as $U_T = R_y^\theta e^{-iH_{\text{eff}}\tau_1}$ and solve for a self-consistent evolution using product states as a variational ansatz. To this end, we consider the situation in which a typical spin returns to its initial state after $2T$: $|\psi(0)\rangle \propto |\psi(2T)\rangle = e^{-i\theta S^y} e^{i\phi_i S^x} e^{-i\theta S^y} e^{-i\phi_i S^x} |\psi(0)\rangle$, and self-consistently determine the interaction-induced rotation angle $\phi_i \equiv \sum_j J_{ij}/r_{ij}^3 \langle S_j^x \rangle \tau_1 \approx \bar{J}_i \tau_1 \langle\psi(0)| S^x |\psi(0)\rangle$, where $|\psi(0)\rangle$ is the initial spin state and $\bar{J}_i = \sum_j J_{ij}/r_{ij}^3$ (see Appendix C). One expects ϕ_i to change sign after each Floquet cycle, because the average polarization $\langle\psi(0)| S^x |\psi(0)\rangle$ should be flipped. Intuitively, the self-consistent solution can be visualized as a closed path on the Bloch sphere (Fig. 4.3d), where each of the four arcs corresponds to one portion of the $2T$-periodic evolution. When $\theta = \pi$, such a solution always exists. More surprisingly, even when $\theta \neq \pi$, a closed path can still be found for sufficiently strong interactions, $|\bar{J}_i \tau_1| > 2|\theta_i - \pi|$; in such cases, the deviation in θ away from π is compensated by the dipolar interactions (Fig. 4.3d). We obtain a theoretical phase boundary by numerically averaging the self-consistent solution over both disordered spin positions and local fields. The resultant phase boundary is in reasonable agreement with the experimental observations for short to moderate interaction times τ_1, but overestimates the boundary at large τ_1 (dashed line, Fig. 4.3b, see Appendix C).

Finally, Fig. 4.4 demonstrates that the discrete time-translation symmetry can be further broken down to $\mathbb{Z}_3$ [10, 11, 12, 94], resulting in DTC order at $\nu = 1/3$. Here, we utilize

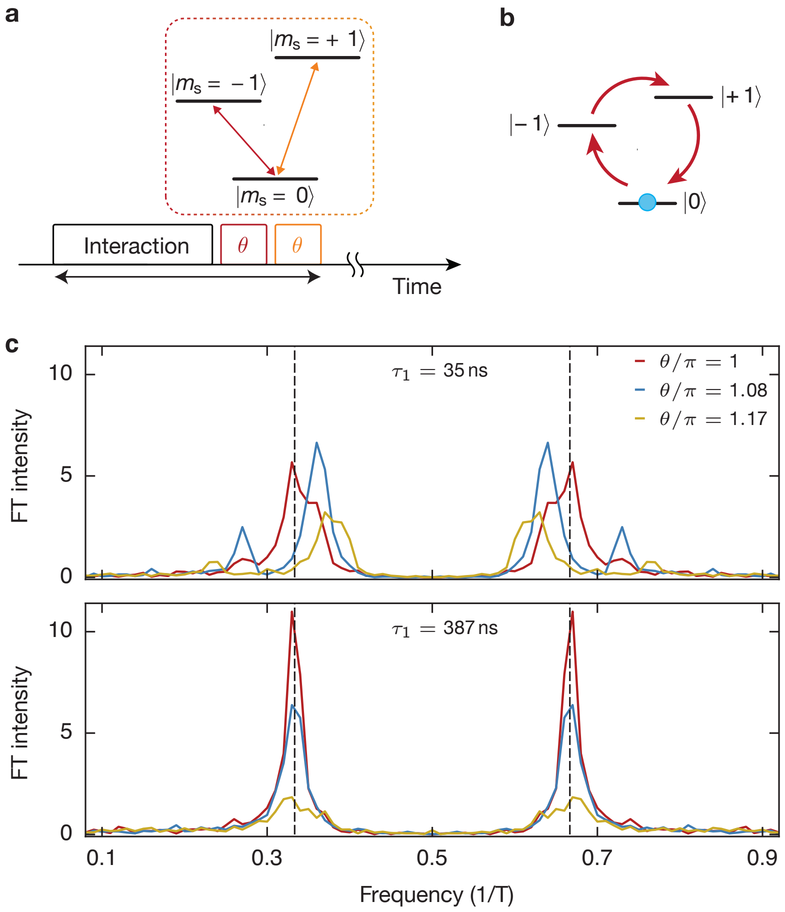

Figure 4.4: $\mathbb{Z}_3$ **discrete time-crystalline order.** **a** Experimental sequence to demonstrate a $3T$-periodic discrete time-crystalline order. A single Floquet cycle is composed of three operations: time evolution under long-range dipolar Hamiltonian and rapid microwave pulses for two different transitions. **b** Visualization of the $3T$-periodicity in the polarization dynamics for the case of $\theta = \pi$. **c** Fourier spectra of the polarization dynamics for two different interaction times and for three different rotation angles θ: 1.00π (red), 1.086π (blue) and 1.17π (yellow). Dashed lines indicate $\nu = 1/3, 2/3$.

all three spin states of the nitrogen-vacancy center. We begin with all spins polarized in the $|m_s = 0\rangle$ state and evolve under the bare dipolar Hamiltonian for a duration τ_1 (see Appendix C). Next, we apply two resonant microwave pulses, each of duration τ_2, first on the transition $|m_s = 0\rangle \rightarrow |m_s = -1\rangle$ and then on the transition $|m_s = 0\rangle \rightarrow |m_s = +1\rangle$.

In combination, this sequence of operations defines a single Floquet cycle with period $T = \tau_1 + 2\tau_2$. As before, we measure the polarization, $P(nT)$, which is defined as the population difference between the $|m_s = 0\rangle$ and $|m_s = -1\rangle$ states (Fig. 4.4a). When each of the applied microwaves corresponds to an ideal π pulse, this sequence realizes a cyclic transition with $\mathbb{Z}_3$ symmetry (Fig. 4.4b), which is explicitly broken by any change in the pulse duration. The Fourier spectra of $P(nT)$ for various pulse durations and two different values of τ_1 are shown in Fig. 4.4c. With weak interactions ($\tau_1 = 35$ ns), the position of the peaks is extremely sensitive to perturbations, but with sufficiently strong interactions ($\tau_1 = 387$ ns) the peaks are pinned to a value of $\nu = 1/3$ despite large perturbations, indicating the observation of $\nu = 1/3$ DTC order. The lifetime of the observed $\nu = 1/3$ DTC order is shorter than that of the $\nu = 1/2$ DTC order, consistent with the presence of additional dynamics in the full dipolar Hamiltonian (see Appendix C). The ability for our system to exhibit stable period-tripling distinguishes it from *bifurcations* in driven, classical systems, in which period-tripling is typically accompanied by regions of chaos [95].

Our observation of DTC order cannot be simply explained within current theoretical frameworks based on either localization [9, 10, 11, 12] or pre-thermalization [90, 93]. In particular, our system with long-range dipolar interactions is not expected to be localized in either the static or the driven case. In the static case, it has previously been demonstrated that our system exhibits slow thermalization associated with critical dynamics [17]. In the driven case, the long-time evolution is governed by the average Hamiltonian $D \approx \sum_i (J_{ij}/r_{ij}^3) S_i^x S_j^x + (\theta - \pi)/T \sum_i S_i^y$, which likewise does not yield localized dynamics[16, 56]. We further note that the effective Hamiltonian of the $\mathbb{Z}_3$ DTC phase includes not only Ising-type interactions but also spin exchange interactions, providing additional channels for thermalization (see Appendix C).

In principle, even in the absence of localization, time-crystalline order can persist for a long, but finite, pre-thermal timescale [90, 93]. Within this timescale, the spin system relaxes to a pre-thermalized state, defined as the thermal ensemble of D with a temperature determined by the energy density of the initial state. Because our initially polarized state is effectively at infinite temperature with respect to D (owing to the anisotropy of the dipolar couplings), we do not expect to observe pre-thermal DTC order. This is in contrast to our actual observations, which show that the lifetime of the DTC order is limited by the depolarization time T_1^ρ due to coupling with the environment [76] (Fig. 4.2c). We have explicitly verified that the DTC order is not greatly affected by varying the initial polarization (see Appendix C). One possible explanation is that, owing to slow critical thermalization [17], the spins in our system do not reach even a pre-thermal state. Finally, the interplay between coherent interactions and dephasing in open systems at long times could also have a role. Detailed understanding of such mechanisms requires further theoretical investigation.

4.3 Theory of critical time crystals

Here, we develop a theoretical treatment of DTC order in systems with long-range interactions. We utilize a perturbative approach to analyze the interplay of long-range interactions, periodic driving, and positional disorder of spins. Focusing on dipolar systems in 3D, we show that although DTC order is only transient, it can persist for asymptotically long times with strongly suppressed thermalization rate. This behavior is intrinsically connected to slow thermalization dynamics of disordered dipolar systems in 3D, which has been previously shown to be consistent with the so-called critical regime [16, 17] without

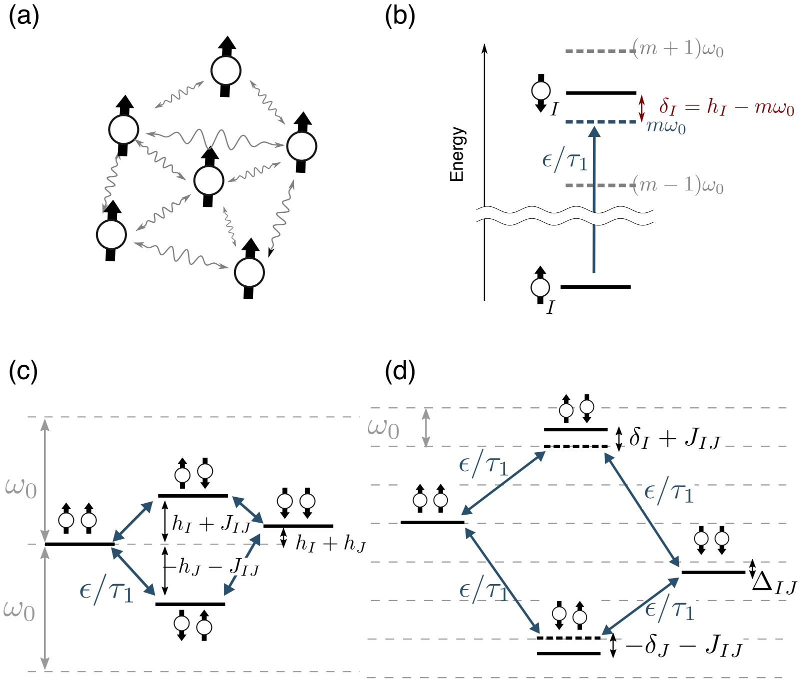

Figure 4.5: (a) Ensemble of randomly positioned spins in 3D interacting via dipolar interactions. (b) Illustration of single-spin-flip processes. (c, d) Energy level diagram for the second-order process of two spins flipping, in two regimes: (c) high frequencies ($\omega_0 \gg W$) and (d) low ($\omega_0 \ll W$) frequencies. The applied field flips a spin with magnitude ϵ/τ_1, which costs energy $\sim h_I - m^*\omega_0$.

periodic drive. As a function of experimental parameters, we find that the relaxation time shows a sharp crossover between a regime where DTC response is robust and a regime where it decays rapidly. This crossover is reminiscent of a phase transition, thereby allowing us to obtain the effective phase diagram of DTC which is in good agreement with experimental results. Thus, our work provides an explanation of the experimental observations introduced in the previous section, and also demonstrates the possibility of the DTC in systems with critical dynamics, a regime which we refer to as ‘critical time crystals’. Furthermore, our perturbative approach can be used to study the non-equilibrium properties in other driven disordered systems with long-range interactions.

Our key results can be understood by considering a simple spin model that describes an ensemble of dipolar interacting NV centers, used in the experiments of Ref. [35]. Using strong microwave excitations, the effective Ising interactions between spins were engineered, described by the following Hamiltonian:

$$H_0 = \sum_i \Omega S_i^x + \sum_{i,j} \frac{J_{ij}}{r_{ij}^3} S_i^x S_j^x, \tag{4.2}$$

where $\vec{S}_i = (S_i^x, S_i^y, S_i^z)$ are Pauli spin-1/2 operators, Ω the strong microwave driving along $\hat{x}$, J_{ij} the orientation dependent coefficient of dipolar interactions with typical strength J_0, and r_{ij} the distance between spins i and j. We assume that the spin-1/2 particles are randomly distributed in three dimensional space with density n_0 and neglect coupling to the environment [Fig. 4.5(a)]. DTC order was observed by interrupting the evolution under Hamiltonian (4.2) with rapid, global pulses that rotate the spin ensemble along the $\hat{y}$-axis by an angle $\pi + \epsilon$. The corresponding Floquet unitary is given by

$$U_F = \exp\left[-i \sum_i (\pi + \epsilon) S_i^y\right] \exp\left[-i H_0 \tau_1\right], \tag{4.3}$$

where τ_1 is the period for which the spins are allowed to interact for. In the experiment, the period is chosen such that $\Omega\tau_1 = 2\pi n$, and therefore Ω can effectively be taken to be 0 in Eq. (4.2). When the system is initialized in a state where all spins are polarized along the $+\hat{x}$ direction, a non-trivial temporal response may be revealed by measuring the average polarization $P(n\tau_1)$ of the ensemble along $\hat{x}$ after n Floquet cycles, or equivalently, $q(n) \equiv (-1)^n P(n\tau_1)$, which serves as an order parameter for the DTC phase. The stability of the DTC order can be ascertained by studying the decay rate of $q(n)$ for large number of cycles as a function of τ_1 and ϵ.

In order to describe the dynamics of $q(n)$, we move into a so-called toggling frame, which rotates by $P_\pi \equiv \prod_j \exp\left[-i\pi S_j^y\right]$ each time a global pulse is applied to the system. Since $P_\pi S_i^x (P_\pi)^{-1} = -S_i^x$, the $2\tau_1$-periodic oscillation in $P(n\tau_1)$ naturally appears as a time-indepdent spin polarization in this new frame. The dynamics of the system is then described by the Floquet unitary $\bar{U}_F = \exp\left[-i\sum_i \epsilon S_i^y\right]\exp\left[-iH_0\tau_1\right]$, or, equivalently, by an effective time-dependent Hamiltonian

$$H(t) = \sum_{ij} \frac{J_{ij}}{r_{ij}^3} S_i^x S_j^x + \epsilon \sum_i S_i^y \sum_n \delta(t - n^-\tau_1). \tag{4.4}$$

Thus, our problem reduces to studying the depolarization dynamics of an initialized polarized spin ensemble under the time evolution of $H(t)$.

Physical picture.—The essence of our analysis is to study resonant spin dynamics that lead to depolarization perturbatively in ϵ, while accounting for energy exchanges provided by the external drive. In particular, since $\sum_n \delta(t - n^-\tau_1) = \frac{1}{\tau_1}\sum_m e^{im\omega_0 t}$, the pulsed periodic spin rotations can be viewed as spin excitation with harmonics of the fundamental frequency $\omega_0 \equiv 2\pi/\tau_1$ and fixed magnitude ϵ/τ_1. While this driving allows energy absorption and emission in integer multiples of ω_0, the interplay of strong interactions and positional disorder suppresses direct energy exchanges such that typical spins depolarize only via indirect higher order processes in ϵ.

Let us first consider the case without perturbations, i.e. $\epsilon = 0$. Then the polarization of each spin along $\hat{x}$ is conserved. When all spins are initially polarized, each spin therefore experiences a mean-field potential $h_i \equiv \sum_{j\neq i}(J_{ij}/r_{ij}^3)\langle S_j^x\rangle$. Due to the random positioning of spins, the strength of h_i is also random with zero mean and variance $W^2 = \langle \frac{1}{4}(\sum_{j\neq i} J_{ij}/r_{ij}^3)^2\rangle$, where $\langle\cdot\rangle$ denotes averaging over different positions.

When $\epsilon \neq 0$, there is depolarization due to spins experiencing a time-varying on-site field along the $\hat{y}$-axis. Let us therefore consider the first order process where spins individually flip due to the action of this field. If a spin experiences a a strong mean-field potential h_i compared to the applied field, that is, if $h_i\tau_1 \gg \epsilon$, then it does not flip – it experiences an effective field that is approximately pointing along the $\hat{x}$-axis and therefore precesses around it without significant depolarization. On the other hand, if $h_i\tau_1$ is close to an integer multiple of 2π, then the spin rotates along the $\hat{y}$-axis and depolarizes. Physically, this corresponds to an effectively resonant excitation of (individual) spins that arises when one of the driving harmonics is tuned close to their energy: $|h_i - m^*\omega_0| < \epsilon/\tau_1$ for some optimal integer m^* [see Fig. 4.5(b)]. Such resonances occur with a small probability in the limit of $\epsilon \ll W\tau_1$, and amount to a reduction of the total polarization by a constant factor proportional to $\epsilon/(\min(W,\omega_0)\tau_1)$. However, if $\epsilon \sim W\tau_1$, a substantial fraction of spins rapidly depolarize due to resonant processes shown in Fig. 4.5(b). Note that the phenomenological phase boundary extracted in Ref. [35], based on the existence of self-consistent closed spin trajectories, is consistent with the perturbative condition $\epsilon \ll W\tau_1$.

We next focus on the second order process illustrated in Fig. 4.5(c,d) in which a pair of spins I and J simultaneously flip their polarizations while exchanging their energies with each other *and* with the external drive. Such processes are resonant when

$$\Delta_{IJ} \approx |h_I + h_J - m^*\omega_0| < J_{IJ}^{\text{eff}}, \tag{4.5}$$

where h_I and h_J are effective on-site potential for spins I and J, m^* is the optimal harmonic number that minimizes the energy difference, and J_{IJ}^{eff} is the effective amplitude of the pair-flip process. The amplitude J_{IJ}^{eff}

$$J_{IJ}^{\text{eff}} \sim \left(\frac{\epsilon}{\tau_1}\right)^2 \frac{J_{IJ}}{r_{IJ}^3}\left(\frac{1}{\delta_I^2} + \frac{1}{\delta_J^2}\right), \tag{4.6}$$

can be estimated from the interference of two paths in second order perturbation theory, as illustrated in Fig. 4.5(c,d). Here $\delta_{I(J)} \equiv \min_{\ell^*}(h_{I(J)} - \ell^*\omega_0)$ is the energy difference between initial/final states and intermediate virtual states, up to extra energy provided by a driving harmonic ℓ^*. We find that J_{IJ}^{eff} is an effective long-range interaction decaying as $\sim 1/r_{IJ}^3$ allowing the flipping of remote spin pairs.

The resonance condition (4.5) is sensitive to ω_0 and behaves qualitatively differently in two limiting cases: (i) $\omega_0 \gg W$ and (ii) $\omega_0 \ll W$ [see Fig. 4.5(c,d)]. In the former case, the optimal choice is $m^* = \ell^* = 0$ since spins cannot absorb or emit such a large energy ω_0. In the latter case, effective energy differences (both Δ_{IJ} and δ_I, δ_J) are bounded by ω_0 as the external drive can always compensate energy in units of ω_0. These considerations yield the scaling $J^{\text{eff}}(r) \sim CJ_0/r^3$ with

$$C \approx \begin{cases} (\epsilon/\tau_1 W)^2 & \text{for } \omega_0 \gg W \\ \epsilon^2 & \text{for } \omega_0 \ll W \end{cases}, \tag{4.7}$$

and the effective range W^{eff} of the energy differences Δ_{IJ} becomes $W^{\text{eff}} \sim W$ for $\omega_0 \gg W$ and $W^{\text{eff}} \sim \omega_0$ for $\omega_0 \ll W$.

We now estimate the probability that a given spin finds a resonant partner within a ball of radius R. This is obtained by integrating the probability of finding such a partner in a shell R and $R + dR$

$$dP = \left(J^{\text{eff}}(R)/W^{\text{eff}}\right) n_0 4\pi R^2 dR, \tag{4.8}$$

from a short distance cut-off a_0 to R, which gives $P(R) \sim \log(R/a_0)$. Here the first factor in Eq. (4.8) is the probability of satisfying Eq. (4.5), and the second factor is the average number of spins within a shell of size R with the density n_0. As this probability diverges, it implies that pair-wise spin flips prevail, and the system thermalizes, with the DTC order slowly decaying over time. We can extract the timescale associated with these pair-spin flip processes using the typical distances R_* of resonant spin pairs. Solving $P(R_*) \sim 1$ gives

$R_* \approx a \exp\left[W^{\text{eff}}/4\pi C J_0 n_0\right]$. Finally, the effective depolarization rate is estimated from the interaction strengths of typical pairs, i.e., $\tilde{\Gamma} \sim J^{\text{eff}}(R_*)$, leading to the decay rate per Floquet cycle $\Gamma \equiv \tilde{\Gamma}\tau_1$:

$$\Gamma \sim \begin{cases} \frac{J_0\epsilon^2}{a_0^3\tau_1 W^2} \exp\left[-\frac{3W^3\tau_1^2}{4\pi J_0 n_0 \epsilon^2}\right] & \text{for } \omega_0 \gg W \\ \frac{J_0\epsilon^2\tau_1}{a_0^3} \exp\left[-\frac{3}{2J_0 n_0 \epsilon^2 \tau_1}\right] & \text{for } \omega_0 \ll W. \end{cases} \tag{4.9}$$

This exponentially slow in $1/\epsilon^2$ decay of the DTC order is a central result of the present Letter, and is a direct consequence of critically slow thermalization of dipolar systems in 3D [16, 17]. Interestingly, the depolarization is exponentially sensitive to the parameters τ_1 and ϵ in two distinct ways: in regime (i) Γ is a function of τ_1^2/ϵ^2 while in regime (ii) it only depends on $1/\epsilon^2\tau_1$. These considerations allow us to identify an effective phase boundary using the criteria $\tau_1^2/\epsilon^2 = A$ or $1/\epsilon^2\tau_1 = B$ with some constants A and B. Remarkably, this boundary illustrated in Fig. 4.6 captures the key features observed in the experiment [35]: the linear growth of ϵ for short τ_1 and slow diminishing of ϵ at longer τ_1.

Technical procedure.—We now outline the technical procedure that formalizes the above discussion (see Appendix C for details). The key idea is to identify a time-dependent unitary transformation of the Hamiltonian $H(t)$ such that non-resonant single spin-flips are essentially "integrated out" and only residual two-spin-flip processes become dominant terms in the effective Hamiltonian $H'(t)$. More specifically, we start from the Hamiltonian (4.4) with H_0 representing the Ising interactions and V the applied field, and perform a time-periodic unitary transformation $Q(t+\tau_1) = Q(t)$, which gives rise to:

$$H'(t) = Q(t)^\dagger \Big(H_0 + \epsilon V \sum_n \delta(t - n^- \tau_1) - i\partial_t\Big) Q(t). \tag{4.10}$$

Our goal is to eliminate terms that are linear in ϵ from $H'(t)$. Following Ref. [96], we look for $Q(t)$ of the form $Q(t) = e^{\epsilon\Omega(t)}$ with anti-Hermitian operator $\Omega(t) = \sum_n \Omega^{(n)} e^{in\omega_0 t}$.

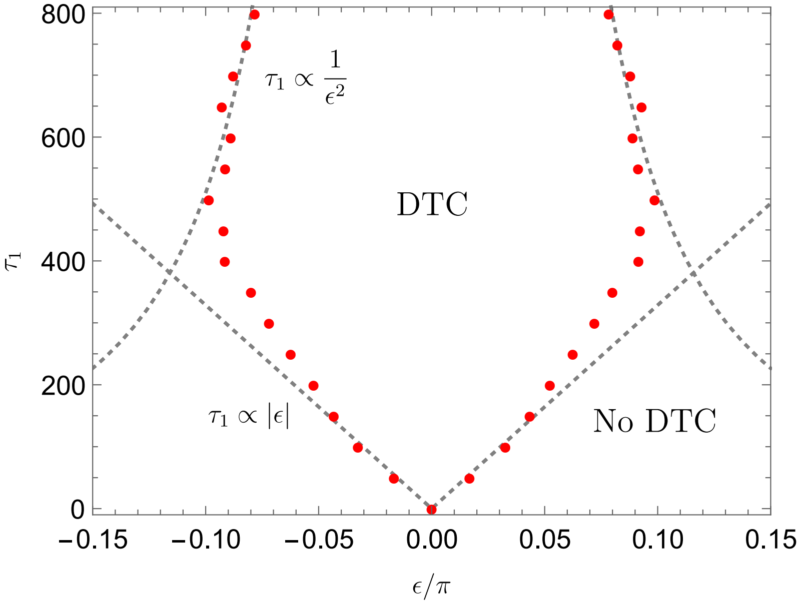

Figure 4.6: Phase diagram of the DTC obtained numerically (see Appendix C for details). Dotted lines indicate limiting behaviors of the phase boundary: at high driving frequencies, the phase boundary is linear, $\tau_1 \propto |\epsilon|$, while for low driving frequencies, it closes up as $\tau_1 \propto 1/\epsilon^2$, c.f. Eq. (4.9). This is in good agreement with the experimental observations of Ref. [35].

Expanding Eq. (4.10) in powers of ϵ, and requiring that the $O(\epsilon)$ term equals 0 gives an equation for the nth Fourier mode $\Omega^{(n)}$:

$$\frac{V}{\tau_1} - [\Omega^{(n)}, H_0] + n\omega_0\Omega^{(n)} = 0. \tag{4.11}$$

The matrix elements of the operator $\hat{\Omega}^{(n)}$ can be computed in the eigenstate basis $|s\rangle$ of H_0 (which is a product state basis in S_i^x operators):

$$\langle s'|\Omega^{(n)}|s\rangle = \frac{\langle s'|V|s\rangle}{(E_s - E_{s'} - n\omega_0)\tau_1}. \tag{4.12}$$

Noting that $V = \sum_i S_i^y$, the operator $\Omega^{(n)}$ has non-zero matrix elements only between spin configurations s and s' that differ by one spin-flip. If $|s\rangle$ and $|s'\rangle$ differ by the value of spin I, $E_s - E_{s'} = 2\sum_{j\neq I} \frac{J_{jI}}{r_{jI}^3} S_j^x(s) S_I^x(s) = 2h_I S_I^x$. We assume that the on-site field h_I is ran-

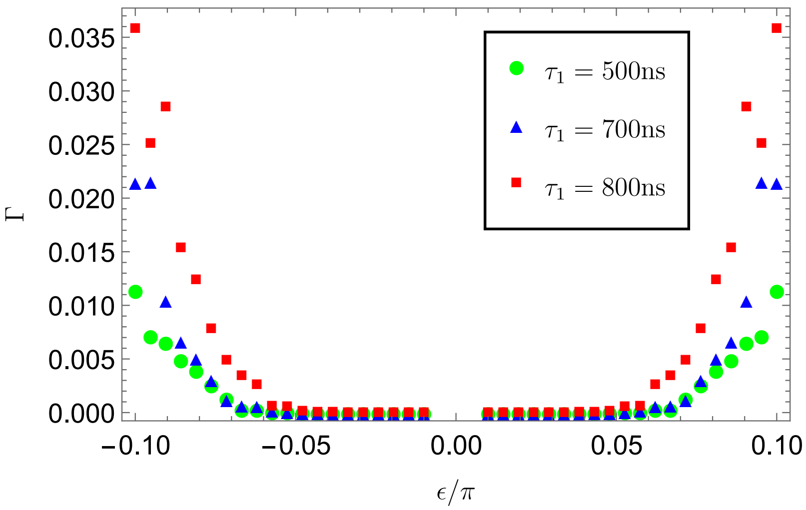

Figure 4.7: Decay rate versus perturbation ϵ for various τ_1s obtained numerically (see Appendix C). One sees a sharp rise of the decay rate as one crosses the DTC phase boundary (determined as the ϵ for which $\Gamma(\epsilon, \tau_1) = 1/100$), which is reminiscent of a phase transition.

dom (due to positional disorder and orientation dependence of J_{ij}) and sufficiently strong such that resonances are rare, i.e. the denominator in (4.12) typically does not diverge and the procedure controlled. Then, the rotated Hamiltonian to second order becomes

$$H'(t) = H_0 - \frac{\epsilon^2}{2}[\Omega(t), V] \sum_n \delta(t - n^- \tau_1) \tag{4.13}$$

A straightforward calculation using expression (4.12) gives an effective Hamiltonian of the following form:

$$H'(t) = H_0 + \sum_{IJ} \frac{A_{IJ} J_{IJ}}{r_{IJ}^3} \left(S_I^+ S_J^+ + h.c.\right) \sum_n \delta(t - n^- \tau_1), \tag{4.14}$$

where $S_I^+ \equiv (S_I^z + iS_I^y)/\sqrt{2}$ is the spin raising operator in S_I^x basis for the spin I, and A_{IJ} is the coefficient

$$A_{IJ} \approx -2 S_I^x(s) S_J^x(s) \left(\frac{\epsilon}{\tau_1}\right)^2 \left(\frac{1}{\tilde{\delta}_I^2} + \frac{1}{\tilde{\delta}_J^2}\right), \tag{4.15}$$

where we introduced the notation $\frac{1}{\tilde{\delta}_J^2} = \sum_\ell \frac{1}{(h_J - \ell\omega_0)^2}$.

The effective Hamiltonian (4.14) contains the larger disordered part H_0, and long-range terms which can flip pairs of spins; the latter are suppressed proportional to ϵ^2, leading to slow relaxation. From Eq. (4.15) it is evident that the amplitudes for flipping a pair of spins depend on h_I, h_J, which in turn are determined by the positions of the spins. Assuming that h_I, h_J take typical values of the order W, and taking the contribution of the harmonic ℓ^* for which $h_J - \ell\omega_0$ is minimized (this gives the leading contribution to $\tilde{\delta}_J$), the expression (4.15) for the two-spin-flip amplitude reduces to the estimate (4.6) above.

We emphasize that the above unitary transformation is distinct from the rotating frame transformations employed to derive effective Hamiltonians in the high-frequency limit [97, 98]. Rather, it utilizes the randomness of our Hamiltonian in order to effectively integrate out non-resonant single spin flip processes.

Phase diagram.—Using the effective Hamiltonian approach described above, we obtain the phase diagram of the critical DTC. To improve upon the estimates for $\Gamma(\epsilon, \tau_1)$, we take into account the fact that the distribution of the potential h_i stems from positional randomness of spins, and numerically sample h_i from a distribution of 2000 spins in a 3D region with density 9.26×10^{-3} nm^{-3} with a short distance cut-off of 3 nm [17].

While Eq. (4.9) already provides analytical predictions for the decay rate Γ by estimating the typical distance R_* of resonant spin pairs, in numerics we find it more amenable to estimate Γ from an explicit depolarization in time profile; the counting arguments in Eq. (4.8) predicts a power-law decay of polarization $q(n)$, from which the decay timescale $1/\Gamma$ is extracted by equating $q(n)$ to a small threshold (see Appendix C). The phase boundary is then identified from a criteria $\Gamma(\epsilon, \tau_1) = \Gamma_* = 1/100$.

This approach yields the phase diagram illustrated in Fig. 4.6, which is in very good agreement with the experimental observations [35]. Note that this phase boundary is consistent with the perturbative condition $\epsilon \ll W\tau_1$. At high driving frequency, the boundary approximately follows a relation $\tau_1 \propto |\epsilon|$ (also obtainable using a semi-classical argument), while at low frequency $\tau_1 \propto 1/\epsilon^2$, which indicates that DTC order becomes less stable as τ_1 is increased, due to the fact that multi-photon processes lead to faster depolarization. The DTC phase is most robust in the crossover regime, where $\omega_0 \sim W$.

We also note that strictly speaking DTC order has finite relaxation rate at any $\epsilon \neq 0, \tau_1 \neq 0$. However, we find that the relaxation rate Γ increases very sharply at a certain value of ϵ, as illustrated in Fig. 4.7, which matches the experimental observations and is reminiscent of a phase transition. Note, however, that unlike for a true phase transition, this increase does not become infinitely sharp even in the thermodynamic limit.

4.4 Conclusion and outlook

A number of remarkable phenomena in quantum dynamics have recently been observed in engineered many-body systems consisting of ten to a few hundred particles [3, 4, 5, 6]. The observations that we have presented here indicate that robust DTC order can occur in large systems without fine-tuned interactions and disorder, even in the regime in which localization is nominally not expected to occur. Our work raises important questions about the role of localization, long-range interactions and coupling to the environment in driven systems and opens up several new avenues for fundamental studies and potential applications. In particular, it should be possible to extend these studies to realize novel dynamical phases in more complex driven Hamiltonians, and to explore if such phases can be used to create and stabilize coherent quantum superposition states for applications such as quantum metrology [18, 19, 20].

We described a new approach to analyze dynamics of periodically driven spin systems with long-ranged interactions and applied it to explain the recently observed surprising stability of DTC in dipolar spin system. The results of our analysis are in very good agreement with experimental observations. They demonstrate that these observations correspond to a novel, critical regime of the DTC order.

Furthermore, our general approach can be applied to analyze the interplay of long-range interactions, randomness, and periodic driving in a broad class of experimental systems. The present analysis focused on the experimentally relevant case of critical interactions, decaying as $1/r^{\alpha}$, where α coincides with the dimensionality of the system, $\alpha = d = 3$. This leads to direct relaxation processes of spin pairs. It is interesting to extend the analysis to the case $\alpha > d$ (e.g. $\alpha = 3, d = 2$), where resonant spin-pair-flip processes are rare and presumably do not provide the main relaxation channel. Experimentally, such a situation can be realized by reducing the dimensionality of the dipolar spins systems. In the static case, relaxation is expected to occur via multi-spin processes: in essence, a sparse resonant network may form, which can act as a heat bath that mediates relaxation of other spins [69, 99]. We expect that future experiments on DTC in reduced dimensions will allow one to probe such delicate interplay of various relaxation mechanisms in driven systems with long-range interactions. Our theoretical approach is well suited for analyzing such systems. Finally, apart from these specific realizations, our analysis demonstrates that the DTC response to periodic perturbations can be used as a sensitive probe of non-equilibrium quantum states and phases of matter.

Chapter 5

Probing Quantum Thermalization of a Disordered Dipolar Spin Ensemble with Discrete Time-Crystalline Order

5.1 Introduction

Thermalization is a universal feature of most many-body systems [4, 6, 100, 101, 102, 103, 104, 105], underlying the applicability of equilibrium statistical mechanics. At the same time, it represents an important limitation for the coherent manipulation of large scale quantum systems in quantum information processing. For these reasons, a detailed understanding of thermalization processes in closed, interacting quantum many-body systems is of great interest to both fundamental and applied science.

Over the last few decades, it has been demonstrated both theoretically and experimentally that thermalization processes in many-body systems can be significantly slowed, or even halted due to strong disorder [3, 5, 16, 17, 63, 66, 89, 106, 107, 108, 109]. The suppression of thermalization allows for novel nonequilibrium states of matter that would otherwise be forbidden in equilibrium. One remarkable example is the discrete time crystal phase in periodically-driven (Floquet) systems [9, 10, 11, 12, 93, 110]. This phase is characterized by a spontaneous breaking of the discrete time-translational symmetry of the drive, which is manifested in local observables exhibiting long-lived, robust oscillations at a subharmonic of the fundamental driving frequency. Signatures of discrete time-crystalline (DTC) order have been observed in various experimental platforms such as trapped ions, electronic and nuclear spin ensembles [35, 68, 111, 112]. Since the stability of DTC order is closely related to the suppression of thermalization processes, these observations also raise the intriguing possibility of using the DTC signal as a tool to study thermalization dynamics in an interacting many-body system.

In this study, we demonstrate that the stability of DTC order can be used as a sensitive, quantitative probe of thermalization behavior in a quantum many-body dipolar system. Specifically, we coherently manipulate a disordered ensemble of dipolar-interacting spins to engineer Floquet dynamics with three different types of interactions. In all cases, robust, long-lived signatures of DTC order can be observed over some range of parameters. By tuning both the Floquet period and the strength of perturbations, we monitor the corresponding changes in the decay of DTC order that ensue, which allows us to study thermalization dynamics in these systems.

Our experimental observations reveal the presence of three distinct thermalization regimes. In the case where the driving period is short compared to the inverse of disorder strength, DTC order is robust over a wide range of perturbation strengths, and we find that spin dynamics is well described by a time-averaged Hamiltonian which sensitively depends on the details of interactions [90, 93, 98, 113, 114]. Thermalization occurs only via rare resonances that are strongly suppressed by the large disorder [52, 56, 69]. At longer periods, the average Hamiltonian description breaks down as the system can exchange energy with the periodic drive, but long-lived DTC order can still persist. This stability can be attributed to critically slow thermalization dynamics arising from the delicate interplay of the long-range nature of interactions with disorder and driving, in agreement with previous observations of a critical DTC regime [17, 35, 110]. At sufficiently long drive periods, DTC order becomes unstable as the system enters a third thermalizing regime, characterized by universal dynamics independent of the interaction details. The universal behavior is consistent with Markovian dephasing of individual spins, implying that the many-body system serves as its own Markovian bath [103, 105, 115, 116, 117]. However, we find that the crossover to this regime depends strongly on the nature of interactions, indicating differences in thermalization dynamics of long-range Ising and other dipolar spin models [118]. Our results have important implications for the dynamical engineering of Hamiltonians [82, 88], novel Floquet phases in many-body systems [67, 94, 119, 120, 121, 122], with applications to quantum metrology [123] and quantum simulations [124].

5.2 Experimental results

Our experiments employ a dense ensemble of nitrogen-vacancy (NV) centers in diamond [15]. Each NV center comprises an $S=1$ electronic spin with internal states $|m_s=0,\pm1\rangle$, which can be initialized, manipulated, and read out by optical and microwave pulses. The high NV center concentration ($\sim$45 ppm) in our sample provides strong mag-

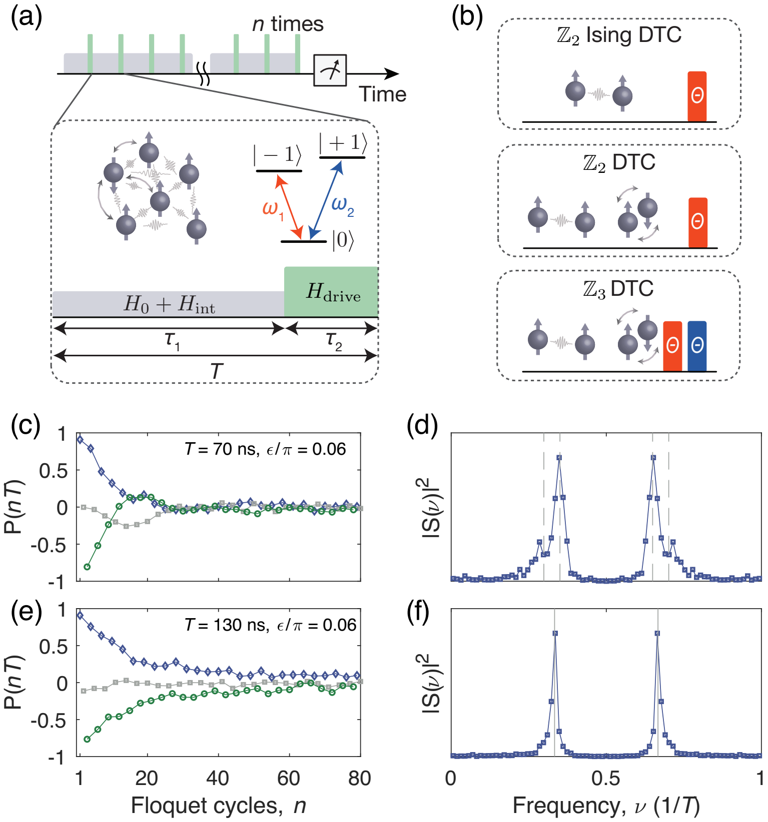

Figure 5.1: **Experimental system and observation of DTC order.** (a) Periodically driven, interacting NV centers. During each Floquet period T (dotted box), NV centers interact for time τ_1, then experience pulsed microwave rotations of duration τ_2, at resonant frequencies ω_1 or ω_2. After n Floquet cycles, the population difference between $|0\rangle$ and $|-1\rangle$ is measured. (b) Distinct Floquet time evolutions realized: $\mathbb{Z}_2$-Ising, with only Ising interactions, and $\mathbb{Z}_2$ & $\mathbb{Z}_3$, with both Ising and spin-exchange interactions. (c-f) Representative time traces of the normalized spin polarization $P(nT)$ and Fourier spectra $|S(\nu)|^2$ of the $\mathbb{Z}_3$ DTC order at a perturbation $\epsilon/\pi = 0.06$ with T = 70 ns (c,d) and 130 ns (e,f). In (c,e), blue, gray, and green points correspond to $P(t)$ at $t \equiv T, 2T, 3T \pmod{3T}$, respectively.

netic dipolar interactions between spins, with interaction strengths significantly exceeding extrinsic decoherence rates [17] (see Appendix D). Our sample has also various sources of disorder, with an energy scale generally larger than the interaction strength between NV centers. A more detailed characterization can be found in Ref. [17, 76] (see Appendix D).

To probe thermalization dynamics, we use pulsed periodic microwave driving to engineer three distinct types of Floquet evolutions, which we denote as $\mathbb{Z}_2$-Ising, $\mathbb{Z}_2$, $\mathbb{Z}_3$. In all cases, a Floquet cycle consists of time evolution under an interacting Hamiltonian for a tunable duration τ_1, followed by strong microwave pulses effecting a global spin rotation:

$$U_F^{(a)} = P_\theta^{(a)} \exp[-iH^{(a)}\tau_1], \tag{5.1}$$

where $a \in \{\mathbb{Z}_2\text{-Ising}, \mathbb{Z}_2, \mathbb{Z}_3\}$, $P_\theta^{(a)}$ is the spin rotation parametrized by a tunable angle θ, and $H^{(a)}$ is an effective Hamiltonian for relevant degrees of freedom of the spin ensemble, containing interaction and disorder terms [Fig. 5.1(a)]. The time durations of $P_\theta^{(a)}$ are fixed at $\tau_2 = 10$ ns ($\mathbb{Z}_2$-Ising and $\mathbb{Z}_2$) or $\tau_2 = 20$ ns ($\mathbb{Z}_3$), such that the Floquet time period $T = \tau_1 + \tau_2$ is dominated by τ_1. For $\mathbb{Z}_2$-Ising and $\mathbb{Z}_2$, the microwave excitation $P_\theta^{(a)}$ is resonant with the $|0\rangle \leftrightarrow |-1\rangle$ transition, and these two states form an effective two-level system. For $\mathbb{Z}_3$, $P_\theta^{\mathbb{Z}_3}$ consists of two consecutive pulses, resonant with $|0\rangle \leftrightarrow |\pm1\rangle$ transitions, thereby exploiting all three spin states [Fig. 5.1(b)]. In the ideal case $\theta = \pi$, $P_\pi^{(a)}$ permutes the populations between two (three) spin states such that they return to the original configuration after two (three) cycles. In the following experiments, we introduce systematic perturbations $\epsilon = \theta - \pi$, whose accuracy is limited to about 1% due to spatial inhomogeneity of the applied field and disorder in the system (see Appendix D).

The effective spin-spin interactions are different in the three cases. For $\mathbb{Z}_2$ and $\mathbb{Z}_3$, spins interact via natural dipole-dipole interactions, which involve both Ising-type interactions and spin exchange between resonant transitions, e.g. $|0\rangle_i \otimes |\pm1\rangle_j \leftrightarrow |\pm1\rangle_i \otimes |0\rangle_j$ for spins i, j (see Appendix D). For $\mathbb{Z}_2$-Ising, strong transverse microwave driving during τ_1 causes the spin-spin interactions in the dressed state basis $|\pm X\rangle = (|0\rangle \pm |-1\rangle)/\sqrt{2}$ to become purely Ising-like (see Appendix D). In our experiments, spins are initially polarized along the corresponding quantization axes ($|0\rangle$ for $\mathbb{Z}_2, \mathbb{Z}_3$ and $|+X\rangle$ for $\mathbb{Z}_2$-Ising). After time evolution by the Floquet unitary $U_F^{(a)}$ for n cycles, the remaining polarization $P(nT)$ along the initialization axis is measured via spin-state-dependent fluorescence.

Experimental observations and analyses.— In all three cases, we observe robust subharmonic responses over a wide range of perturbation strengths ϵ and Floquet periods T. As an example, Fig. 5.1(c-f) shows typical time traces of $P(nT)$ and their Fourier spectra $|S(\nu)|^2$ for $\mathbb{Z}_3$, for two different T at finite ϵ (see Appendix D). For very short T, $P(nT)$ shows a modulated decaying signal, and $|S(\nu)|^2$ displays broad sidepeaks at ϵ-dependent locations away from $\nu = 1/3$ [Fig. 5.1(c,d)]. For larger T, $P(nT)$ instead exhibits long-lived oscillations with a period of three cycles, reflected in a sharp spectral peak pinned at $\nu = 1/3$, indicating that the subharmonic response is stabilized by interactions [Fig. 5.1(e,f)]. Generally, for an integer $m > 1$, we associate the signature of $\mathbb{Z}_m$ DTC order with the presence of $\nu = 1/m$ peaks in the Fourier spectrum that are sharp and robust against perturbations ϵ.

To quantitatively probe the stability of DTC order as a function of parameters ϵ and T, we examine the crystalline fraction f, defined as the normalized spectral weight at the expected frequency $\nu = 1/m$ ($m = 2, 3$) in the late time ($n \geq 40$) dynamics of $P(nT)$, after initial transients in the dynamics have decayed away. For each T, we identify the value of ϵ at $f = 0.1$ as the phenomenological phase boundary where DTC order is lost [Fig. 5.2(a-c)]. Focusing first on short T, we find in all three cases that the phase boundaries are linear in the ϵ-T plane, similar to prior observations [35, 68, 111]. However, closer inspection [Fig. 5.2(d)] reveals that DTC order extends to a wider range of ϵ in $\mathbb{Z}_2$ & $\mathbb{Z}_3$ than in $\mathbb{Z}_2$-Ising. This is surprising since spin-exchange interactions should intuitively aid thermalization and make DTC order less stable, although it is known that long-range

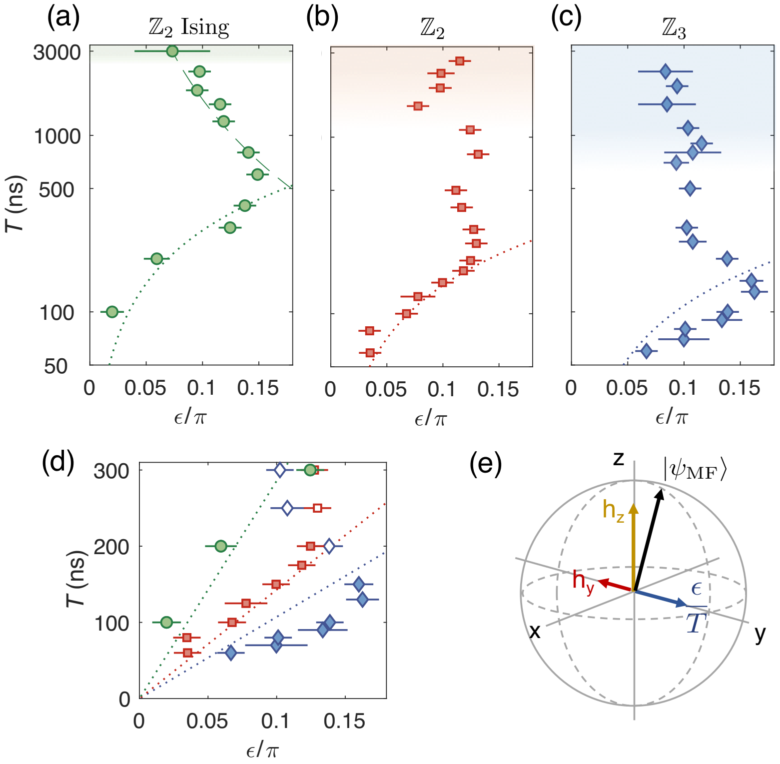

Figure 5.2: **Phase diagram of DTC order for short drive periods.** (a-c) Phase diagrams in semi-log scale. The phase boundary (markers) is identified as a crystalline fraction of 10%. The dotted line indicates the linear phase boundary predicted by a self-consistent mean-field analysis (see Appendix D). Shaded areas denote a universal dephasing regime corresponding to Markovian thermalization where $T > T^*$ (see Figure 4). In (a), the dashed line represents the theoretical prediction from Ref. [110]. Errorbars denote 95% confidence intervals of the phase boundary (see Appendix D). (d) Short-T phase diagram in linear scale (markers as in (a-c)). (e) Bloch sphere illustrating the screening effect of spin-exchange interactions. h_z and h_y are mean fields arising from Ising and spin-exchange interactions respectively, and ϵ/T is the perturbing field. The black arrow corresponds to the mean field solution $|\psi_{\mathrm{MF}}\rangle$.

interactions can sometimes have a regularizing effect on dynamics [125].

From Fig. 5.2(a-c), we observe that the linear phase boundaries do not extend indefinitely with increasing T, but instead bend inwards, albeit with different shapes between the different Floquet Hamiltonians. To investigate thermalization dynamics in this longer

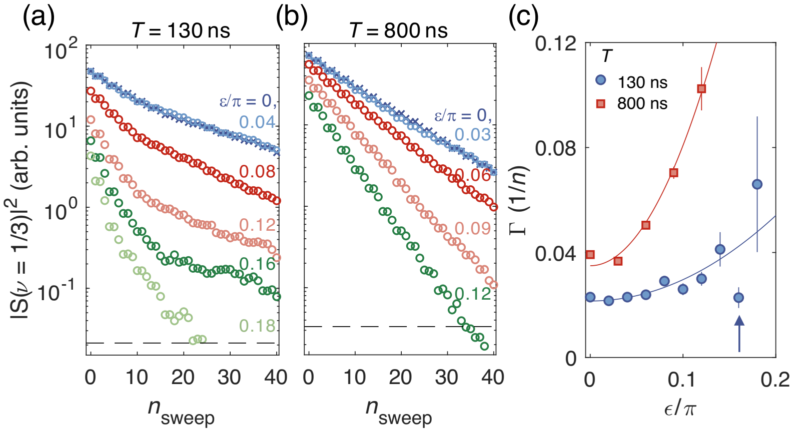

Figure 5.3: **Long interaction time behavior of DTC order.** (a,b) Temporal decay of $\mathbb{Z}_3$ DTC order $|S(\nu = 1/3)|^2$, for different ϵ, as a function of sweeping window position n_{sweep}. Dashed lines denote the noise floor. (c) Late-time decay rate Γ as a function of ϵ, with phenomenological quadratic fit. Each data point results from an average over simple exponential fits of $|S(\nu = 1/3)|^2$ starting from $n_{\text{sweep}} = 15-20$ to exclude initial transients resulting from a short-time, non-universal dephasing. Error bars denote the statistical error of the fit results. The arrow indicates the mean-field phase boundary.

T regime, we examine the decay of DTC order. Specifically, we perform a Fourier transform of $P(nT)$ over a window of cycles $n \in [n_{\text{sweep}}, n_{\text{sweep}} + L - 1]$, where $L = 36$ is fixed, and extract the subharmonic peak height $\mathcal{S} = |S(\nu = 1/m)|^2$, $(m = 2, 3)$. By sweeping the starting position n_{sweep}, we produce a time trace of the peak height, which allows us to track how the DTC order decays in time. Fig. 5.3(a-b) shows typical decay profiles of $\mathbb{Z}_3$ DTC order, for two different T. For T slightly beyond the linear phase boundary regime, the decay exhibits a stretched exponential profile, with late-time decay rates Γ nearly independent of ϵ [Fig. 5.3(a)]. In contrast, for long T, the decay profile of $\mathcal{S}$ approaches a simple exponential, characteristic of Markovian dynamics [Fig. 5.3(b)]. Γ also becomes sensitive to ϵ, indicating an instability of the subharmonic signal [Fig. 5.3(c)]. We have verified that the other Floquet Hamiltonians also exhibit qualitatively similar changes in behavior of

$\mathcal{S}$ (see Appendix D).

To quantify the crossover between different decay profiles, we phenomenologically fit $\mathcal{S}$ with a stretched exponential $A\exp[-(n_{\text{sweep}}/n_T)^{\beta}]$. For a given T, we compute the exponent $\overline{\beta}$ governing the decay of the stretched exponential, averaged over different ϵ. For all Floquet sequences, we find that $\overline{\beta}$ increases from ∼0.6 (stretched exponential) with increasing T, before saturating at 1 (single-exponential), albeit with different saturation timescales T^* [Fig. 5.4(a)]. We note there is a slight falling off for very long T, which we attribute to convolution effects with the longitudinal spin relaxation (T_1) [76] (see Appendix D). We employ a saturation fit $\overline{\beta} = 1/(1 + (c_1/T)^{c_2})$ and extract the Floquet period T^* at which $\overline{\beta} = 0.9$. Interestingly, T^* coincides with the timescale beyond which Γ as a function of ϵ collapses onto a universal quadratic shape, with curvature approximately equal to 1/2 up to an offset Γ_0 [Fig. 5.4(b)]. Physically, Γ_0 is attributable to a combination of T_1 depolarization of spins and dephasing during the finite rotation pulses (see Appendix D). For the $\mathbb{Z}_2$-Ising, $\mathbb{Z}_2$, $\mathbb{Z}_3$ cases, we find that $T^* = 2.64(5), 1.20(5), \text{and}\, 0.45(2)\, \mu s$ respectively. As expected, T^* is longest for the $\mathbb{Z}_2$-Ising case, indicating that thermalization proceeds slower when only Ising interactions are present.

The above observations suggest the existence of three thermalization regimes: a short-T regime where spin-exchange interactions seem to stabilize DTC order, an intermediate-T regime where DTC order persists but is less stable, and a long-T, apparently universal regime where subharmonic responses are unstable, decaying at a rate $\Gamma = \epsilon^2/2$, and thus cannot be associated with stable DTC order.

To explain our observations in the short-T regime, we turn to a mean-field analysis. When T is sufficiently short compared to the inverse of disorder strength, we can describe the dynamics of the amplitude of $P(nT)$ by an effective, static Hamiltonian D by going into an appropriately chosen moving frame (the so-called toggling frame, see Appendix D). Keeping only the lowest order terms in T and ϵ, we obtain

$$\begin{aligned}
D^{\mathbb{Z}_2\text{-Ising}} &= \sum_{ij} \frac{J_{ij}}{r_{ij}^3} S_i^x S_j^x + \frac{\epsilon}{T} \sum_i S_i^y, \\
D^{\mathbb{Z}_2} &= \sum_{ij} \frac{J_{ij}}{r_{ij}^3} \left(S_i^x S_j^x + S_i^y S_j^y - S_i^z S_j^z \right) + \frac{\epsilon}{T} \sum_i S_i^y, \\
D^{\mathbb{Z}_3} &= \sum_{ij} \frac{J_{ij}}{r_{ij}^3} \sum_{ab} \left(\delta_{ab} - \frac{1}{3} \delta_{a\pm1,b} \right) \sigma_i^{ab} \sigma_j^{ba} + \frac{\epsilon}{3T} \sum_i R_i,
\end{aligned}$$

where J_{ij}, r_{ij} are the orientation-dependent coefficient of dipolar interactions and distance between spins i, j, S_i^μ are spin-1/2 operators for the two levels $|0\rangle$, $|-1\rangle$, $R_i = (\sigma_i^{+1,0} + \sigma_i^{-1,0} + i\sigma_i^{+1,-1} + h.c.)$, and $\sigma_i^{ab} = |a\rangle \langle b|$ with $a, b \in \{0, \pm1\}$. Now, for each Hamiltonian, we seek a self-consistent steady state solution at the mean-field level in the toggling frame, corresponding to a stable subharmonic response in the lab frame. We find that such solutions exist when $|\epsilon| \leq \epsilon_c = aJ_{MF}T$, where J_{MF} is the total mean-field interaction strength and a equals 1/2, 1, and 4/3 for $\mathbb{Z}_2$-Ising, $\mathbb{Z}_2$, and $\mathbb{Z}_3$ DTC respectively, which yields a linear phase boundary prediction in reasonable agreement with the experimental data [Fig. 5.2(d)]. The wider phase boundary in $\mathbb{Z}_2$, $\mathbb{Z}_3$ than $\mathbb{Z}_2$-Ising can also be understood from the self-consistent mean-field wavefunction: one finds that spin-exchange terms, having opposite signs to the Ising terms, generate a screening field that partially cancels the perturbing external field (see Fig. 5.2(e), see Appendix D).

The preceding mean-field analysis is expected to break down when T is larger than the inverse of disorder energy scales. Then, resonances due to absorption/emission of energy quanta from/into the drive can occur more readily, giving rise to more thermalization channels. However, the apparent stability of the DTC order even in this regime can be

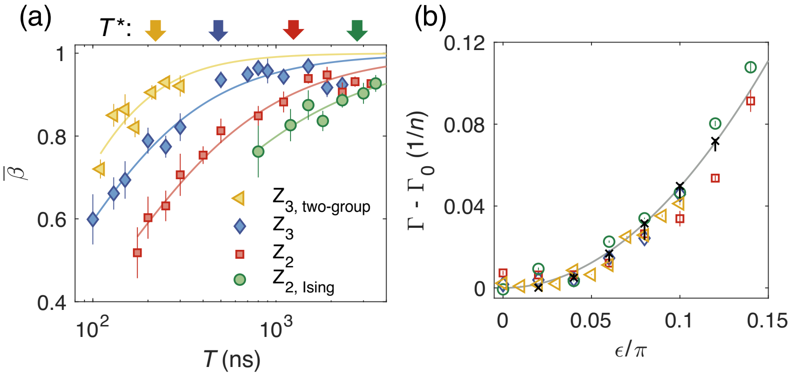

Figure 5.4: **Universal thermalization dynamics for different Floquet Hamiltonians.** (a) Exponents of the stretched exponential fits versus T. Data points denote the average over β values extracted at different ϵ, errorbars are the standard deviation of the mean. Lines denote fits to extract the saturation timescale T^* (arrows), identified where $\overline{\beta} = 0.9$. (b) Late-time decay rate Γ as a function of ϵ (after a global offset Γ_0 has been subtracted, see Appendix D) at T = 3.5, 3.5, 2.3 and 0.3 μs for the $\mathbb{Z}_2$-Ising, $\mathbb{Z}_2$, $\mathbb{Z}_3$, and two-group $\mathbb{Z}_3$ cases, respectively (markers as in (a)). Solid line indicates a dephasing model fit, predicting $\Gamma = \epsilon^2/2 + \Gamma_0$. Error bars as in Fig. 5.3(c). Cross markers show numerical results of an infinite-range, interacting spin system with both Ising and spin-exchange interactions (see Appendix D). Errorbars in the numerics represent the standard deviation of decay rate distributions for different realizations.

explained—at least in the $\mathbb{Z}_2$-Ising case—by a critical DTC regime [110], in which the interplay of long-range interactions, dimensionality, disorder and driving leads to critically slow dynamics, and yields a phase boundary narrowing prediction of $\epsilon_c \sim 1/\sqrt{T}$. Indeed, Fig. 5.2(a) shows that this scaling fits the experimental data extremely well. In contrast, for the $\mathbb{Z}_2$ and $\mathbb{Z}_3$ cases, signatures of stable DTC order remain but are more fragile, existing only in a relatively narrow region. Furthermore, the scaling of the experimentally obtained phase boundaries differs from the $\mathbb{Z}_2$-Ising case.

The observed universal quadratic scaling of decay rates at sufficiently long T can be qualitatively explained by dephasing of individual spins, due to a proliferation of resonances, independent of the details of the thermalizing Hamiltonian. We consider a model (see Appendix D) where each spin is projected onto its quantization axis within one Floquet cycle due to strong dephasing, leading to Markovian population dynamics, wherein the net ensemble polarization reduces by a factor of $\cos(\epsilon)$ per cycle. This yields a decay rate $\Gamma = -\log[\cos(\epsilon)] \approx \epsilon^2/2$, which agrees well with the experimental observations [Fig. 5.4(b)] upon allowing for an offset Γ_0 due to external depolarization processes. To probe the origin of dephasing, we perform an additional $\mathbb{Z}_3$ experiment with doubled spin density (see Appendix D), and find that T^* is halved to $0.21(4)\,\mu$s [Fig. 5.4(a)]. Moreover, the independently estimated dephasing time due to the external bath is much longer than the T^* values (see Appendix D), strongly suggesting that dephasing dominantly arises from intrinsic, coherent spin-spin interactions. Indeed, exact diagonalization studies of a strongly interacting toy model of N spin-1/2 particles, coupled via all-to-all random interactions $\sum_{ij} J_{ij}/\sqrt{N}\,[\alpha(S_i^x S_j^x + S_i^y S_j^y) - S_i^z S_j^z]$ with $\alpha = 0, 1$, and which are periodically rotated by an angle $\pi + \epsilon$, yield a decay rate $\epsilon^2/2$ of the subharmonic signal for sufficiently long Floquet periods $J_{ij}T \gg 1$ [Fig. 5.4(b)]. However, we note that the Ising case ($\alpha = 0$) shows a much slower approach to the Markovian regime in finite-size scaling than the spin-exchange case ($\alpha = 1$) (see Appendix D).

Our observations of the relative stability and distinct scaling of the critical DTC regime in the $\mathbb{Z}_2$-Ising case as well as its long T^* value, indicate important differences in the thermalization dynamics of systems with different types of long-range interactions. This is in broad agreement with recent analytical and numerical studies of thermalization [69, 118, 126]; however, a detailed and better understanding of these differences is a challenging task which deserves further investigation.

5.3 Conclusion and outlook

We have demonstrated that the stability of DTC order can be used to sensitively and quantitatively probe thermalization dynamics of a many-body system. In particular, we have explored how the interplay of disorder, periodic driving, and interactions gives rise to different thermalization regimes. Our results shed light on the mechanisms through which many-body quantum systems approach thermal equilibrium, an important aspect in the quest for full control over quantum matter.

Chapter 6

Fault-Tolerant Quantum Metrology Beyond the Interaction Limit

6.1 Introduction

Quantum sensors harness the remarkable features of quantum mechanics to achieve superior spatial resolution, spectral resolution and sensitivity, serving as powerful tools for the exploration of fundamental physics [127], with applications in material science [128] and biochemical analysis [129, 130]. One key figure of merit for all applications of quantum metrology is sensitivity. A natural approach to improving sensitivity is to utilize a dense ensemble of individual sensors and take advantage of parallel averaging. However, beyond a certain density, undesired interactions between sensors start to affect the coherence of the ensemble, limiting its sensitivity (Fig. 6.1A). Moreover, on-site disorder and control errors give rise to inhomogeneities in the response of individual sensors and result in a further decrease in sensitivity. While some of these issues have been addressed in the context of

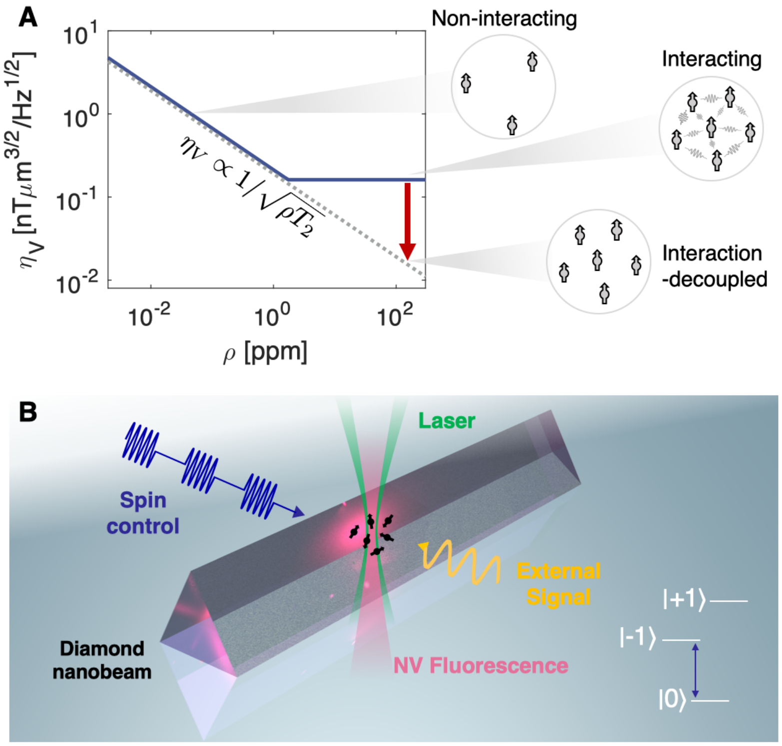

Figure 6.1: **Interaction limit to spin ensemble quantum sensing.** **(A)** Volume-normalized magnetic field sensitivity as a function of spin density. The dashed line denotes the standard quantum limit scaling and the solid curve shows the behaviour when interactions between spins are taken into account for the typical readout efficiency factor $C = 0.01$ [134]. The sensitivity plateaus beyond a critical density due to a coherence time reduction. Fault-tolerant interaction decoupling (red arrow) allows us to break the interaction limit. **(B)** Illustration of the black diamond nanobeam used as a spin ensemble quantum sensor. Microwave and optical excitation are delivered to the NV spins to control and read out their spin states, and an AC magnetic field is used as a target sensing signal. The inset shows the three magnetic sublevels, $|0\rangle$ and $|\pm 1\rangle$, in the ground state of NV centers, where two levels, $|0, -1\rangle$ are addressed using resonant microwave driving. All measurements are performed at room temperature under ambient conditions.

nuclear magnetic resonance (NMR) experiments [131, 132, 133], these experiments have not focused on AC field sensing in the interaction-limited regime, in the presence of strong disorder, crucial for electronic spin ensemble-based sensors.

We address this challenge by designing and implementing a new protocol for quantum sensing with disordered interacting spin ensembles. Our method uses robust periodic manipulation (Floquet engineering) of ensemble spin dynamics [135] to generate a pulse sequence with high sensitivity to an external signal of interest, while simultaneously decoupling the effects of interactions and disorder, and remaining fault-tolerant against the leading-order imperfections arising from the finite pulse durations and experimental control errors. We show that all of these conditions are captured by a set of simple design rules imposed on the pulse sequence, which allow us to break the sensitivity limit set by the spin-spin interactions.

6.2 Experimental methods

Our experimental system consists of a dense electronic spin ensemble of NV centers in diamond [17, 76], as shown in Fig. 6.1B. NV centers exhibit long-lived spin coherence even at room temperature and are excellent quantum sensors [136, 137] for magnetic fields [134, 138], electric fields [139], pressure [140, 141], and temperature [30, 142, 143]. Our sample has a high density of NV centers (∼45 ppm), with long-range magnetic dipolar interactions between the spins as well as strong on-site disorder originating from other paramagnetic impurities, inhomogeneous strain in the diamond lattice, and local electric fields [17, 76, 141]. The bulk diamond is etched into a nanobeam to improve control homogeneity and confine the probing volume to $V = 8.1(9) \times 10^{-3}$ μm^3. The NV center ground state is an electronic $S = 1$ spin, and we apply a static magnetic field to isolate an ensemble of effective two-level systems formed of NVs with the same crystallographic orientation (∼11 ppm). We initialize and detect the spin states optically and use resonant microwave excitation to drive coherent spin dynamics.

Our spin system, including the control fields and the external AC sensing field, is described by the Hamiltonian [17]

$$H = H_s + H_\Omega(t) + H_{\text{AC}}(t), \tag{6.1}$$

where the internal system Hamiltonian is $H_s = \sum_i h_i S_i^z + \sum_{ij} \frac{J_{ij}}{r_{ij}^3}(S_i^x S_j^x + S_i^y S_j^y - S_i^z S_j^z)$, global spin-control pulses are given by $H_\Omega(t) = \sum_i(\Omega_i^x(t) S_i^x + \Omega_i^y(t) S_i^y)$ and the external target signal is $H_{\text{AC}}(t) = \gamma_{\text{NV}} B_{\text{AC}} \cos(2\pi f_{\text{AC}} t - \phi) \sum_i S_i^z$. Here, S_i^μ ($\mu = x, y, z$) are spin-1/2 operators, h_i is a random on-site disorder potential that follows a normal distribution with standard deviation $W = (2\pi)\ 4.0$ MHz, J_{ij}/r_{ij}^3 is the anisotropic dipolar interaction strength between two spins of the same crystallographic orientation at a distance r_{ij}, with an average strength of $J = (2\pi)\ 0.1$ MHz at a typical separation [17], $\Omega_i^{x,y}(t)$ are the global control amplitudes exhibiting weak position dependence due to spatial field inhomogeneities, γ_{NV} is the gyromagnetic ratio of the NV center, and B_{AC}, f_{AC} and ϕ are the amplitude, frequency and phase of the target AC signal, respectively.

6.3 Fault-tolerant interaction decoupling

In our dense NV ensemble, we observe that the $1/e$ coherence decay time T_2 of the spin echo [144] is limited to only $1.0\ \mu s$ (Fig. 6.2C, gray crosses). The conventional method to extend T_2 beyond the spin echo is the XY-8 dynamical decoupling sequence [145, 146, 147], consisting of equally-spaced π pulses along the $\hat{x}$ and $\hat{y}$ axes (Fig. 6.2A, top row). In our system, however, the XY-8 sequence only provides a small improvement and is limited by strong spin-spin interactions ($T_2 = 1.6\ \mu$s, Fig. 6.2C, blue squares).

In order to significantly extend T_2 in the presence of interactions, we use a novel ap-

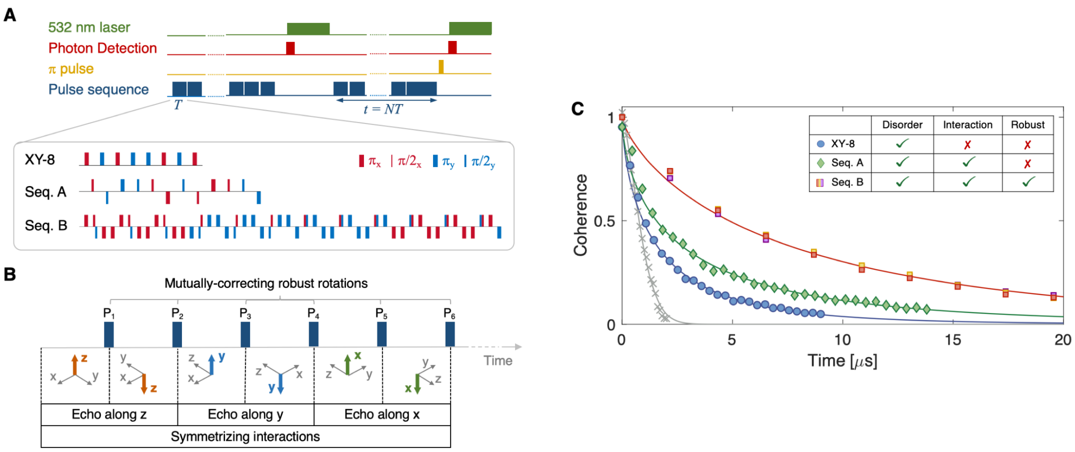

Figure 6.2: **Fault-tolerant dynamical decoupling.** **(A)** Measurement protocol. NVs are initialized using pulsed laser excitation at 532 nm (green trace) and read out through emitted photons detected by a single photon counting module (red trace). We perform N repetitions of a sensing sequence unit of length T (blue trace) and repeat the same measurement with an additional π pulse (yellow trace) acting on the NV centers for differential readout of the spin state. The box illustrates the details of different pulse sequences, XY-8, Seq. A and Seq. B, composed of $\pi/2$ and π rotations along $\hat{x}$ and $\hat{y}$ axes. **(B)** Key concepts for sequence design. The sequence is described by pulses P_i and the time-dependent frame transformation of the system between the pulses. We highlight the orientation of each rotated frame by the axis that points along the $\hat{z}$ axis of the fixed external reference frame. Decoupling sequences are designed by imposing average Hamiltonian conditions on the evolution of the highlighted axis. For example, the effects of disorder can be cancelled by implementing an echo-like evolution, $+\hat{\mu} \rightarrow -\hat{\mu}$ where $\mu = x, y, z$ (top row), and interactions are symmetrized by equal evolution in each of the $\hat{x}, \hat{y}$ and $\hat{z}$ axes in the transformed frames (bottom row). Additionally, the pulse sequence is designed to mutually correct rotation angle errors and finite pulse duration effects. **(C)** Experimental performance of different sequences with their respective decoupling features (inset). We fit the decoherence profile with a stretched exponential $e^{-(t/T_2)^\alpha}$ (solid curves) to extract the coherence time T_2 for each sequence. A simple spin-echo (gray crosses), XY-8 (blue circles) and Seq. A (green diamonds) show $T_2 = 0.98(2)$ μs, $1.6(1)$ μs, and $2.8(1)$ μs with $\alpha = 1.5(1), 0.66(2)$, and $0.61(3)$, respectively. Seq. B (squares), designed to correct for leading order effects of interactions, disorder and control imperfections, gives $T_2 = 7.9(2)$ μs with $\alpha = 0.75(2)$. We confirm that its coherence time is independent of the initial state prepared along $\hat{x}, \hat{y}$ and $\hat{z}$ axes, as shown in red, yellow and purple, respectively. All sequences have pulse spacing $\tau = 25$ ns and π-pulse width $\tau_\pi = 20$ ns.

proach to design pulse sequences that fully suppress interactions and disorder to leading order, and are fault-tolerant against rotation angle errors and finite pulse duration effects. More specifically, we employ average Hamiltonian theory to engineer the system Hamiltonian through pulsed periodic manipulation of the spins [135]. A sequence composed of n equidistant control pulses $\{P_k; k = 1, 2, .., n\}$ with spacing τ defines a unitary operator over a period T given by $\mathcal{U}(T) = P_k e^{-iH_s\tau} \cdots P_1 e^{-iH_s\tau}$. If the pulse spacing τ is much shorter than the timescales of the system Hamiltonian ($\tau \ll \frac{1}{W}, \frac{1}{J}$), the unitary operator $\mathcal{U}(T)$ can effectively be approximated by a time-independent average Hamiltonian as $\mathcal{U}(T) \approx e^{-iH_{\text{avg}}T}$, with $H_{\text{avg}} = \frac{1}{T}\sum_{k=1}^{n} \tilde{H}_k$, and $\tilde{H}_k = (P_{k-1} \cdots P_1)^\dagger H_s (P_{k-1} \cdots P_1)$, $\tilde{H}_1 = H_s$ [135]. Motivated by this picture, we aim to develop a pulse sequence which generates a desirable form of H_{avg} from the H_s intrinsic to the system.

Intuitively, Hamiltonian engineering can be understood as the result of a sequence of frame transformations which rotate the interaction-picture operators (Fig. 6.2B): for example, a π-pulse flips $S_i^z \to -S_i^z$, while a $\pi/2$-pulse rotates $S_i^z \to \pm S_i^{x,y}$. Importantly, the average Hamiltonian is uniquely specified by the transformations of the S^z operator in the interaction picture. This significantly simplifies the procedure to find desired pulse sequences. For example, any pulse sequence in which the transformed S^z operator spends equal time along the positive and negative direction for each axis—effectively producing a spin echo along all three axes—suppresses the effects of on-site disorder. Similarly, in order to symmetrize the anisotropic dipolar interaction into an isotropic Heisenberg form (where polarized states are eigenstates), we require that the transformed S^z operator spend an equal amount of time in each of three $\hat{x}$, $\hat{y}$, $\hat{z}$ directions. Furthermore, one can prioritize one condition over another to find a pulse sequence that better suits a given system; since disorder is dominant in our spin ensemble ($W \gg J$), we perform the echo operation more frequently than interaction symmetrization.

In realistic situations, the above analysis will be severely affected by various imperfections, such as the finite durations and errors of each control pulse. Crucially, however, the effective Hamiltonian capturing these imperfections, δH_{avg}, can also be described using the interaction-picture S^z operator, allowing us to write down simple algebraic conditions for suppressing the dominant effects of disorder and interactions during the finite pulses as well as the impact of rotation angle errors. We can thus systematically generate pulse sequences that are fault-tolerant to all of these imperfections, yielding a pure Heisenberg Hamiltonian with $\delta H_{\text{avg}} = 0$.

To illustrate the importance of robust sequence design, we examine the decoupling efficiency of a pulse sequence (Seq. A in Fig. 6.2A) that decouples disorder and interactions in the ideal pulse limit, but does not suppress all pulse-related imperfections. This is a generalization of the WAHUHA sequence [88], where in addition to interaction symmetrization, we also decouple the effects of disorder during the free precession periods. Compared to XY-8, only a modest increase in coherence time is observed with $T_2 = 2.8\ \mu$s (Fig. 6.2C, green diamonds), indicating that the remaining imperfections play an important role. To address these imperfections, we use our full formalism to design Seq. B, as shown in Fig. 6.2A. Due to its fault-tolerance against all leading-order effects, it shows a significant extension of coherence time compared to the sequences described above, reaching $T_2 = 7.9\ \mu$s (Fig. 6.2C, squares). Moreover, we confirm that the coherence time is independent of the initial state. We expect the T_2 reached here to be limited by higher-order terms and microwave waveform distortions.

6.4 Modulation functions and optimal sensing

In order to perform quantum sensing, the dynamics of the spin ensemble must be sensitive to the target sensing signal. AC magnetic field sensing typically uses periodic inversions of the spin operator between S^z and $-S^z$ in the interaction picture, driven by a train of equidistant π pulses at a separation of $\frac{1}{2f_{\mathrm{AC}}}$. This modulation causes cumulative precession of the sensor spin when the AC field sign change coincides with the frame inversion, resulting in high sensitivity to a signal field at f_{AC}. Our interaction-decoupling sequences explore all three frame directions S^x, S^y, S^z and AC selectivity requires synchronized periodic frame inversions in each of the three axes while preserving the desired H_{avg} and suppressing δH_{avg} to maintain long coherence times.

In Fig. 6.3A we illustrate how this is achieved in Seq. B. The pulses lead to periodic changes in the sign and orientation of the interaction-picture S^z operator, depicted by the time-domain modulation functions for each axis direction, F_x, F_y and F_z. The detailed resonance characteristics of the pulse sequence can be characterized by the Fourier transforms $\tilde{F}_\mu(f) = |\tilde{F}_\mu(f)|e^{-i\tilde{\phi}_\mu(f)}$ of F_μ for $\mu = x, y, z$, where $\tilde{\phi}_\mu(f)$ is the spectral phase for a given axis μ. Fig. 6.3B shows the calculated spectral intensities along different axes, $|\tilde{F}_x(f)|^2$,$|\tilde{F}_y(f)|^2$, and $|\tilde{F}_z(f)|^2$, as well as the total intensity $|\tilde{F}_t(f)|^2$. At the dominant resonance of the total intensity (red arrow in Fig. 6.3B), all three axes exhibit a phase-locked periodic sign modulation (Fig. 6.3A), leading to constructive phase accumulation and high sensitivity.

In order to intuitively understand our sensing protocol and quantify its sensitivity, we

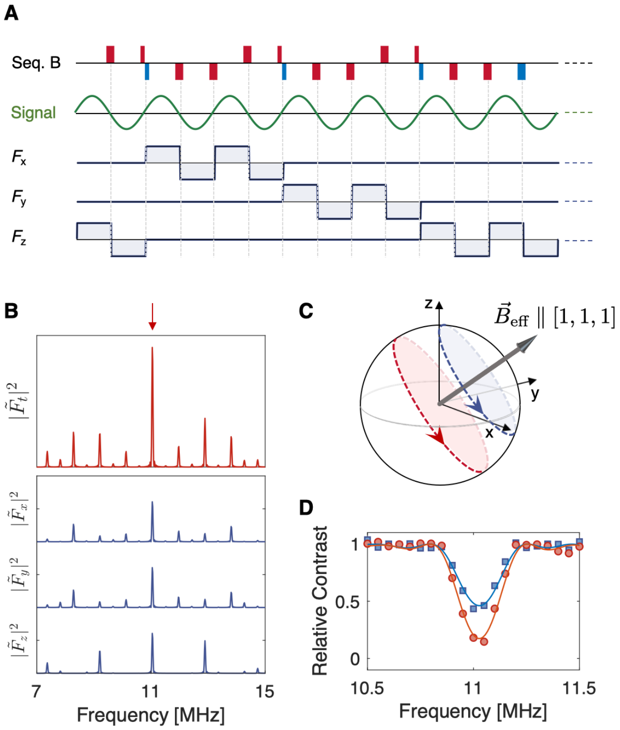

Figure 6.3: **Optimal sensing with unconventional spin state preparation.** **(A)** Pulse sequence (top row) and three-axis time-domain modulation functions (blue solid curves) for the first 14 free evolution times of Seq. B. Red/blue bars in Seq. B indicate rotation pulses as defined in Fig. 6.2A. The modulation period along each axis is synchronized to an AC sensing signal (green curve). **(B)** Frequency-domain modulation function $|\tilde{F}_{x,y,z}(f)|^2$ for Seq. B, with pulse spacing $\tau = 25$ ns and π-pulse width $\tau_\pi = 20$ ns. The total strength $|\tilde{F}_t(f)|^2$ is obtained from individual axis amplitudes $\tilde{F}_{x,y,z}(f)$ in consideration of their relative phases in the frequency domain. The principal resonance is highlighted by a red arrow, yielding maximum sensitivity. **(C)** Illustration of the effective magnetic field created by Seq. B at the principal resonance. In the average Hamiltonian picture, the $\hat{z}$-direction sensing field in the external reference frame transforms to the [1,1,1]-direction field $\vec{B}_{\rm eff}$ in the effective spin frame with a reduced strength. Optimal sensitivity is achieved by initializing the spins into the plane perpendicular to the effective magnetic field direction. This optimal state preparation allows the spins to precess along the trajectory with the largest contrast (red dashed line). For comparison, the precession evolution for initialization to the conventional $\hat{x}$ axis is shown as a blue dashed line. **(D)** Sensing resonance spectra near the principal resonance. The optimal initialization (red) shows greater contrast than the $\hat{x}$-axis initialization (blue). Markers indicate experimental data and solid lines denote theoretical predictions calculated from the frequency-domain modulation functions.

generalize the average Hamiltonian analysis to incorporate AC signal fields, finding

$$H_{\text{avg,AC}} = \gamma_{\text{NV}} B_{\text{AC}} \sum_i \text{Re}\left[\sum_{\mu=x,y,z} \tilde{F}_\mu(f_{\text{AC}}) S_i^\mu e^{i\phi}\right] = \gamma_{\text{NV}} \sum_i \vec{B}_{\text{eff}} \cdot \vec{S}_i, \tag{6.2}$$

where $\vec{B}_{\text{eff}}$ is an effective magnetic field vector in the interaction picture which appears static to the driven spins. This allows a simple interpretation of our scheme: the spins undergo a precession around $\vec{B}_{\text{eff}}$, with the field orientation and magnitude determined by the frequency-domain modulation functions $\tilde{F}_\mu$ and $|\tilde{F}_t|$, respectively. In our optimal Seq. B, the signal at the principal resonance f_{AC} gives rise to $|\tilde{F}_x| = |\tilde{F}_y| = |\tilde{F}_z|$ with $\tilde{\phi}_x = \tilde{\phi}_y = \tilde{\phi}_z$, leading to $\vec{B}_{\text{eff}} \propto [\frac{1}{3}, \frac{1}{3}, \frac{1}{3}]$ with the total strength $|\vec{B}_{\text{eff}}|$ reduced by a factor $1/\sqrt{3}$. We note that this reduction is fundamental and, in fact, close to optimal, given the requirements to suppress the effects of spin-spin interactions via symmetrization. However, despite the reduction, the sensitivity is still improved when the coherence time is extended by interaction-suppresion. The sensitivity to signal B_{AC} is maximized when the spins are initialized perpendicular to the $\vec{B}_{\text{eff}}$ direction—to allow the largest precession orbit (Fig. 6.3C)—and the corresponding optimal readout requires an unconventional rotation axis $[-1, 1, 0]$ and angle $\cos^{-1}(\sqrt{2/3})$ to bring the precession plane parallel to the $\hat{z}$ axis. Indeed, as shown in Fig. 6.3D, we observe a larger contrast when spins are initialized in an optimal direction along $[1, 1, -2]$, compared to an initialization in the $\hat{x}$ direction.

6.5 Demonstration of sensitivity enhancement

Having demonstrated long coherence times and optimal initialization and measurement conditions with Seq. B, we proceed to characterize its sensitivity, and compare it to the conventional XY-8 sequence. Magnetic field sensitivity is defined as the minimum detectable

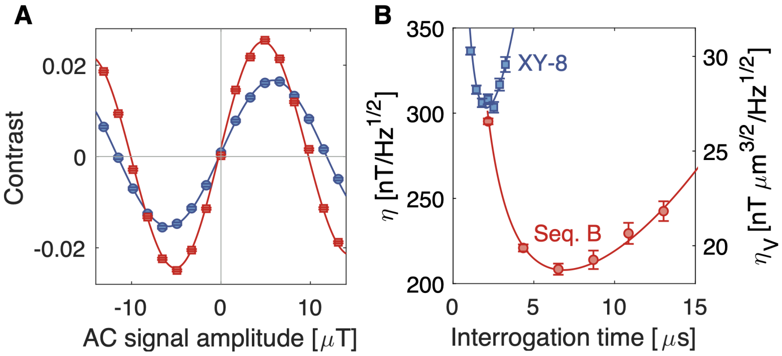

Figure 6.4: **Demonstration of sensitivity enhancement.** **(A)** Observed spin contrast as a function of AC magnetic field strength, for the XY-8 sequence (blue) and for Seq. B (red). The fit is a sinusoidal oscillation with an exponentially decaying profile. Seq. B shows a steeper slope at zero field, indicating that it is more sensitive than XY-8 to the external field. The interrogation times, $t = 2.16$ μs for XY-8 and $t = 6.52$ μs for Seq. B, are independently optimized to achieve maximal sensitivity. **(B)** Extracted absolute sensitivity η and volume-normalized sensitivity $\eta_V = \eta\sqrt{V}$ with sensing volume $V = 8.1(9) \times 10^{-3}$ μm^3 as a function of interrogation time t (error bars are given for η). A comparison of the two sequences at their respective optimal sensing times reveals that Seq. B outperforms XY-8 by $\sim$30%.

signal amplitude per unit time [136], and is given by $\eta = \frac{\sigma_S}{|dS/dB_{\mathrm{AC}}|}$. Here, S is the sensor signal contrast, σ_S is the uncertainty of S for one second of averaging, and $|dS/dB_{\mathrm{AC}}|$ is the gradient of S with respect to the field amplitude B_{AC}.

Figure 6.4A shows the measured contrast S as a function of B_{AC} under optimal conditions for Seq. B and XY-8, where we choose parameters for each of the two sequences to optimize their respective absolute sensitivities. The resonant AC signal induces a precession of the sensor spins, resulting in sinusoidal modulations of S as a function of B_{AC}. We find that Seq. B shows a significantly steeper maximum slope than XY-8, indicating that it is more sensitive to the external signal. This is due to a combination of optimal state preparation and readout schemes and significantly improved coherence time, despite a reduced effective signal strength $|\vec{B}_{\mathrm{eff}}|$ in Seq. B. In Fig. 6.4B, we show the sensitivity scaling with interrogation time, finding good agreement with the theoretical prediction $\eta(t) \propto e^{(t/T_2)^\alpha} \frac{\sqrt{t+T_p}}{t}$, where α is the exponent of the decoherence profile and T_p is the sensor initialization and readout overhead. By optimizing the sensing time to obtain minimal η, we extract the best volume-normalized sensitivity, $\eta_V = \eta\sqrt{V}$, for each sequence. We find that Seq. B, designed with our fault-tolerant optimal sensing approach, reaches more than 30% improvement in sensitivity over the conventional XY-8 sequence. With these enhancements, we demonstrate $\eta_V = 19(2)$ nT $\cdot$ $\mu\text{m}^{3/2}/\sqrt{\text{Hz}}$ for Seq. B, among the best volume-normalized sensitivities for solid-state magnetometers measured thus far [148].

6.6 Conclusions and outlook

Our work establishes a novel approach to ensemble quantum sensing by utilizing fault-tolerant interaction decoupling, and provides the first demonstration of a solid-state ensemble quantum sensor operating in a new regime beyond the interaction limit. Our techniques can be combined with existing technical improvements including optimized spin control pulses [149, 150], spin-bath engineering [151, 152, 153], photon-collection optimization [148, 154, 155], double-quantum magnetometry [153, 156, 157], and novel diamond growth techniques [158, 159, 160, 161, 162], which together may push the volume-normalized sensitivity to below picotesla level in a μm^3 volume for higher spin densities (see Fig. 6.1A). This will open the door to many applications, such as nanoscale nuclear magnetic resonance [129, 130, 163, 164, 165] and investigations of strongly correlated condensed matter systems [128]. In addition, we also envisage that the fault-tolerant sequence design presented in this work can be extended to engineer a broad class of many-body Hamiltonians [82], providing a useful tool to explore non-equilibrium phenomena in driven quantum systems [35, 68, 163, 164, 165, 166] as well as to create highly entangled states for interaction-assisted quantum metrology [20, 123, 167].

Appendix A

Supporting Material of Chapter 2

A.1 Fluorescence dynamics

We utilize a green laser ($\lambda = 532$ nm) to initialize and read out the spin state of NV centers. Due to a two-photon absorption process this excitation can cause ionization of NV centers, resulting in an out-of-equilibrium charge distribution around the excitation spot. This charge distribution relaxes even without illumination, as discussed in the main text. In practice, such charge dynamics can affect the spin-state readout by changing the average fluorescence emission rates (NV^0 vs NV^-). In this section, we explain how to avoid this problem.

The effect of charge dynamics on fluorescence emission rate is illustrated in Fig. A.1a. Under green laser illumination (0-200 μs) the fluorescence emission rate initially increases as spins are polarized, but then quickly decreases as NV centers get ionized (due to preferential collection from the NV^- phonon sideband). Following the polarization of spins at varying laser power, we record the florescence after a variable time evolution t with and without an extra microwave π-pulse at the end of the evolution (empty and full circles Fig. A.1a). We find that the observed fluorescence levels are asymmetric and for high power increase as a function of time. This fluorescence increase is caused by previously ionized NV centers, relaxing back to equilibrium. This effect is particularly dominant at high green excitation power, where ionization at the focal spot is increased. However, as demonstrated in Fig A.1b, the difference in fluorescence with and without the extra π-pulse is independent from the applied green laser power. This result implies that one can use such a differential readout to mediate the contribution of charge dynamics and reliably extract the spin depolarization time scales. Additionally, the use of a low power green laser ($\sim$10 μW) can help reduce the effects of charge dynamics during the experiment. Note, that a similar technique has previously been used to robustly measure spin dynamics in high density NV samples [36].

A.2 Estimation of dipolar spin diffusion timescale

One potential mechanism of spin-density dependent depolarization is that polarized spins diffuse out of the probing volume via dipolar interactions. Here, we estimate the timescale of such spin diffusion using a classical diffusion equation. In our experiments, the probing volume is determined by the confocal excitation spot size $w \sim 200$ nm. Note that this estimate assumes a bulk diamond excitation, approximated by a 2D model, due to the large extent of the excitation spot in the direction normal to the diamond surface. The effective diffusion coefficient D can then be estimated from the average spacing among NV centers $a \sim 5$ nm and the typical flip-flop time $\tau \sim 9.5$ μs (calculated from $J/4 = (2\pi)$ 105 kHz), $D \approx a^2/\tau \sim 2.6$ nm$^2/\mu$s. Assuming that the spin polarization ini-

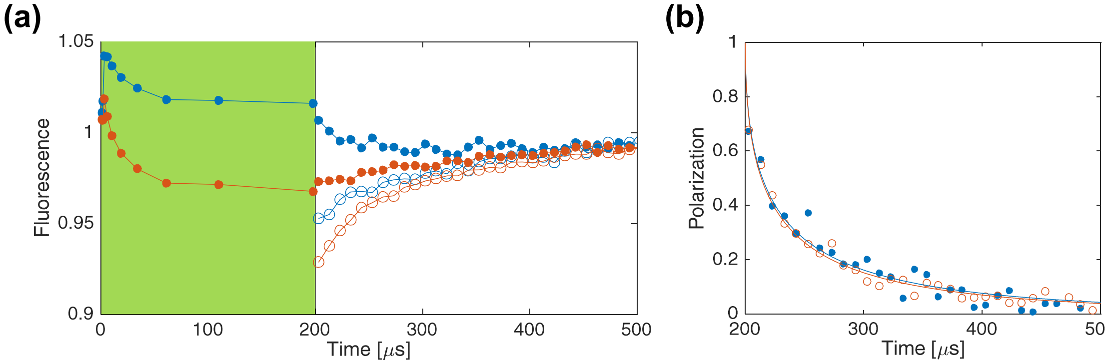

Figure A.1: **Fluorescence Dynamics.** **(a)** Fluorescence emission measurements for two different green laser powers, 10 μW (solid blue data) 40 μW (solid red data). An initial green laser pulse with length 200 μs is used to polarize the spin states of NV centers and reach a charge equilibrium state. After a wait time t, another green pulse is used to read out the spin state. The fluorescence emission rate is measured for both the polarization pulse (green background) and the readout pulse (white background, as a function of t). The emission rate is normalized by an equilibrium value obtained at sufficiently late time ($>$ 500 μs). Empty circles correspond to similar measurements with the addition of microwave π-pulse shortly before readout. **(b)** Spin polarization decay as a function of time, extracted from the difference between filled and empty circles from (a) for both excitation powers.

tially follows a Gaussian distribution with spatial width w, the classical diffusion equation predicts the polarization profile at later time t

$$P(t,\vec{r}) = \frac{e^{-\frac{r^2}{2(w^2+Dt)}}}{2(w^2+Dt)\pi}, \tag{A.1}$$

where one finds that the spin polarization density at $r = 0$ is reduced by a factor of 2 at time $t \sim w^2/D \sim 15$ ms. This timescale is more than two orders of magnitude slower than experimentally measured depolarization times. We note that our estimation ignores the effect of inhomogeneous distribution of NV transition frequencies arising from the presence of other magnetic impurities in diamond; such disorder in transition energies further suppresses resonant spin flip-flop dynamics. For this reason, we rule out spin diffusion as the sole mechanism of ensemble depolarization.

A.3 Rate equation model

In order to estimate the decay rates of two independent depolarization channels γ_1 and γ_2 (Fig. 1a, main text), we analyze the population changes in $|m_s = 0\rangle$ and $|m_s = +1\rangle$ after initialization into $|m_s = -1\rangle$ (Fig. A.2b). For this we employ the following simple rate equation model

$$\frac{d}{dt}\begin{bmatrix} P^{|-1\rangle} \\ P^{|0\rangle} \\ P^{|+1\rangle} \end{bmatrix} = \begin{bmatrix} -\gamma_1-\gamma_2 & \gamma_1 & \gamma_2 \\ \gamma_1 & -2\gamma_1 & \gamma_1 \\ \gamma_2 & \gamma_1 & -\gamma_1-\gamma_2 \end{bmatrix} \begin{bmatrix} P^{|-1\rangle} \\ P^{|0\rangle} \\ P^{|+1\rangle} \end{bmatrix},$$

where $P^{|-1\rangle}$, $P^{|0\rangle}$, and $P^{|+1\rangle}$ are the normalized populations in each spin states. When spins are initialized into $|m_s = -1\rangle$ at $t = 0$, the solution of the rate equation model predicts

$$P^{|-1\rangle}(t) - P^{|0\rangle}(t) = \frac{1}{2}e^{-(\gamma_1+2\gamma_2)t} + \frac{1}{2}e^{-3\gamma_1 t} \tag{A.2}$$

$$P^{|0\rangle}(t) - P^{|+1\rangle}(t) = \frac{1}{2}e^{-(\gamma_1+2\gamma_2)t} - \frac{1}{2}e^{-3\gamma_1 t}. \tag{A.3}$$

In our experiments, however, the decay rates γ_1 and γ_2 are random variables, giving rise to stretched exponential profiles. Consequently, the measured population differences become

$$P^{|-1\rangle}(t) - P^{|0\rangle}(t) = \frac{1}{2}e^{-\sqrt{(\gamma_1+2\gamma_2)t}} + \frac{1}{2}e^{-\sqrt{3\gamma_1 t}} \tag{A.4}$$

$$P^{|0\rangle}(t) - P^{|+1\rangle}(t) = \frac{1}{2}e^{-\sqrt{(\gamma_1+2\gamma_2)t}} - \frac{1}{2}e^{-\sqrt{3\gamma_1 t}}. \tag{A.5}$$

Fitting Eq. (A.4) and (A.5) to experimental data, we extract $\gamma_1 = 10.6 \pm 0.6$ kHz and $\gamma_2 = 1.1 \pm 0.7$ kHz. As shown in Fig. A.2b, this simple theory prediction and the experiment data are in excellent agreement. In particular, we notice that $\gamma_1 \gg \gamma_2$, implying that the spin state decay is induced by a local magnetic noise which changes only one unit of magnetization at a time, $\Delta m_s = \pm 1$.

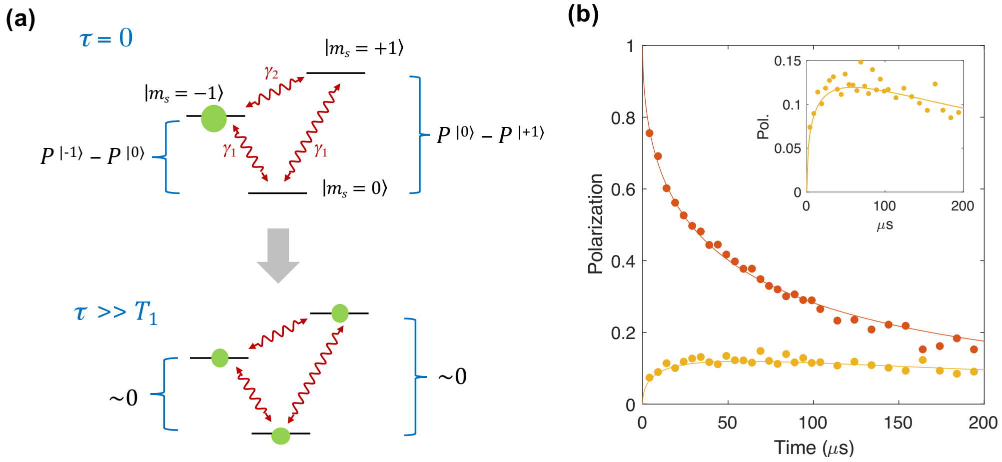

Figure A.2: **Magnetic Noise Model.** **(a)** Schematic level diagram depicting population distribution at $\tau = 0$ (after initialization into $|-1\rangle$) and at $\tau >> T_1$. Possible relaxation channels with rates γ_1 and γ_2 are indicated as red arrows. **(b)** Population difference over time between $|-1\rangle$ and $|0\rangle$ (red data) as well as between $|+1\rangle$ and $|0\rangle$ (orange data) after initialization into $|-1\rangle$. Solid lines indicate the results of the rate equation model, fit to the data. Inset shows a zoom-in of the $|+1\rangle$ - $|0\rangle$ data for better visibility.

A.4 Detailed analysis of spin-fluctuator model

In this section, we provide a detailed analysis of our fluctuator model. As described in the main text, we assume that a fraction of NV centers, with density n_f, undergo rapid depolarization at rate γ_f. Their positions and orientations are randomly distributed. These fluctuators interact with normal spins via dipolar interactions, inducing depolarization. Here, we derive four characteristic features of the observed depolarization dynamics presented in the main text: (a) spin-state dependent polarization rates and preferential decay, (b) stretched exponential decay of ensemble polarization, (c) the resonant feature of depolarization rates as two groups of NV centers become degenerate, and (d) the extension of spin lifetime via spin-locking. Note that the quantitative analysis in (c) allows us to extract the values of γ_f and n_f from the experimental data presented in the main text (Fig. 2c of the main text). We use those extracted parameters to predict the spin lifetime T_1^ρ under spin-locking, which shows reasonable agreement with the data (Fig. 2d of the main text). This section is organized in the following order. First, we compute the effective depolarization rate of a normal spin induced by dipolar interaction with a single fluctuator. We will show that such a mechanism results in spin-state dependent T_1 and preferential decay. Second, we show that interactions with multiple fluctuators located at random positions results in a distribution of effective decay rates $\rho(\gamma)$. We will explicitly compute the ensemble depolarization $P(t) = \int_0^\infty \rho(\gamma) e^{-\gamma t} d\gamma = e^{-\sqrt{t/T_1}}$ and provide an analytic expression for T_1 in terms of microscopic parameters. Finally, we will apply these results to various scenarios to predict the resonant features in Fig. 2c of the main text and the extension of spin lifetime in Fig. 2d of the main text.

A.4.1 Single spin interacting with single fluctuator

We begin our analysis by considering a system of a single spin and a single fluctuator that interact via Hamiltonian H_{int}. The total Hamiltonian of such a system is given as

$$H = H_1 + H_2 + H_{\text{int}} \tag{A.6}$$

where H_1 and H_2 are single particle Hamiltonians for a normal spin and a fluctuator, respectively. The details of H_1 and H_2 varies over different experiments. For example, in typical T_1 measurements where an external magnetic field is aligned along the quantization axis of NV centers, the single particle Hamiltonians are diagonal in the natural spin basis $H_{1/2} = \sum_{m_s \in \{0,\pm1\}} \omega_{m_s} |m_s\rangle \langle m_s|$, where the energy eigenvalues ω_{m_s} in the rotating frame are random number of order $W \sim (2\pi)\ 9$ MHz, owing to inhomogeneous broadening of the system. When strong spin-locking with Rabi frequency Ω is applied between $|m_s = 0\rangle$ and $|m_s = -1\rangle$ transition, a dressed state basis is preferred, where $H_{1/2} = \pm(\Omega/2)\,|\pm\rangle\,\langle\pm| + \omega_0\,|m_s = 0\rangle\,\langle m_s = 0|$ with $|\pm\rangle = (|m_s = 0\rangle \pm |m_s = -1\rangle)/\sqrt{2}$ as defined in the main text. Later, we will also consider a situation where H_1 and H_2 are diagonal in the different basis. Such a case arises when the normal spin and the fluctuator are oriented in different directions. Here, for simplicity, we assume a generic eigenbasis $\{|i\rangle\}$ and $\{|\alpha\rangle\}$ for H_1 and H_2, so that

$$H_1 = \sum_{i\in\{1,2,3\}} \omega_i\,|i\rangle\,\langle i| \quad \text{and} \quad H_2 = \sum_{\alpha\in\{a,b,c\}} \omega_\alpha\,|\alpha\rangle\,\langle\alpha|\,, \tag{A.7}$$

where ω_i and ω_α are corresponding energies in the rotating frame. In addition to coherent dynamics, the fluctuator undergoes rapid incoherent dynamics. Hence, the dynamics of the system are governed by a quantum master equation

$$\dot{\rho} = -i[H, \rho] + L[\rho] \tag{A.8}$$

$$L[\rho] = \sum_k L_k \rho L_k^\dagger - \frac{1}{2}\left(L_k^\dagger L_k \rho + \rho L_k^\dagger L_k\right), \tag{A.9}$$

where ρ is the density matrix of the system and L_k are decay operators. In our model, we consider six decay processes as illustrated in Fig. A.3(a) with identical decay rates γ_f, i.e., $L_k = \sqrt{\gamma_f}\,|m_s = \alpha\rangle\,\langle m_s = \beta|$ with $(\alpha, \beta) \in \{(+1, -1), (-1, +1), (+1, 0), (0, +1), (-1, 0), (0, -1)\}$.

In order to derive the effective master equation for a spin, we use the Born-Markov approximation together with secular approximations [168]. In such a description, the quantum state of the system is approximated by $\rho = \rho_1 \otimes \rho_{\text{thm}}$, where ρ_1 is the reduced density matrix of the normal spin and ρ_{thm} is the equilibrium state of the fluctuator, such that $L[\rho_1 \otimes \rho_{\text{rhm}}] = 0$. In our model, the equilibrium state is a maximally mixed state $\rho_{\text{thm}} = \frac{1}{3}I$. These approximations are well justified due to the hierarchy of the coupling strengths $J_{ij} \ll |\omega_{ij}| \ll \gamma_f$, where $\omega_{ij} = \omega_i - \omega_j$ are the energy difference between eigen-

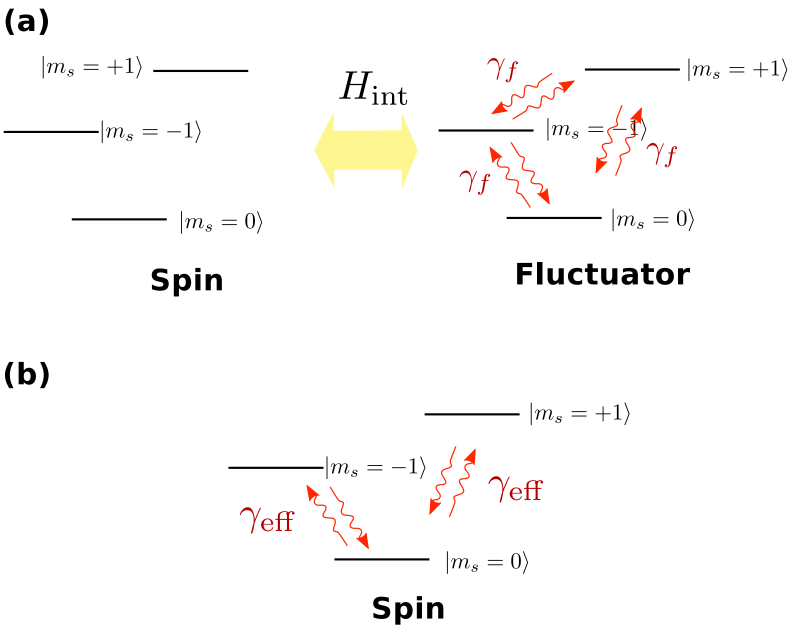

Figure A.3: **Spin-Fluctuator interaction (a)** Level diagram showing a single spin interacting with a single fluctuator. The fluctuator undergoes rapid incoherent depolarization at a rate γ_f. **(b)** Effective incoherent dynamics of a spin due to fluctuator interactions.

states and J_{ij} are typical dipolar interaction strengths. Under these approximations, the effective dynamics of a spin become

$$\dot{\rho_1} = -i[H_1,\rho_1] + L^{\text{eff}}[\rho_1], \tag{A.10}$$

where the first and second terms describe the coherent dynamics by the Hamiltonian H_1 and the induced dynamics by interactions with the fluctuator, respectively. Following standard procedures [168], we obtain

$$L^{\text{eff}}[\rho] \approx \sum_{i,j}\sum_{\alpha\beta\gamma\delta} C^{ij}_{\alpha\beta} C^{ji}_{\gamma\delta} S^{\alpha\beta\gamma\delta}(\omega_{ij}) \Big[\left|j\right\rangle\left\langle i\right| \rho \left|i\right\rangle\left\langle j\right| - \left|i\right\rangle\left\langle i\right| \rho \Big] + h.c. \tag{A.11}$$

$$+ \sum_{i\neq k}\sum_{\alpha\beta\gamma\delta} C^{ii}_{\alpha\beta} C^{kk}_{\gamma\delta} S^{\alpha\beta\gamma\delta}(\omega_{ij}) \Big[\left|k\right\rangle\left\langle k\right| \rho \left|i\right\rangle\left\langle i\right| - \left|i\right\rangle\left\langle i\right| \left|k\right\rangle\left\langle k\right| \rho \Big] + h.c. \tag{A.12}$$

where $C^{ij}_{\alpha\beta}$ is a matrix element of the interaction defined as $C^{ij}_{\alpha\beta} \equiv \left\langle i\alpha\right| H_{\text{int}} \left|j\beta\right\rangle$ with

$i, j \in \{1, 2, 3\}$ and $\alpha, \beta \in \{a, b, c\}$, and $S^{\alpha\beta\gamma\delta}$ is the spectral response function of the fluctuator defined as

$$S^{\alpha\beta\gamma\delta}(\omega) = \int_0^\infty e^{i\omega\tau} \langle\beta| e^{\tau\mathcal{L}_2}\Big[|\gamma\rangle \langle\delta| \rho_{\text{thm}}\Big] |\alpha\rangle \,. \tag{A.13}$$

where the superoperator $\mathcal{L}_2[\cdot] = -i[H_2, \cdot] + L[\cdot]$ describes the time evolution of the fluctuator. For the decay channels illustrated in Fig. A.3, the spectral response function $S^{\alpha\beta\gamma\delta}$ can be simplified by

$$S^{\alpha\beta\gamma\delta}(\omega) = \delta_{\beta\gamma}\delta_{\alpha\delta}S^{\alpha\beta}(\omega) \equiv \delta_{\beta\gamma}\delta_{\alpha\delta} \begin{cases} \frac{1}{3}\cdot\frac{1}{i(\omega+\omega_{\alpha\beta})-2\gamma_f} & \text{for } \alpha \neq \beta \\ \frac{1}{9}\cdot\left(\frac{1}{i\omega}+\frac{2}{i\omega-3\gamma_f}\right) & \text{for } \alpha = \beta \end{cases} . \tag{A.14}$$

Since H_{int} is Hermitian, we can use the relation $C^{ij}_{\alpha\beta} = (C^{ji}_{\beta\alpha})^*$ to obtain

$$L^{\text{eff}}[\rho] \approx \sum_{i,j}\sum_{\alpha\beta} |C^{ij}_{\alpha\beta}|^2 S^{\alpha\beta}(\omega_{ij})\Big[|j\rangle \langle i| \rho |i\rangle \langle j| - |i\rangle \langle i| \rho\Big] + h.c. \tag{A.15}$$

$$+ \sum_{i\neq k}\sum_{\alpha\beta} C^{ii}_{\alpha\beta}C^{kk}_{\beta\alpha}S^{\alpha\beta}(0)\Big[|k\rangle \langle k| \rho |i\rangle \langle i| - |i\rangle \langle i| |k\rangle \langle k| \rho\Big] + h.c. \tag{A.16}$$

Finally, introducing

$$\Gamma_{ij} = 2\sum_{\alpha\beta} |C^{ij}_{\alpha\beta}|^2 \text{Re}\Big[S^{\alpha\beta}(\omega_{ij})\Big] \quad \& \quad \Delta_{ij} = 2\sum_{\alpha\beta} |C^{ij}_{\alpha\beta}|^2 \text{Im}\Big[S^{\alpha\beta}(\omega_{ij})\Big], \tag{A.17}$$

the effective superoperator simply becomes

$$L^{\text{eff}}[\rho] = \sum_{ij}\Gamma_{ij}\Big[|j\rangle \langle i| \rho |i\rangle \langle j| - \frac{1}{2}\left(|i\rangle \langle i| \rho + \rho |j\rangle \langle j|\right)\Big] \tag{A.18}$$

$$- i\sum_{ij}\Delta_{ij}\left[|i\rangle \langle i|, \rho\right] \tag{A.19}$$

$$+ \sum_{i\neq k}\sum_{\alpha\beta} C^{ii}_{\alpha\beta}C^{kk}_{\beta\alpha}S^{\alpha\beta}(0)\Big[|k\rangle \langle k| \rho |i\rangle \langle i|\Big] + h.c. \tag{A.20}$$

Here, we clearly see three types of terms: (i) depolarization or dephasing at rates Γ_{ij}, (ii) energy corrections Δ_{ij} to coherent dynamics, and (iii) additional dephasing from diagonal interactions. Here, we are most interested in the depolarization processes Γ_{ij} under various conditions. In particular, we note that the dipolar interaction under secular approximation is given by

$$H_{dd} \approx -J_0/r^3\big[\,(g+ih)\left(\left|+1,0\right\rangle\left\langle 0,+1\right| + \left|0,-1\right\rangle\left\langle -1,0\right|\right) + h.c. + qS_i^zS_j^z\big], \tag{A.21}$$

where $J_0 = (2\pi)\ 52$ MHz $\cdot$ nm^3 is the dipolar interaction strength, r is the distance, and g, h, and q are coefficients of order unity that depend on the relative orientation of the spin and fluctuator:

$$\begin{aligned} g =& \frac{1}{2}\Big[3\left(\hat{r}\cdot\hat{x}_s\right)\left(\hat{r}\cdot\hat{x}_f\right) - \hat{x}_s\cdot\hat{x}_f + 3\left(\hat{r}\cdot\hat{y}_s\right)\left(\hat{r}\cdot\hat{y}_f\right) - \hat{y}_s\cdot\hat{y}_f\Big] && \text{(A.22)}\\ h =& \frac{1}{2}\Big[3\left(\hat{r}\cdot\hat{x}_s\right)\left(\hat{r}\cdot\hat{y}_f\right) - \hat{x}_s\cdot\hat{y}_f - 3\left(\hat{r}\cdot\hat{y}_s\right)\left(\hat{r}\cdot\hat{x}_f\right) + \hat{y}_s\cdot\hat{x}_f\Big] && \text{(A.23)}\\ q =& 3\left(\hat{r}\cdot\hat{z}_s\right)\left(\hat{r}\cdot\hat{z}_f\right) - \hat{z}_s\cdot\hat{z}_f && \text{(A.24)} \end{aligned}$$

with unit vectors $(\hat{x}_a, \hat{y}_a, \hat{z}_a)$ characterizing the quantization axis of the spin ($a = s$) or fluctuator ($a = f$) [17]. Importantly, this interaction does not contain any transitions between $|m_s = +1\rangle$ to $|m_s = -1\rangle$, resulting in vanishing decay rates between the two states, i.e. $\Gamma_{+1,-1} = \Gamma_{-1,+1} = 0$. Consequently, the interaction-induced dynamics of a spin can be modeled as in Fig. A.3, which exhibit spin-state dependent depolarization rates as well as preferential decays described in the previous section. More specifically, the induced decay rate is

$$\gamma = \frac{J_0^2}{r^6}\left(|g^2| + |h|^2\right)\frac{2}{3}\frac{2\gamma_f}{(\delta\omega)^2 + 4\gamma_f^2} \equiv \frac{J_0^2}{r^6}\frac{s^2}{\gamma_f}, \tag{A.25}$$

where $\delta\omega$ is the energy difference (due to inhomogeneous broadening) between the spin and the fluctuator, and s is a dimensionless number of order unity that characterizes the orientation dependent coefficients of the dipolar interaction as well as spectral responses

$$s^2 = \frac{2}{3}(|g|^2 + |h|^2)\frac{2\gamma_f^2}{\delta\omega^2 + 4\gamma_f^2}. \tag{A.26}$$

A.4.2 Derivation of stretched exponential decay

In an ensemble, the net decay rate γ_s^{eff} of a spin is given as the sum of rates induced by multiple nearby fluctuators. Consequently, the decay rates vary from one spin to another, and the ensemble polarization decays as sum of multiple simple exponentials, whose temporal profile depends on the probability distribution of effective decay rates $\rho(\gamma)$. Here, we compute this distribution and show that the ensemble polarization decays as a stretched exponential

$$P(t) = e^{-\sqrt{t/T_1}}. \tag{A.27}$$

We will see that the exponent, $1/2$, arises as a consequence of incoherent dipole-dipole interaction in 3D. We start with a single spin located at the origin $\vec{r} = 0$ and consider its effective depolarization rate induced by fluctuators at $\{\vec{r}_1, \vec{r}_2, \ldots, \vec{r}_N\}$. The polarization decays as a simple exponential with the rate given by $\gamma_s^{\text{eff}} = \sum_i \gamma_i$, where γ_i is the decay rate induced by fluctuator i. From the previous section, we have shown that each γ_i can be written as $\gamma_i = \frac{J_0^2}{r_i^6}\frac{s_i^2}{\gamma_f}$. The probability distribution $\rho(\gamma_s^{\text{eff}})$ is obtained by averaging $\delta\left(\sum_i \gamma_i - \gamma_s^{\text{eff}}\right)$ over all possible configurations of fluctuators: different number N, positions, and orientations

$$\rho(\gamma_s^{\text{eff}}) = \int d\{\vec{r}_i\}\ \text{Prob}(\{\vec{r}_i\})\ \delta\left(\sum_i \gamma_i - \gamma_s^{\text{eff}}\right). \tag{A.28}$$

When the positions of fluctuators are homogeneously distributed with density n_f, we can analytically compute $\rho(\gamma_s^{\text{eff}})$:

$$\rho(\gamma_s^{\text{eff}}) = \sum_N \int_{\mathcal{D}} dr_1 \dots dr_N \left(\prod_{i=1}^{N} e^{-\frac{4\pi}{3} n_f (r_i^3 - r_{i-1}^3)} 4\pi n_f r_i^2 \right) e^{-\frac{4\pi}{3} n_f (R^3 - r_N^3)} \left\langle \delta \left(\sum_i \gamma_i - \gamma_s^{\text{eff}} \right) \right\rangle_s \tag{A.29}$$

$$= \int_{-\infty}^{\infty} dz \frac{e^{i\gamma_s^{\text{eff}} z}}{\sqrt{2\pi}} \sum_N \int_{\mathcal{D}} dr_1 \dots dr_N \left(\prod_{i=1}^{N} e^{-\frac{4\pi}{3} n_f (r_i^3 - r_{i-1}^3)} 4\pi n_f r_i^2 \left\langle e^{-i\gamma_i z} \right\rangle_s \right) e^{-\frac{4\pi}{3} n_f (R^3 - r_N^3)} \tag{A.30}$$

where the domain of the integral is $\mathcal{D} = r_0 \leq r_1 \leq r_2 \cdots \leq r_N \leq R$ with the shortest (largest) distance cut-off r_0 (R), z is a dummy variable introduced for $\delta(x) = \int_{-\infty}^{\infty} dz e^{ixz}/\sqrt{2\pi}$, and $\langle \cdot \rangle_s$ represents the averaging of all possible orientations of a fluctuator with fixed distance. We denote this distribution with Prob(s). Now, we see that

$$\rho(\gamma_s^{\text{eff}}) = \int_{-\infty}^{\infty} dz \frac{e^{i\gamma_s^{\text{eff}} z}}{\sqrt{2\pi}} e^{-\frac{4\pi}{3} n_f (R^3 - r_0^3)} \sum_N \frac{1}{N!} \left[\int_{r_0}^{R} 4\pi n_f r^2 dr \int \text{Prob}(s)\, ds\, e^{-i \frac{J_0^2}{\gamma_f r_i^6} s^2 z} \right]^N \tag{A.31}$$

$$= \int_{-\infty}^{\infty} dz \frac{e^{i\gamma_s^{\text{eff}} z}}{\sqrt{2\pi}} e^{-\frac{4\pi}{3} n_f (R^3 - r_0^3)} \sum_N \frac{1}{N!} \left[\int_{u_0}^{U} \frac{4\pi n_f}{3} du \int \text{Prob}(s)\, ds\, \sqrt{(J_0^2 s^2/\gamma_f)|z|} e^{-i \frac{\text{sgn}(z)}{u^2}} \right]^N \tag{A.32}$$

where we introduced $u = r^3/\sqrt{(J_0^2 s^2/\gamma_f)|z|}$ and similarly u_0 and U for $r = r_0$ and $r = R$. Here, the integration over u can be done analytically. Note that we are interested in the limit of large R and small r_0, which corresponds to $u_0 \ll 1$ (behavior at long enough time) and $U \gg 1$ (before the boundary effect becomes relevant).

$$\int_{u_0}^{U} du e^{-i\, \text{sgn}(z)/u^2} \approx U - (1 + \text{sgn}(z) i)\sqrt{\pi/2}. \tag{A.33}$$

Finally, we obtain

$$\rho(\gamma) \approx \int_{-\infty}^{\infty} dz \frac{e^{i\gamma z}}{\sqrt{2\pi}} e^{-\frac{4\pi n_f}{3}\sqrt{\pi/2}(1+\mathrm{sgn}(z)i)\int \mathrm{Prob}(s)\sqrt{(J_0^2 s^2/\gamma_f)|z|}ds} \tag{A.34}$$

$$= \int_{-\infty}^{\infty} dz \frac{e^{i\gamma z}}{\sqrt{2\pi}} e^{(iz/T)^{1/2}} = \frac{e^{-1/(4\gamma T)}}{\sqrt{4\pi\gamma^3 T}} \tag{A.35}$$

where we introduced the time scale

$$\frac{1}{T} \equiv \left(\frac{4\pi n_f J_0 \eta}{3}\right)^2 \frac{\pi}{\gamma_f} \tag{A.36}$$

with the orientation averaged $\eta \equiv \int ds[s\mathrm{Prob}(s)]$. The ensemble depolarization profile $P(t)$ can be computed from $\rho(\gamma_s^{\mathrm{eff}})$:

$$P(t) = \int_0^{\infty} \rho(\gamma) e^{-\gamma t} d\gamma = e^{-\sqrt{t/T}}. \tag{A.37}$$

A.4.3 Enhanced depolarization of two degenerate NV groups

When all four groups of NV centers with different quantization axes are spectrally separated, e.g. in Fig. 1b upper curve in the main text, the spin exchange interactions between NV centers in distinct groups are strongly suppressed due to a large energy mismatch. In such case, the depolarization dynamics of a spin are dominated by interactions with fluctuators within the same group. When two groups of NV centers are brought onto resonance, e.g. Fig. 1b lower curve in the main text, the inter-group dipolar interactions cannot be neglected, resulting in an enhanced effective depolarization rate. This effect can be quantitatively analyzed by modifying the probability distribution

$$\mathrm{Prob}(s) = \frac{1}{4}\,\mathrm{Prob}^{\mathrm{same}}(s) + \frac{1}{4}\,\mathrm{Prob}^{\mathrm{diff}}(s) + \frac{1}{2}\cdot 0, \tag{A.38}$$

where $\mathrm{Prob}^{\mathrm{same}}(s)$ and $\mathrm{Prob}^{\mathrm{diff}}(s)$ correspond to the probability distributions of s for dipolar interactions within a group and between two near-resonant groups, respectively. The other two groups with probability $1/2$ do not induce resonant depolarization. Crucially, the latter distribution depends on the spectral distance δ because s is a function of energy mismatch between a spin and a fluctuator:

$$s^2 = \frac{2}{3}(|g|^2 + |h|^2)\frac{2\gamma_f^2}{(\delta\omega + \delta)^2 + 4\gamma_f^2}. \tag{A.39}$$

Averaging over all orientations, we obtain

$$\int \text{Prob}^{\text{same}}(s)\ s\ ds = \sqrt{\frac{2}{3}} \cdot \frac{2}{3\sqrt{3}} \cdot \sqrt{\frac{2\gamma_f^2}{\delta\omega^2 + 4\gamma_f^2}} \tag{A.40}$$

$$\int \text{Prob}^{\text{diff}}(s)\ s\ ds \simeq \sqrt{\frac{2}{3}} \times 0.6507 \times \sqrt{\frac{2\gamma_f^2}{(\delta\omega + \delta)^2 + 4\gamma_f^2}}, \tag{A.41}$$

where the middle factors arise from angular averaging of the matrix elements g and h of dipolar interactions. Interestingly, the angle-averaged matrix element of flip-flop interaction is slightly larger for inter-group interaction than for intra-group interaction $0.6507 > 2/3\sqrt{3}$, which explains the fact that the depolarization rate at the two-group resonance $\delta = 0$ is slightly larger than four times that of a single group. We note that for the theory curves presented in the main text we further average over the energy mismatch $\delta\omega$ arising from inhomogeneous broadening, which we model using a Gaussian distribution with full width at half maximum (FWHM) $W \sim (2\pi)\ 9$ MHz.

A.4.4 Extension of spin lifetime via spin-locking

Under strong driving conditions of a spin-locking sequence, the preferred quantization axes of spins and fluctuators are re-defined by the microwave driving. Specifically, in the rotating frame the eigenstates of a single particle Hamiltonian become $|\pm\rangle = (|m_s = 0\rangle \pm |m_s = -1\rangle)/\sqrt{2}$ and $|m_s = +1\rangle$ with corresponding energy eigenvalues $\pm\Omega/2$ and 0 (up to on-site disorder due to the inhomogeneous broadening). Interestingly, the intra-group flip-flop interactions in this basis are strongly suppressed:

$$\langle +,-|\, H_{dd}\, |-,+\rangle = 0 \tag{A.42}$$

$$\langle \pm, m_s = +1|\, H_{dd}\, |m_s = +1, \pm\rangle = -J_0/r^3(g/2), \tag{A.43}$$

which implies that the spin lifetime T_1^ρ along the $|\pm\rangle$ states is limited by resonant exchange with the third state $|m_s = +1\rangle$. The matrix element of such a process is suppressed by a factor of 2, which, together with the three level nature of the rate model in Eq. (A.2), leads to a factor of $2^2 \times 3 = 12$ improvement for T_1^ρ compared to T_1. For the theory curves presented in the main text (Fig. 4), we also include the effects of off-resonant interactions as well as interactions between different groups as in the previous section.

A.5 Charge diffusion model

To model the observed charge state dynamics, we consider a classical diffusion equation, $\partial_t \delta n = D(\partial_{xx} + \partial_{yy})\delta n$, where D is the diffusion constant and δn is the normalized excess or depletion of the NV$^-$ charge state of NV centers compared to the equilibrium value (charge differential). We note that these charge diffusion experiments have been performed on a bulk piece of diamond under confocal excitation. However, due to the increased size of the confocal excitation spot in the direction normal to the diamond surface, we assume an effective 2D system. For a local electron tunneling process, the diffusion constant can be expressed as $D = a^2/T_{hop}$, where $a \sim 5$ nm is the typical NV separation, and T_{hop} is the electron hopping time. Figure A.4a-d summarizes the prediction of the diffusion model for $T_{hop} = 10$ ns as a function of time, after the system is initialized into

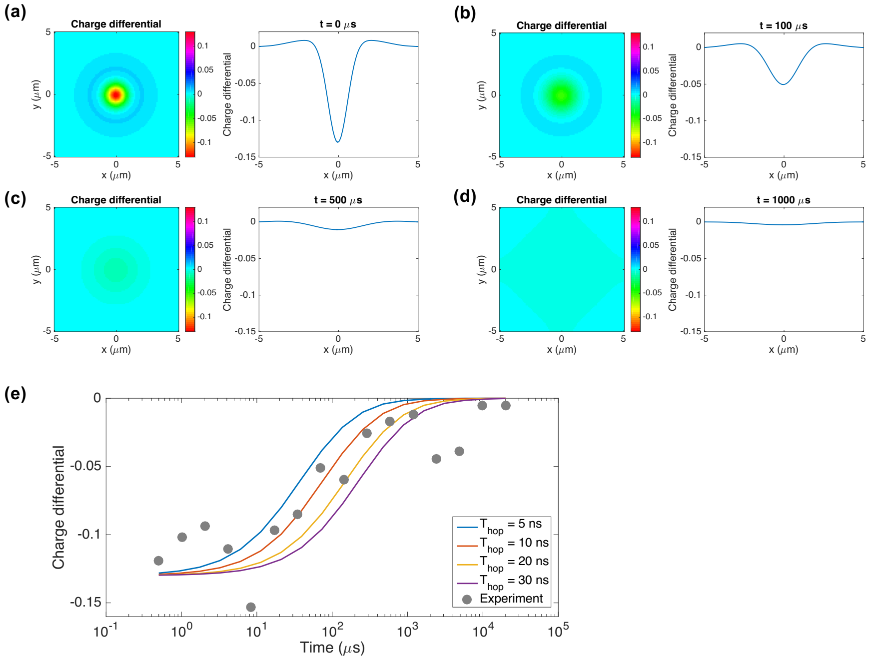

Figure A.4: **Charge-state Dynamics. (a)-(d)** Simulated two-dimensional charge distribution (relative increase of NV$^-$ population compared to equilibrium) at different times after initialization, (a) τ = 0, (b) τ = 100, (c) τ = 500 and (d) τ = 1000 μs. We assumed an electron hopping timescale, T_{hop} = 10 ns, and typical hopping distance, a = 5 nm. **(e)** Charge differential at the center measured over time (grey data). Colored solid lines indicate the diffusion simulation results calculated for different hopping times T_{hop}.

an out-of-equilibrium charge state (modeled after Fig. 4c of the main text). We calculate the expected rates of charge recovery at the center for various hopping rates, showing good agreement with the observed data when $T_{hop} \sim 10$ ns.

Appendix B

Supporting Material of Chapter 3

B.1 Materials and methods

B.1.1 Sample fabrication

The diamond sample used in this work (type-Ib, $\sim$4 mm in diameter) was grown via high pressure and high temperature (HPHT), at 5.5 GPa and 1350 ^{o}C, using a Fe-Co alloy as a solvent. The main source of paramagnetic impurities was provided by substitutional nitrogen atoms in the neutral charge state (P1 centers) at a concentration of $\sim$100 ppm. A diamond plate of thickness $\sim$1 mm was obtained via laser cutting and polishing. To obtain NV centers, high energy electron irradiation was performed at $\sim$2 MeV with a flux of 1.3-1.4$\cdot 10^{13}$ e$\cdot$cm$^{-2}\cdot$s^{-1} and in-situ annealing at 700-800 ^{o}C up to a total fluence of 1.4$\cdot 10^{19}$ cm^{-2} (total time of 285 hrs). Additional annealing at 1000 ^{o}C for 2 hrs in vacuum was performed after half as well as after the full irradiation time. This process resulted in the diamond with NV centers of a concentration $\sim$45 ppm, corresponding to $\sim$5 nm of average separation and $\sim (2\pi)$ 420 kHz dipole-dipole interaction strength. To control the region of optical excitation, we used angle etching to create a beam-shaped piece of diamond, of 20 μm length and $\sim$300 nm width, and transferred it onto our coplanar waveguide [83].

B.1.2 Optical Setup

As shown in Fig. B.1A, the optical setup consists of a home-built confocal microscope with a Nikon Plan Fluor 100x oil immersion objective (NA = 1.3). The sample is mounted on a xyz-piezoelectric stage in the focal plane of the microscope. Excitation of the ensemble of NV centers is performed by illuminating a green laser ($\lambda = 532$ nm) with average power less than 50 μW. Short laser pulses are generated by an acousto-optic modulator (AOM) from Isomet in a double pass configuration. The $\lambda/2$-waveplate at the objective allows the control over the polarization of excitation light. NV centers emits fluorescence into the phonon sideband (630-800 nm), which is isolated from the excitation laser by a dichroic mirror. An additional 650 nm long-pass filter further suppresses the detection of unwanted signal. After passing a pinhole the collection beam is then focused onto a single photon counting avalanche photodiode (APD) to achieve detections with confocal resolution.

To probe the spin dynamics over time, we used a pulse sequence illustrated in Fig. B.1B. We repeat the same pulse sequence twice, but include an extra π-pulse right before the read-out at end of the second sequence. The photon-count difference between the two read-outs allows us to measure the NV polarization, while being insensitive to changes in the background fluorescence due to charge dynamics [76].

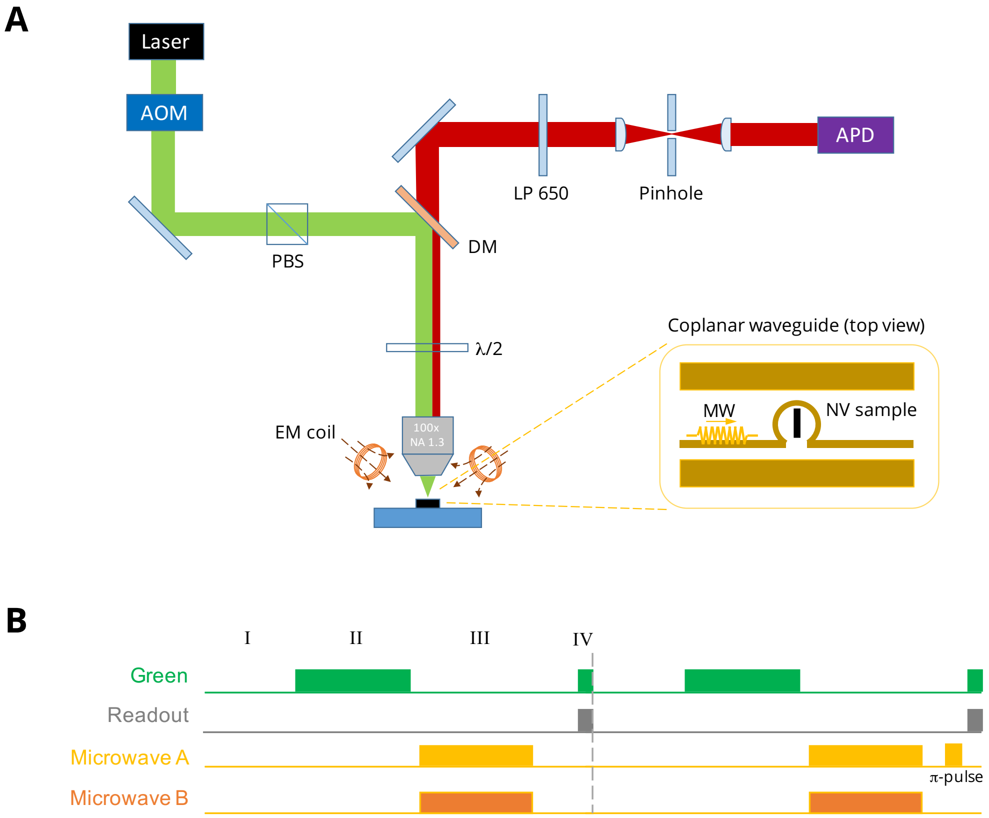

Figure B.1: **Schematic of the Optical Setup and the Pulse Sequence.** (**A**) Green and red lines indicate the optical paths (excitation: green, collection: red). An acousto-optic modulator (AOM) is used to control green laser duration. A dichroic mirror (DM) spectrally filters out the fluorescence from NV centers for electronic spin state readout. A 650 nm long pass filter additionally helps to filter fluorescence emission, corresponding to the phonon sideband (PSB) of NV centers. A 5-μm pinhole is used in combination with a single photon counting avalanche photodiode (APD) to achieve confocal detection. A polarizing beam splitter (PBS) is used to polarize the excitation beam. With the addition of a $\lambda/2$ waveplate we get control over the incident green polarization onto the diamond sample. The sample is placed ontop of a coplanar microwave (MW) structure in the shape of an omega (inset). Three electromagnetic coils are used to create a static magnetic field up to $\sim$300 Gauss in an arbitrary direction. (**B**) Typical experimental sequence used to measure NV dynamics. I: charge equilibration; II: spin polarization; III: experimental sequence; IV: spin readout.

B.1.3 Microwave setup

To coherently control the electronic spin states of NV centers we deliver microwaves to the sample through an impedance-matched coplanar waveguide fabricated on a glass coverslip. An omega-shaped microstructure (with an inner diameter 20 μm) at the center of the waveguide allows us to achieve Rabi frequencies up to $\sim(2\pi)$ 100 MHz. In Fig. B.2, we illustrate the schematic diagram of the microwave control system. In order to have full control over two groups of NV centers with different transition frequencies, we employ two independent microwave circuits. In each circuit, a RF signal generator (Rohde & Schwarz SMIQ06B) produces the main driving frequency; an IQ mixer (Marki IQ1545LMP) generates pulsed signals; a low-pass microwave filter (Mini-Circuits VLF-3000+) suppresses unwanted higher-order harmonics of fundamental frequencies; and a DC block (Picosecond 5501a) additionally isolates the signals from low-frequency noises. After separately amplified (ZHL-16W-43+), two RF signals are then combined by a power combiner (Mini-Circuits ZFRSC-42-S+) and delivered to our sample. The inset of Fig. B.2 depicts the detailed configuration of analog inputs (AI) connected to the IQ mixers. An arbitrary waveform generator (The Tektronix AWG7052) defines the duration and the phase of the pulses with a temporal resolution of 1 ns. For fine tuning of the voltage offset on the I and Q ports, a DC voltage is applied to the AWG signal. The addition of a 10-dB attenuator between the voltage source and the combiner suppresses unwanted reflections (see inset of Fig. B.2).

B.1.4 Magnetic field setup

For an external magnetic field, we use three water-cooled electromagnetic (EM) coils, which can provide a B-field up to $\sim$300 Gauss in an arbitrary orientation (see Fig. B.1A and B.3A). As shown in Fig. B.3B, we calibrate the magnetic field by recording electron spin resonance (ESR) spectra at various values of currents in the coils; since the Hamiltonian

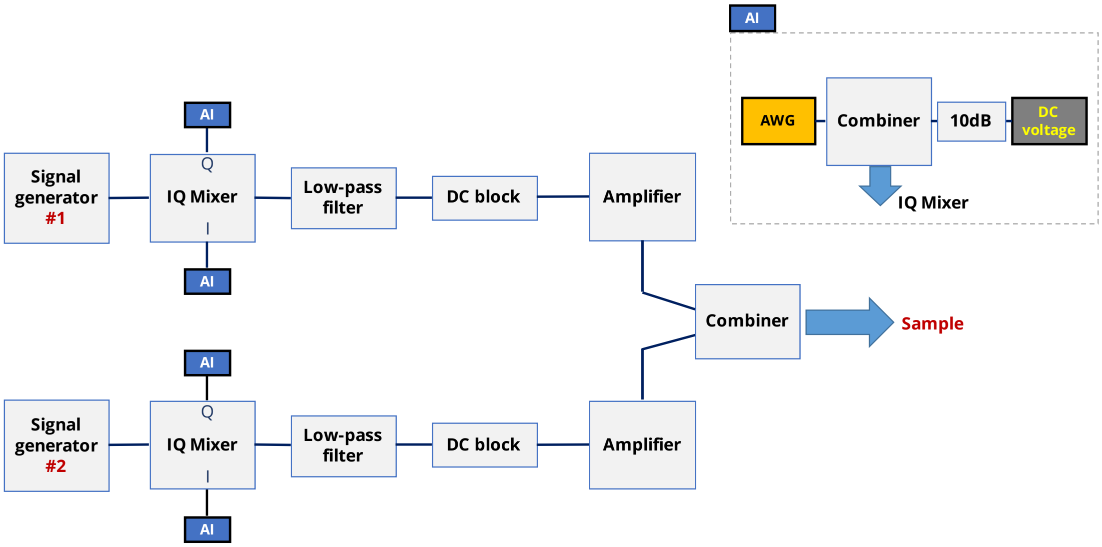

Figure B.2: **Schematic of the Microwave Control Setup.** Two sets of independent microwave circuits are used to achieve full control over two separate groups of NV centers at different transition frequencies. A 3 GHz low-pass filter suppresses unwanted higher-order harmonics. The two microwave paths are separately amplified to avoid saturation and then combined and sent to the diamond sample. In order to precisely control the microwave pulse length as well as phase, each path is sent through an IQ mixer controlled by an arbitrary waveform generator (AWG) output. The inset shows the detailed configuration of analog inputs connected to the IQ mixers used to define microwave pulse length and phase. In order to finely tune the voltage offset of the I and Q port, to achieve high isolation, a DC voltage source is combined with the AWG signal. The addition of an attenuator allows the suppression of unwanted reflections.

of a NV center in the presence of a magnetic field is known, the magnetic field at the position of our sample can be extracted from transitions frequencies of NV centers. For this process we utilize all four groups $\{A, B, C, D\}$ of NV centers oriented in different crystallographic axes of diamond lattice, e.g., A = [111], B = [$\bar{1}\bar{1}$1], C = [1$\bar{1}\bar{1}$], and D = [$\bar{1}$1$\bar{1}$] (see Fig. B.3C). Fig. B.3D shows an ESR spectrum when the B-field is aligned along [111] direction; group A exhibits the largest Zeeman splitting, while the other groups B, C, and D become degenerate. In Fig. B.3E, the direction of an external B-field is perpendicular to the sample surface, i.e., B $\|$ [001], resulting in four degenerate groups.

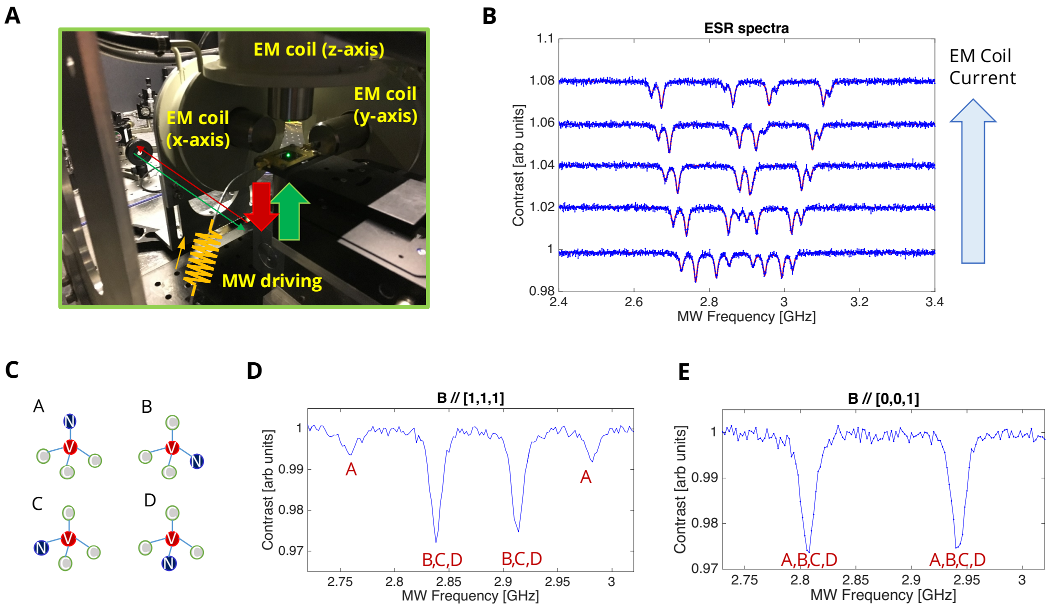

Figure B.3: **Magnetic Field Calibration and Control.** **(A)** Three electromagnetic (EM) coils are located in the vicinity of the diamond sample in order to provide an external magnetic field (B-field) in an arbitrary direction with an amplitude up to ∼300 Gauss. **(B)** To calibrate the coil's magnetic field, electron spin resonance (ESR) spectra are recorded for different values of coil currents. **(C)** The diamond lattice allows for four different crystallographic orientations of NV centers. The different groups A, B, C, and D of NV centers are characterized by their N-V axis orientations, i.e., A = [111], B = $[\bar{1}\bar{1}1]$, C = $[1\bar{1}\bar{1}]$, and D = $[\bar{1}1\bar{1}]$. **(D)** Measured ESR spectrum for the B-field aligned along the [111] direction. Group A exhibits the largest Zeeman splitting (highest projected $B_{||}$) because the spin quantization axis of group A is parallel to the chosen B-field. **(E)** Measured ESR spectrum for the B-field aligned along the [001] direction. Due to the [100] cutting direction of the diamond, all 4 NV groups form the same angle to the surface. With the external B-field being perpendicular to the sample surface, this leads to groups A-D having degenerate B field projections.

B.2 Characterization of experimental system

B.2.1 On-site potential disorder

The ESR linewidth of an NV ensembles is influenced by multiple factors. To discuss and estimate their contributions we introduce the ground state hamilitonian of the electronic spin state of a single NV center:

$$H = \left(\hbar\Delta_0 + d_{||}E^z_{||}\right) S_z^2 + \gamma_{NV}(\vec{S}\cdot\vec{B}) - d_\perp \left[E^x_\perp \left(S_xS_y + S_yS_x\right) + E^y_\perp \left(S_x^2 - S_y^2\right)\right], \tag{B.1}$$

where S_x, S_y and S_z denote the spin-1 matrices and $\hbar$ the reduced Planck constant; $\Delta_0 \approx (2\pi)2.87$ GHz, γ_{NV} = (2π) 2.8 MHz G^{-1}, $d_{||}$ = (2π) 0.35 Hz cm V^{-1} and $d_\perp$ = (2π) 17 Hz cm V^{-1} are the zero field splitting, the gyromagnetic ratio, axial and perpendicular components of the ground triplet state permanent electric dipole moment of a NV center [169]. $B_{||(\perp)}$ and $E_{||(\perp)}$ are projection of the effective magnetic and electric field parallel (perpendicular) to the NV axis. To a leading order, we ignore the effect of the perpendicular magnetic field noise $\delta B_\perp$, since it influence less on the spin coherence than the parallel one $\delta B_{||}$, owing to the large zero field splitting.

To account for effects of the local NV environment we include in $B_{||}$ and $E_{||(\perp)}$ on-site potential disorders originating from randomly distributed magnetic fields due to nuclear spins (i.e. ^{13}C or ^{14}N) and paramagnetic impurities (i.e. P1 centers) as well as fields caused by local electric fields and lattice strain. To quantify the different contributions to the ESR linewidth, we conduct Ramsey spectroscopy in distinct basis states as listed in Fig. B.4A. Since each basis has a well defined sensitivity to different physical noise sources, our Ramsey measurements provide insight into the local environment of the NV centers. Table B.1 lists the effects of magnetic and electric field noise on free induction decay of several different basis states. Figure B.4 shows the outcome of Ramsey spectroscopy in the five different bases defined in B.1 .

As seen in the table B.1, each coherent superposition can effectively probe different types of noise components, enabling us to quantify the relative strengths of the on-site

Definition	Wavefunction	Precession rate	Noise	$1/T_2^*$
$\|\psi_1\rangle$	$(\|0\rangle + \|1\rangle)/\sqrt{2}$	$\gamma_{NV} B_\parallel + d_\parallel E_\parallel$	$\delta B_\parallel, \delta E_\parallel$	$\pi[\Gamma_{B_\parallel} + \Gamma_{E_\parallel}]$
$\|\psi_2\rangle$	$(\|0\rangle + \|-1\rangle)/\sqrt{2}$	$\gamma_{NV} B_\parallel + d_\parallel E_\parallel$	$\delta B_\parallel, \delta E_\parallel$	$\pi[\Gamma_{B_\parallel} + \Gamma_{E_\parallel}]$
$\|\psi_3\rangle$	$(\|1\rangle + \|-1\rangle)/\sqrt{2}$	$2\gamma_{NV} B_\parallel$	$\delta B_\parallel$	$2\pi\Gamma_{B_\parallel}$
$\|\psi_4\rangle$	$(\|0\rangle + \|D\rangle)/\sqrt{2}$	$d_\parallel E_\parallel + d_\perp E_\perp$	$\delta E_\parallel, \delta E_\perp$	$\pi[\Gamma_{E_\parallel} + \Gamma_{E_\perp}]$
$\|\psi_5\rangle$	$(\|0\rangle + \|B\rangle)/\sqrt{2}$	$d_\parallel E_\parallel + d_\perp E_\perp$	$\delta E_\parallel, \delta E_\perp$	$\pi[\Gamma_{E_\parallel} + \Gamma_{E_\perp}]$

Table B.1: Five different basis states used for characterizing the local on-site disorder. The dark ($|D\rangle \equiv (|1\rangle - |-1\rangle)/\sqrt{2}$) and bright states ($|B\rangle \equiv (|1\rangle + |-1\rangle)/\sqrt{2}$) are prepared by applying an off-axis magnetic field perpendicular to an NV symmetry axis. Γ is a noise source-dependent inhomogeneous broadening contributing to the linewidth of the ESR.

potential disorder. Using the identity $\Gamma = 1/\pi T_2^*$ and the relations given in the last column of table B.1, we can estimate a value for the different noise sources $\Gamma_{B_\parallel}$, $\Gamma_{E_\parallel}$, and $\Gamma_{E_\perp}$. The discrepancy in T_2^* between $|\psi_1\rangle$ and $|\psi_2\rangle$ (as well as $|\psi_4\rangle$ and $|\psi_5\rangle$) in experimental data is presumably due to frequency-dependent field noise. By averaging these results, we can extract the three inhomogeneous broadening factors as $\Gamma_{B_\parallel}$ = 3.78(3) MHz, $\Gamma_{E_\parallel}$ = 2.18(8) MHz and $\Gamma_{E_\perp}$ = 4.30(13) MHz. The measured ESR linewidth $\Gamma_{\text{meas}} = \sqrt{8\ln 2}W \approx$ 9.4 MHz (see Fig. 3.1D) roughly agrees up to a factor of $\sim$1.5 with the calculated $\Gamma_{\text{calc}} \approx$ 6.0 MHz. According to this analysis, the random on-site disorder in our sample seems to result from both electric and magnetic fields with comparable weights.

B.2.2 Estimation of NV density and dipolar interaction strength

Due to the high density of NVs within our sample, the spin-echo coherence time is limited by interactions, as discussed in the main text. In particular, using the double electron-electron resonance (DEER) sequence presented in Fig. 2A in the main text, we verified experimentally that the additional dephasing of group A indeed originates from interactions with group B. Fig. B.5 shows a measurement result of the DEER sequence in which

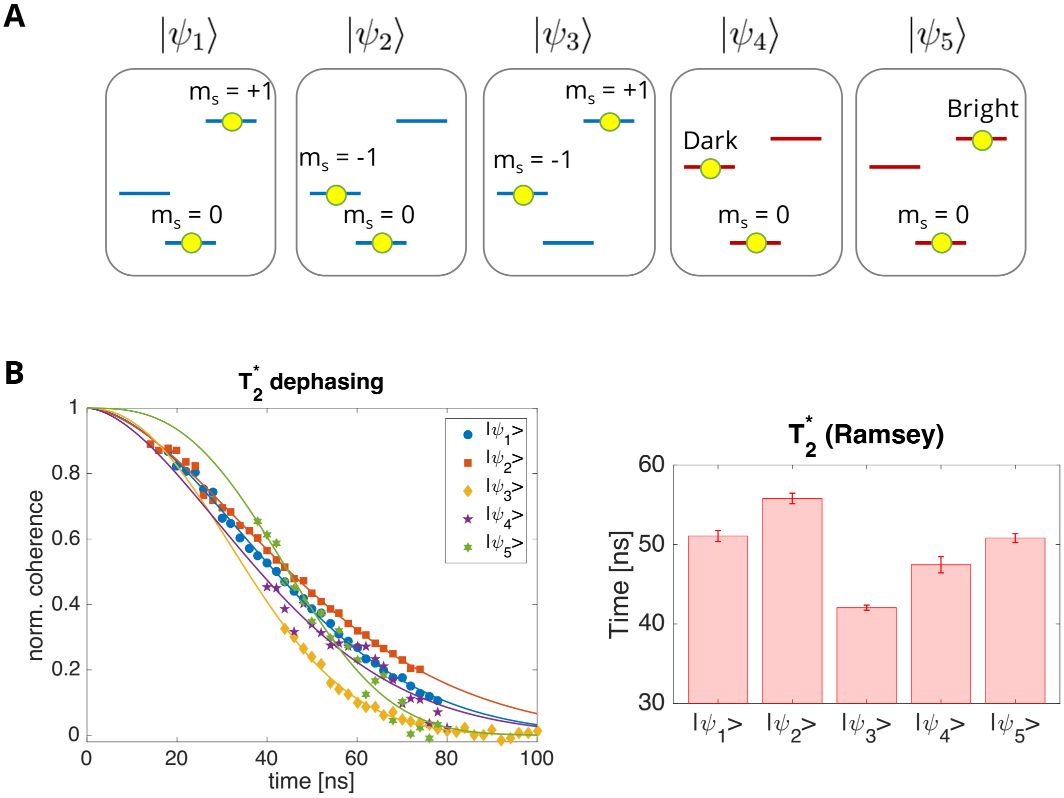

Figure B.4: T_2^* **and** T_2 **Measurements of different Basis States.** **(A)** Different initial conditions used for coherence measurements. By aligning the magnetic field parallel (perpendicular) to the NV axis, the eigenbasis for the spin state of NV centers becomes $\{|m_s = 0\rangle, |m_s = +1\rangle, |m_s = -1\rangle\}$ ($\{|m_s = 0\rangle$, $|Dark\rangle$, $|Bright\rangle\}$), where Bright and Dark states are defined as even and odd combination of the original bare spin states $|m_s = -1\rangle$ and $|m_s = +1\rangle$. **(B)** Ramsey spectroscopy data and extracted decay timescale for different initial states.

we probe the relative spin-echo amplitude at a fixed time τ as a function of driving frequency of group B. It shows a clear resonance when $\omega = \omega_0^B$, indicating that inter-group interactions between group A and B lead to enhanced dephasing.

To quantitatively analyze the dependence of decoherence rate on the spin density, we study the dynamics of interacting spins using the exact diagonalization method with the effective Hamiltonian of Eq. (B.24). Comparing the numerical result to the experimental

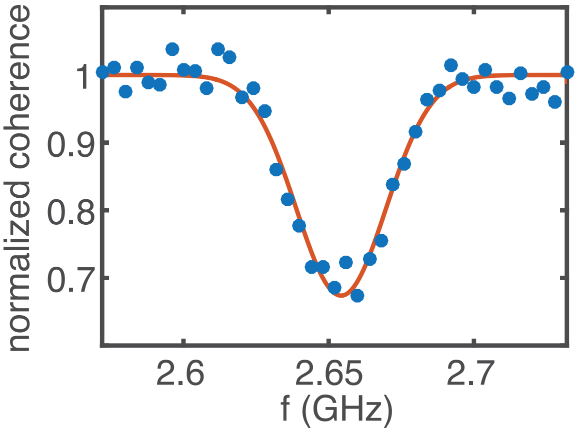

Figure B.5: **Intra-group Interaction Probed via Double Electron-Electron Resonance.** The relative, normalized spin echo coherence time at a fixed time τ as a function of driving frequency of group B.

data allows us to extract the density of NV spins in our sample. Specifically, we simulate the time evolution of 12 NV spins under a spin echo pulse sequence protocol. The total NV concentrations selected for simulations are 5, 20, 40, 60, 70, 80 and 100 ppm. We averaged over $\sim$500 realizations of positional disorder, resulting in a single smooth coherence curve under the spin echo sequence. We fit the coherence decay with a simple exponential function and extract the decoherence rate, $\gamma_T \equiv 1/T_2$. Fig. B.6A summarizes the spin echo simulation results as a function of the number of resonant NV groups (effective density), where a linear dependence of γ_T is identified for all the density values. We model the decoherence rate as $\gamma_T(\nu) = \gamma_b(\nu) + \nu\gamma_0(\nu)$, where ν is the number of resonant NV groups, γ_b and γ_0 are density-dependent, bare and dipolar interaction-induced dephasing rates, respectively. Such linear dependence of γ_T on ν is also confirmed in the experiment (see Fig. 2B in main text). By comparing γ_0 between the experiment and the simulation, we estimate the NV density in our sample to be $\sim$45 ppm (see Fig. B.6B).

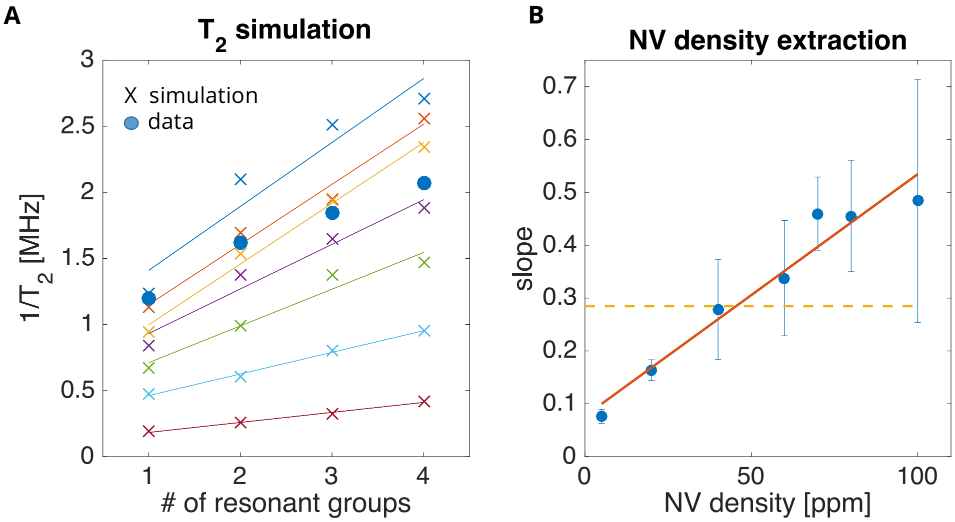

Figure B.6: **NV Density Extraction via Spin Echo Simulation.** **(A)** Comparison of the spin echo simulation results at different concentrations (crosses) to the measured data (circles). The total NV concentrations selected for the simulation are 5, 20, 40, 60, 70, 80 and 100 ppm. Solid lines are linear fits to the simulation to extract both γ_b and γ_0 in the main text. **(B)** The NV concentration can be extracted by comparing the slopes (γ_0) taken from the numerical simulations to the extracted slope of the experiment data (orange dashed line).

B.2.3 Inhomogeneity of microwave field

Hartmann-Hahn resonances rely on the exact matching of Rabi frequencies of two driving fields $\Omega_A = \Omega_B$. Hence, stable and precise control of the driving strength is essential in our experiments. To this end, we estimate the inhomogeneity of our microwave driving field, by measuring the decay time of Rabi oscillations at various driving strengths (Fig. B.7).

In an ideal case, the lifetime of Rabi oscialltions generally increases due to suppression of disorder (T_2^*). At higher driving strength ($W_{\text{eff}} \sim \delta^I$) this lifetime should saturate due to the effect of Ising interaction. In our measurements however we observe a slight decrease in lifetime at high driving strengths, which is well explained by a 1.1% variation in Rabi

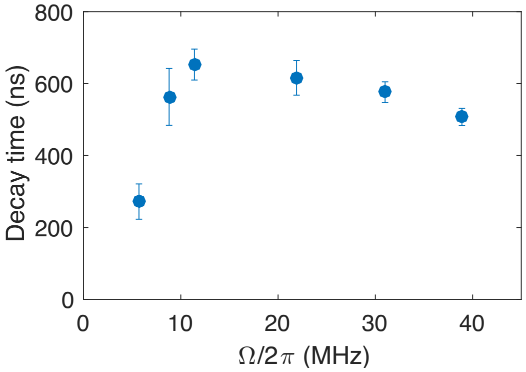

Figure B.7: **Rabi Oscillation Measurement.** Decay time of Rabi oscillations as a function of Rabi frequency Ω.

frequency. We attribute this variation to spatial inhomogeneity in the driving field. With the strongest driving in our measurement $\Omega = (2\pi)$ 32 MHz, this effect leads to a spread in Rabi frequencies of $\sim (2\pi)$ 0.3 kHz. While it is still smaller than the effective disorder $\sim (2\pi)$ 0.6 kHz, such an inhomogeniety ultimately limits the maximum driving strength of our thermalization experiments.

B.3 Effective Hamiltonian of a driven system

In this section, we derive the effective Hamiltonian for a driven, dipolar interacting spin ensemble. The main idea is to work in a frame that is rotating along each NV group's quantization axis at corresponding driving frequency (ω_0^A and ω_0^B for group A and B, respectively). If the difference between ω_0^A and ω_0^B is large compared to the interaction strength, then one can ignore exchange interactions between spins from different groups (secular approximation). This results in distinct forms of intra- and inter-group interactions. We project the original Hamiltonian into two-level systems, and derive the effective

Hamiltonian.

We start with the Hamiltonian for dipolar interacting NV centers

$$H = \sum_i H_i^0 + \sum_i H_i^d(t) + \sum_{ij} H_{ij}^{dd}, \tag{B.2}$$

where H_i^0 is a single particle Hamiltonian for a spin at site i, $H_i^d(t)$ is time-dependent driving, and H_{ij}^{dd} is the magnetic dipole-dipole interaction between spins at sites i and j. The first term H_i^0 includes Zeeman coupling to an external magnetic field, the zero field splitting of a NV center, and any other disordered potentials arising from couplings to paramagnetic impurities as described in the main text. In our experiments, dominant contributions for H_i^0 come from the zero-field splitting $\sim (2\pi)$ 2.87GHz and Zeeman field projected along the quantization axis (a few hundred MHz), which are two orders of magnitude larger than the rest of the couplings. Setting $\hbar = 1$, we can write

$$H_i^0 \approx (\Delta_0 + \delta_{0,i}) \left(\hat{c}_i \cdot \vec{S}_i\right)^2 + (\Delta_B(\hat{c}_i) + \delta_{B,i}) \left(\hat{c}_i \cdot \vec{S}_i\right) \tag{B.3}$$

where $\vec{S}_i$ are spin-1 vector operators, $\hat{c}_i$ is the unit vector along the quantization axis of the spin, $\Delta_0 = (2\pi)$ 2.87 GHz is the zero-field splitting, $\Delta_B(\hat{c}_i)$ is the Zeeman splitting along $\hat{c}_i$, and $\delta_{0,i}$ and $\delta_{B,i}$ are on-site disorder potentials. If the external magnetic field $\vec{B}$ is oriented in a way that $\Delta_B(\hat{c}_i)$ for different groups are sufficiently separated (compared to the driving strength), one can effectively address distinct groups independently. Below we assume such a case and consider resonant driving of two groups A and B using microwave frequencies $\omega_0^{A(B)} = \Delta_0 - \Delta_B(\hat{c}_{A(B)})$. The Hamiltonian for such driving is given as $H_i^d(t) = \gamma_{NV} \vec{B}_{\text{MW}} \cdot \vec{S}_i \cos(\omega_0 t)$, where γ_{NV} is the gyromagnetic ratio of the NV center, and $\vec{B}_{\text{MW}}$ is the microwave field vector. Now moving into the rotating frame with unitary transformation $U(t) = \exp\left[-i\left(\sum_i \Delta_0(\hat{c}_i \cdot \vec{S}_i)^2 + \Delta_B(\hat{c}_i)(\hat{c}_i \cdot \vec{S}_i)\right) t\right]$ and applying rotating wave approximations, we obtain the effective single particle Hamiltonian

$$\begin{aligned}\bar{H}_i &= U^\dagger(t)\left[H_i^0 + H_i^d(t)\right]U(t) - iU^\dagger \frac{d}{dt}U && \text{(B.4)}\\ &= (\delta_{0,i} + \delta_{B,i})\left|1\right\rangle\left\langle 1\right| + (\delta_{0,i} - \delta_{B,i})\left|-1\right\rangle\left\langle -1\right| + \frac{\Omega}{2}\left(\left|-1\right\rangle\left\langle 0\right| + h.c.\right), && \text{(B.5)}\end{aligned}$$

where $\{\left|1\right\rangle, \left|0\right\rangle, \left|-1\right\rangle\}$ is the basis of spin states along its quantization axis and Ω is the Rabi frequency of the driving.

The effective interaction among spins can be obtained in a similar way as follows. We start with the dipole-dipole interaction between spin-i and spin-j

$$H_{ij}^{dd} = -\frac{J_0}{r^3}\left(3\left(\vec{S}_i \cdot \hat{r}\right)\left(\vec{S}_j \cdot \hat{r}\right) - \vec{S}_i \cdot \vec{S}_j\right), \tag{B.6}$$

where $J_0 = (2\pi)\ 52\ \text{MHz} \cdot \text{nm}^3$ and $\vec{r}$ is the relative position between two spins. In the rotating frame, we obtain the effective interaction by replacing $\vec{S}_i \mapsto U^\dagger(t)\vec{S}_i U(t)$. Since we are interested in the interaction in the basis of each NV's own quantization axis, we first explicitly rewrite $\vec{S}_i$ in terms of (S_i^x, S_i^y, S_i^z) in a coordinate system where $\hat{z}_i$ is parallel to the quantization axis $\hat{c}_i$

$$\begin{aligned}\bar{H}_{ij}^{dd} = U^\dagger(t)H_{ij}^{dd}U(t) = -J_0/r^3\Big[&\big(3\left(\hat{r}\cdot\hat{x}_i\right)\left(\hat{r}\cdot\hat{x}_j\right) - \hat{x}_i\cdot\hat{x}_j\big)S_i^x S_j^x && \text{(B.7)}\\ &+ \big(3\left(\hat{r}\cdot\hat{y}_i\right)\left(\hat{r}\cdot\hat{y}_j\right) - \hat{y}_i\cdot\hat{y}_j\big)S_i^y S_j^y && \text{(B.8)}\\ &+ \big(3\left(\hat{r}\cdot\hat{x}_i\right)\left(\hat{r}\cdot\hat{y}_j\right) - \hat{x}_i\cdot\hat{y}_j\big)S_j^x S_j^y && \text{(B.9)}\\ &+ \big(3\left(\hat{r}\cdot\hat{y}_i\right)\left(\hat{r}\cdot\hat{x}_j\right) - \hat{y}_i\cdot\hat{x}_j\big)S_i^y S_j^x && \text{(B.10)}\\ &+ \big(3\left(\hat{r}\cdot\hat{z}_i\right)\left(\hat{r}\cdot\hat{z}_j\right) - \hat{z}_i\cdot\hat{z}_j\big)S_i^z S_j^z\Big] && \text{(B.11)}\\ &+H_{\text{rest}}, && \text{(B.12)}\end{aligned}$$

where H_{rest} contains all the other terms of the form $S^x S^z, S^y S^z, S^z S^x, S^z S^y$.

We now perform rotating wave approximations. This is very well justified because the typical strength of the interaction is much weaker than the driving frequency $J_0/r^3 \sim (2\pi)$ 0.4 MHz $\ll \omega_0^{A,B} \sim (2\pi)$ 2.5 GHz. First, we note that S^x and S^y operators are rapidly oscillating in time while S^z remains invariant, $[S_i^z, U(t)] = 0$. Therefore, every term in H_{rest} may be safely ignored. Then, introducing

$$g_{ij}^{+} = \frac{1}{2}\Big[3\,(\hat{r}\cdot\hat{x}_i)\,(\hat{r}\cdot\hat{x}_j) - \hat{x}_i\cdot\hat{x}_j + 3\,(\hat{r}\cdot\hat{y}_i)\,(\hat{r}\cdot\hat{y}_j) - \hat{y}_i\cdot\hat{y}_j\Big] \tag{B.13}$$

$$g_{ij}^{-} = \frac{1}{2}\Big[3\,(\hat{r}\cdot\hat{x}_i)\,(\hat{r}\cdot\hat{x}_j) - \hat{x}_i\cdot\hat{x}_j - 3\,(\hat{r}\cdot\hat{y}_i)\,(\hat{r}\cdot\hat{y}_j) + \hat{y}_i\cdot\hat{y}_j\Big] \tag{B.14}$$

$$h_{ij}^{+} = \frac{1}{2}\Big[3\,(\hat{r}\cdot\hat{x}_i)\,(\hat{r}\cdot\hat{y}_j) - \hat{x}_i\cdot\hat{y}_j + 3\,(\hat{r}\cdot\hat{y}_i)\,(\hat{r}\cdot\hat{x}_j) - \hat{y}_i\cdot\hat{x}_j\Big] \tag{B.15}$$

$$h_{ij}^{-} = \frac{1}{2}\Big[3\,(\hat{r}\cdot\hat{x}_i)\,(\hat{r}\cdot\hat{y}_j) - \hat{x}_i\cdot\hat{y}_j - 3\,(\hat{r}\cdot\hat{y}_i)\,(\hat{r}\cdot\hat{x}_j) + \hat{y}_i\cdot\hat{x}_j\Big] \tag{B.16}$$

$$q_{ij} = 3\,(\hat{r}\cdot\hat{z}_i)\,(\hat{r}\cdot\hat{z}_j) - \hat{z}_i\cdot\hat{z}_j, \tag{B.17}$$

we can simply rewrite

$$\bar{H}_{ij}^{dd} \approx -J_0/r^3\big[g_{ij}^{+}(S_i^xS_j^x + S_i^yS_j^y) + h_{ij}^{-}(S_i^xS_j^y - S_i^yS_j^x) + q_{ij}S_i^zS_j^z \tag{B.18}$$

$$+ g_{ij}^{-}(S_i^xS_j^x - S_i^yS_j^y) + h_{ij}^{+}(S_i^xS_j^y + S_i^yS_j^x)\big]. \tag{B.19}$$

Here, g^+ and h^- terms correspond to "flip-flop" type transitions, exchanging one unit of spin polarization,

$$(S_i^xS_j^x + S_i^yS_j^y) = |{+}0\rangle\langle 0{+}| + |{+}{-}\rangle\langle 00| + |00\rangle\langle{-}{+}| + |0{-}\rangle\langle{-}0| + h.c. \tag{B.20}$$

$$(S_i^xS_j^y - S_i^yS_j^x) = i\big(|{+}0\rangle\langle 0{+}| + |{+}{-}\rangle\langle 00| + |00\rangle\langle{-}{+}| + |0{-}\rangle\langle{-}0|\big) + h.c. \tag{B.21}$$

In addition, owing to the strong anharmonic level structure, we may also ignore flip-flop transitions between levels with large energy differences, e.g. terms such as $|{+}{-}\rangle\langle 00|$. Finally, we ignore the terms in Eq. (B.19) as they correspond to double flip-up or flip-down and rapidly oscillate in time. After these approximations, the effective interaction becomes

$$\bar{H}^{dd}_{ij} \approx -J_0/r^3 \big[\left(g^{+}_{ij} + i h^{-}_{ij} \right) |{+0}\rangle \langle 0{+}| + |0{-}\rangle \langle {-0}| + h.c. + q_{ij} S^z_i S^z_j \big]. \tag{B.22}$$

Now we divide into two cases depending on whether spins i and j belong to the same group or to different groups. In the former case, the quantization axes coincide, and we can simplify $h^{-}_{ij} = 0$, $g^{+}_{ij} = \frac{1}{2}(1 - 3\cos^2\theta)$, and $q_{ij} = -(1 - 3\cos^2\theta)$ with $\cos\theta \equiv \hat{z}\cdot\hat{r}$. In the latter case, the flip-flop terms are again rapidly oscillating, and only the Ising interaction $S^z_i S^z_j$ remains, resulting in

$$\bar{H}^{dd}_{ij} \approx \begin{cases} -\frac{J_0 q_{ij}}{r^3}\left(-\frac{|{+0}\rangle\langle 0{+}| + |0{-}\rangle\langle {-0}| + h.c.}{2} + S^z_i S^z_j \right) & \text{same group} \\ -\frac{J_0 q_{ij}}{r^3} S^z_i S^z_j & \text{different groups} \end{cases} . \tag{B.23}$$

These interactions as well as the single particle terms conserve the total population of spins in $|+\rangle$. Therefore, once the system is initialized into a state with no population in $|+\rangle$, the dynamics remains in the manifold spanned by $|-\rangle$ and $|0\rangle$. Projecting $\sum_i \bar{H}_i + \sum_{ij} \bar{H}^{dd}_{ij}$ into this manifold, we obtain the Hamiltonian for an effective two-level system. Introducing spin-1/2 operators $\vec{s}$ for two levels $|-\rangle$ and $|0\rangle$, we obtain $H_T = H_A + H_B + H_{AB}$, where

$$H_{A(B)} = \sum_{i \in A(B)} \left[(\delta_{0,i} - \delta_{B,i}) s^z_i + \Omega_{A(B)} s^x_i \right] + \sum_{i,j \in A(B)} \frac{J_0 q_{ij}}{r^3_{ij}} \left(s^x_i s^x_j + s^y_i s^y_j - s^z_i s^z_j \right), \tag{B.24}$$

$$H_{AB} = -\sum_{i \in A, j \in B} \frac{J_0 q_{ij}}{r^3_{ij}} s^{z_A}_i s^{z_B}_j, \tag{B.25}$$

up to a constant.

Finally, we remark one particularly interesting aspect of this Hamiltonian in the dressed-state basis, i.e., quantization along s^x_i. With sufficiently strong driving, s^x_i becomes a good spin polarization basis, and one can rewrite the interactions in terms of $s^{\pm} = s^y \pm i s^z$, wherein the intra-group interaction becomes $\propto s^x_i s^x_j + (s^+_i s^+_j + s^-_i s^-_j)/2$ and the inter-group interaction $\propto (s_i^+ s_j^- + s_i^+ s_j^+ + h.c.)$. Here, we find that spin exchange terms $(s_i^+ s_j^- + h.c.)$ are missing in the intra-group interaction. Omitting the energy non-conserving terms such as $s_i^+ s_j^+$ (secular approximation with a strong driving strength Ω), we obtain the effective Hamiltonian described in the main text.

B.4 Resonance counting theory

In this section, we provide a detailed study of the single particle resonance counting theory. We will first focus on the case of quenched on-site potential disorder, deriving the disorder-dependent power-law relaxation presented in the main text. Then, we generalize the result to the case when disordered potentials are time-dependent.

B.4.1 Disorder-dependent power-law decay

As discussed in the main text, we estimate the survival probability of a single spin excitation based on a simple counting argument. At time t, we compute the probability $\text{Pr}(k;t)$ that the central spin is connected to $k-1$ other spins via a network of resonances, as defined in the main text. Assuming that the population of the excitation is equally shared among a resonating cluster, the survival probability is given as

$$P(t) \approx \sum_{k=1}^{\infty} \frac{1}{k} \text{Pr}(k;t). \tag{B.26}$$

reducing our problem to the computation of $\text{Pr}(k;t)$. Below we will show that the dominant contributions arise from $k=1$, suggesting that finding a single resonant partner is usually enough to delocalize the spin excitation over the entire sample.

In general, the exact calculation of $\text{Pr}(k;t)$ is difficult. This is because the connectivity of the resonance network is correlated due to the spatial structure (d-dimensional Euclidean space) as well as a given assignment of random on-site potentials, e.g., if spin pairs (a,b) and (b,c) are pair-wise resonant, it is likely that the pair (a,c) is also resonant, etc. However, the qualitative behavior of $\text{Pr}(k;t)$ can still be well-understood by ignoring these correlations. In such a case, we may assume that the number of resonant partners ℓ for a spins is drawn from a probability distribution $p(\ell)$ and that this process can be iterated for each partner. We note that such a process may not terminate, in which case the central excitation becomes delocalized over a macroscopic number of spins. We first compute $p(\ell)$ as a function of time t. For $\ell = 0$, a spin of interest (spin-i) must not have any resonating spins at any distance from r_{min} to $R(t) \equiv (J_0 t)^{1/3}$, where r_{min} is the short-distance cut-off. Hence, $p(0;t)$ is given as a product of probabilities:

$$p(0;t) = \prod_{r_{\text{min}} \le r < R(t)} \left(1 - 4\pi n r^2 dr \frac{\beta J_0/r^3}{W_{\text{eff}}}\right) \tag{B.27}$$

$$= \exp\left[-\int_{r_{\text{min}}}^{R(t)} \frac{4\pi n Q_{\text{res}}}{r} dr\right] \tag{B.28}$$

where $4\pi n r^2 dr$ is the probability of finding a spin at distance r, and $Q_{\text{res}} = \beta J_0/(W_{\text{eff}} r^3)$ is the probability that the spin resonates with the spin-i. Defining $\lambda(t) = 4\pi Q_{\text{res}}(\ln R(t) - \ln r_{\text{min}})$, we obtain $p(0;t) = \exp[-\lambda(t)]$. Similarly, we can calculate $p(\ell;t)$ for $\ell > 0$, and obtain $p(\ell;t) = \frac{1}{\ell!}\left(\lambda(t)\right)^\ell e^{-\lambda(t)}$, which is the Poisson distribution with mean $\lambda(t)$.

To show that the dominant contribution of Eq. (B.26) arises from the $k = 1$ term, we consider the probability of the termination of the resonance finding process, P_{term}. It satisfies the self-consistency equation

$$P_{\text{term}} = e^{-\lambda} + \sum_{\ell=1}^{\infty} \frac{\lambda^\ell e^{-\lambda}}{\ell!} \left(P_{\text{term}}\right)^\ell, \tag{B.29}$$

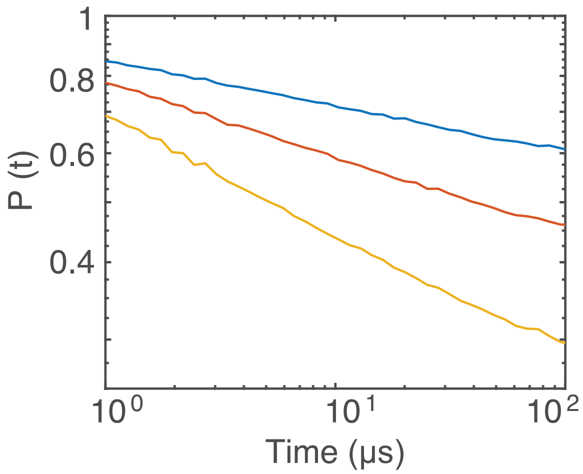

Figure B.8: **Single-particle simulation of power-law dynamics.** Blue, red, and yellow curve correspond to $\Omega = (2\pi)$ 3, 8, and 20 MHz, respectively. For the simulations, we use 10^4 spins and average over more than 10^3 disorder realizations.

where the first term corresponds to the case where the initial spin does not have any resonance up to time t, while the second term implies the termination of each sub-graph generated from ℓ resonant spins. For sufficiently large λ, P_{term} becomes small, and its contribution is dominated by the first term ($\ell = 0$). In our case, $\lambda(t)$ is a function of time which diverges in the limit $t \to \infty$. As we are interested in the late time dynamics, we may consider the first term only. In terms of $\text{Pr}(k;t)$, this corresponds to approximating $\text{Pr}(k;t) \sim 0$ for $k > 2$. Finally, noting that that $\text{Pr}(k = 1;t) = p(0;t)$, we recover the expression in the main text.

We numerically test the analytic resonance counting that predicts the power-law decay dynamics. In the limit of single-particle excitation, the survival probability $P(t) = |\langle\psi(t)|\psi(0)\rangle|^2$ can be computed at any time t after the time evolution of a system under H_{eff} (See Eq. (1) in the main text). Considering physically relevant parameters used in the experiments, we verify such power-law decay dynamics for up to 10^4 spins as shown in

Fig. B.8. Moreover, we confirm the extracted power-law exponent is inversely proportional to effective disorder W_{eff} (Fig. 4C in the main text), further substantiating the thermalization mechanism based on rare resonances. The power-law exponents extracted from the simulations are summarized in Fig. B.12A.

B.4.2 Interplay between dimensionality and long-range interaction

The critical nature of a disordered dipolar spin ensemble in three dimensions originates from the interplay between long-range interactions and dimensionality. To see this, we can generalize the resonance counting analysis for a situation in which a single particle excitation is located in a d-dimensional spin system with long-range coupling decaying as $1/r^{\alpha}$. In such a setting, the survival probability $P(t)$ can be expressed as,

$$P(t) = \exp\left[-\int_{r_{\text{min}}}^{R(t)} n S_d r^{d-1} \frac{\beta J_0/r^{\alpha}}{W_{\text{eff}}} dr\right] \tag{B.30}$$

$$= \exp\left[-\frac{n S_d \beta J_0}{W_{\text{eff}}} \int_{r_{\text{min}}}^{R(t)} r^{d-\alpha-1} dr\right], \tag{B.31}$$

where S_d is the surface area of the d-dimensional volume. In fact, the argument of $P(t)$, $\int_{r_{\text{min}}}^{R(t)} r^{d-\alpha-1} dr$, is associated with the probability of finding a resonance up to the distance $R(t)$ reachable at time t. Hence, when the dimensionality d is larger (smaller) than the interaction strength α, the above integral diverges (converges) as $R(t)$ becomes large, which implies delocalization (localization) of the single particle excitation. In the critical case where d is equal to α, the resonance probability increases at a slow logarithmic rate, resulting in the power-law relaxation of the initial spin state as derived in Eq. (2) in the main text. In the limit of single particle excitations we therefore associate our system dynamics to such criticality behavior. However, due to the presence of many-spin excitations, much richer dynamics may appear at longer times. We attribute the deviation of power-law dynamics at late times observed in our experiments to this effect.

B.4.3 Time-dependent disorder

Now we consider the case of time-dependent disorder. For concreteness, we assume that the on-site potential disorder is given as a sum of a static and a dynamical disorder potential, $\tilde{\delta}_i(t) = \tilde{\delta}_i^s + \tilde{\delta}_i^d(t)$, where the static part $\tilde{\delta}_i^s$ (dynamical part $\tilde{\delta}_i^d(t)$) is random with zero mean and standard deviation W_s (W_d). While $\tilde{\delta}_i^s$ is time-independent, the dynamical component $\tilde{\delta}_i^d(t)$ changes over time by uncorrelated jumps at a rate $\Gamma = 1/\tau_d$. Here, we focus on an experimentally relevant regime where $W_s \gg W_d \gtrsim nJ_0 > 1/\tau_d$.

As already mentioned in the main text, we modify the resonance criteria as follows. Two spins at sites i and j are on resonance at time t if: (1) *at any point in time* $t' < t$, their energy mismatch is smaller than their dipolar interaction strength, $|\tilde{\delta}_i(t') - \tilde{\delta}_j(t')| < \beta J_{ij}/r_{ij}^3$, and (2) the interaction occurs within the time-scale t, $J_{ij}/r_{ij}^3 > 1/t$. While the second part of the condition is unchanged, the first part now captures that a pair may be brought into resonance by spectral jumps. Under the hierarchy of $W_s \gg W_d \gtrsim nJ_0 > 1/\tau_d$, the condition (1) can be approximated by two independent events: (a) the static energy mismatch is small enough, $|\tilde{\delta}_i^s - \tilde{\delta}_j^s| < W_d$, and (b) the dynamical energy mismatch is smaller than the coupling strength, $|\tilde{\delta}_i^d(t') - \tilde{\delta}_j^d(t')| < \beta J_{ij}/r_{ij}^3$ at some time $t' < t$. In combination, the condition (1) is satisfied with the probability

$$P_{\text{res}}(r,t) \approx \frac{W_d}{W_s}\left(1 - e^{-\frac{\beta J_0/r^3}{W_d}\frac{t}{\tau_d}}\left(1 - \frac{\beta J_0/r^3}{W_d}\right)\right) \tag{B.32}$$

which is the product of probabilities for conditions (a) and (b). For the second factor, we used the probability that the initial configuration is off-resonant, $(1 - \frac{\beta J_0/r^3}{W_d})$, and the probability that none of the subsequent spectral jumps brings them into resonance $e^{-\frac{\beta J_0/r^3}{W_d}\frac{t}{\tau_d}}$. We note that, in practice, one should use $\max(0, 1-\beta J_0/W_d r^3)$ instead of $(1-\beta J_0/W_d r^3)$ since a probability cannot be less than zero. Finally, the survival probability is obtained by requiring no resonance at every distance r up to $R(t) = (J_0 t)^{1/3}$

$$\overline{P(t)} = \exp\left[-\int_{r=r_0}^{R(t)} 4\pi n r^2 P_{\text{res}}(r,t)dr\right], \tag{B.33}$$

where r_0 is the short distance cut-off of the NV separations. We use the cut-off distance $r_0 \sim 1.4$ nm, at which the corresponding dipole-dipole interaction is $J_0/r_0^3 \sim (2\pi)\ 20$ MHz. Due to dipole blockade, a pair of NV centers closer than r_0 cannot be addressed by microwave driving of Rabi frequency $\Omega \sim (2\pi)\ 20$ MHz, which we use for initial preparations of spin states. Those spins do not participate in the spin exchange dynamics due to large energy mismatch. We note that, $\lim_{\Gamma\to 0} P_{\text{res}}(r,t) \to Q_{\text{res}}(r) = \beta J_0/(W_s r^3)$ and the Eq. (B.33) correctly reduces to the disorder-dependent power-law decay. In the presence of a small but finite $\Gamma = 1/\tau_d$, integrating Eq. (B.33) using Eq. (B.32) yields,

$$\overline{P(t)} = P_1(t)P_0(t), \tag{B.34}$$

where

$$P_1(t) = \exp\left[-\frac{4\pi n}{3}\frac{W_d}{W_s}\left\{J_0(t-t_0) - J_0(te^{-\frac{\beta}{W_d\tau_d}} - t_0 e^{-\frac{t}{t_0}\frac{\beta}{W_d\tau_d}})\right\}\right] \tag{B.35}$$

$$P_0(t) = \exp\left[-\frac{4\pi n J_0\beta}{3W_s}\left\{(1+t/\tau_d)\mathcal{G}[0,\frac{\beta}{W_d\tau_d}] - (1+t/\tau_d)\mathcal{G}[0,\frac{t}{t_0}\frac{\beta}{W_d\tau_d}]\right\}\right]. \tag{B.36}$$

Here $\mathcal{G}$ is an incomplete Gamma function. In the limit of the hierarchy $W_s \gg W_d \gtrsim nJ_0 >$

$1/\tau_d$, we can simplify:

$$P_1(t) \approx C_1 \exp\left[-\frac{4\pi n}{3}\frac{W_d}{W_s}\left(J_0 t(1 - e^{-\frac{\beta}{W_d\tau_d}})\right)\right] \tag{B.37}$$

$$\approx C_1 \exp\left[-\frac{4\pi n J_0 \beta}{3W_s}\frac{t}{\tau_d}\right] \tag{B.38}$$

$$\equiv C_1 \exp[-t/T^*], \tag{B.39}$$

where C_1 is a time-independent prefactor and

$$T^* = \frac{3W_s\tau_d}{4\pi n J_0\beta} \propto \frac{W_s\tau_d}{nJ_0}. \tag{B.40}$$

Similarly, $P_0(t)$ can also be simplified as,

$$P_0(t) \approx C_2 \exp\left[-\frac{4\pi n J_0\beta}{3W_s}\left\{\mathcal{G}[0, \frac{\beta}{W_d\tau_d}] - \mathcal{G}[0, \frac{t}{t_0}\frac{\beta}{W_d\tau_d}]\right\}\right] \tag{B.41}$$

$$\approx C_2' \exp\left[-\frac{4\pi n J_0\beta}{3W_s}\ln(t/t_0)\right] \tag{B.42}$$

$$= C_2'(t/t_0)^{-\frac{4\pi n J_0\beta}{3W_s}}. \tag{B.43}$$

Here we used the approximation $\mathcal{G}(0,z) \approx -\ln(z) + \gamma + \mathcal{O}(z)$ for $z \ll 1$. Once again, we rediscover the power-law decay (Eq. (B.43)) predicted in the main text, but now only up to a finite time T^*:

$$\overline{P(t)} = P_1(t)P_0(t) \propto e^{-t/T^*}t^{-\frac{4\pi n J_0\beta}{3W_s}}. \tag{B.44}$$

Therefore, according to the Eq. (B.44), the weak time-dependent disorder results in a multiplicative exponential correction to the power-law decay up to $t < T^*$, beyond which the thermalization accelerates substantially. Furthermore, our theory model predicts that T^* is linearly proportional to the static disorder strength W_s, which is consistent with our observations (See Fig. 3D and Fig. 4D in the main text).

B.5 Detailed analysis of thermalization experiments

B.5.1 Effective disorder control under spin-locking conditions

To investigate the interplay between disorder and interaction experimentally, it is required to tune both disorder and interaction in a controlled way. In our experiments, we rely on a spin-locking technique in which both the energy spacing and the on-site disorder of a spin ensemble can be controlled in a continuous fashion.

As discussed in the main text, spin-locking allows us to prepare spins in the dressed state basis. In the new basis, the energy eigenstates are $|\pm\rangle \approx (|m_s = 0\rangle \pm |m_s = -1\rangle)/\sqrt{2}$ and are split by an effective Rabi frequency of a spin-lock field, $\Omega_{\text{eff}} = \sqrt{\Omega^2 + \delta^2}$, where Ω is the driving strength and δ is the on-site disorder in the bare frame. Owing to a random distribution of δ, the new level spacing Ω_{eff} is also a random variable. Therefore, an effective disorder under the spin-locking condition can be defined as,

$$W_{\text{eff}} \equiv \sqrt{\text{Var}[\Omega_{\text{eff}}]} = \sqrt{E[\Omega^2 + \delta^2] - E[\sqrt{\Omega^2 + \delta^2}]^2}, \tag{B.45}$$

where $\text{Var}[X]$ and $E[X]$ are the variance and expectation value of a random variable X. Since the disorder in the bare frame follows a Gaussian distribution with a standard deviation W, the expectation values can be expressed as

$$E[\Omega^2 + \delta^2] = \frac{1}{\sqrt{2\pi W^2}} \int_{-\infty}^{+\infty} d\delta \; [\Omega^2 + \delta^2] e^{-\delta^2/2W^2} \tag{B.46}$$

$$E[\sqrt{\Omega^2 + \delta^2}] = \frac{1}{\sqrt{2\pi W^2}} \int_{-\infty}^{+\infty} d\delta \; \sqrt{\Omega^2 + \delta^2} e^{-\delta^2/2W^2}. \tag{B.47}$$

In the case of weak driving ($\Omega \ll \delta$), $W_{\text{eff}} \approx \sqrt{\text{Var}[\delta]} = W$; namely, the effective disorder is almost equal to that in the bare frame. However, as the driving strength Ω increases we

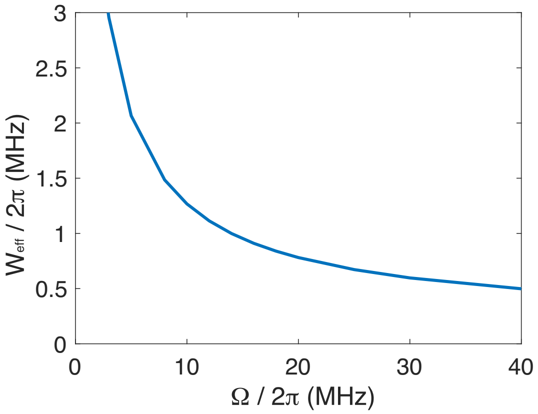

Figure B.9: **Effective disorder under spin locking conditions.** Based on the resonance counting argument, the effective disorder W_{eff} can be computed as a function of the Rabi frequency Ω.

find $W_{\text{eff}} \approx \sqrt{\text{Var}[\frac{\delta^2}{2\Omega}]} = \frac{W^2}{\sqrt{2}\Omega}$. Hence, the effective disorder W_{eff} can be tuned by adjusting the Rabi frequency Ω in the dressed state basis.

We note that the probability distribution of Ω_{eff} is highly asymmetric, which may lead to small corrections to our counting argument at a quantitative level. To this end, for our numerical computations, we use an alternative definition of W_{eff} which is consistent with our resonance counting argument. Recall that two spins at site i and j with separation r are defined to be on resonance when $|\tilde{\delta}_i - \tilde{\delta}_j| < \beta J_0/r^3$ and that we assumed this occurs with probability $Q_{\text{res}} \propto (J_0/r^3)/W_{\text{eff}}$. Therefore, the effective disorder strength W_{eff} should be defined in the same way from the full distribution of Ω_{eff}. More specifically, we compute the probability $q(\xi)$ that two independent random variables $\tilde{\delta}_i$ and $\tilde{\delta}_i$ satisfy $|\tilde{\delta}_i - \tilde{\delta}_j| < \xi$ for a small parameter ξ. In the limit of $\xi \ll W^2/\sqrt{2}\Omega$, the probability $q(\xi)$ is linearly proportional to ξ. Then, we define the effective disorder as $W_{\text{eff}} \equiv \lim_{\xi\to 0} \xi/q(\xi)$. Fig. B.9 shows the dependence of W_{eff} as a function of Ω. In the limit of large Ω, the effective disorder scales as $W_{\text{eff}} \propto 1/\Omega$, as expected.

B.5.2 Effects of incoherent dynamics

In our Hartman-Hahn experiments, the spin dynamics are governed by both coherent cross-relaxation and incoherent depolarization. These two effects have qualitatively different dependence on the driving strength and can be clearly distinguished in our observations. To perform a detailed analysis of the results presented in the main text, we focus on the coherent dynamics by normalizing our data at the Hartman-Hahn resonance $\Omega_A = \Omega_B$ via a sufficiently detuned case $|\Omega_A - \Omega_B| \gg nJ_0$, at which the spin relaxations are dominated by incoherent dynamics (Fig. B.10, blue line). Such normalization can be justified only if the two effects are independent and multiplicative. This is the case if the incoherent dynamics are induced by an independent Markovian noise, which results in an exponential and multiplicative factor $e^{-\gamma t}$. In our experiment, however, we observe a stretched exponential $e^{-\sqrt{t/T}}$ decay profile from incoherent dynamics (Fig. 2D in the main text). Below, we explain why such incoherent decays are still factorizable.

Our incoherent dynamics can be modeled as follows. (See Ref. [76] for more details). Each spin at site i undergoes incoherent depolarization at rate γ_i. This rate γ_i is determined by the microscopic local environment of the spin and follows a random distribution $\rho(\gamma; T_1^\rho)$, such that the ensemble averaged polarization decays as a stretched exponential

$$e^{-\sqrt{t/T_1^\rho}} = \int_0^\infty \rho(\gamma; T_1^\rho) e^{-\gamma t} d\gamma. \tag{B.48}$$

The analytical expression as well as the microscopic origin of the distribution $\rho(\gamma; T_1^\rho)$ are presented in Ref. [76]. At the Hartman-Hahn condition, both the incoherent process and the coherent cross-relaxation lead to depolarization (see Fig. B.10). Hence, at time t, the rate of depolarization for spin-i is given by $\dot{p}_i(t) = -[\gamma_i + f_i(t)]p_i(t)$, where $f_i(t)$ is the rate of cross-relaxation (which generally depends on the state of other spins). This cross-

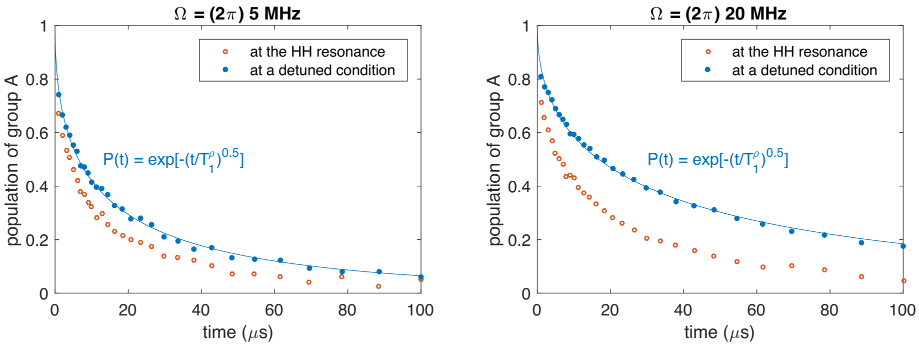

Figure B.10: **Unnormalized experimental Data.** Two data sets with different common Rabi frequencies of $\Omega = (2\pi)$ [5, 20] MHz are presented at the Hartmann-Hahn resonance (red) and at the far-detuned case (blue). For the detuned signal, a stretched exponential of power 0.5 is fitted to the data.

relaxation, once averaged over an ensemble, leads to a power-law decay as derived in the previous section. The differential equation for the polarization is exactly solvable with the solution $p_i(t) = e^{-\gamma_i t} e^{\int_0^t f_i(t')dt'}$, where one finds a multiplicative exponential factor $e^{-\gamma_i t}$. Crucially, this effect is still factorizable, even after ensemble averaging:

$$\langle p_i(t) \rangle_{\text{ensemble}} = \int_0^\infty \rho(\gamma; T_1^\rho) e^{-\gamma_i t} d\gamma \left\langle e^{\int_0^t f_i(t')dt'} \right\rangle_{\text{ensemble}} \propto e^{-\sqrt{t/T_1^\rho}} \cdot t^{-\eta}, \tag{B.49}$$

where η is the disorder dependent exponent derived in the main text. Physically, this factorization arises because the microscopic environment for each spin, which determines coherent as well as incoherent dynamics, is random and independent. For this reason, in the experiment, we normalize the polarization decay at the Hartmann-Hahn resonance (Fig. B.10, red line) by the incoherent decay at the far-detuned case (Fig. B.10, blue line).

B.5.3 Dependence of thermalization dynamics on bath polarization

In Fig. B.11, the theory prediction from Eq. (B.33) is compared with experimental data for various Rabi frequencies and two different initial polarizations of group B spins.

The functional profiles of the decay are consistent with power laws for over a decade, followed by accelerated, though still sub-diffusive relaxation at late times. In the power-law regime, we find that the power-law decay exponents depend on the initial polarization of group B spins (Fig. B.12A). This is consistent with our theory; for single-particle dynamics, we expect that the power-law exponent scales as $\sim nJ/W_{\text{eff}}$, where n is the density of oppositely polarized spins. Indeed, when group B is initially unpolarized, the exponents are decreased by a factor of two compared to the fully polarized case, consistent with our theory at a quantitative level.

To characterize the late-time acceleration of the polarization decay, we use the time-dependent model where the pair-resonance counting criteria are modified as discussed in the previous section. By fitting the experimental data to our model using a Monte-Carlo (MC) optimization, we extract the parameters of the dynamical disorder strength W_d and spectral diffusion time $\tau_d = 1/\Gamma$. Here, we assume W_d as a global fit parameter which is independent from Ω; this is because we expect W_d to be predominantly determined by the mean-field interaction strength. In contrast, τ_d may in principle be dependent on Ω since the fluctuations of the Ising mean-field potential depend on the thermalization speed and hence also on the effective disorder strength tuned by Ω. To this end, we performed two independent MC optimizations where we (i) treat W_d as global (Ω-*independent*) and τ_d as local (Ω-*dependent*) variables (Fig. B.11A), or instead (ii) fix both parameters as global variables (Fig. B.11B). For the static effective disorder, we use the theory-predicted values $W_s \sim W^2/\Omega$ (as described previously). Naturally, owing to the larger number of fit parameters, a global W_d with local τ_d variation (Fig. B.11A) shows better agreement than a global W_d together with with global τ_d (Fig. B.11B). In the latter case, extracted fit

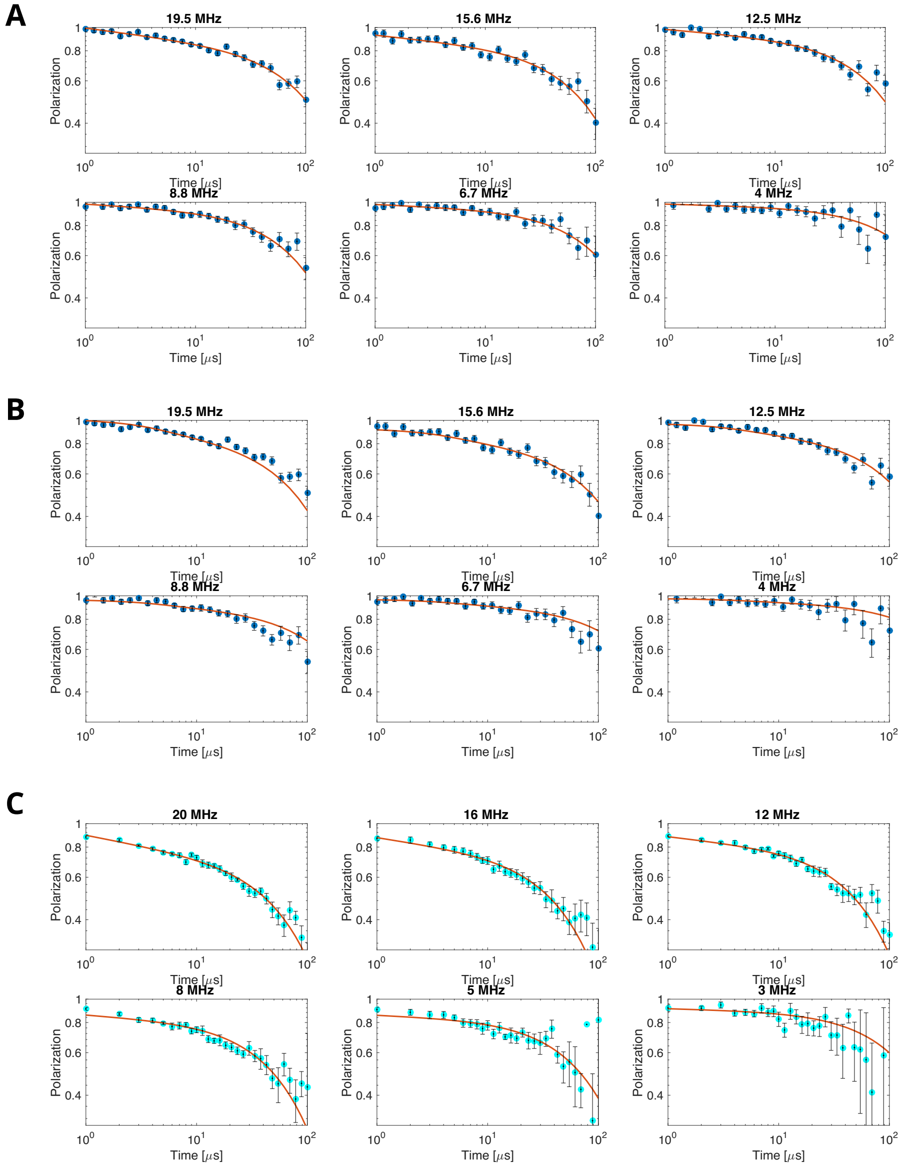

Figure B.11: **Polarization decay of a NV ensemble under Hartmann-Hahn conditions.** An initially polarized group A spin ensemble interacts with **(A,B)** unpolarized and **(C)** fully polarized group B. Solid lines are theoretical fits based upon a time-dependent disorder model with extracted parameters (W_d, τ_d) via a Monte-Carlo optimization. In **(A,C)**, the spectral diffusion time τ_d is dependent on the Rabi frequency, while in **(B)** τ_d is independent of the applied Rabi frequency. The dynamical disorder strength W_d is a Ω-independent, global variable in all three cases.

parameters W_d and τ_d are (2π) 46 ± 14 kHz and 43 ± 9 μs, respectively.

In the former case (Fig. B.11A), the extracted dynamical disorder $W_d \sim (2\pi)$ 0.5 MHz is consistent with the expected strength of the Ising interaction, suggesting that spin-spin interactions play an important role for the time-dependent disorder. Furthermore, τ_d is also consistent with the observed NV depolarization timescale, including contributions from both coherent cross-relaxation and incoherent spin depolarization. We note that in the fully polarized case the extracted values for τ_d are smaller than those in the unpolarized case (Fig. B.12B). We speculate that this could be due to faster coherent spin-exchange dynamics in the former case, giving rise to a faster fluctuation in δ^I, responsible for the accelerated thermalization dynamics at late times.

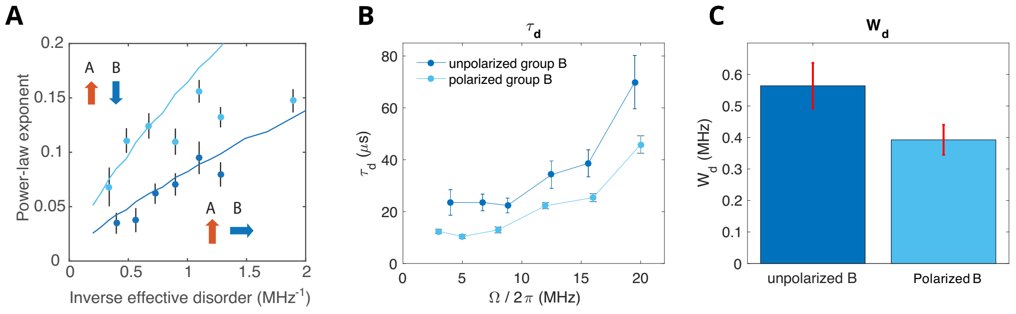

Figure B.12: **Fitted parameters of the time-dependent disorder model extracted from a Monte-Carlo optimization. (A)** Exponents of the power-law decay of group A polarization with oppositely polarized (light blue) and unpolarized (dark blue) group B as a function of inverse effective disorder. Solid lines correspond to numerical simulation results. **(B)** The extracted τ_d as a function of Rabi frequency. Light and dark blue point corresponds to fully oppositely polarized and unpolarized group B spin states, respectively. **(C)** The extracted dynamical disorder W_d. All errorbars are evaluated from the standard deviation of the optimized parameter after running 10 independent Monte-Carlo runs.

Appendix C

Supporting Material of Chapter 4

C.1 Methods

C.1.1 Experimental sequence

Initial polarization of NV centers into $|m_s = 0\rangle$ is performed via laser illumination at a wavelength of 532 nm, a power of $50\ \mu$W and a duration of 100 μs. Subsequent application of a microwave $-\pi/2$ pulse along the $\hat{y}$ axis is used to coherently rotate the spin ensemble into $|+\rangle = (|m_s = 0\rangle + |m_s = -1\rangle)/\sqrt{2}$. The spins are then subjected to continuous driving at a Rabi frequency $2\pi \times 54.6$ MHz along the $\hat{x}$ axis for a duration τ_1. This so-called spin-locking technique suppresses two-spin (flip-flip and flop-flop) processes, owing to energy conservation, and decouples spins from their environment [17]. In our sample, this technique leads to spin lifetimes of $T_1^\rho \approx 60\ \mu$s [76]. Finally, we apply a short microwave pulse along the $\hat{y}$ axis over an angle $\theta \approx \pi$. We repeat this Floquet cycle with various values of θ, controlled by changing the Rabi driving strength as well as the pulse duration. The imperfection in microwave manipulations (for initialization into $|+\rangle$ as well as rotation angles θ) amounts to 0.9%, arising from a combination of spatial inhomogeneity of the driving field (0.8%) as well as on-site potential disorder (0.6%). Following a coherent time evolution, the spin state of the NV ensemble is optically detected by applying a final $\pi/2$ pulse along the $\hat{y}$ axis and measuring the population difference in the $|m_s = 0\rangle$ and $|m_s = -1\rangle$ basis. The polarization is defined as $P = \mathcal{P}_0 - \mathcal{P}_{-1}$ with $\mathcal{P}_a$ denoting the population in spin state a, and is determined by calibrating the NV fluorescence using a Rabi oscillation contrast measurement. To avoid heating of the sample, resulting in drifts in the Rabi frequency, a waiting time of $600 - 900\,\mu$s is implemented before the sequence is repeated. The minimum spacing between microwave pulses is maintained at 1 ns.

To understand the effect of different initial states on the DTC phase, we replaced the initial $-\pi/2$ pulse with a $-\pi/3$ pulse. This results in the preparation of a global spin state, which is rotated from the $\hat{x}$ axis by $\pi/6$. Despite this change, the measured lifetime of the DTC order ($47.6 \pm 2.4\,\mu$s) agrees well with that of the polarized spin state ($49.2 \pm 3.3\,\mu$s), demonstrating that DTC order is insensitive to the initial state.

C.1.2 Experimental identification of phase boundary

To identify the position of the phase boundary in our experiment, we define the crystalline fraction f as $f = |S(\nu = \frac{1}{2})|^2 / \sum_\nu |S(\nu)|^2$. Error bars in f are calculated via error propagation in consideration of the noise floor in the Fourier spectrum; each measured spectrum contains a background noise level σ_n, resulting in a variation of f as,

$$\delta f = f\sqrt{\left(\sigma_n/|S(\nu=\frac{1}{2})|^2\right)^2 + \left(N\sigma_n/\sum_\nu |S(\nu)|^2\right)^2 - 2N\sigma_n^2/\left(|S(\nu=\frac{1}{2})|^2\sum_\nu |S(\nu)|^2\right)}, \tag{C.1}$$

where $N = 50$ is the number of points in the Fourier spectrum. This gives rise to an uncertainty in the crystalline fraction: $f \in [f-\delta f, f+\delta f]$ (Fig. 3a in the main text). To extract the phase boundary, we use a phenomenological, super-Gaussian function

$$F_{\tau_1}(\theta) = \begin{cases} f_{\tau_1}^{\max}\exp\left[-\frac{1}{2}\left(\frac{|\theta-\theta_0|}{\sigma_-}\right)^p\right] & ,\theta \le \theta_0 \\ f_{\tau_1}^{\max}\exp\left[-\frac{1}{2}\left(\frac{|\theta-\theta_0|}{\sigma_+}\right)^p\right] & ,\theta \ge \theta_0 \end{cases} \tag{C.2}$$

where $\sigma_\pm$, θ_0, p are the characteristic width, central position and the power of the super-Gaussian fit, and $f_{\tau_1}^{\max}$ is the maximum value of the crystalline fraction for a given duration τ_1. The proposed function naturally captures the observed asymmetry in the phase boundary. We define the phase boundary as the rotation angle $\theta_\pm$ at which $F_{\tau_1}(\theta_\pm)$ = 0.1; that is, $\theta_\pm = \theta_0 \pm \sigma_\pm\left[2\ln(f_{\tau_1}^{\max}/0.1)\right]^{\frac{1}{p}}$. Errors in the phase boundary are derived from the fit uncertainties.

C.1.3 Theoretical description

As a variational ansatz, we consider the time evolution of a homogeneous product state of the form $|\Psi\rangle = |\psi_0\rangle^{\otimes N}$ with $|\psi_0\rangle = \cos(\theta_0/2)|+\rangle + \sin(\theta_0/2)e^{i\phi_0}|-\rangle$, where $|\pm\rangle = (|m_s=0\rangle \pm |m_s=-1\rangle)/\sqrt{2}$. The qualitative behavior does not change even if we allow spins to be oriented in different directions. An approximate eigenstate for the time evolution over two periods is obtained by solving the equation for a single spin, $|\psi_0\rangle = e^{-i\theta S^y}e^{i\phi_i S^x}e^{-i\theta S^y}e^{-i\phi_i S^x}|\psi_0\rangle$ with a self-consistently determined $\phi_i = \bar{J}_i\langle\psi_0|S^x|\psi_0\rangle$ where

$\bar{J}_i = \sum_j J_{ij}/r_{ij}^3$ is the total strength at site i. The sign of ϕ_i is flipped in the second evolution as the spin polarization along the $\hat{x}$ direction alternates in each cycle. Note that we have ignored the effects of the on-site disorder potential Δ_i, interactions during global rotations and rotations induced by Ω_x. This is justified due to the high microwave driving strength $\Omega_{x(y)} \gg W$ and $\Omega_x \tau_1$ being integer multiples of 2π. (The effects of on-site disorder are fully included in the numerical computations.) A non-trivial solution ($\theta_0 \neq \pm\pi$) is obtained if the first two rotations result in a vector that is rotated by π along the $\hat{y}$ axis (Fig. 3d in the main text), which is satisfied when $\phi_0 = m\pi - \phi_i/2$ with $m \in \mathbb{Z}$ and $\cot\theta_0 = -(-1)^m \tan(\theta/2)\sin(\phi_i/2)$. Solving for $\cos^2\theta_0$ yields

$$\cos^2\theta_0 = \frac{\tan^2(\theta/2)\sin^2(\phi_i/2)}{1+\tan^2(\theta/2)\sin^2(\phi_i/2)}. \tag{C.3}$$

Using $\phi_i = \bar{J}_i\tau_1\cos\theta_0$, one can show that a solution exists only when $|\tan(\theta/2)\bar{J}_i\tau_1/4| > 1$, implying that $|\theta-\pi| < |\bar{J}_i\tau_1/2|$ in the vicinity of $\theta \approx \pi$. The linear dependence of the phase boundary is consistent with the phase diagram provided in Ref. [12]. As long as a solution exists, small variations in θ correspond to a smooth deformation of the closed trajectory. Therefore, the existence of such a closed path stabilizes the time-crystalline phase. We emphasize that such a $2T$-periodic path is a consequence of interactions; without the change of sign in ϕ_i, the eigenstates of the unitary evolution over one or two periods coincide, and therefore, unless the rotation angle is fine-tuned, T-periodic motion cannot be broken into a $2T$ period. The eigenstates of unitary evolution over one period can be obtained as even and odd linear combinations, $(|\Psi\rangle \pm e^{-i\epsilon_i}U_1|\Psi\rangle)/\sqrt{2}$, where $U_1 = \otimes_i(e^{-i\theta S_i^y}e^{-i\phi_i S_i^x})$, and the quasi-energy eigenvalue is given by $e^{i2\epsilon_i} = \langle\Psi|(U_1)^2|\Psi\rangle$.

To estimate the phase boundary, we numerically solve the self-consistency equation. Here, we include the effects of on-site disorder potential Δ_i in all four rotations as well as the disorder in $\bar{J}_i$ arising from the random positions of NV centers. The distribution of $\bar{J}_i$ is simulated for 1000 spins, randomly distributed in three dimensions with an average separation r_0 and minimum cutoff distance $r_{\text{min}} = 3$ nm (limited by NV-NV electron tunneling [76]). Instead of $\cos(\theta_0)$, we solve for a self-consistent distribution for $\cos(\theta_0)$, where $\langle S^x \rangle$ is defined as the mean of the distribution. The average order parameter $\langle \cos^2 \theta_0 \rangle$ is computed for various values of τ_1 and θ and compared with a threshold value of 0.1 in order to identify the phase boundary. The experimental and numerical phase boundaries are asymmetric about $\theta = \pi$. We attribute this to the inherently asymmetric distribution of the effective rotation angle, $\theta_i \approx \tau_2 \sqrt{\Omega_y^2 + \Delta_i^2 + \bar{J}_i^{\,2}}$, which causes the transition to occur earlier for positive deviations $\theta - \pi$.

While we assumed ϕ_i to be a classical variable in this analysis, the interaction induced rotation angle is an operator $\hat{\phi}$ that exhibits quantum fluctuations and leads to non-trivial quantum dynamics. Under such dynamics, spins get entangled, resulting in mixed state density matrices. These effects cannot be ignored in the case of long interaction times, effectively limiting the present description. We believe that the diminished range of θ in the experimentally obtained phase diagram (Fig. 3b in the main text) is related to this effect.

C.1.4 Rotary echo sequence

Certain features similar to DTC order could potentially arise from spatially inhomogeneous microwave driving along the $\hat{x}$ axis during the spin-locking sequence. This leads to variations in the effective, single-particle disorder in the dressed state basis, which could give rise to an effective self-correcting dynamical decoupling that might resemble DTC order [87]. In particular, in the spin-locking sequence, spins precess along the axis

$(\Omega_x(r_i) + \bar{J}_i)\hat{x} + \Delta_i\hat{z}$, with effective Rabi frequency $\Omega^{\text{eff}}_{x,i} = \sqrt{(\Omega_x(r_i) + \bar{J}_i)^2 + \Delta_i^2}$, where $\Omega_x(r_i)$ is the spatially inhomogeneous Rabi frequency, $\bar{J}_i$ is the mean-field Ising interaction, and Δ_i characterizes the quasi-static on-site disorder. In the case of strong driving ($\Omega_x \gg \Delta_i, \bar{J}_i$), this precession axis is determined by Ω_x and spins undergo dephasing dominated by global microwave inhomogeneities. If the net rotation during one spin-locking cycle is an odd integer multiple of π, this could accidentally lead to an XY-sequence [87] that may result in $2T$-periodicity. In our measurements, we always choose τ_1 as an integer multiple of $2\pi/\Omega_x$ to minimize such effects.

Although it has been shown theoretically that disorder alone is insufficient (in the absence of interactions) for stabilizing DTC order [9, 10, 11, 12], to experimentally demonstrate that the accidental decoupling is not responsible for the observed DTC ordering, we implement a "rotary echo" sequence, wherein after half the interaction time τ_1 the microwave driving is flipped from Ω_x to $-\Omega_x$ (Fig. C.1a). In the limit of strong driving, such a sequence eliminates the phase acquired between the two dressed states for each spin, regardless of the exact value of Ω_x. As shown in Fig. C.1b, the lifetimes of the DTC order are nearly identical between the cases of the rotary echo and continuous $+\hat{x}$ driving. Moreover, the rotary echo spin polarization maintains a larger amplitude at late times, excluding the possibility of self-correcting dynamical decoupling as the origin of the observed DTC order.

C.1.5 Markovian dephasing effects on discrete time-crystalline order

The presence of the sub-harmonic peak at $\nu = 1/2$ at small values of $\theta - \pi$ can, in principle, also be explained based on fast Markovian dephasing in the dressed state basis.

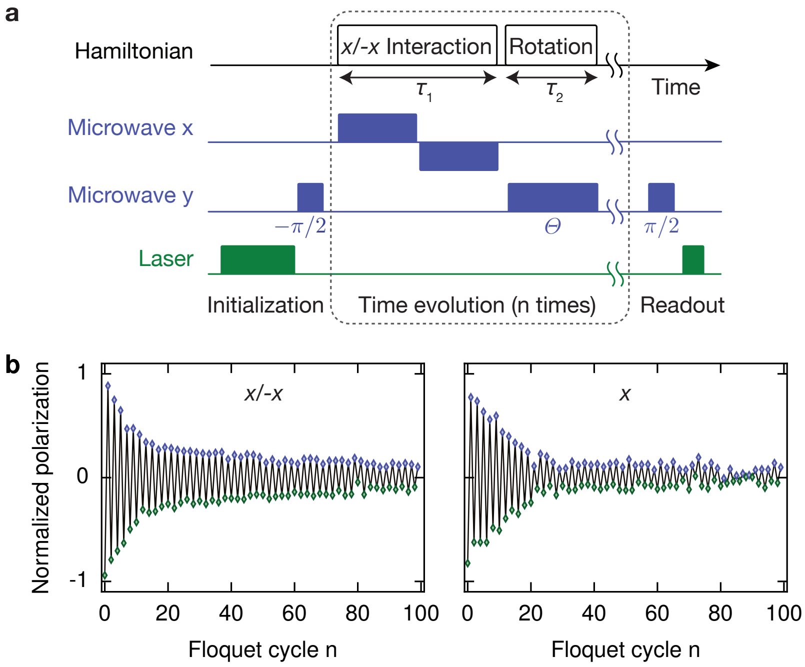

Figure C.1: **Effect of Rotary Echo Sequence.** **a** Experimental sequence: during the interaction interval τ_1, the phase of the microwave driving along $\hat{x}$ is inverted after τ_1/2. **b** Comparison of time traces of $P(nT)$ in the presence (left) and absence (right) of an $\hat{x}$/-$\hat{x}$ rotary echo sequence at similar τ_1 and θ (left: $\tau_1 = 379$ ns, $\theta = 0.979\pi$; right: $\tau_1 = 384$ ns, $\theta = 0.974\pi$). The rotary echo leads to more pronounced $2T$-periodic oscillations at long time. The microwave frequencies used in the rotary echo sequence are $\Omega_x = 2\pi \times 52.9$ MHz and $\Omega_y = 2\pi \times 42.3$ MHz.

Indeed, for sufficiently fast dephasing, coherences along both $\hat{y}$ and $\hat{z}$ will be eliminated after each rotation, R_y^θ. Thus, the only evolution that remains is the population dynamics along $\hat{x}$, which exhibits 2T-periodicity from the alternating sign. Microscopically, such strong dephasing could potentially originate from either dipolar interactions between the spins or from coupling to an external (Markovian) environment.

Intuitively, the result of such dephasing can be understood as an “effective” projective measurement of polarization along $\hat{x}$ in each Floquet cycle, reminiscent of the quantum Zeno effect. In order to quantify and distinguish such dephasing-induced sub-harmonic rigidity, we consider the dynamics (over one Floquet period) of a single spin undergoing Markovian dephasing, with super-operator $\hat{\mathcal{D}}[\rho] = -\frac{\gamma}{2}\left(\rho - 4S^x\rho S^x\right)$ and dephasing rate γ. Assuming $\theta - \pi \ll 1$, evolution falls into two well known limits. In the under-damped limit (weak dephasing), $S(\nu)$ exhibits two Lorentzian peaks at $\nu = \pm\eta$ with a linewidth set by $\gamma\tau_1$, where τ_1 is the spin-locking duration and $\cos(2\pi\eta) = \cos\theta(1 + e^{\gamma\tau_1})/2$. In the over-damped limit (strong dephasing), $S(\nu)$ (at late times) exhibits a peak at $\nu = 1/2$ with a linewidth (in Floquet units)

$$\Gamma \approx \frac{(\theta - \pi)^2}{2\tanh(\gamma\tau_1/2)}. \tag{C.4}$$

These over-damped oscillations of the spin polarization exhibit sign flips between the even and odd cycles, leading to a sub-harmonic Fourier response reminiscent of DTC order.

While strong Markovian dephasing can indeed result in a $\nu = 1/2$ sub-harmonic peak, we observe three distinct experimental signatures clearly showing that our observations are not governed by this effect. First, the linewidth, Γ, of the sub-harmonic peak should be quadratically sensitive to the deviation of θ from π. This is in stark contrast with our experimental observations shown in Fig. 2d in the main text, where this linewidth Γ is essentially independent of θ within the DTC phase. Second, according to the dephasing model, the lifetime of the 3T-periodic DTC order is expected to be longer than that of the 2T-periodic DTC order owing to enhanced dephasing (from a lack of spin-locking) in the bare basis [76]. However, we observe the exact opposite behavior. Finally, Markovian dephasing requires an effective environment with a relatively fast sub-μs correlation time. This is also inconsistent with our experimental observations. In particular, we performed Rabi oscillation decay measurements with a rotary echo sequence, resulting in a lower bound of $1.5\,\mu$s on the Markovian dephasing time T_2. This time scale still includes contributions from static on-site disorder and interactions, and thus the Markovian dephasing rate is, in fact, significantly slower than this. Indeed, we have independently extracted the typical timescales of disorder fluctuations in our system [17], and we find that they are similar ($60\,\mu$s) to depolarization timescale under spin-locking dynamics. Effects resulting from such slow dephasing should be completely negligible within a typical Floquet period. Thus, we conclude that fast dephasing alone does not explain the observed DTC order.

At the same time, in the time crystalline order description based on interacting spin models [9, 10, 11, 12], the time crystalline order is expected to be robust and is not expected to exhibit any functional dependence on the angle θ, in complete agreement with experimental observations. This is also the case for our self-consistent description. We finally note that the interplay between coherent interactions and dephasing could potentially play a role in stabilizing DTC order at longer interaction times. Detailed understanding of such mechanisms require further theoretical investigation.

C.1.6 Effective Hamiltonian for $\mathbb{Z}_3$ symmetry breaking phase

Using microwave driving resonant with two different transitions (Fig. 4a in the main text), we realize dynamics involving all three spin states and observe a robust $3T$-periodic time-crystalline order. The unitary matrix of the time evolution during the fundamental period T is given as

$$U_3 = e^{-i\sum_i(\sigma^i_{-1,0}+\sigma^i_{0,-1})\theta/2} e^{-i\sum_i(\sigma^i_{+1,0}+\sigma^i_{0,+1})\theta/2} e^{-iH_2\tau}, \tag{C.5}$$

where $\sigma^i_{a,b} \equiv |m_s = a\rangle\langle m_s = b|$ for spin-i and $H_2 = H_{\text{dis}} + H_{\text{int}}$ is the effective Hamiltonian of NV centers for all three spin states including on-site disorder potentials $H_{\text{dis}} =$

$\sum_i \Delta_i^+ \sigma_{+1,+1}^i + \Delta_i^- \sigma_{-1,-1}^i$ and dipolar interactions for spin-1 particles[?]

$$H_{\text{int}} = \sum_{ij} \frac{J_{ij}}{r_{ij}^3} \left[-\frac{\sigma_{+1,0}^i \sigma_{0,+1}^j + \sigma_{-1,0}^i \sigma_{0,-1}^j + h.c.}{2} + (\sigma_{+1,+1}^i - \sigma_{-1,-1}^i)(\sigma_{+1,+1}^j - \sigma_{-1,-1}^j) \right]. \tag{C.6}$$

We note that this Hamiltonian is obtained in the rotating frame under the secular approximation. The Hamiltonian H_2 conserves the total population in any of the three spin states, $\mathcal{P}_a = \sum_i \sigma_{aa}^i$ with $a \in \{0, \pm 1\}$. If each microwave pulse realizes a π pulse ($\theta = \pi$), their combination results in a cyclic transition $R_3^\pi : |m_s = +1\rangle \mapsto -|m_s = -1\rangle \mapsto i\,|m_s = 0\rangle \mapsto |m_s = +1\rangle$, and the population $\mathcal{P}_a$ becomes periodic over three periods. Under such evolution, the effective Hamiltonian over three periods is given by $D_3^\pi = \left[H_2 + (R_3^\pi)^{-1} H_2 R_3^\pi + (R_3^\pi)^{-2} H_2 (R_3^\pi)^2\right]/3$, in which on-site disorders average to zero, and the interactions are modified to

$$D_3^\pi = \sum_{ij} \frac{J_{ij}}{r_{ij}^3} \left[\sum_a \sigma_{aa}^i \sigma_{aa}^j - \frac{1}{3} \sum_{a \neq b} \sigma_{ab}^i \sigma_{ba}^j \right]. \tag{C.7}$$

The first term describes Ising-like interactions that shift energy when any pair of spins are in the same state, and the second term corresponds to spin-exchange interactions that allow polarization transport. These additional exchange interactions may lead to a shorter lifetime of the DTC order as compared to that of the $\nu = 1/2$ DTC order. For small perturbations in the microwave pulse angle $\epsilon = \theta - \pi$, the effective dynamics, to leading order, are governed by

$$D_3^{\pi+\epsilon} \approx D_3^\pi + \frac{\epsilon}{3\tau} \sum_j \left(\sigma_{+1,0}^j + \sigma_{-1,0}^j + i\sigma_{+1,-1}^j + h.c. \right), \tag{C.8}$$

which explicitly breaks the conservation laws for $\mathcal{P}_a$.

C.2 Drive-assisted thermalization

In this section, we present the details on the technical procedure used to rotate the depolarization inducing Hamiltonian

$$H(t) = \sum_{ij} \frac{J_{ij}}{r_{ij}^3} S_i^x S_j^x + \epsilon \sum_i S_i^y \sum_n \delta(t - n^- \tau_1), \tag{C.9}$$

into an effective Hamiltonian $H'(t)$.

As mentioned in the main text, because of the disorder in the interactions, single spin-flip processes, effected by the action of a single operator S_i^y (i.e. the off-diagonal $O(\epsilon)$ term in Eq. (C.9)), are typically not resonant and do not induce significant depolarization. One has to consider other channels for depolarization which are of higher order in ϵ, such as two, three, spin-flip processes, and inquire if they are resonant processes – if so, then the dominant channel of decay is the one that governs the asymptotic behavior of depolarization dynamics.

The purpose of the transformation we employ is thus to extract the terms that give rise to dominant depolarization processes: we will rotate the original Hamiltonian in such a way that off-diagonal terms that generate non-resonant processes are 'integrated out', giving a resulting effective Hamiltonian $H'(t)$ whose leading order off-diagonal terms generate resonant proceses. In our system, it will turn out that the dominant decay channel is given by two spin-flip processes.

To that end, let us perform this transformation in detail. We write the unitary time evolution operator $U(t) = \mathcal{T} e^{-i \int_0^t H(t') dt'}$, generated by Eq. (C.9), as

$$U(t) = Q(t) \tilde{U}(t) Q^\dagger(0), \tag{C.10}$$

where we have yet to define the unitary $Q(t)$. With this decomposition, $\tilde{U}(t)$ is given by

$$\tilde{U}(t) = \mathcal{T}e^{-i\int_0^t H'(t)dt}, \tag{C.11}$$

i.e. it is generated by a rotated time-dependent Hamiltonian (via the Schrodinger equation):

$$H'(t) = Q(t)^\dagger \left(H_0 + \epsilon V \sum_n \delta(t - n^- \tau_1) - i\partial_t \right) Q(t), \tag{C.12}$$

where

$$H_0 = \sum_{ij} \frac{J_{ij}}{r_{ij}^3} S_i^x S_j^x, \tag{C.13}$$

$$V = \sum_i S_i^y. \tag{C.14}$$

Here $J_{ij} = J_0 q_{ij}$ where $q_{ij} = -(1 - 3(\hat{z} \cdot \hat{r}_{ij})^2)$ encodes the angular dependence of the interactions between spins (i, j), as in Ref. [35].

We will pick $Q(t)$ to be time-periodic; then because $Q(n\tau_1) = Q(0)$, the expected value of observables as a function of time, such as the polarization (of one site) $S_i^x(n\tau_1)$, is given by

$$\begin{aligned}
&\langle\psi|S_i^x(n\tau_1)|\psi\rangle = \langle\psi|U^\dagger(n\tau_1)S_i^x U(n\tau_1)|\psi\rangle \\
&\quad = \langle\tilde{\psi}|\tilde{U}^\dagger(n\tau_1)\tilde{S}_i^x \tilde{U}(n\tau_1)|\tilde{\psi}\rangle, \\
&|\tilde{\psi}\rangle = Q^\dagger(0)|\psi\rangle \\
&\tilde{S}_i^x = Q^\dagger(0) S_i^x Q(0),
\end{aligned} \tag{C.15}$$

where $|\psi\rangle$ is the initial state which we take to be polarized in the x-direction. In other words, $Q(0)$ is just some static rotation that rotates both the state and observable.

If in addition $Q(0)$ is a 'small' rotation (as we will choose, and to be made precise below), then both the state and observable are close to the unrotated ones,$|\tilde{\psi}\rangle \approx |\psi\rangle$ and

$\tilde{S}_i^x \approx S_i^x$, and one can conclude that

$$\langle\psi|S_i^x(n\tau_1)|\psi\rangle \approx \langle\psi|\tilde{U}^\dagger(n\tau_1)S_i^x\tilde{U}(n\tau_1)|\psi\rangle. \tag{C.16}$$

That is, the time dependence (and consequently, depolarization) is completely captured in $\tilde{U}(t)$ and hence, $H'(t)$, the rotated effective Hamiltonian.

Now let us construct $Q(t)$, which we write as $Q(t) = e^{\epsilon\Omega(t)}$, where ϵ is explicitly the small parameter and $\Omega(t)$ a periodic anti-Hermitian operator. Expanding Eq. (C.12) we get

$$\begin{aligned} H'(t) = H_0 &+ \epsilon\left(V\sum_n \delta(t-n^-\tau_1) - [\Omega, H_0] - i\partial_t\Omega\right) \\ &+ \epsilon^2\left(\frac{1}{2}[\Omega,[\Omega,H_0]] - [\Omega,V]\sum_n \delta(t-n^-\tau_1) + \frac{i}{2}[\Omega,\partial_t\Omega]\right) + \cdots . \end{aligned}$$

Utilizing a procedure similar to Ref. [96], we equate the order ϵ piece to 0 with the constraint that $\Omega(t)$ is time-periodic. Note that this transformation is distinct from the transformations employed in Refs. [97, 98] to generate effective Hamiltonians in high-frequency driven systems. There, the small parameter was the inverse of the driving frequency ω, but here, in anticipation that we will take into account the disorder in the interactions, the small parameter is served by ϵ, the strength of the off-diagonal perturbation to H_0. Decomposing $\Omega(t)$ in terms of its Fourier modes $\Omega(t) = \sum_n \Omega^{(n)}e^{in\omega_0 t}$, where $\omega_0 = 2\pi/\tau_1$, and using the fact the Fourier transform of the Dirac comb $\sum_n \delta(t-n^-\tau_1)$ is $\frac{1}{\tau_1}\sum_n e^{-in\omega_0 t}$, the equation that the n-th Fourier mode has to obey is

$$\frac{V}{\tau_1} - [\Omega^{(n)}, H_0] + \omega_0 n\Omega^{(n)} = 0. \tag{C.17}$$

In the basis of the eigenstates $|s\rangle$ of H_0 which are product states in the x-direction, we can therefore write the solution as

$$\langle s'|\Omega^{(n)}|s\rangle = \frac{\langle s'|V|s\rangle}{(E_s - E_{s'} - n\omega_0)\tau_1}. \tag{C.18}$$

Note that since $V = \sum_i S_i^y$, the eigenstates s and s' representing spin configurations in the matrix element of $\Omega^{(n)}$ can only differ by one spin-flip. If $|s\rangle$ and $|s'\rangle$ differ at the Ith spin,

$$E_s - E_{s'} = 2 \sum_{j \neq I} \frac{J_{jI}}{r_{jI}^3} S_j^x(s) S_I^x(s), \tag{C.19}$$

where $S_j^x(s)$ represents the S^x component of the jth spin for the configuration $|s\rangle$, which for the starting state is just $+\frac{1}{2}$.

Because of the disorder in J_{ij}/r_{ij}^3 (accorded for by the random positions and relative angles between the spins), resonances (i.e. terms where the denominator ≈ 0) are controlled, provided

$$\frac{\epsilon}{\tau_1} \ll \min_{m \in \mathbb{Z}} \left| \left(2 \sum_{i \neq J} \frac{J_{iJ}}{r_{iJ}^3} S_i^x(s) S_J^x(s) - m\omega_0 \right) \right|. \tag{C.20}$$

This gives us a condition that our perturbative procedure should work only for

$$\epsilon < \min(W, \omega_0)\tau_1, \tag{C.21}$$

where W^2 is the variance of the interactions,

$$W^2 = \left\langle 4 \left(\sum_{i \neq J} \frac{J_{iJ}}{r_{iJ}^3} S_i^x(s) S_J^x(s) \right)^2 \right\rangle. \tag{C.22}$$

The angular brackets represent averaging over different spins i, and we have used the fact that the mean is 0. In that case, the corresponding fraction of spins that are resonant is then small, and goes as $\sim \frac{\epsilon}{\min(W,\omega)\tau_1}$.

The rotated Hamiltonian (C.17) then becomes

$$H'(t) = H_0 - \frac{\epsilon^2}{2} [\Omega(t), V] \sum_n \delta(t - n^- \tau_1) + \cdots . \tag{C.23}$$

Let us concentrate on the second term and look at its matrix elements. This is

$$-\frac{\epsilon^2}{2\tau_1} \langle s'| \sum_{n,m} [\Omega^{(m)}, V] |s\rangle e^{i\omega_0 (m+n)t}. \tag{C.24}$$

Now $\Omega^{(m)}$ and V are sums of terms which each individually flip a single spin, so $|s\rangle$ and $|s'\rangle$ can differ by either only zero spin flips (i.e. $|s'\rangle = |s\rangle$) or two spin flips ($|s'\rangle = |s_{IJ}\rangle$) where s_{IJ} stands for the spin configuration s with the I-th and J-th spins flipped. The diagonal process (zero spin flips) leads to a renormalization of the energy of H_0, while the off-diagonal process where V flips spin I and $\Omega^{(m)}$ flips spin J results in the matrix element

$$\begin{aligned} &-\frac{\epsilon^2}{2\tau_1}\sum_{m,n}\langle s_{IJ}|\Omega_J^{(m)}V_I - V_I\Omega_J^{(m)}|s\rangle e^{i\omega_0(m+n)t} \\ =&-\frac{\epsilon^2}{2\tau_1}\sum_{m,k} e^{i\omega_0 kt}\left(\langle s_{IJ}|\Omega_J^{(m)}|s_I\rangle - \langle s_J|\Omega_J^{(m)}|s\rangle\right). \end{aligned} \tag{C.25}$$

The term in the parenthesis is

$$\begin{aligned} &-\frac{1}{(E_{s_I}-E_{s_{IJ}}-m\omega_0)\tau_1}+\frac{1}{(E_s-E_{s_J}-m\omega_0)\tau_1} \\ =&-\frac{1}{(2\sum_{i\neq I,J}\frac{J_{iJ}}{r_{iJ}^3}S_i^x(s)S_J^x(s)-2\frac{J_{IJ}}{r_{IJ}^3}S_I^x(s)S_J^x(s)-m\omega_0)\tau_1} \\ &+\frac{1}{(2\sum_{i\neq J}\frac{J_{iJ}}{r_{iJ}^3}S_i^x(s)S_J^x(s)-m\omega_0)\tau_1} \\ \approx&-\frac{4\frac{J_{IJ}}{r_{IJ}^3}S_I^x(s)S_J^x(s)}{\tau_1\left(2\sum_{i\neq J}\frac{J_{iJ}}{r_{iJ}^3}S_i^x(s)S_J^x(s)-m\omega_0\right)^2}, \end{aligned} \tag{C.26}$$

where $\omega_0 = 2\pi/\tau_1$.

Using this, we can thus write the rotated Hamiltonian (C.23) in operator form:

$$\begin{aligned} H'(t) \approx H_0 + \sum_{IJ}\frac{A_{IJ}J_{IJ}}{r_{IJ}^3}(S_I^+S_J^+ + h.c.)\sum_n \delta(t-n^-\tau_1) \\ + O(\epsilon^3), \end{aligned} \tag{C.27}$$

where $S_I^+ \equiv S_I^y + iS_I^z$ is the spin raising operator in the S_I^x basis for spin I, A_{IJ} is the coefficient of the interactions between two spins (I, J), given by

$$A_{IJ} = \left(\frac{\epsilon^2}{\tau_1^2}\right) \sum_m \frac{-2S_I^x(s)S_J^x(s)}{\left(2\sum_{i\neq J}\frac{J_{iJ}}{r_{iJ}^3}S_i^x(s)S_J^x(s) - m\omega_0\right)^2} + (I \leftrightarrow J). \tag{C.28}$$

This effective Hamiltonian gives Eqs. (5, 13) and (14) in the main text. Note that technically speaking, Eqs. (C.26) when written in operator form would also give flip-flop terms $S_I^+ S_J^- + h.c.$. However, because we are ultimately interested in the dynamics of depolarization beginning from an initial polarized state in the $\hat{x}$ direction, and moreover such flip-flop terms are polarization conserving, they do not contribute to depolarization and so we drop them in the effective Hamiltonan.

Depending on the two limits of high or low frequencies ($\omega_0 \gg W$ or $\omega_0 \ll W$ respectively), A_{IJ} has qualitatively different behaviors. Its scaling behavior with respect to ϵ and τ_1 can be extracted in those limits, which is Eq. (6) in the main text. Thus, this gives rise to different behaviors for the depolarization rate in the two limiting cases, and can ultimately be used to determine the phase boundary of the critical time crystal, as was done in the main text.

C.3 Numerical extraction of phase boundary

In this section, we describe the numerical procedure used to 1) determine the decay rate Γ as a function of the perturbation ϵ, and 2) obtain the phase diagram of the critical DTC shown in the main text. Assuming that the initial state is polarized in the x-direction, we first generated the probability distribution $P(h_I)$ of h_I, which is the mean-field potential field felt by spin I, i.e. $h_I = \frac{1}{2}\sum_{j\neq I}\frac{J_{Ij}}{r_{Ij}^3}$. Here $J_{ij} = J_0 q_{ij}$ and $q_{ij} = -(1-3(\hat{z}\cdot\hat{r}_{ij})^2)$ encodes the angular dependence of two spins (i,j). We modeled this by uniformly distributing $N = 2000$ spins in a 3-torus of linear dimension $L = 60$ nm, with a minimum (UV) distance cut-off $r_{\mathrm{UV}} = 3$ nm, and caculating for each spin h_i. Such a choice of parameters gives a particle density of $n_0 = 9.26\times 10^{-3}$ nm^{-3}. Using $J_0 = 2\pi\times 52$ MHz nm^{-3} as in the experiments, we can characterize this distribution by its variance W^2, which gives $W = 4.49$ MHz.

From this distribution, we then drew two values (h_I, h_J), provided that they are each not resonant. That is, we discarded values if

$$\frac{\epsilon/\tau_1}{|h_{I/J} - m\omega_0|} > \alpha_1 \text{ for all } m\in\mathbb{Z}, \tag{C.29}$$

where α_1 is some fixed $O(1)$ number. We determined this number from the condition that along the line $W\tau_1 = |\epsilon|$ where our perturbative analysis holds, at least 80% of the spins are not resonant. In the region where $W\tau_1 > \epsilon$, this implies that $> 80\%$ of the spins are off-resonant. In our simulation, $\alpha_1 = 3.7$. Then, (h_I, h_J) represent the mean-field potentials felt by spins I and J respectively.

Next, we estimated the probability that the two spins (I, J) a distance r apart form a resonant pair. In principle this is obtained by comparing the effective hopping $J_{\mathrm{eff}}(r) \equiv A_{IJ}J_{IJ}/r^3$, against the minimum quasi-energy gap Δ. Here

$$A_{IJ}J_{IJ} \sim -\left(\frac{\epsilon^2}{\tau_1^2}\right) J_0\overline{q_{IJ}}\sum_m\left(\frac{1}{(h_I - m\omega_0)^2} + \frac{1}{(h_J - m\omega_0)^2}\right) \tag{C.30}$$

and $\Delta \approx \min_m |h_I + h_J - m\omega_0|$. The bar over the angular dependence q_{ij} represents the typical angular dependence; this can be derived analytically and gives $\overline{q_{ij}} = 2/\sqrt{5}$. In other words, for a fixed r, if

$$\frac{J_{\text{eff}}(r)}{\Delta} > \alpha_2, \tag{C.31}$$

where α_2 is another order one number, then this spin pair is resonant. We take $\alpha_2 = 3.4$.

In practice, we make a simplifying assumption that for large enough r, which we call d, the probability of finding two spins a distance r apart which are resonant is small and is simply proportional to $J_{\text{eff}}(r)/\alpha_2\Delta \propto 1/r^3$ (we have numerically checked this assumption holds).

Then, one can simplify the counting of resonant pairs by just estimating the the probability $\mathcal{P}$ of finding two spins some fixed distance d apart. We generate 4000 pairs (I, J), and count the number of pairs that satisfy Eq. (C.31) for $r = d$; the fraction of such pairs is $\mathcal{P}$. To get the probability of resonant pairs at distances $R > d$, we can then just multiply $\mathcal{P}$ by the factor $(d/r)^3$. In the simulations, we obtain d as the distance for which the last step of Eq. C.26 is justified, that is, if $W \sim J_0\overline{q_{ij}}/d^3$, which gives $d = 4.02$ nm for the parameters we have used.

Having determined $\mathcal{P}$, we extracted the decay rate $\Gamma(\epsilon, \tau_1)$. The survival of polarization probability is given by a power law $P(t) = (t/t_0)^{-q}$ where $q \propto \mathcal{P}$. This can be derived as the product of probabilities of having no resonant spins at each distance $[r, r + dr]$ up to $R(t) = (J_0 t)^{1/3}$ [35]:

$$P(t) = \prod_{r=r_{\text{UV}}}^{R(t)} \left(1 - 4\pi n_0 r^2 dr \frac{\overline{A_{IJ}J_{IJ}}}{d^3\alpha_2\Delta}\frac{d^3}{r^3}\right) = (t/t_0)^{-q}, \tag{C.32}$$

where

$$\begin{aligned} q &= \frac{4\pi n_0 d^3}{3}\left(\frac{\overline{A_{IJ}J_{IJ}}}{\alpha_2\Delta d^3}\right), \\ t_0 &= \frac{r_{\text{UV}}^3}{J_0}. \end{aligned} \tag{C.33}$$

The factor in the parenthesis $\left(\frac{\overline{A_{IJ}J_{IJ}}}{\alpha_2 \Delta d^3}\right)$ is the probability $\mathcal{P}$, and hence we see $q \propto \mathcal{P}$.

The dimensionless decay rate per Floquet cycle Γ can then be obtained from $\Gamma(\epsilon, \tau_1) = 1/n^*(\epsilon, \tau_1)$ where $n^*(\epsilon, \tau_1)$ is the number of Floquet cycles such that $P(t)$ drops to some fixed threshold $1/A$. Solving $P(n^*\tau_1) = 1/A$ for n^* yields

$$\Gamma(\epsilon, \tau_1) = \frac{\tau_1}{t_0} e^{-\beta/\mathcal{P}}, \tag{C.34}$$

where

$$\beta = \frac{3\log(A)}{4\pi n_0 d^3}. \tag{C.35}$$

We take $A = 10$; physically this corresponds to the situation where the polarization drops to 10% of its starting value.

Lastly, to get the phase diagram, we estimated the phase boundary of the time crystal as the contour in the ϵ-τ_1 plane satisfying $\Gamma(\epsilon, \tau_1) = \Gamma_* = 1/100$. In other words, the phase boundary demarcates the regions in ϵ-τ_1 parameter space having significant decay after 100 Floquet cycles or not. The choice of 100 Floquet cycles was picked to match the experimental observations. Referring to Fig. 2 in the main text, one sees the linear ($\tau_1 \propto |\epsilon|$) phase boundary for small τ_1, and also the 'closing up' of the phase boundary, $\tau_1 \propto 1/\epsilon^2$, for large τ_1, as predicted by our theory.

Appendix D

Supporting Material of Chapter 5

D.1 Experimental system

Details of our sample and experimental setup have been described previously in Refs. [17, 35, 76]. The nitrogen-vacancy (NV) center in diamond has a spin triplet ground state, labelled as $|m_s = 0, \pm 1\rangle$. We use a diamond sample containing a high concentration of NV centers (about 45 ppm), which results in strong magnetic dipolar interactions with a typical interaction strength of $2\pi \times 420\,\text{kHz}$. Random positional disorder as well as lattice strain and paramagnetic impurities (P1 centers and ^{13}C nuclear spins) give rise to a Gaussian-distributed on-site disorder at the NVs with standard deviation $2\pi \times 4.0\,\text{MHz}$.

The diamond sample contains four subgroups of NV centers, each oriented along one of the four different crystallographic axes of the crystal. For the single group measurements, an external magnetic field is applied along one of the crystallographic axes, allowing us to spectrally isolate and independently address the $|0\rangle \leftrightarrow |+1\rangle$ and $|0\rangle \leftrightarrow |-1\rangle$ transitions of the NV group. By using a resonant microwave with different phases, we can apply $\hat{x}$ and

$\hat{y}$-rotations to each of the transitions of the spins. At the beginning of each experimental sequence, we initialize the spins into the $|0\rangle$ spin state via 532 nm laser illumination. For high NV density samples, higher laser powers ($> 100\ \mu$W) induce a charge instability of negatively charged NVs, leading to a decrease in spin-polarization contrast [76, 170]. To avoid such charge dynamics, we operate at a power of $50\,\mu$W and use a long repolarization duration of $100\,\mu$s. We then apply the desired Floquet pulse sequence. At the end of each experimental sequence, we measure the population difference between the $|-1\rangle$ and $|0\rangle$ states. We also insert a wait time ($\sim$100 μs) between consecutive sequences to allow the charge states to equilibrate and reduce microwave heating effects.

For the two-group measurements, we bring two groups of NV centers into resonance by aligning the magnetic field along the bisecting line of the NV axes, in the (1,1,0)-direction relative to the host diamond lattice (the two NV groups are chosen to be in the (1,1,1) and (1,1,-1) directions). These two NV groups will thus have identical transition frequencies (to within $2\pi \times 2$ MHz) and can interact via Ising and spin-exchange interactions, while remaining spectrally isolated from the other NV groups. In addition, the two NV groups are chosen to have similar projections of the microwave driving field, experiencing the same spin rotation for a fixed duration of the microwave pulse. The difference in the rotation angle between the two groups is estimated to be less than 2%.

D.2 Interaction-limited coherence

To test whether the decoherence of the dense ensemble is dominated by dipolar interactions among NV centers, we employ an XY8-N dynamical decoupling sequence, with N being the number of repetitions of the XY8 block [171]. Dynamical decoupling sequences such as XY8-N and CPMG have been utilized for various spin systems to investigate the effect of an external spin bath [46]. Typically, as N increases, the coherence time of spins is significantly extended due to more effective decoupling from the spin bath, approaching the longitudinal depolarization time T_1 [46]. However, interactions between like spins are not decoupled by these sequences, and hence if the coherence time is limited by their mutual interactions, then we shall not see a significant extension of coherence time.

As shown in Fig. D.1, we measure a decoherence rate $1/T_2$ of 0.7 MHz, independent of the number of repetitions N. To reduce finite pulse-width effects in the rotation pulses, we used a short π pulse (6 ns). Furthermore, when doubling the spin-spin interaction strength by using two resonant NV groups, we observe a two-fold-enhanced decoherence rate of 1.5 MHz. The observed linear dependence of the decoherence rate on the NV density has also been identified using a spin-echo sequence [17]. In addition, the correlation time of the external spin bath in our sample was estimated to be $\tau_d \sim 40\ \mu s$ [17], which corresponds to the timescale at which extrinsic noise from the environment can be regarded as Markovian. Indeed, τ_d is significantly longer than the decoherence times $T_2 \sim 1\ \mu s$ measured in the dynamical decoupling sequences. This, together with the long correlation time of the bath, strongly suggests that the coherence time is limited by coherent NV-NV interactions.

D.3 Implementing the Floquet Hamiltonians

While for the $\mathbb{Z}_2$-Ising and $\mathbb{Z}_2$ cases, we only address the transition between the $|0\rangle$ and $|-1\rangle$ spin states at resonance frequency ω_1, in the $\mathbb{Z}_3$ case, the spin transition between $|0\rangle$ and $|+1\rangle$ at resonance frequency ω_2 is also addressed (see Fig. 1(b) in the main text). In the $\mathbb{Z}_2$-Ising case, we continuously drive the spins during an interaction period τ_1 (spin-

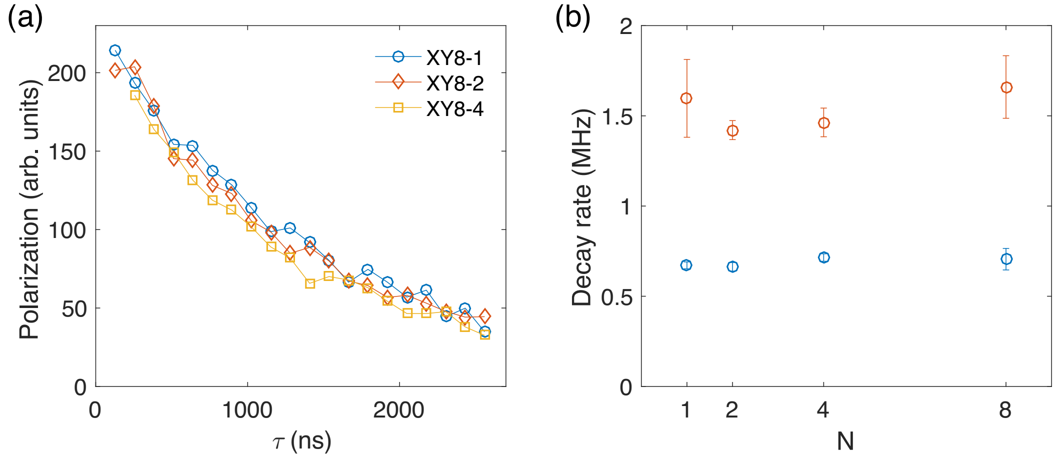

Figure D.1: **NV ensemble coherence measured using the XY8-N dynamical decoupling sequence.** (a) Time traces and (b) decay rates of the NV ensemble coherence probed using the XY8-N sequence. In (b), decay rates are extracted from a simple exponential fit to (a). Blue and red data points in (b) correspond to the single- and two-group measurements, respectively.

locking) to engineer the spin-spin interaction Hamiltonian. For pulsed rotations, we choose a Rabi frequency of $2\pi \times 50$ MHz, corresponding to a π pulse of 10 ns. Perturbations in the global spin rotation are implemented by varying the Rabi frequencies while keeping the pulse duration fixed to τ_2 =10 ns for each pulsed rotation. In the following, we provide detailed explanations for each Floquet Hamiltonian.

D.3.1 $\mathbb{Z}_2$-Ising DTC order

The $\mathbb{Z}_2$-Ising DTC order, exhibiting period-doubled oscillations when the system only has Ising interactions, has already been demonstrated in both ion traps [68] and NV ensembles [35]. Due to the large frequency difference between the $|0\rangle \leftrightarrow |-1\rangle$ and $|0\rangle \leftrightarrow |+1\rangle$ transitions in the presence of an external magnetic field, the NV center can be thought of as an effective spin-1/2 system when only one transition is resonantly driven. In our experiments, we use the following pulse sequence to realize $\mathbb{Z}_2$-Ising DTC order. Prior to the Floquet driving, we apply a $\pi/2$ pulse along the $-\hat{y}$ axis to initialize all spins into $|{+X}\rangle \equiv (|0\rangle + |{-1}\rangle)/\sqrt{2}$. The Floquet period T consists of an interaction duration lasting τ_1 and a global spin rotation of length τ_2. During τ_1, we suppress spin-exchange interactions by continuously driving the spins with a Rabi frequency of $2\pi \times 41.7$ MHz along the $\hat{x}$ axis. Afterwards, we perform a global spin rotation by an angle $\theta = \pi + \epsilon$ around the $\hat{y}$ axis. After n repetitions of the Floquet period, a $\pi/2$ pulse along the $\hat{y}$ axis is applied to read out the spin polarization along the $\hat{x}$ axis. In the rotating frame, the effective Hamiltonian for the $\mathbb{Z}_2$-Ising case can be described as

$$H(t) = \sum_i (\Omega_x(t) S_i^x + \Omega_y(t) S_i^y + \Delta_i S_i^z) + \sum_{ij} \frac{J_{ij}}{r_{ij}^3} S_i^x S_j^x \tag{D.1}$$

where $\Omega_x(t)$ and $\Omega_y(t)$ are the Rabi frequencies for spin-locking and rotation pulses, and are turned on only during the interaction and rotation parts in each period, respectively. Here, J_{ij} is the orientation-dependent interaction strength and r_{ij} is the distance between the NV centers at site i and j, respectively, Δ_i is the on-site disorder field at site i, and $\vec{S} = \{S^x, S^y, S^z\}$ are the spin-1/2 operators. It has been shown that the long-time evolution of a fast periodically-driven system is governed by an average Hamiltonian for times exponentially long in the driving frequency [98, 172]. Applying average Hamiltonian theory in the toggling frame (Eq. (2) in the main text) to Eq. (D.1) transforms it into

$$D^{\mathbb{Z}_2,\text{Ising}} \simeq \sum_i \frac{J_{ij}}{r_{ij}^3} S_i^x S_j^x + \frac{\epsilon}{T} \sum_i S_i^y. \tag{D.2}$$

We note that the average Hamiltonian for the $\mathbb{Z}_2$-Ising case is equivalent to a long-range transverse-field Ising model. Here, $\epsilon = \theta - \pi$ is the perturbation due to imperfect rotations away from π. Intuitively, the Ising interaction in Eq. (D.2) gives rise to a long-range spatiotemporal correlation of spins along the $\hat{x}$ axis when the total mean-field interaction strength $J_{\mathrm{MF}} = \langle \sum_i J_{ij}/r_{ij}^3 \rangle$ dominates over the perturbation ϵ/T. $\langle \cdots \rangle$ denotes averaging over different positional configurations of disordered spins.

D.3.2 $\mathbb{Z}_2$ DTC order

We are also interested in probing period-doubled oscillations in the presence of spin-exchange interactions, which we here denote as $\mathbb{Z}_2$ DTC order to distinguish from the preceding case with Ising terms only. If we work along the $\hat{z}$ axis in the bare basis, without any microwave driving during the interaction period τ_1, both spin-exchange and Ising interactions will be present in the effective Hamiltonian. In the experiment, we first initialize the spins into the $|0\rangle$ spin state. During τ_1, spins evolve under the bare dipolar Hamiltonian, which includes both Ising and spin-exchange interactions. After τ_1, the spins are all rotated by an angle $\theta = \pi + \epsilon$ around the $\hat{y}$ axis in the subspace spanned by $|0\rangle$ and $|-1\rangle$. After n repetitions of the Floquet period, we read out the spin polarization along the $\hat{z}$ axis. Treating the NV center as an effective spin-1/2 system, the effective Hamiltonian for the $\mathbb{Z}_2$ DTC order (in the rotating frame) can be expressed as follows:

$$H(t) = \sum_i \Omega_y(t) S_i^y + \Delta_i S_i^z + \sum_{ij} \frac{J_{ij}}{r_{ij}^3} \left(S_i^x S_j^x + S_i^y S_j^y - S_i^z S_j^z \right), \tag{D.3}$$

where $S_i^x S_j^x + S_i^y S_j^y = \frac{1}{2}(S_i^+ S_j^- + S_i^- S_j^+)$ is the spin-exchange interaction term that leads to flip-flop processes between the spins at sites i and j. Here, $S^{\pm} = S^x \pm i S^y$. To capture the long-time behavior of the $\mathbb{Z}_2$ DTC order, we apply average Hamiltonian theory to Eq. (D.3), which yields

$$D^{\mathbb{Z}_2} \simeq \sum_i \frac{J_{ij}}{r_{ij}^3} \left(S_i^x S_j^x + S_i^y S_j^y - S_i^z S_j^z \right) + \frac{\epsilon}{T} \sum_i S_i^y. \tag{D.4}$$

Compared to the transverse-field Ising model described above, Eq. (D.4) additionally contains spin-exchange interactions. Interestingly, the mean-field analysis detailed in the section, *Mean-Field Description for Short Interaction Time Regime*, reveals that in the fast Floquet driving limit, i.e., $2\pi/T \gg J_{ij}/r_{ij}^3$, the DTC phase becomes more robust against perturbations due to the presence of the spin-exchange interaction. As depicted in Fig. 2(d) of the main text, we attribute this behavior to the creation of an additional mean-field by the spin-exchange interactions, which counteracts and reduces the perturbation strength ϵ.

D.3.3 $\mathbb{Z}_3$ DTC order

To observe $\mathbb{Z}_3$ DTC order, in which the system exhibits period-tripled oscillations, we work in the bare basis while utilizing all three spin states $|m_s = 0, \pm 1\rangle$. We start with all spins polarized into the $|0\rangle$ state and evolve under the bare spin-1 dipolar Hamiltonian for a duration τ_1. Subsequently, we apply two resonant microwave pulses, first on the transition $|0\rangle \leftrightarrow |-1\rangle$ and then on the transition $|0\rangle \leftrightarrow |+1\rangle$. The two consecutive rotation pulses are separated by 1 ns to avoid microwave interference. The combination of these operations defines a Floquet cycle with period T. After n repetitions of the Floquet period, we measure the population difference between the $|0\rangle$ and $|-1\rangle$ spin states. When each of the applied pulses corresponds to a perfect π-pulse, this sequence realizes a cyclic transition with $\mathbb{Z}_3$ symmetry. However, this discrete symmetry is explicitly broken by imperfect rotations whose angle deviates from $\theta = \pi$. Considering the full spin-1 nature of the NV centers, we describe the effective Hamiltonian for the $\mathbb{Z}_3$ DTC order as

$$H(t) = \sum_i \Omega^-(t)(\sigma_i^{-1,0} + \sigma_i^{0,-1}) + \Omega^+(t)(\sigma_i^{+1,0} + \sigma_i^{0,+1}) + \Delta_i^- \sigma_i^{-1,-1} + \Delta_i^+ \sigma_i^{+1,+1} \tag{D.5}$$

$$+ \sum_{ij} \frac{J_{ij}}{r_{ij}^3} \left[-\frac{\sigma_i^{+1,0}\sigma_j^{0,+1} + \sigma_i^{-1,0}\sigma_j^{0,-1} + h.c.}{2} + (\sigma_i^{+1,+1} - \sigma_i^{-1,-1})(\sigma_j^{+1,+1} - \sigma_j^{-1,-1}) \right], \tag{D.6}$$

where $\Omega^-(t)$ and $\Omega^+(t)$ are the Rabi frequencies for the rotation pulses acting on the lower $|0\rangle \leftrightarrow |-1\rangle$ and upper $|0\rangle \leftrightarrow |+1\rangle$ transitions, respectively, and are turned on separately only during the rotation period τ_2. Here, $\sigma_i^{ab} = |a\rangle_i \langle b|$, and Δ_i^- and Δ_i^+ are the on-site disorders for the lower and upper transitions of the spin at site i. In our experiment, we choose a common Rabi frequency $|\Omega^-| = |\Omega^+|$ and tune its amplitude to control the spin rotation angle θ. For fast Floquet driving, the evolution is governed by the following average Hamiltonian (in the toggling frame):

$$D^{\mathbb{Z}_3} \simeq \sum_{ij} \frac{J_{ij}}{r_{ij}^3} \sum_{ab} \left(\delta_{ab} - \frac{1}{3}\delta_{a\pm1,b} \right) \sigma_i^{ab}\sigma_j^{ba} + \frac{\epsilon}{3T} \sum_i \left(\sigma_i^{+1,0} + \sigma_i^{-1,0} + i\sigma_i^{+1,-1} + h.c. \right), \tag{D.7}$$

where, in the first term, $\sum_{ab} \delta_{ab}(\sigma_i^{ab}\sigma_j^{ba})$ and $\sum_{ab} \delta_{a\pm1,b}(\sigma_i^{ab}\sigma_j^{ba})$ represent the Ising and spin-exchange interactions, respectively. Similar to the $\mathbb{Z}_2$ DTC order, the presence of flip-flop processes in the $\mathbb{Z}_3$ DTC sequence also leads to a reduction in the effective perturbation strength, making the $\nu = 1/3$ DTC order more robust. Further details are provided in the section, *Mean-Field Description for Short Interaction Time Regime*.

D.3.4 Two-group $\mathbb{Z}_3$ DTC order

By tuning the orientation of an externally applied magnetic field, we spectrally overlap two NV groups to within $(2\pi) \times 2$ MHz. For the implementation of the Floquet Hamiltonian, we follow the same protocol used for the single-group $\mathbb{Z}_3$ DTC order. However, it is noteworthy that the interaction Hamiltonian for the two-group $\mathbb{Z}_3$ DTC order is not perfectly identical to Eq. (D.6) owing to different crystallographic axes of the two NV groups. Depending on the spatial orientation of the two spins belonging to different groups, the relative strength as well as sign between the Ising and spin-exchange interactions can be different; on average however, the relative sign between Ising and spin-exchange terms is still negative. Despite such differences, the two-group $\mathbb{Z}_3$ DTC order also shows universal thermalizing dynamics in the long interaction time regime, consistent with the single-group DTC measurements (see the section below, *Universality in Long Interaction Time Regime*).

D.4 Phase boundary extraction

To experimentally extract the DTC phase boundary, we follow the method developed in our previous manuscript, Ref. [35]. In short, we quantify the DTC order by using the crystalline fraction, defined as $f = |S(\nu = 1/2)|^2 / \sum_\nu |S(\nu)|^2$ and $f = 2|S(\nu = 1/3)|^2 / \sum_\nu |S(\nu)|^2$ for the $\mathbb{Z}_2$ and $\mathbb{Z}_3$ DTC order, respectively. Here, $|S(\nu)|^2$ is the spectral power obtained from the Fourier transform of spin polarization $P(nT)$ measured at an integer number of Floquet periods T,

$$|S(\nu)|^2 = \left| \sum_{n=n_i}^{n_f} P(nT) e^{-i2\pi\nu(n-n_i)/(n_f-n_i+1)} \right|^2, \tag{D.8}$$

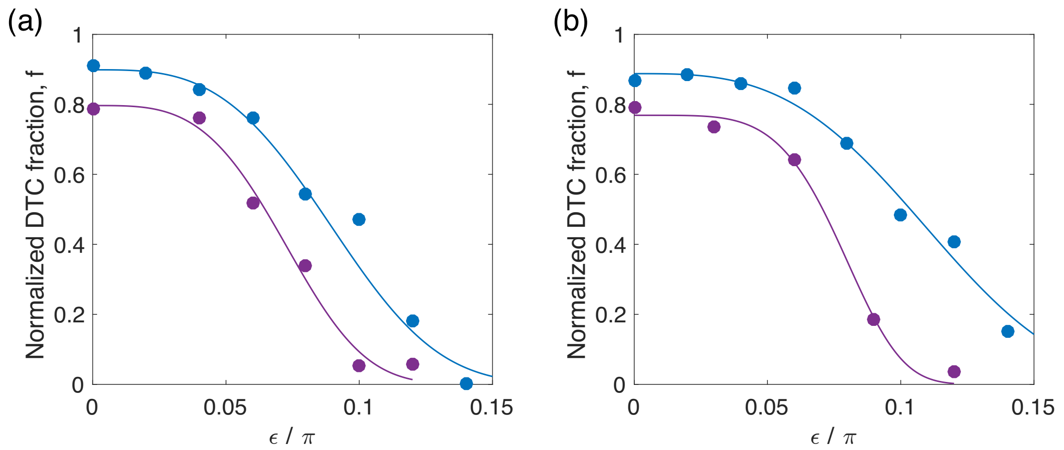

Figure D.2: **Late-time crystalline fraction analysis.** (a) $\mathbb{Z}_2$ case with T = 200 ns (blue) and T = 1900 ns (purple). (b) $\mathbb{Z}_3$ case with T = 130 ns (blue) and T = 800 ns (purple). In (a,b), solid lines represent the super-Gaussian fits.

where only the late-time ($n \geq n_i = 40$) polarization is included to suppress the effects of initial transients resulting from a short-time, non-universal dephasing (see main text). For typical measurements, we set n_f to 80. For the $\mathbb{Z}_3$ case, the factor of 2 in f takes into account the mirror symmetry of the Fourier-transform spectra with respect to $\nu = 1/2$. At each Floquet period T, we examine f as a function of ϵ.

Fig. D.2 shows representative data together with a phenomenological super-Gaussian fit function

$$f_T(\epsilon) = f_T^{\max} \exp\left[-\frac{1}{2}\left(\frac{|\epsilon-\epsilon_0|}{\sigma}\right)^p\right], \tag{D.9}$$

where ϵ_0, σ, p are the central position, characteristic width, and power of the super-Gaussian fit, and $f_T^{\max}$ is the maximum value of the crystalline fraction for a given Floquet period T. As p increases, the functional profile becomes flat when $|\epsilon-\epsilon_0| < \sigma$ and rolls off sharply when $|\epsilon-\epsilon_0| > \sigma$. We identify the phase boundary at a given T as the value of ϵ for which $f_T = 0.1$ (see Fig. 2(a-c) in the main text). Horizontal errorbars on the phase boundary correspond to a 95% confidence interval from the fit.

D.5 Mean-field analysis for short interaction time regime

In this section, we provide a simple description of the dynamics in the short interaction time regime (or equivalently, fast Floquet drive regime), where the Floquet drive energy scale $\omega_0 = (2\pi)/T$ is larger than the on-site disorder strength as well as typical interaction strengths in the system. In such a case, the system cannot effectively absorb or emit energy from/to the drive, and the dynamics can be well-captured by an average Hamiltonian model [135].

In the following, we analyze the system under the framework of mean-field theory to understand the conditions for the emergence of an ordered stationary state, which will aid in understanding the phase boundary at short interaction times. Note that our system is favorable to such mean-field analysis as it has long-range interactions among spins in high dimensionality.

First, we consider the case of $\mathbb{Z}_2$-Ising, where there are only Ising interactions between the spins, arriving at results that are consistent with previous analysis [35]. The average Hamiltonian in two Floquet cycles, with imperfect rotation angle $\pi + \epsilon$, is given by

$$D^{\mathbb{Z}_2,\text{Ising}} \simeq \sum_{ij} \frac{J_{ij}}{r_{ij}^3} S_i^z S_j^z + \frac{\epsilon}{T} \sum_i S_i^y \tag{D.10}$$

$$= \sum_{ij} \frac{J_{ij}}{r_{ij}^3} \sum_{\mu\nu} C_{\mu\nu} S_i^\mu \otimes S_j^\nu + \sum_{i\mu} h_\mu S_i^\mu, \tag{D.11}$$

with $C_{\mu\nu}$ being a diagonal matrix with diagonal elements $(0, 0, 1)$ and $h_\mu = (0, \frac{\epsilon}{T}, 0)$ (we have permuted the basis definition for ease of comparison with the $\mathbb{Z}_2$ case). Here S_i^μ ($\mu \in \{x, y, z\}$) are the spin-1/2 operators acting on the two-level system of interest, and in the final step we have written the expression in a more general form for ease of analysis under other interparticle interactions. Note that the static on-site disorder has been echoed out to leading order in this effective Hamiltonian owing to periodic rotation pulses in the lab frame.

Under the mean-field approximation, we replace two-body interactions with single-body terms by taking the expectation values of one of the spins: $S_i^\mu \otimes S_j^\nu \mapsto S_i^\mu \langle S_j^\nu \rangle$. We then self-consistently evaluate the expectation value $\langle S_j^\nu \rangle$ by plugging in the corresponding values calculated from spin i. Replacing the disordered interaction strength J_{ij}/r_{ij}^3 by a total mean-field interaction strength $J_{\text{MF}} = \langle \sum_i J_{ij}/r_{ij}^3 \rangle$, we obtain the mean-field Hamiltonian

$$H_{\text{MF}} = \sum_\mu \left(J_{\text{MF}} \sum_\nu C_{\mu\nu} \langle S^\nu \rangle + h_\mu \right) S^\mu, \tag{D.12}$$

with $C_{\mu\nu}$ and h_μ given above. With H_{MF}, we seek a stationary solution for the density matrix of a spin $\rho = \frac{I_{2\times 2}}{2} + \sum_\mu \rho_\mu S^\mu$ under the dynamics defined by H_{MF}:

$$\dot{\rho} = i[\rho, H_{\text{MF}}] = 0, \tag{D.13}$$

subject to the self-consistency condition

$$\langle S^\mu \rangle = \text{tr}\,[S^\mu \rho] = \rho_\mu / 2. \tag{D.14}$$

Solving this set of equations yields two solutions, only one of which allows a nonzero expectation value of $\langle S^z \rangle$. This solution imposes $\rho_x = \frac{2(\epsilon/T)}{J_{\text{MF}}}$ and $\rho_y = 0$. Given the restriction

$$\text{tr}\left[\rho^2\right] \leq 1 \tag{D.15}$$

on the density matrix and using the relation $\mathrm{tr}[S^\mu S^\nu] = \delta_{\mu\nu}/2$, we find that $\sum_\mu \rho_\mu^2 \leq 1$. Thus, a stationary self-consistent mean-field solution exists only when $|\epsilon|/T \leq J_{\mathrm{MF}}/2$.

The mean-field approach implies a linear phase boundary at short Floquet periods, with a slope given by the interaction strength of the system with prefactor $1/2$; this is consistent with the procedure employed in previous papers, where the same result was derived by examining the rotations of Floquet eigenstates under self-consistent mean-fields. An intuitive understanding of the derivation presented above is that it allows us to find a self-consistent product-state ansatz, for which the rotation induced by interaction with other spins compensates the imperfect rotations imposed by the Floquet drive. Therefore, the robust DTC response can be understood as the existence of a period-doubled trajectory that is stable against perturbations. As we shall see below, a similar intuition applies to the case with spin-exchange interactions as well.

Now, we consider the case of $\mathbb{Z}_2$ with Ising as well as spin-exchange interactions. The average Hamiltonian in two Floquet cycles, with imperfect rotation angle $\pi + \epsilon$, is given by

$$D^{\mathbb{Z}_2} \simeq \sum_{ij} \frac{J_{ij}}{r_{ij}^3} \left(-S_i^x S_j^x - S_i^y S_j^y + S_i^z S_j^z \right) + \frac{\epsilon}{T} \sum_i S_i^y \tag{D.16}$$

$$= \sum_{ij} \frac{J_{ij}}{r_{ij}^3} \sum_{\mu\nu} C_{\mu\nu} S_i^\mu \otimes S_j^\nu + \sum_{i\mu} h_\mu S_i^\mu, \tag{D.17}$$

where now the coefficient matrices are: $C_{\mu\nu}$ diagonal with elements $(-1, -1, 1)$ and $h_\mu = (0, \frac{\epsilon}{T}, 0)$. Repeating the same procedure using Eq. (D.13) and Eq. (D.14), we find that the solution with nonzero expectation value of $\langle S^z \rangle$ is given by $\rho_x = 0$ and $\rho_y = \frac{(\epsilon/T)}{J_{\mathrm{MF}}}$. Eq. (D.15) gives the normalization condition for a stationary self-consistent mean-field solution as $|\epsilon|/T \leq J_{\mathrm{MF}}$. Thus, we expect the phase boundary at short interaction periods, in the presence of spin-exchange interactions, to remain linear, but with a two-fold increase in slope that results in a phase boundary width twice as wide as the case of Ising interactions.

This result can also be intuitively understood by examining dynamics on the Bloch sphere (see Fig. 2(d) in the main text); in the self-consistent solution above, the spins develop a nonzero expectation value along the positive $\hat{y}$ axis, which in turn generates a mean-field along the negative $\hat{y}$ axis due to the spin-exchange terms in the Hamiltonian. This mean-field along the $\hat{y}$-direction counteracts the applied external perturbation ϵ/T, resulting in a smaller effective perturbation. Therefore, the DTC order becomes more robust and the phase boundary expands to a larger ϵ value compared to the case where there are only Ising interactions.

We note that the additional stabilizing effect arising from the spin-exchange interactions is present when the initial state is polarized and the spin-exchange terms have opposite signs to the Ising terms, e.g. $J_{ij}(-[S^xS^x + S^yS^y] + S^zS^z)$, regardless of the overall sign of the interaction. Geometrically, this can be seen by considering how a pair of interacting spins evolves under the action of an applied perturbation (a similar intuition can be generalized to clusters of spins). In the absence of perturbations ϵ and with a polarized initial state, a stationary solution occurs when the spins are pointing in the same direction along the $\hat{z}$-axis; depending on the global sign of the mutual interaction $sgn(\sum_j J_{ij})$, this will correspond to each spin being either aligned or anti-aligned to its local field. When a perturbation is applied, the spin direction will adiabatically follow the total field. This means that in the case of a positive interaction $\sum_j J_{ij} > 0$ (aligned), the spins will tilt in the same direction as the applied field, while for a negative interaction $\sum_j J_{ij} < 0$ (anti-aligned), the spins will tilt in the opposite direction. The expectation value of the spin vector thus depends on the sign of $\sum_j J_{ij}$, and hence the mean-field acting on each spin, which has an additional factor of

J_{ij}, will always have the correct sign to counteract the applied perturbation. Therefore, the spin-exchange terms will lead to a reduction in perturbations only when they have opposite signs to the Ising terms.

Finally, we perform a similar derivation for the case of $\mathbb{Z}_3$. As previously derived [**?**], the effective Hamiltonian over three Floquet periods is given by

$$D^{\mathbb{Z}_3} \simeq \sum_{ij} \frac{J_{ij}}{r_{ij}^3} \sum_{ab} \left(\delta_{aa} - \frac{1}{3}\delta_{a\pm1,b} \right) \sigma_i^{ab}\sigma_j^{ba} + \frac{\epsilon}{3T}\sum_i \left(\sigma_i^{+1,0} + \sigma_i^{-1,0} + i\sigma_i^{+1,-1} + h.c. \right) \tag{D.18}$$

$$= \sum_{ij} \frac{J_{ij}}{r_{ij}^3} \sum_{\mu\nu} C_{\mu\nu}\lambda_i^\mu \otimes \lambda_j^\nu + \sum_{i\mu} h_\mu \lambda_i^\mu, \tag{D.19}$$

where $\sigma_i^{ab} = |a\rangle_i\langle b|$ for a spin at site i, and in the last line we have re-expressed the Hamiltonian in the orthonormal Gell-Mann matrix basis λ^μ, which satisfies $\mathrm{tr}[\lambda^\mu\lambda^\nu] = 2\delta_{\mu\nu}$. The coefficient matrices are: $C_{\mu\nu}$ is a diagonal matrix, with diagonal elements $C_{\mu\mu} = (-\frac{1}{6}, -\frac{1}{6}, -\frac{1}{6}, -\frac{1}{6}, -\frac{1}{6}, -\frac{1}{6}, \frac{1}{2}, \frac{1}{2})$, and $h = (\frac{\epsilon}{3T}, \frac{\epsilon}{3T}, 0, 0, 0, -\frac{\epsilon}{3T}, 0, 0)$. Our convention is such that the last two Gell-Mann matrices correspond to nonzero population imbalances between the different spin states.

Working in the spin-1 manifold, we write the density matrix as $\rho = \frac{I_{3\times3}}{3} + \sum_\mu \rho_\mu \lambda^\mu$. Repeating the same procedure using the spin-1 equivalents of Eq. (D.13) and Eq. (D.14), we find solutions to the self-consistent equations. Of the solutions to this set of equations, the only physically-relevant (normalizable) solution with nonzero expectation value in the population imbalance (in the limit of $\epsilon \to 0$) is given by

$$\rho_1 = \rho_2 = -\rho_6 = \frac{(\epsilon/T)}{4J_{\mathrm{MF}}}, \tag{D.20}$$

$$\rho_3 = \rho_4 = \rho_5 = 0, \tag{D.21}$$

and ρ_7, ρ_8 are arbitrary numbers depending on the initial conditions and satisfying the normalization requirements. Using the trace orthonormality of Gell-Mann matrices, we find that Eq. (D.15) imposes the constraint $\sum_\mu \rho_\mu^2 \leq 1/3$, which implies that a self-consistent solution exists when $|\epsilon|/T \leq 4J_{\mathrm{MF}}/3$. This shows that the phase boundary is expected to be even wider in the case of $\mathbb{Z}_3$ with Ising and spin-exchange interactions, compared to the preceding two cases.

In conclusion, we have derived the conditions for which a stationary self-consistent mean-field solution exists at the average Hamiltonian level, for each of the different DTC realizations and their associated interaction Hamiltonians. To summarize, we have found that

$$\frac{|\epsilon|}{J_{\mathrm{MF}}T} \leq \begin{cases} \frac{1}{2}, & \mathbb{Z}_2 \text{ DTC with Ising interactions;} \\ 1, & \mathbb{Z}_2 \text{ DTC with Ising and spin-exchange interactions;} \\ \frac{4}{3}, & \mathbb{Z}_3 \text{ DTC with Ising and spin-exchange interactions.} \end{cases} \tag{D.22}$$

As shown in Fig. 2 of the main text, these theoretical predictions are in fairly good agreement with the experimental phase boundaries. We note that the total mean-field interaction strength $J_{MF} = 2\pi\times$ 350 kHz is consistent with the independently extracted typical interaction strength of the system $\sim 2\pi \times 105$ kHz [17], as can be seen from the phase diagrams in Ref. [35, 110], which used Monte Carlo simulations to estimate the total mean-field on each individual spin due to the combination of all other spins.

D.6 Lifetime analysis

The late-time decay rate Γ of the DTC peak height is extracted in two steps. First, the height of the $\nu = 1/2$ ($\mathbb{Z}_2$) or $\nu = 1/3$ ($\mathbb{Z}_3$) peak is determined by short-time Fourier transforms on local sections of the time trace, covering cycles n_{sweep} to $n_{\text{sweep}} + L - 1$, where n_{sweep} is the starting point of the section and the section length $L = 36$ is used for both cases. Fig. D.3 shows representative traces and decay rates of DTC peak heights for the $\mathbb{Z}_2$ and two-group $\mathbb{Z}_3$, while data for the $\mathbb{Z}_2$-Ising and $\mathbb{Z}_3$ can be found in Ref. [35] and the main text, respectively. As shown in the figure, there is a clear difference in the functional profile between short and long T, transitioning from a stretched to simple exponential decay. To extract the late-time decay rate Γ, the peak height data is fitted to a single exponential decay starting from $n_{\text{sweep}} = 15 - 20$, where the transient initial decay is negligible. To account for the influence of the fit starting point, we extract the fit results from $n_{\text{sweep}} = 15$ to $n_{\text{sweep}} = 20$ and associate the mean decay rate with Γ. The errors of the fits are determined by selecting the maximum of the following two error estimates: the mean individual fit error or the standard deviation of the fit results for the set of starting values. Exemplary late-time decay rates are shown in Fig. D.3(c,f) for short and long Floquet periods and the two different Hamiltonians. For short Floquet periods, we observe that DTC order is indeed robust to perturbations, manifested as a negligible ϵ-dependence of Γ. However, at long Floquet periods, DTC signals are no longer stable against the perturbations, developing a quadratic behavior as a function of ϵ with a coefficient close to 1/2. Detailed analysis of this behavior is discussed in the following section.

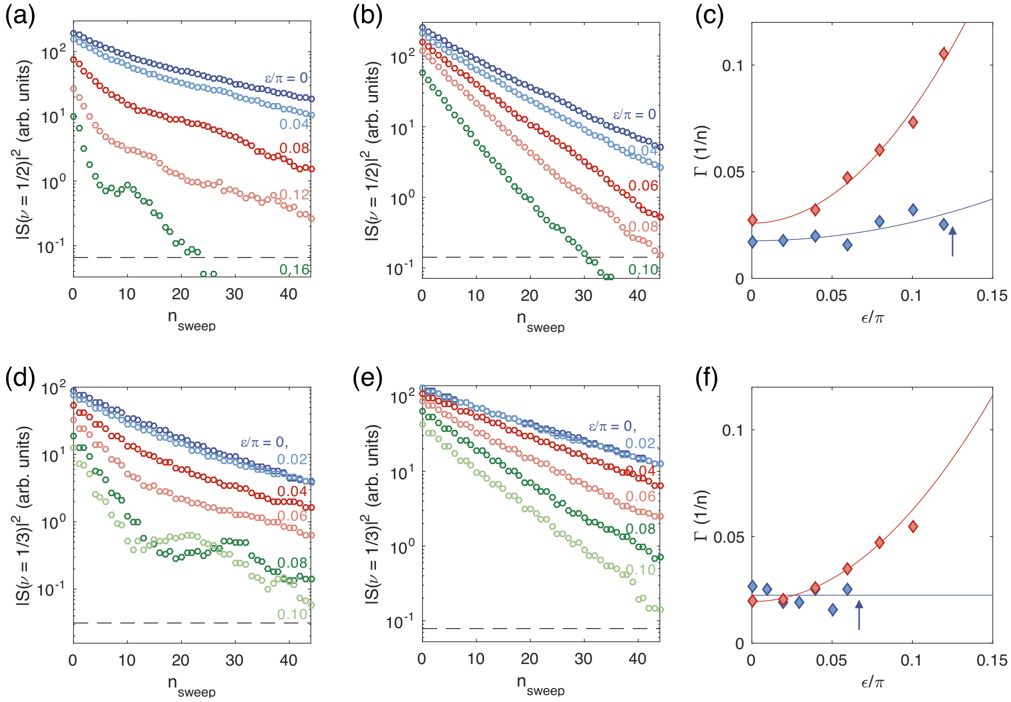

Figure D.3: **Probing decay rates of DTC order at short and long interaction times.** Representative time traces and late-time decay rates of (a-c) $\mathbb{Z}_2$ and (d-f) two-group $\mathbb{Z}_3$ DTC peak heights. In (a,b,d,e), we present the time traces at (a) T = 200 ns and (b) T = 1900 ns for the $\mathbb{Z}_2$, and (d) T = 70 ns and (e) T = 250 ns for the two-group $\mathbb{Z}_3$, respectively, and the dashed gray lines denote noise floors. In (c,f), the late-time decay rates of DTC order as a function of perturbation strength are compared between short and long interaction times for each case. In (c), blue and red data correspond to T = 200 ns and T = 1900 ns, respectively, while in (f), they correspond to T = 70 ns and T = 250 ns. Arrows indicate the phase boundary for short interaction times where either the crystalline fraction drops below 10% or sidepeaks away from the DTC peak position are predominant. Solid lines are phenomenological quadratic fits, $\Gamma(\epsilon) = \Gamma_0 + a\epsilon^2$.

D.7 Approach to dephasing regime

As seen in Fig. 3(a,b) in the main text, the functional profile of the DTC order decay differs depending on the length of the Floquet period T; at short T, the decay profile follows a stretched exponential, while at long T, it turns into a single exponential. To quantify these qualitative differences, we phenomenologically fit the DTC order decay profile using

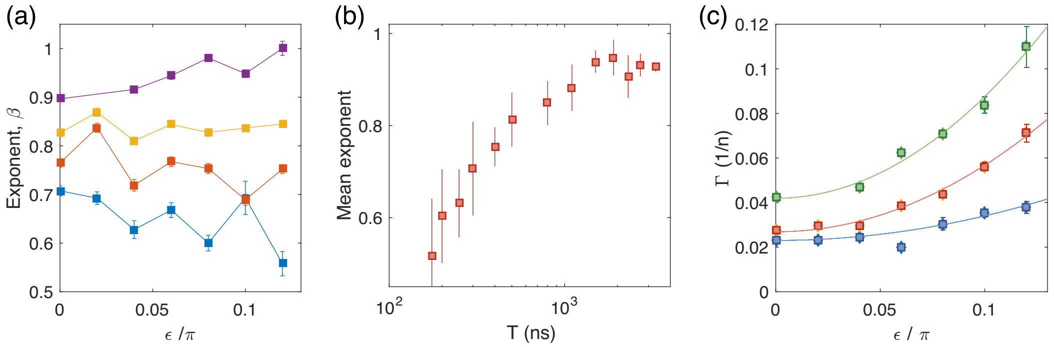

Figure D.4: **Crossover in the dynamics of DTC order approaching the dephasing regime.** (a) Exponent as a function of perturbation strength ϵ. The exponents are extracted from a stretched exponential decay fitted to $\mathbb{Z}_2$ DTC signals probed at different Floquet periods: T = 250 ns (blue), 400 ns (red), 800 ns (yellow), and 1900 ns (purple). (b) Mean exponent $\overline{\beta}$ as a function of T. (c) Late-time decay rate of $\mathbb{Z}_2$ DTC order measured at T = 200 ns (blue), 800 ns (red), and 1900 ns (green). Solid lines are phenomenological quadratic fits.

a stretched exponential function $A\exp[-(n_{\text{sweep}}/n_{\tau})^{\beta}]$, with exponent β and characteristic decay constant n_{τ}. In Fig. D.4(a), the extracted β is displayed as a function of T and ϵ for the $\mathbb{Z}_2$ case. As seen in the figure, β has a more pronounced dependence on T compared to its dependence on ϵ. The same qualitative behavior is also observed for other cases including $\mathbb{Z}_2$-Ising and $\mathbb{Z}_3$. Therefore, we proceed to monitor the mean $\overline{\beta}$ and its errorbar at each T by estimating the mean and statistical fluctuation of the local β values extracted at different perturbations ϵ. As presented in Fig. D.4(b), as T increases, $\overline{\beta}$ also increases continuously to $\sim$1 consistently for all four DTC cases (see Fig. 4(b) in the main text). We attribute the saturation exponent slightly less than 1 to the convolution of the decay profile with the bare T_1 decay profile, the latter following a stretched exponential profile with exponent $1/2$ [76].

In addition to the changes in the functional profile, we also investigate the change in DTC stability at different Floquet periods by examining the late-time decay rate Γ of DTC

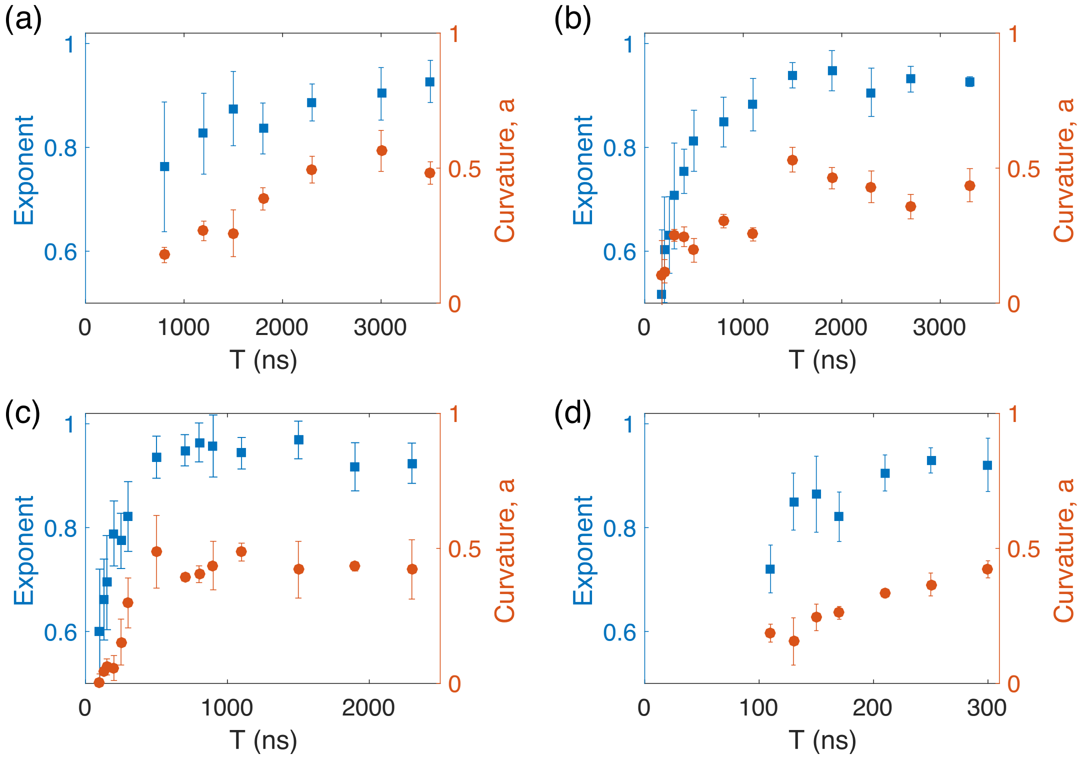

Figure D.5: **Correlation between late-time decay rate and functional profile of DTC order decay.** Curvature a from the fit $\Gamma = \Gamma_0 + a\epsilon^2$, and exponent $\overline{\beta}$, are compared as a function of T for the different cases of (a) $\mathbb{Z}_2$-Ising, (b) $\mathbb{Z}_2$, (c) $\mathbb{Z}_3$, and (d) two-group $\mathbb{Z}_3$. We see that the curvature and exponent approach saturation at comparable interaction timescales.

order. Fig. D.4(c) shows the DTC decay rate profiles as a function of ϵ, measured at short, intermediate, and long T for the $\mathbb{Z}_2$ case. As expected, at short T, the $\mathbb{Z}_2$ DTC order shows a robust Γ fairly independent of perturbation strength ϵ. At intermediate T, however, the plateau region manifesting the rigidity shrinks, and accordingly, DTC order starts to die out at a smaller perturbation than that of shorter T. More interestingly, at long T, we find that the behavior is well captured by a dephasing model predicting $\Gamma(\epsilon) = \epsilon^2/2$ up to a finite global offset Γ_0. In the main text, we present the $\mathbb{Z}_3$ data exhibiting similar behaviors (see Fig. 3(c) and Fig. 4(b)).

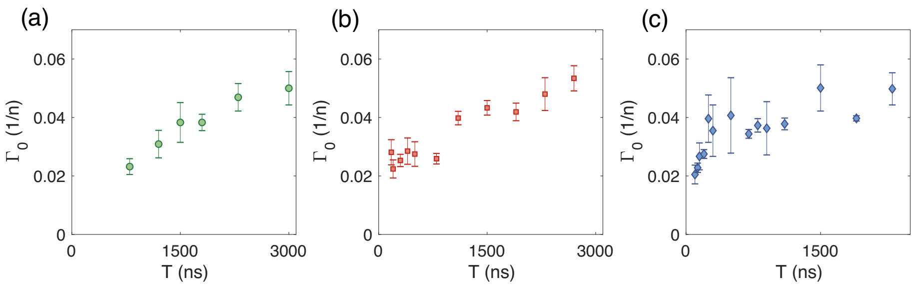

Figure D.6: **Dependence of offset decay rate Γ_0 on Floquet period.** (a) $\mathbb{Z}_2$-Ising, (b) $\mathbb{Z}_2$, (b) $\mathbb{Z}_3$ cases.

To identify such crossovers in the dynamics of DTC order, we perform a phenomenological fit using $\Gamma(\epsilon) = \Gamma_0 + a\epsilon^2$, with a T-dependent offset Γ_0 and curvature a. The extracted a values as a function of T are presented in Fig. D.5, together with the exponent $\overline{\beta}$ evaluated independently from the stretched exponential fit. Surprisingly, we find a similar saturation behavior in the curvature a probed as a function of T; the curvature a also saturates around 0.5 for all cases, consistent with the simple dephasing model explaining the DTC dynamics in the limit of long T (see following section). The correlation between the curvature a and exponent $\overline{\beta}$ confirms that there exists a gradual crossover in the late-time DTC dynamics, approaching the dephasing regime associated with thermalization. In order to demarcate the dephasing regime in each of the different DTC realizations, we identify a transition point $T^\star$ where $\overline{\beta}$ increases above 0.9. The error on $T^\star$ corresponds to the statistical error of a saturation fit, $\beta = 1/(1+(c_1/T)^{c_2})$, where $c_{1,2}$ are free parameters.

As seen in Figure D.6, Γ_0 increases linearly with T, with a slope that is consistent with the depolarization rate $1/T_1$ of our spin system: for the $\mathbb{Z}_2$-Ising, $\mathbb{Z}_2$, $\mathbb{Z}_3$ cases, the inverse slopes in units of microseconds are 60(8), 86(10), and 110(26) μs, respectively. The finite offset as one extrapolates the linear curve to $T = 0$ is likely a result of the finite duration of rotation pulses: for the $\mathbb{Z}_2$-Ising, $\mathbb{Z}_2$, $\mathbb{Z}_3$ cases, the finite offsets in units of inverse Floquet cycles are 0.01(5), 0.022(2), and 0.026(2), respectively.

D.8 Universality in long interaction time regime

We now consider the DTC response in the long interaction time regime (or equivalently, slow Floquet drive regime), where the Floquet drive energy scale $\omega_0 = 2\pi/T$ is smaller than both the on-site disorder strength and typical interaction strengths in the system. In this regime, we expect the system to be able to absorb/emit energy from/to the drive to compensate energy differences, leading to a reduced disorder strength that is smaller than typical interaction strengths in the system. Intuitively, many different spin configurations will become resonant with each other due to the significantly reduced disorder, giving rise to faster thermalization.

Phenomenologically, we may describe this limit by a simple model, in which we assume that the system effectively thermalizes during one Floquet cycle. As the dipolar interaction conserves total polarization, we model the dynamics during the interaction period as an effective dephasing, in which the spin coherence is lost and only population information remains.

First, we consider the $\mathbb{Z}_2$ case. In the fully-dephased limit, the microscopic form of the interaction Hamiltonian ceases to matter as long as it conserves total polarization. The action of the DTC sequence on the ensemble-averaged density matrix ρ can be viewed as the alternation of a unitary rotation

$$U_{\mathbb{Z}_2,\epsilon} = \begin{pmatrix} -\sin(\frac{\epsilon}{2}) & -i\cos(\frac{\epsilon}{2}) \\ -i\cos(\frac{\epsilon}{2}) & -\sin(\frac{\epsilon}{2}) \end{pmatrix}, \tag{D.23}$$

and a dephasing channel

$$\rho \mapsto \sum_{\mu\in\{0,1\}} |\mu\rangle\langle\mu|\rho|\mu\rangle\langle\mu|, \tag{D.24}$$

where we denote the two spin states as $|0\rangle$ and $|1\rangle$. As the dephasing channel eliminates coherences in ρ, we can model the time evolution in terms of population dynamics with a rate equation $p_\mu = R_{\mathbb{Z}_2,\mu\nu}p_\nu$, where $p_\mu = \rho_{\mu\mu}$ is the population in the spin state $|\mu\rangle$ and the evolution matrix $R_{\mathbb{Z}_2,\mu\nu} = |(U_{\mathbb{Z}_2,\epsilon})_{\mu\nu}|^2$. For the $\mathbb{Z}_2$ case, the long-time decay rate $\gamma_{\mathbb{Z}_2}$ is given by the smallest non-zero eigenvalue $\lambda_{\mathbb{Z}_2}$ of $R^2_{\mathbb{Z}_2}$ via $\exp(-2\gamma_{\mathbb{Z}_2}) = \lambda_{\mathbb{Z}_2}$. Plugging in the preceding expressions for $R_{\mathbb{Z}_2}$ and expanding to leading order in ϵ, we find that

$$R^2_{\mathbb{Z}_2} = \begin{pmatrix} \sin(\frac{\epsilon}{2})^2 & \cos(\frac{\epsilon}{2})^2 \\ \cos(\frac{\epsilon}{2})^2 & \sin(\frac{\epsilon}{2})^2 \end{pmatrix}^2 = \begin{pmatrix} 1-\frac{\epsilon^2}{2} & \frac{\epsilon^2}{2} \\ \frac{\epsilon^2}{2} & 1-\frac{\epsilon^2}{2} \end{pmatrix} + O\left(\epsilon^3\right), \tag{D.25}$$

which has eigenvalues 1 and $1-\epsilon^2$. The eigenvalue corresponding to an eigenvector with nonzero S^z expectation value is $1-\epsilon^2 \approx \exp(-2\gamma_{\mathbb{Z}_2})$. Hence, the decay rate in this limit turns out to be $\gamma_{\mathbb{Z}_2} = \frac{\epsilon^2}{2}$. This result is in good agreement with the dependence of the observed decay rate on ϵ at long interaction times.

We now consider the $\mathbb{Z}_3$ case, again in the limit where the system is expected to thermalize within one Floquet cycle. We use ρ to denote the ensemble-averaged density matrix for the spin-1 particles. We may write the rotation matrices as

$$U_{\mathbb{Z}_3,\epsilon} = \begin{pmatrix} -\sin(\frac{\epsilon}{2}) & -i\cos(\frac{\epsilon}{2}) & 0 \\ -i\cos(\frac{\epsilon}{2}) & -\sin(\frac{\epsilon}{2}) & 0 \\ 0 & 0 & 1 \end{pmatrix} \begin{pmatrix} 1 & 0 & 0 \\ 0 & -\sin(\frac{\epsilon}{2}) & -i\cos(\frac{\epsilon}{2}) \\ 0 & -i\cos(\frac{\epsilon}{2}) & -\sin(\frac{\epsilon}{2}) \end{pmatrix} \tag{D.26}$$

$$= \begin{pmatrix} -\sin(\frac{\epsilon}{2}) & \frac{1}{2}i\sin(\epsilon) & -\cos^2(\frac{\epsilon}{2}) \\ -i\cos(\frac{\epsilon}{2}) & \sin^2(\frac{\epsilon}{2}) & \frac{1}{2}i\sin(\epsilon) \\ 0 & -i\cos(\frac{\epsilon}{2}) & -\sin(\frac{\epsilon}{2}) \end{pmatrix} \tag{D.27}$$

and the dephasing channel as

$$\rho \mapsto \sum_{\mu\in\{-1,0,1\}} |\mu\rangle\langle\mu|\rho|\mu\rangle\langle\mu|, \tag{D.28}$$

where the sum runs over all three spin states. The rate equation for populations has the rate-mapping matrix $R_{\mathbb{Z}_3,\mu\nu} = |(U_{\mathbb{Z}_3,\epsilon})_{\mu\nu}|^2$, which in the limit of small $\epsilon \ll \pi$, gives

$$R^2_{\mathbb{Z}_3} = \begin{pmatrix} 1-\epsilon^2 & \frac{\epsilon^2}{2} & \frac{\epsilon^2}{2} \\ \frac{\epsilon^2}{2} & 1-\epsilon^2 & \frac{\epsilon^2}{2} \\ \frac{\epsilon^2}{2} & \frac{\epsilon^2}{2} & 1-\epsilon^2 \end{pmatrix} + O\left(\epsilon^4\right), \tag{D.29}$$

with eigenvalues 1 and $1-\frac{3}{2}\epsilon^2$ (degeneracy 2). The resulting decay rate satisfies $\exp(-3\gamma_{\mathbb{Z}_3}) \approx 1-\frac{3}{2}\epsilon^2$, so that $\gamma_{\mathbb{Z}_3} \approx \frac{\epsilon^2}{2}$. Thus, for the $\mathbb{Z}_3$ case, we also expect an asymptotic decay rate scaling as $\epsilon^2/2$ in the thermalizing regime.

In conclusion, we have demonstrated that, when the Floquet period T is sufficiently long such that the system dynamics effectively behaves as thermalizing within each cycle, the decay rate of the subharmonic signal should scale as $\Gamma = \epsilon^2/2$. In reality, however, there will be additional decays Γ_0 due to interaction-induced dephasing associated with a finite pulse width [111] as well as other imperfections, as discussed in the previous section.

D.9 Numerical simulations in long interaction time regime

To lend support to the dephasing picture in the long interaction time regime, we carry out numerical simulations based on the exact diagonalization of a many-body Hamiltonian subject to a periodic drive. More specifically, we consider the following toy model consisting of an infinite-range interacting spin-1/2 system, which captures how spin-spin interactions lead to rapid dephasing of individual spins, and ultimately thermalize the system,

$$H(t) = \sum_i \Omega_y(t) S_i^y + \sum_{ij} \frac{J_{ij}}{\sqrt{N}} \left[\alpha (S_i^x S_j^x + S_i^y S_j^y) - S_i^z S_j^z \right], \tag{D.30}$$

where $\Omega_y(t) = (\pi + \epsilon)\delta(t - T)$ characterizes a periodic imperfect rotation of spins, J_{ij} is a random coupling strength sampled from a uniform distribution, i.e., $J_{ij} \sim \mathcal{U}[-1, 1]$, and α is a coefficient tuning the strength of spin-exchange interactions relative to that of Ising interactions. In the following simulations, we consider only two cases of $\alpha = 1$ (both spin-exchange and Ising) and $\alpha = 0$ (pure Ising) for relevance to the experiment.

Figure D.7 shows the simulation results for the periodically-driven, infinite-range coupled spin system ($N = 18,\ \epsilon/\pi = 0.06,\ JT = 10$, where $J \equiv \max J_{ij}/\sqrt{N}$). All spins are initially polarized along the same direction (z-axis) and interact with one another via both Ising and spin-exchange interactions with $\alpha = 1$. We simulate ~300 disorder realizations and all of them exhibit period-doubled oscillations decaying over time with differing decay constants [Fig. D.7(a)]. For analysis, we extract the individual decay rates by fitting the late-time data ($n > 40$) to a simple exponential. Interestingly, we find that a majority of the realizations display a similar decay rate very close to $\Gamma = \epsilon^2/2$ as seen in Fig. D.7(b). Repeating the same simulations with varying perturbation strength ϵ, we identify the most

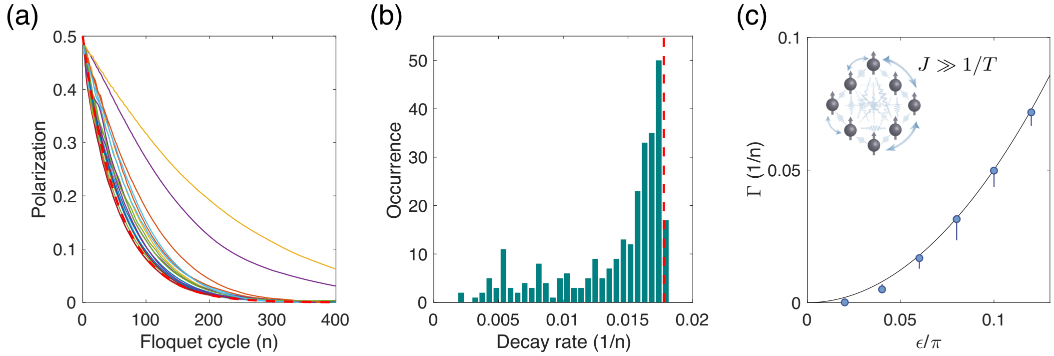

Figure D.7: **Simulation results for an infinite-range interacting spin system subject to a periodic drive.** (a) Twenty individual profiles of global spin polarization from different disorder realizations, probed at every even period. The red dashed line represents a simple exponential decay with a decay constant of $\Gamma = \epsilon^2/2$. (b) Histogram of late-time decay rates from the individual time traces. The vertical red dashed line indicates a position of $\Gamma = \epsilon^2/2$. (c) Most probable late-time decay rate as a function of perturbation strength ϵ, extracted from (b). Errorbars indicate the standard deviation of the distribution in the histogram fitted to an asymmetric Gaussian function. In (a-c), the perturbation strength is set to $\epsilon/\pi = 0.06$. We chose a system size $N = 18$, long Floquet drive period $T = 10/J$, and included both spin-exchange and Ising interactions between the spins with $\alpha = 1$. The spins are initially polarized along the same direction (z-axis).

probable decay rates as well as the standard deviation of the distribution from each histogram, and plot them as a function of ϵ [Fig. D.7(c)]. Indeed, the extracted decay rates from the simulations agree well with the expected scaling of $\Gamma = \epsilon^2/2$, consistent with the experimental observations [see Fig. 4(b) in the main text]. These numerical results substantiate our picture of thermalization in the long interaction time regime, that the dynamics can be effectively described by single-spin dephasing induced by the rest of the system acting as its own Markovian bath.

In the case of purely Ising interactions ($\alpha = 0$), we employ a different initial state $|\Psi\rangle = |\psi_1\rangle \otimes |\psi_{2,\dots,N}\rangle$, where $|\psi_1\rangle = |\uparrow\rangle$ and $|\psi_{2,\dots,N}\rangle$ is a $2^{(N-1)}$-dimensional complex random vector representing a highly entangled state for the remaining $(N-1)$ spins, to

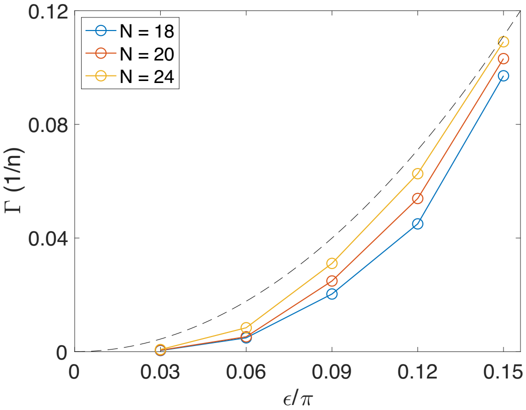

Figure D.8: **Simulation results for an infinite-range Ising-interacting spin system subject to a periodic drive.** (a) local spin polarization probed at every even period, $P(t) = \langle\psi_1(t)| S_1^z |\psi_1(t)\rangle$, with an initial state $|\Psi\rangle = |\psi_1\rangle \otimes |\psi_{2,\ldots,N}\rangle$, where $|\psi_1\rangle = |\uparrow\rangle$ and $|\psi_{2,\ldots,N}\rangle$ is a $2^{(N-1)}$-dimensional complex random vector. The late-time decay rate scaling for different system sizes $N = 18, 20, 24$ are presented. The dashed line represents a dephasing fit $\Gamma = \epsilon^2/2$. We chose a long Floquet drive period $T = 10/J$, and allowed only Ising interactions between the spins with $\alpha = 0$.

be less sensitive to different disorder realizations. After each Floquet cycle, we probe the local polarization of the initially polarized spin $P(t) = \langle\psi_1(t)| S_1^z |\psi_1(t)\rangle$. As shown in Fig. D.8, we find that the resulting late-time decay rates of subharmonic oscillations is also approaching the expected $\Gamma = \epsilon^2/2$ scaling as the system size N increases. However, the finite-size-scaling approach to the Markovian regime is apparently slower than the case of spin-exchange interactions ($\alpha = 1$), as the largest system of size $N = 24$ still yields decay rates that are slower than the Markovian dephasing limit $\Gamma = \epsilon^2/2$. These observations suggest potential differences in the thermalization dynamics of systems with different types of interaction, requiring further investigations.

Bibliography

[1] R. Adler. A study of locking phenomena in oscillators. *Proceedings of the IRE*, 34(6):351–357, 1946.

[2] M. C. Cross and P. C. Hohenberg. Pattern formation outside of equilibrium. *Rev. Mod. Phys.*, 65:851–1112, Jul 1993.

[3] M. Schreiber, S. S. Hodgman, P. Bordia, H. P. Lüschen, M. H. Fischer, R. Vosk, E. Altman, U. Schneider, and I. Bloch. Observation of many-body localization of interacting fermions in a quasirandom optical lattice. *Science*, 349(6250):842–845, 2015.

[4] T. Langen, S. Erne, R. Geiger, B. Rauer, T. Schweigler, M. Kuhnert, W. Rohringer, I. E. Mazets, T. Gasenzer, and J. Schmiedmayer. Experimental observation of a generalized Gibbs ensemble. *Science*, 348(6231):207–211, 2015.

[5] J. Smith, A. Lee, P. Richerme, B. Neyenhuis, P. W. Hess, P. Hauke, M. Heyl, D. A. Huse, and C. Monroe. Many-body localization in a quantum simulator with programmable random disorder. *Nature Physics*, 12(10):907, 2016.

[6] A. M. Kaufman, M. E. Tai, A. Lukin, M. Rispoli, R. Schittko, P. M. Preiss, and M. Greiner. Quantum thermalization through entanglement in an isolated many-body system. *Science*, 353(6301):794–800, 2016.

[7] F. Wilczek. Quantum time crystals. *Physical review letters*, 109(16):160401, 2012.

[8] T. Li, Z.-X. Gong, Z.-Q. Yin, H. Quan, X. Yin, P. Zhang, L.-M. Duan, and X. Zhang. Space-time crystals of trapped ions. *Physical review letters*, 109(16):163001, 2012.

[9] V. Khemani, A. Lazarides, R. Moessner, and S. L. Sondhi. Phase structure of driven quantum systems. *Physical review letters*, 116(25):250401, 2016.

[10] D. V. Else, B. Bauer, and C. Nayak. Floquet time crystals. *Physical review letters*, 117(9):090402, 2016.

[11] C. W. von Keyserlingk, V. Khemani, and S. L. Sondhi. Absolute stability and spatiotemporal long-range order in floquet systems. *Physical Review B*, 94(8):085112, 2016.

[12] N. Y. Yao, A. C. Potter, I.-D. Potirniche, and A. Vishwanath. Discrete time crystals: rigidity, criticality, and realizations. *Physical review letters*, 118(3):030401, 2017.

[13] F. Jelezko, T. Gaebel, I. Popa, A. Gruber, and J. Wrachtrup. Observation of coherent oscillations in a single electron spin. *Physical review letters*, 92(7):076401, 2004.

[14] L. Childress, M. G. Dutt, J. Taylor, A. Zibrov, F. Jelezko, J. Wrachtrup, P. Hemmer, and M. Lukin. Coherent dynamics of coupled electron and nuclear spin qubits in diamond. *Science*, 314(5797):281–285, 2006.

[15] M. W. Doherty, N. B. Manson, P. Delaney, F. Jelezko, J. Wrachtrup, and L. C. Hollenberg. The nitrogen-vacancy colour centre in diamond. *Physics Reports*, 528(1):1–45, 2013.

[16] P. W. Anderson. Absence of diffusion in certain random lattices. *Physical review*, 109(5):1492, 1958.

[17] G. Kucsko, S. Choi, J. Choi, P. C. Maurer, H. Zhou, R. Landig, H. Sumiya, S. Onoda, J. Isoya, F. Jelezko, et al. Critical thermalization of a disordered dipolar spin system in diamond. *Physical review letters*, 121(2):023601, 2018.

[18] C. Deutsch, F. Ramirez-Martinez, C. Lacroûte, F. Reinhard, T. Schneider, J.-N. Fuchs, F. Piéchon, F. Laloë, J. Reichel, and P. Rosenbusch. Spin self-rephasing and very long coherence times in a trapped atomic ensemble. *Physical review letters*, 105(2):020401, 2010.

[19] A. M. Rey, L. Jiang, M. Fleischhauer, E. Demler, and M. D. Lukin. Many-body protected entanglement generation in interacting spin systems. *Phys. Rev. A*, 77:052305, May 2008.

[20] P. Cappellaro and M. D. Lukin. Quantum correlation in disordered spin systems: Applications to magnetic sensing. *Physical Review A*, 80(3):032311, 2009.

[21] L. Childress, R. Walsworth, and M. Lukin. Atom-like crystal defects. *Physics Today*, 67(10):38, 2014.

[22] F. Dolde, I. Jakobi, B. Naydenov, N. Zhao, S. Pezzagna, C. Trautmann, J. Meijer, P. Neumann, F. Jelezko, and J. Wrachtrup. Room-temperature entanglement between single defect spins in diamond. *Nature Physics*, 9(3):139–143, 2013.

[23] X. Michalet, F. Pinaud, L. Bentolila, J. Tsay, S. Doose, J. Li, G. Sundaresan, A. Wu, S. Gambhir, and S. Weiss. Quantum dots for live cells, in vivo imaging, and diagnostics. *science*, 307(5709):538–544, 2005.

[24] I. Lovchinsky, A. Sushkov, E. Urbach, N. de Leon, S. Choi, K. De Greve, R. Evans, R. Gertner, E. Bersin, C. Müller, et al. Nuclear magnetic resonance detection and spectroscopy of single proteins using quantum logic. *Science*, 351(6275):836–841, 2016.

[25] R. Amsüss, C. Koller, T. Nöbauer, S. Putz, S. Rotter, K. Sandner, S. Schneider, M. Schramböck, G. Steinhauser, H. Ritsch, et al. Cavity qed with magnetically coupled collective spin states. *Physical Review Letters*, 107(6):060502, 2011.

[26] G. Waldherr, P. Neumann, S. Huelga, F. Jelezko, and J. Wrachtrup. Violation of a temporal bell inequality for single spins in a diamond defect center. *Physical Review Letters*, 107(9):090401, 2011.

[27] W. Pfaff, T. H. Taminiau, L. Robledo, H. Bernien, M. Markham, D. J. Twitchen, and R. Hanson. Demonstration of entanglement-by-measurement of solid-state qubits. *Nature Physics*, 9(1):29–33, 2013.

[28] B. Hensen, H. Bernien, A. Dréau, A. Reiserer, N. Kalb, M. Blok, J. Ruitenberg, R. Vermeulen, R. Schouten, C. Abellán, et al. Loophole-free bell inequality violation using electron spins separated by 1.3 kilometres. *Nature*, 526(7575):682–686, 2015.

[29] J. Maze, P. Stanwix, J. Hodges, S. Hong, J. Taylor, P. Cappellaro, L. Jiang, M. G. Dutt, E. Togan, A. Zibrov, et al. Nanoscale magnetic sensing with an individual electronic spin in diamond. *Nature*, 455(7213):644–647, 2008.

[30] G. Kucsko, P. Maurer, N. Y. Yao, M. Kubo, H. Noh, P. Lo, H. Park, and M. D. Lukin. Nanometre-scale thermometry in a living cell. *Nature*, 500(7460):54–58, 2013.

[31] H. Mamin, M. Kim, M. Sherwood, C. Rettner, K. Ohno, D. Awschalom, and D. Rugar. Nanoscale nuclear magnetic resonance with a nitrogen-vacancy spin sensor. *Science*, 339(6119):557–560, 2013.

[32] P. C. Maurer, G. Kucsko, C. Latta, L. Jiang, N. Y. Yao, S. D. Bennett, F. Pastawski, D. Hunger, N. Chisholm, M. Markham, et al. Room-temperature quantum bit memory exceeding one second. *Science*, 336(6086):1283–1286, 2012.

[33] N. Y. Yao, L. Jiang, A. V. Gorshkov, Z.-X. Gong, A. Zhai, L.-M. Duan, and M. D. Lukin. Robust quantum state transfer in random unpolarized spin chains. *Physical Review Letters*, 106(4):040505, 2011.

[34] N. Y. Yao, L. Jiang, A. V. Gorshkov, P. C. Maurer, G. Giedke, J. I. Cirac, and M. D. Lukin. Scalable architecture for a room temperature solid-state quantum information processor. *Nature Communications*, 3:800, 2012.

[35] S. Choi, J. Choi, R. Landig, G. Kucsko, H. Zhou, J. Isoya, F. Jelezko, S. Onoda, H. Sumiya, V. Khemani, et al. Observation of discrete time-crystalline order in a disordered dipolar many-body system. *Nature*, 543(7644):221, 2017.

[36] M. Mrózek, D. Rudnicki, P. Kehayias, A. Jarmola, D. Budker, and W. Gawlik. Longitudinal spin relaxation in nitrogen-vacancy ensembles in diamond. *EPJ Quantum Technology*, 2(1):1–11, 2015.

[37] A. Jarmola, A. Berzins, J. Smits, K. Smits, J. Prikulis, F. Gahbauer, R. Ferber, D. Erts, M. Auzinsh, and D. Budker. Longitudinal spin-relaxation in nitrogen-vacancy centers in electron irradiated diamond. *Applied Physics Letters*, 107:242403, 2016.

[38] G. Feher and E. Gere. Electron spin resonance experiments on donors in silicon. ii. electron spin relaxation effects. *Physical Review*, 114(5):1245, 1959.

[39] K. Shrivastava. Theory of spin–lattice relaxation. *physica status solidi (b)*, 117(2):437–458, 1983.

[40] N. Manson, J. Harrison, and M. Sellars. Nitrogen-vacancy center in diamond: Model of the electronic structure and associated dynamics. *Physical Review B*, 74(10):104303, 2006.

[41] D. Redman, S. Brown, R. Sands, and S. Rand. Spin dynamics and electronic states of n-v centers in diamond by epr and four-wave-mixing spectroscopy. *Physical Review Letters*, 67(24):3420, 1991.

[42] M. Walker. At 5 spin-lattice relaxation rate for non-kramers ions. *Canadian Journal of Physics*, 46(11):1347–1353, 1968.

[43] A. Jarmola, V. Acosta, K. Jensen, S. Chemerisov, and D. Budker. Temperature-and magnetic-field-dependent longitudinal spin relaxation in nitrogen-vacancy ensembles in diamond. *Physical Review Letters*, 108(19):197601, 2012.

[44] S. Kolkowitz, A. Safira, A. High, R. Devlin, S. Choi, Q. Unterreithmeier, D. Patterson, A. Zibrov, V. Manucharyan, H. Park, et al. Probing johnson noise and ballistic transport in normal metals with a single-spin qubit. *Science*, 347(6226):1129–1132, 2015.

[45] S. R. Hartmann and E. L. Hahn. Nuclear double resonance in the rotating frame. *Physical Review*, 128(5):2042, 1962.

[46] N. Bar-Gill, L. M. Pham, A. Jarmola, D. Budker, and R. L. Walsworth. Solid-state electronic spin coherence time approaching one second. *Nature Communications*, 4:1743, 2013.

[47] M. J. Biercuk, H. Uys, A. P. VanDevender, N. Shiga, W. M. Itano, and J. J. Bollinger. Optimized dynamical decoupling in a model quantum memory. *Nature*, 458(7241):996–1000, 2009.

[48] R. H. Dicke. Coherence in spontaneous radiation processes. *Physical Review*, 93(1):99, 1954.

[49] J. Cardellino, N. Scozzaro, M. Herman, A. J. Berger, C. Zhang, K. C. Fong, C. Jayaprakash, D. V. Pelekhov, and P. C. Hammel. The effect of spin transport on spin lifetime in nanoscale systems. *Nature Nanotechnology*, 9(5):343–347, 2014.

[50] G. Berman, B. Chernobrod, V. Gorshkov, and V. Tsifrinovich. Spin diffusion and relaxation in a nonuniform magnetic field. *Physical Review B*, 71(18):184409, 2005.

[51] B. Vugmeister. Spin diffusion and spin–lattice relaxation in paramagnetic crystals. *Physica Status Solidi (b)*, 90(2):711–718, 1978.

[52] L. S. Levitov. Delocalization of vibrational modes caused by electric dipole interaction. *Physical Review Letters*, 64(5):547, 1990.

[53] B. Shields, Q. Unterreithmeier, N. De Leon, H. Park, and M. Lukin. Efficient readout of a single spin state in diamond via spin-to-charge conversion. *Physical review letters*, 114(13):136402, 2015.

[54] K. Iakoubovskii, G. Adriaenssens, and M. Nesladek. Photochromism of vacancy-related centres in diamond. *Journal of Physics: Condensed Matter*, 12(2):189, 2000.

[55] Y. Doi, T. Fukui, H. Kato, T. Makino, S. Yamasaki, T. Tashima, H. Morishita, S. Miwa, F. Jelezko, Y. Suzuki, et al. Pure negatively charged state of the nv center in n-type diamond. *Physical Review B*, 93(8):081203, 2016.

[56] N. Y. Yao, C. R. Laumann, S. Gopalakrishnan, M. Knap, M. Mueller, E. A. Demler, and M. D. Lukin. Many-body localization in dipolar systems. *Physical Review Letters*, 113(24):243002, 2014.

[57] M. Serbyn, M. Knap, S. Gopalakrishnan, Z. Papić, N. Y. Yao, C. Laumann, D. Abanin, M. D. Lukin, and E. A. Demler. Interferometric probes of many-body localization. *Physical Review Letters*, 113(14):147204, 2014.

[58] R. Weaver. Anderson localization of ultrasound. *Wave motion*, 12(2):129–142, 1990.

[59] D. S. Wiersma, P. Bartolini, A. Lagendijk, and R. Righini. Localization of light in a disordered medium. *Nature*, 390(6661):671–673, 1997.

[60] T. Schwartz, G. Bartal, S. Fishman, and M. Segev. Transport and Anderson localization in disordered two-dimensional photonic lattices. *Nature*, 446(7131):52–55, 2007.

[61] G. Roati, C. D'Errico, L. Fallani, M. Fattori, C. Fort, M. Zaccanti, G. Modugno, M. Modugno, and M. Inguscio. Anderson localization of a non-interacting bose–einstein condensate. *Nature*, 453(7197):895–898, 2008.

[62] J. Billy, V. Josse, Z. Zuo, A. Bernard, B. Hambrecht, P. Lugan, D. Clément, L. Sanchez-Palencia, P. Bouyer, and A. Aspect. Direct observation of anderson localization of matter waves in a controlled disorder. *Nature*, 453(7197):891–894, 2008.

[63] D. M. Basko, I. L. Aleiner, and B. L. Altshuler. Metal–insulator transition in a weakly interacting many-electron system with localized single-particle states. *Annals of Physics*, 321(5):1126–1205, 2006.

[64] V. Oganesyan and D. A. Huse. Localization of interacting fermions at high temperature. *Physical review b*, 75(15):155111, 2007.

[65] A. Pal and D. A. Huse. Many-body localization phase transition. *Physical review b*, 82(17):174411, 2010.

[66] J.-y. Choi, S. Hild, J. Zeiher, P. Schauß, A. Rubio-Abadal, T. Yefsah, V. Khemani, D. A. Huse, I. Bloch, and C. Gross. Exploring the many-body localization transition in two dimensions. *Science*, 352(6293):1547–1552, 2016.

[67] A. C. Potter, T. Morimoto, and A. Vishwanath. Classification of interacting topological Floquet phases in one dimension. *Physical Review X*, 6(4):041001, 2016.

[68] J. Zhang, P. Hess, A. Kyprianidis, P. Becker, A. Lee, J. Smith, G. Pagano, I.-D. Potirniche, A. C. Potter, A. Vishwanath, et al. Observation of a discrete time crystal. *Nature*, 543(7644):217, 2017.

[69] A. L. Burin. Energy delocalization in strongly disordered systems induced by the long-range many-body interaction. *arXiv preprint cond-mat/0611387*, 2006.

[70] C. P. Slichter. *Principles of magnetic resonance*, volume 1. Springer Science & Business Media, 2013.

[71] A. J. Vega. Relaxation in spin-echo and spin-lock experiments. *Journal of Magnetic Resonance (1969)*, 65(2):252–267, 1985.

[72] P. Robyr, B. H. Meier, and R. R. Ernst. Radio-frequency-driven nuclear spin diffusion in solids. *Chemical Physics Letters*, 162(6):417–423, 1989.

[73] X. Wu and S. Zhang. Selective polarization inversion and depolarization of 13C in cross relaxation in NMR. *Chemical Physics Letters*, 156(1):79–81, 1989.

[74] S. Zhang, B. H. Meier, and R. R. Ernst. Polarization echoes in NMR. *Physical Review Letters*, 69(14):2149, 1992.

[75] G. Balasubramanian, P. Neumann, D. Twitchen, M. Markham, R. Kolesov, N. Mizuochi, J. Isoya, J. Achard, J. Beck, J. Tissler, and others. Ultralong spin coherence time in isotopically engineered diamond. *Nature Materials*, 8(5):383–387, 2009.

[76] J. Choi, S. Choi, G. Kucsko, P. C. Maurer, B. J. Shields, H. Sumiya, S. Onoda, J. Isoya, E. Demler, F. Jelezko, et al. Depolarization dynamics in a strongly interacting solid-state spin ensemble. *Physical review letters*, 118(9):093601, 2017.

[77] C. Belthangady, N. Bar-Gill, L. M. Pham, K. Arai, D. Le Sage, P. Cappellaro, and R. L. Walsworth. Dressed-state resonant coupling between bright and dark spins in diamond. *Physical review letters*, 110(15):157601, 2013.

[78] A. D. Mirlin, Y. V. Fyodorov, F.-M. Dittes, J. Quezada, and T. H. Seligman. Transition from localized to extended eigenstates in the ensemble of power-law random banded matrices. *Physical Review E*, 54(4):3221, 1996.

[79] V. Kravtsov, O. Yevtushenko, P. Snajberk, and E. Cuevas. Lévy flights and multifractality in quantum critical diffusion and in classical random walks on fractals. *Physical Review E*, 86(2):021136, 2012.

[80] P. C. Maurer, J. R. Maze, P. L. Stanwix, L. Jiang, A. V. Gorshkov, A. A. Zibrov, B. Harke, J. S. Hodges, A. S. Zibrov, A. Yacoby, and others. Far-field optical imaging and manipulation of individual spins with nanoscale resolution. *Nature Physics*, 6(11):912–918, 2010.

[81] P. Hauke, M. Heyl, L. Tagliacozzo, and P. Zoller. Measuring multipartite entanglement through dynamic susceptibilities. *Nature Physics*, 12(8):778, 2016.

[82] S. Choi, N. Y. Yao, and M. D. Lukin. Dynamical engineering of interactions in qudit ensembles. *Physical review letters*, 119(18):183603, 2017.

[83] M. J. Burek, N. P. de Leon, B. J. Shields, B. J. Hausmann, Y. Chu, Q. Quan, A. S. Zibrov, H. Park, M. D. Lukin, and M. Lončar. Free-standing mechanical and photonic nanostructures in single-crystal diamond. *Nano Letters*, 12(12):6084–6089, 2012.

[84] E. Kaminishi, T. Mori, T. N. Ikeda, and M. Ueda. Entanglement pre-thermalization in a one-dimensional Bose gas. *Nature Physics*, 11(12):1050–1056, 2015.

[85] S. Choi, N. Y. Yao, S. Gopalakrishnan, and M. D. Lukin. Quantum control of many-body localized states. *arXiv preprint arXiv:1508.06992*, 2015.

[86] N. Y. Yao, C. R. Laumann, and A. Vishwanath. Many-body localization protected quantum state transfer. *arXiv preprint arXiv:1508.06995*, 2015.

[87] G. De Lange, Z. Wang, D. Riste, V. Dobrovitski, and R. Hanson. Universal dynamical decoupling of a single solid-state spin from a spin bath. *Science*, 330(6000):60–63, 2010.

[88] J. Waugh, L. Huber, and U. Haeberlen. Approach to high-resolution nmr in solids. *Physical Review Letters*, 20(5):180, 1968.

[89] R. Nandkishore and D. A. Huse. Many-body localization and thermalization in quantum statistical mechanics. *Annu. Rev. Condens. Matter Phys.*, 6(1):15–38, 2015.

[90] D. A. Abanin, W. De Roeck, and F. Huveneers. Exponentially slow heating in periodically driven many-body systems. *Physical review letters*, 115(25):256803, 2015.

[91] P. Bruno. Impossibility of spontaneously rotating time crystals: a no-go theorem. *Physical review letters*, 111(7):070402, 2013.

[92] H. Watanabe and M. Oshikawa. Absence of quantum time crystals. *Phys. Rev. Lett.*, 114:251603, Jun 2015.

[93] D. V. Else, B. Bauer, and C. Nayak. Prethermal phases of matter protected by time-translation symmetry. *Physical Review X*, 7(1):011026, 2017.

[94] C. W. von Keyserlingk and S. L. Sondhi. Phase structure of one-dimensional interacting Floquet systems. II. Symmetry-broken phases. *Phys. Rev. B*, 93:245146, Jun 2016.

[95] T.-Y. Li and J. A. Yorke. Period three implies chaos. *The American Mathematical Monthly*, 82(10):985–992, 1975.

[96] D. A. Abanin, W. De Roeck, and F. Huveneers. Theory of many-body localization in periodically driven systems. *Annals of Physics*, 372:1–11, 2016.

[97] D. Abanin, W. De Roeck, W. W. Ho, and F. Huveneers. A rigorous theory of many-body prethermalization for periodically driven and closed quantum systems. *Communications in Mathematical Physics*, 354(3):809–827, 2017.

[98] D. A. Abanin, W. De Roeck, W. W. Ho, and F. Huveneers. Effective hamiltonians, prethermalization, and slow energy absorption in periodically driven many-body systems. *Physical Review B*, 95(1):014112, 2017.

[99] D. B. Gutman, I. V. Protopopov, A. L. Burin, I. V. Gornyi, R. A. Santos, and A. D. Mirlin. Energy transport in the anderson insulator. *Phys. Rev. B*, 93:245427, Jun 2016.

[100] J. M. Deutsch. Quantum statistical mechanics in a closed system. *Phys. Rev. A*, 43(4):2046, 1991.

[101] M. Srednicki. Chaos and quantum thermalization. *Phys. Rev. E*, 50(2):888, 1994.

[102] M. Rigol, V. Dunjko, and M. Olshanii. Thermalization and its mechanism for generic isolated quantum systems. *Nature*, 452(7189):854, 2008.

[103] L. D'Alessio, Y. Kafri, A. Polkovnikov, and M. Rigol. From quantum chaos and eigenstate thermalization to statistical mechanics and thermodynamics. *Advances in Physics*, 65(3):239–362, 2016.

[104] F. Borgonovi, F. Izrailev, L. Santos, and V. Zelevinsky. Quantum chaos and thermalization in isolated systems of interacting particles. *Physics Reports*, 626:1–58, 2016.

[105] G. Casati and B. Chirikov. *Quantum chaos: between order and disorder*. Cambridge University Press, 2006.

[106] I. Gornyi, A. Mirlin, and D. Polyakov. Interacting electrons in disordered wires: Anderson localization and low-t transport. *Phys. Rev. Lett.*, 95(20):206603, 2005.

[107] D. A. Abanin, E. Altman, I. Bloch, and M. Serbyn. Ergodicity, entanglement and many-body localization. *arXiv preprint arXiv:1804.11065*, 2018.

[108] P. Roushan, C. Neill, J. Tangpanitanon, V. Bastidas, A. Megrant, R. Barends, Y. Chen, Z. Chen, B. Chiaro, A. Dunsworth, et al. Spectroscopic signatures of localization with interacting photons in superconducting qubits. *Science*, 358(6367):1175–1179, 2017.

[109] K. X. Wei, C. Ramanathan, and P. Cappellaro. Exploring localization in nuclear spin chains. *Phys. Rev. Lett.*, 120:070501, Feb 2018.

[110] W. W. Ho, S. Choi, M. D. Lukin, and D. A. Abanin. Critical time crystals in dipolar systems. *Phys. Rev. Lett.*, 119(1):010602, 2017.

[111] J. Rovny, R. L. Blum, and S. E. Barrett. Observation of discrete-time-crystal signatures in an ordered dipolar many-body system. *Phys. Rev. Lett.*, 120:180603, May 2018.

[112] S. Pal, N. Nishad, T. S. Mahesh, and G. J. Sreejith. Temporal order in periodically driven spins in star-shaped clusters. *Phys. Rev. Lett.*, 120:180602, May 2018.

[113] T. Mori, T. Kuwahara, and K. Saito. Rigorous bound on energy absorption and generic relaxation in periodically driven quantum systems. *Phys. Rev. Lett.*, 116:120401, Mar 2016.

[114] T. Kuwahara, T. Mori, and K. Saito. Floquet–magnus theory and generic transient dynamics in periodically driven many-body quantum systems. *Annals of Physics*, 367:96–124, 2016.

[115] A. R. Kolovsky and A. Buchleitner. Quantum chaos in the bose-hubbard model. *EPL (Europhysics Letters)*, 68(5):632, 2004.

[116] A. Tomadin, R. Mannella, and S. Wimberger. Many-body interband tunneling as a witness of complex dynamics in the bose-hubbard model. *Phys. Rev. Lett.*, 98(13):130402, 2007.

[117] L. F. Santos, F. Borgonovi, and F. M. Izrailev. Chaos and statistical relaxation in quantum systems of interacting particles. *Phys. Rev. Lett.*, 108(9):094102, 2012.

[118] A. Safavi-Naini, M. Wall, O. Acevedo, A. Rey, and R. Nandkishore. Quantum dynamics of disordered spin chains with power-law interactions. *arXiv preprint arXiv:1806.03339*, 2018.

[119] C. W. von Keyserlingk and S. L. Sondhi. Phase structure of one-dimensional interacting floquet systems. i. abelian symmetry-protected topological phases. *Phys. Rev. B*, 93:245145, Jun 2016.

[120] R. Roy and F. Harper. Abelian floquet symmetry-protected topological phases in one dimension. *Physical Review B*, 94(12):125105, 2016.

[121] D. V. Else and C. Nayak. Classification of topological phases in periodically driven interacting systems. *Phys. Rev. B*, 93(20):201103, 2016.

[122] F. Nathan, D. Abanin, E. Berg, N. H. Lindner, and M. S. Rudner. Stability of anomalous floquet insulators. *arXiv preprint arXiv:1712.02789*, 2017.

[123] S. Choi, N. Y. Yao, and M. D. Lukin. Quantum metrology based on strongly correlated matter. *arXiv preprint arXiv:1801.00042*, 2017.

[124] B. P. Lanyon, C. Hempel, D. Nigg, M. Müller, R. Gerritsma, F. Zähringer, P. Schindler, J. Barreiro, M. Rambach, G. Kirchmair, et al. Universal digital quantum simulation with trapped ions. *Science*, 334(6052):57–61, 2011.

[125] L. F. Santos, F. Borgonovi, and G. L. Celardo. Cooperative shielding in many-body systems with long-range interaction. *Phys. Rev. Lett.*, 116(25):250402, 2016.

[126] K. Tikhonov and A. Mirlin. Many-body localization transition with power-law interactions: Statistics of eigenstates. *Phys. Rev. B*, 97(21):214205, 2018.

[127] G. Tino and F. Vetrano. Is it possible to detect gravitational waves with atom interferometers? *Classical and Quantum Gravity*, 24(9):2167, 2007.

[128] F. Casola, T. van der Sar, and A. Yacoby. Probing condensed matter physics with magnetometry based on nitrogen-vacancy centres in diamond. *Nature Reviews Materials*, 3(1):17088, 2018.

[129] N. Aslam, M. Pfender, P. Neumann, R. Reuter, A. Zappe, F. F. de Oliveira, A. Denisenko, H. Sumiya, S. Onoda, J. Isoya, et al. Nanoscale nuclear magnetic resonance with chemical resolution. *Science*, 357(6346):67–71, 2017.

[130] D. R. Glenn, D. B. Bucher, J. Lee, M. D. Lukin, H. Park, and R. L. Walsworth. High-resolution magnetic resonance spectroscopy using a solid-state spin sensor. *Nature*, 555(7696):351, 2018.

[131] P. Mansfield. Symmetrized pulse sequences in high resolution nmr in solids. *Journal of Physics C: Solid State Physics*, 4(11):1444, 1971.

[132] D. Burum and W. Rhim. Analysis of multiple pulse nmr in solids. iii. *The Journal of Chemical Physics*, 71(2):944–956, 1979.

[133] D. Cory, J. Miller, and A. Garroway. Time-suspension multiple-pulse sequences: Applications to solid-state imaging. *Journal of magnetic resonance*, 90:205–213, 1990.

[134] J. Taylor, P. Cappellaro, L. Childress, L. Jiang, D. Budker, P. Hemmer, A. Yacoby, R. Walsworth, and M. Lukin. High-sensitivity diamond magnetometer with nanoscale resolution. *Nature Physics*, 4(10):810, 2008.

[135] U. Haeberlen and J. Waugh. Coherent averaging effects in magnetic resonance. *Physical Review*, 175(2):453, 1968.

[136] C. L. Degen, F. Reinhard, and P. Cappellaro. Quantum sensing. *Reviews of modern physics*, 89(3):035002, 2017.

[137] R. Schirhagl, K. Chang, M. Loretz, and C. L. Degen. Nitrogen-vacancy centers in diamond: nanoscale sensors for physics and biology. *Annual review of physical chemistry*, 65:83–105, 2014.

[138] C. Degen, M. Poggio, H. Mamin, C. Rettner, and D. Rugar. Nanoscale magnetic resonance imaging. *Proceedings of the National Academy of Sciences*, 106(5):1313–1317, 2009.

[139] F. Dolde, H. Fedder, M. W. Doherty, T. Nöbauer, F. Rempp, G. Balasubramanian, T. Wolf, F. Reinhard, L. C. Hollenberg, F. Jelezko, et al. Electric-field sensing using single diamond spins. *Nature Physics*, 7(6):459, 2011.

[140] M. W. Doherty, V. V. Struzhkin, D. A. Simpson, L. P. McGuinness, Y. Meng, A. Stacey, T. J. Karle, R. J. Hemley, N. B. Manson, L. C. Hollenberg, et al. Electronic properties and metrology applications of the diamond nv- center under pressure. *Physical review letters*, 112(4):047601, 2014.

[141] T. Mittiga, S. Hsieh, C. Zu, B. Kobrin, F. Machado, P. Bhattacharyya, N. Rui, A. Jarmola, S. Choi, D. Budker, et al. Imaging the local charge environment of nitrogen-vacancy centers in diamond. *Physical review letters*, 121(24):246402, 2018.

[142] P. Neumann, I. Jakobi, F. Dolde, C. Burk, R. Reuter, G. Waldherr, J. Honert, T. Wolf, A. Brunner, J. H. Shim, et al. High-precision nanoscale temperature sensing using single defects in diamond. *Nano letters*, 13(6):2738–2742, 2013.

[143] D. M. Toyli, F. Charles, D. J. Christle, V. V. Dobrovitski, and D. D. Awschalom. Fluorescence thermometry enhanced by the quantum coherence of single spins in diamond. *Proceedings of the National Academy of Sciences*, 110(21):8417–8421, 2013.

[144] E. L. Hahn. Spin echoes. *Physical review*, 80(4):580, 1950.

[145] H. Y. Carr and E. M. Purcell. Effects of diffusion on free precession in nuclear magnetic resonance experiments. *Physical review*, 94(3):630, 1954.

[146] S. Meiboom and D. Gill. Modified spin-echo method for measuring nuclear relaxation times. *Review of scientific instruments*, 29(8):688–691, 1958.

[147] T. Gullion, D. B. Baker, and M. S. Conradi. New, compensated carr-purcell sequences. *Journal of Magnetic Resonance (1969)*, 89(3):479–484, 1990.

[148] T. Wolf, P. Neumann, K. Nakamura, H. Sumiya, T. Ohshima, J. Isoya, and J. Wrachtrup. Subpicotesla diamond magnetometry. *Physical Review X*, 5(4):041001, 2015.

[149] N. Khaneja, T. Reiss, C. Kehlet, T. Schulte-Herbrüggen, and S. J. Glaser. Optimal control of coupled spin dynamics: design of nmr pulse sequences by gradient ascent algorithms. *Journal of magnetic resonance*, 172(2):296–305, 2005.

[150] P. Doria, T. Calarco, and S. Montangero. Optimal control technique for many-body quantum dynamics. *Physical review letters*, 106(19):190501, 2011.

[151] G. De Lange, T. Van Der Sar, M. Blok, Z.-H. Wang, V. Dobrovitski, and R. Hanson. Controlling the quantum dynamics of a mesoscopic spin bath in diamond. *Scientific reports*, 2:382, 2012.

[152] H. S. Knowles, D. M. Kara, and M. Atatüre. Observing bulk diamond spin coherence in high-purity nanodiamonds. *Nature materials*, 13(1):21, 2014.

[153] E. Bauch, C. A. Hart, J. M. Schloss, M. J. Turner, J. F. Barry, P. Kehayias, S. Singh, and R. L. Walsworth. Ultralong dephasing times in solid-state spin ensembles via quantum control. *Physical Review X*, 8(3):031025, 2018.

[154] D. Le Sage, L. M. Pham, N. Bar-Gill, C. Belthangady, M. D. Lukin, A. Yacoby, and R. L. Walsworth. Efficient photon detection from color centers in a diamond optical waveguide. *Physical Review B*, 85(12):121202, 2012.

[155] H. Clevenson, M. E. Trusheim, C. Teale, T. Schröder, D. Braje, and D. Englund. Broadband magnetometry and temperature sensing with a light-trapping diamond waveguide. *Nature Physics*, 11(5):393, 2015.

[156] K. Fang, V. M. Acosta, C. Santori, Z. Huang, K. M. Itoh, H. Watanabe, S. Shikata, and R. G. Beausoleil. High-sensitivity magnetometry based on quantum beats in diamond nitrogen-vacancy centers. *Physical review letters*, 110(13):130802, 2013.

[157] H. Mamin, M. Sherwood, M. Kim, C. Rettner, K. Ohno, D. Awschalom, and D. Rugar. Multipulse double-quantum magnetometry with near-surface nitrogen-vacancy centers. *Physical review letters*, 113(3):030803, 2014.

[158] A. Edmonds, U. D?Haenens-Johansson, R. Cruddace, M. Newton, K.-M. Fu, C. Santori, R. Beausoleil, D. Twitchen, and M. Markham. Production of oriented nitrogen-vacancy color centers in synthetic diamond. *Physical Review B*, 86(3):035201, 2012.

[159] T. Fukui, Y. Doi, T. Miyazaki, Y. Miyamoto, H. Kato, T. Matsumoto, T. Makino, S. Yamasaki, R. Morimoto, N. Tokuda, et al. Perfect selective alignment of nitrogen-vacancy centers in diamond. *Applied Physics Express*, 7(5):055201, 2014.

[160] J. Michl, T. Teraji, S. Zaiser, I. Jakobi, G. Waldherr, F. Dolde, P. Neumann, M. W. Doherty, N. B. Manson, J. Isoya, et al. Perfect alignment and preferential orientation of nitrogen-vacancy centers during chemical vapor deposition diamond growth on (111) surfaces. *Applied Physics Letters*, 104(10):102407, 2014.

[161] M. Lesik, T. Plays, A. Tallaire, J. Achard, O. Brinza, L. William, M. Chipaux, L. Toraille, T. Debuisschert, A. Gicquel, et al. Preferential orientation of nv defects in cvd diamond films grown on (113)-oriented substrates. *Diamond and Related Materials*, 56:47–53, 2015.

[162] T. R. Eichhorn, C. A. McLellan, and A. C. Jayich. Optimizing the formation of depth-confined nitrogen vacancy center spin ensembles in diamond for quantum sensing. *arXiv preprint arXiv:1901.11519*, 2019.

[163] D. Rugar, H. Mamin, M. Sherwood, M. Kim, C. Rettner, K. Ohno, and D. Awschalom. Proton magnetic resonance imaging using a nitrogen–vacancy spin sensor. *Nature nanotechnology*, 10(2):120, 2015.

[164] T. Häberle, D. Schmid-Lorch, F. Reinhard, and J. Wrachtrup. Nanoscale nuclear magnetic imaging with chemical contrast. *Nature nanotechnology*, 10(2):125, 2015.

[165] S. J. DeVience, L. M. Pham, I. Lovchinsky, A. O. Sushkov, N. Bar-Gill, C. Belthangady, F. Casola, M. Corbett, H. Zhang, M. Lukin, et al. Nanoscale nmr spectroscopy and imaging of multiple nuclear species. *Nature Nanotechnology*, 10(2):129, 2015.

[166] J. Choi, H. Zhou, S. Choi, R. Landig, W. W. Ho, J. Isoya, F. Jelezko, S. Onoda, H. Sumiya, D. A. Abanin, et al. Probing quantum thermalization of a disordered dipolar spin ensemble with discrete time-crystalline order. *Physical Review Letters*, 122(4):043603, 2019.

[167] M. Kitagawa and M. Ueda. Squeezed spin states. *Physical Review A*, 47(6):5138, 1993.

[168] C. Gardiner and P. Zoller. *Quantum Noise: A Handbook of Markovian and Non-Markovian Quantum Stochastic Methods with Applications to Quantum Optics*, volume 56. Springer Science & Business Media, 2004.

[169] E. Van Oort and M. Glasbeek. Electric-field-induced modulation of spin echoes of nv centers in diamond. *Chemical Physics Letters*, 168(6):529–532, 1990.

[170] R. Giri, F. Gorrini, C. Dorigoni, C. Avalos, M. Cazzanelli, S. Tambalo, and A. Bifone. Coupled charge and spin dynamics in high-density ensembles of nitrogen-vacancy centers in diamond. *Physical Review B*, 98(4):045401, 2018.

[171] T. Staudacher, F. Shi, S. Pezzagna, J. Meijer, J. Du, C. A. Meriles, F. Reinhard, and J. Wrachtrup. Nuclear magnetic resonance spectroscopy on a (5-nanometer) 3 sample volume. *Science*, 339(6119):561–563, 2013.

[172] F. Machado, G. D. Meyer, D. V. Else, C. Nayak, and N. Y. Yao. Exponentially slow heating in short and long-range interacting floquet systems. *arXiv preprint arXiv:1708.01620*, 2017.